Statistical Analysis, Monitoring and Control of the Production of High Performance Lightweight Metal Matrix Nanocomposites

Jianguo Wu

A dissertation submitted in partial fulfillment of the requirements for the degree of

Doctor of Philosophy

(Industrial and Systems Engineering)

at the

UNIVERSITY OF WISCONSIN-MADISON

2015

Data of final oral examination: 06/09/2015

The dissertation is approved by the following members of the Final Oral Committee:

Shiyu Zhou, Committee Chair, Professor, Department of Industrial and Systems Engineering

Oguzhan Alagoz, Associate Professor, Department of Industrial and Systems Engineering

Ananth Krishnamurthy, Associate Professor, Department of Industrial & Systems Engineering

Jingshan Li, Professor, Department of Industrial and Systems Engineering

Sijian Wang, Associate Professor, Department of Statistics

ACKNOWLEDGEMENTS

The research presented in this dissertation benefited from valuable insights and support of many people. It is my pleasure to express my sincere gratitude to all of them.

First and foremost, I would like to thank my PhD advisor, Prof. Shiyu Zhou for his outstanding guidance, mentorship and full support in my PhD studies. Words cannot express my heartfelt gratitude for his efforts towards my development as a good researcher and a future academic mentor. I have been so lucky to benefit from not only his expertise in academic research, but also his great personality in all other aspects.

I would also like to thank my doctoral committee members Prof. Ananth Krishnamurthy, Prof. Oguzhan Alagoz, Prof. Jingshan Li, and Prof. Sijian Wang for serving on my committee and providing helpful suggestions to improve my dissertation. I would like to thank Prof. Kam-Wah Tsui from Department of Statistics for serving on my committee in my preliminary exam.

I would like to give my sincere gratitude to Prof. Xiaochun Li, one main collaborator of my research. Most of my research experiments have been conducted in his laboratory. Without his full support and guidance, my research study would not have been so smooth. I have benefited a lot from his energetic attitude towards research, his easy-going personality and his full support in my research, job and scholarship applications.

I want to thank Prof. Yong Chen from The University of Iowa.. Prof. Chen's insightful guidance and comments helped me a lot in my research.

I wish to thank Dr. Hongseok Choi, Dr. Lianyi Chen, Jiaquan Xu and Yi Sun from Prof. Xiaochun Li's lab. They helped me a lot in fabricating nanocomposites samples and taking microscopic images.

My thanks also go to my friends in my lab: Qiang Zhou, Yuan Yuan, Devashish Das, Junbo Son, Yuhang Liu and Raed Kontar. Thank you for being supportive and accompanying me in my PhD studies. You really make my life in Madison enjoyable and memorable.

Lastly and most importantly, I want to thank my wife Liang Xie, my parents and parents-in-law for their unconditional love, support and encouragement. Without their support, I would not have made this achievement in my life. My wife's encouragement and support is one important reason that directs me towards an academic life. I also want to give my special thanks to my parents. I am very lucky to have them as my parents, to have their full support on my education and to make them proud.

ABSTRACT

Light metal (e.g. Al, Mg) based metal matrix nanocomposites (MMNCs), where metal alloys are reinforced with ceramic nanoparticles, have been intensively studied recently because of their significant properties, such as high strength, machinability, and creep resistance at elevated temperature. While light metal MMNCs promise to offer superior properties, the fabrication of high quality MMNCs is very challenging. It is extremely difficult for the conventional methods, such as stir casting, to distribute and disperse nanoparticles uniformly in metal melts. Due to their large surface-to-volume ratio and poor wettabililty in most molten metal, nanoparticles tend to agglomerate and cluster together, which is detrimental to the final performance of MMNCs. Ultrasonic dispersion assisted fabrication of MMNCs is a very promising technology that can meet the needs of both uniform distribution of nanoparticles and fabrication of large and complex structural components. However, there are two significant and fundamental issues in scaling up the system for mass production of high quality MMNCs. First, there is a lack of in-situ process optimization and monitoring method to control the fabrication quality. Second, there are no effective and easy-to-implement quality inspection techniques to evaluate the quality of the fabricated MMNCs. The objective of this dissertation is to address these two issues, i.e., to control the fabrication quality from both *on-line* and *off-line* aspects, and thus to facilitate the transition of this emerging process from lab environment to a scale-up industrial production.

To control and optimize the nanoparticle dispersion process, a high speed data acquisition system is designed, which is able to collect the cavitation noise signals from the high temperature molten metal with high sampling frequency. Based on the cavitation physics, acoustic attenuation theory and experimental observations, the nanoparticles are found to be well

dispersed when the cavitation noise signals are steady. Therefore the in-situ monitoring and control of nanoparticle dispersion is formulated to an on-line steady state detection problem. Two robust on-line steady state detection algorithms are developed using multiple change-point models and Bayesian inference techniques. The first algorithm is based on the particle filtering techniques while the second one uses the exact Bayesian inference method. Extensive numerical analysis shows that the proposed methods are much more accurate and robust than other existing methods.

Ultrasonic non-destructive testing is used to evaluate the microstructures of the fabricated MMNCs. The between-curve variation of ultrasonic attenuation curves is found to be highly related with the distribution of nanoparticle reinforcements and uniformity of microstructures. A hypothesis test based on the estimated attenuation variance is developed and it could accurately differentiate bad samples from good ones. A hierarchical linear model with level-2 variance heterogeneity is proposed to describe the relationship between ultrasonic attenuation profiles and the microstructural parameters for ultrasonic attenuation based quality control. An integrated Bayesian framework for model estimation, model selection, and inference of the microstructural parameters is proposed and implemented through blocked Gibbs sampling, intrinsic Bayes factor, and importance sampling. The effectiveness of the proposed approach is illustrated through intensive numerical and case studies.

Specific contributions of this thesis include: (1) a novel data acquisition system to monitor the cavitation process, (2) discovery of the relation between the ultrasonic noise of cavitation and nanoparticle dispersion status, (3) two robust on-line steady state detection algorithms which can be used not only in the monitoring of the ultrasonic dispersion process, but also in many other

process monitoring and control areas, (4) discovery of the qualitative relation between ultrasonic attenuation and microstructures of MMNCs, (5) hierarchical linear modeling of ultrasonic attenuation profiles for quality inference and control of MMNCs.

In the future, the dissertation work can be extended in the following aspects: (1) further signal analysis and experimental verification for particle dispersion process monitoring; (2) statistical process control charts on attenuation profiles for ultrasonic attenuation based quality inspection of MMNCs; (3) 3-dimention microstructural modeling, wave propagation simulation and uncertainty quantification.

TABLE OF CONTENTS

LIST OF FIGURES

LIST OF TABLES

1 Introduction

1.1 Background

1.1.1 Lightweight Metal Based Metal-matrix Nanocomposites

Due to the increasing concerns on the energy efficiency and carbon emission, the need for structural components of high performance lightweight material is growing continuously, especially in the aerospace and automobile industries. Energy saving and carbon emission reduction will result from the application of lightweight and high strength materials. For example, it saves 7% fuel consumption for every 10% reduction in vehicle mass [1]. In the commercial aircraft industry, weight savings has been estimated to be $450/kg, and in spacecraft, it can reach up to $40,000/kg [2]. Light weighted alloys, e.g., aluminum alloys, are promising light weight materials, due to their high strength-to-weight ratio, long fatigue life and excellent damping characteristics. They are considered to be an alternative to conventional steels and the more expensive super alloys. For example, the amount of aluminum per North American light vehicle has increased from 258 lb. in 2000 to about 365 lb. in 2014 and is forecasted to grow significantly to 547 lb. by 2025 (Figure 1-1). Aluminum alloys account for nearly 80% of the materials used in the components of the aircrafts.

In order to achieve better energy efficiency and higher material properties, considerable research effort has been directed to the metal-matrix composites (MMCs), a kind of hybrid material where micro-scale reinforcements are embedded into a ductile metal matrix to obtain

characteristics that are superior to the original metal matrix material [3]. MMCs combine metallic properties (high ductility and toughness) with reinforcements characteristics (high strength and modulus, etc), thus leading to a greater strength to shear and compression, higher stiffness and higher service temperature capabilities, etc. Reinforcing materials include carbides (e.g., SiC, B_4C), nitrides (e.g., Si_3N_4, AlN), oxides (e.g., Al_2O_3, SiO_2), as well as elemental materials (e.g., C, Si) [4]. The reinforcements may be in the form of continuous fibers [5, 6], particles [4, 7, 8], and whiskers [9] etc.
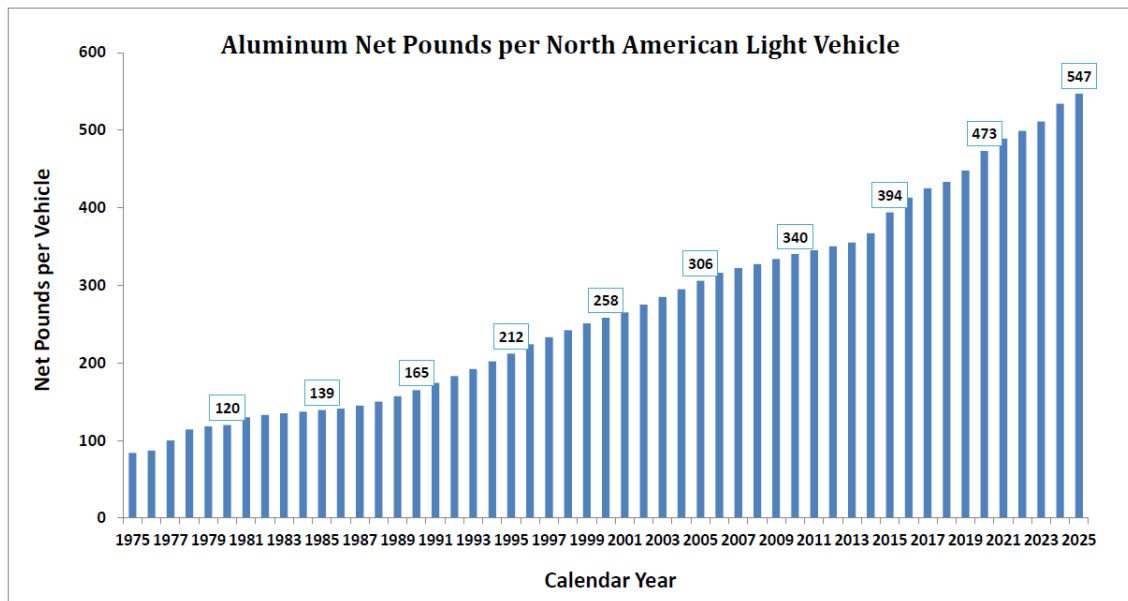
Figure 1-1: Aluminum net pounds per North American light vehicle [10]

Although MMCs offer many advantages, they do have shortcomings, such as low fracture toughness, low ductility and creep resistance, and low machinability. Metal matrix nanocomposites (MMNCs), where the ceramic nanoparticles (less than 100nm) are used as the reinforcement, have merged as a promising alternative to overcome the limitations of the conventional MMCs. Uniformly dispersed nanoparticles, even with a very low volume fraction,

provides a good balance between the strengthener and inter-particle spacing effects to maximize the yield strength and creep resistance while retaining good matrix ductility. Moreover, MMNCs could offer a significant improved performance at elevated temperatures [11].

1.1.2 Challenges in the Fabrication of MMNCs

While nanoparticle reinforced composites promise to offer superior properties, the fabrication of MMNCs is very difficult. Evenly dispersing the nanoparticles into the metal matrix is one of the key challenges in the mass production of MMNCs. The current processing technologies are still neither reliable nor cost effective to produce bulk MMNCs with reproducible structures and properties. Mechanical mixing (e.g. high energy ball milling) of metallic and ceramic powders [12-14] is generally used for the blending of powders to fabricate bulk MMNCs. This procedure is energy and time consuming as well as costly. Particle clustering and agglomeration present serious problems for the uniform blending of matrix and nanoparticles. In-situ reinforcement formation is still neither reliable nor flexible for high volume production of structural components with complex shapes [15-18]. Conventional solidification processing methods, such as mechanical stir casting[19] and squeeze casting [9] have been applied to produce microparticle (sizes above 5~10µm) reinforced aluminum MMCs. Stir casting is an versatile and cost-effective method for near-net-shape formation of bulk composites into complex shapes. It would be desirable to produce as-cast lightweight components of MMNCs with good reinforcement distribution and structural integrity. However, it is extremely difficult for the conventional mechanical stirring method to distribute and disperse nano-scale particles uniformly in metal melts. Due to their large surface-to-volume ratio and their poor wettability in most metal melts, nanoparticles tend to agglomerate and cluster together [20-22], as shown in

(Figure 1-2), which is detrimental for the final component performances and its machinability. Therefore, there is a strong need of a reliable and cost effective dispersion of nanoparticles in metal melts for the solidification processing of bulk high performance MMNCs.
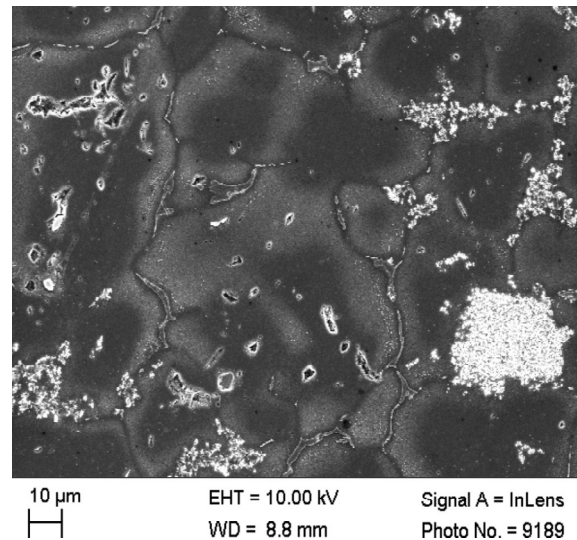
Figure 1-2: Clustered nanoparticles (Al_2O_3) within the A206 metal matrix [23]

1.1.3 Ultrasonic Cavitation based Fabrication of MMNCs

Ultrasonic cavitation is an enabling technology for particle dispersion in liquid [11, 24, 25]. High-intensity ultrasonic waves (with intensity above $10^6 W/m^2$ and frequency above 18KHz) are cost effective and reliable for liquid-based materials processing in that they generate important non-linear effects in liquids. The basic idea is to shoot a beam of ultrasonic sound through the particle-liquid system. Then due to local violent pressure variations caused by ultrasonic vibrations [26], we will get a "cavitation" phenomenon, which refers to the formation, growth, oscillation, and implosive collapse of gas or vapor bubbles in liquids caused by the ultrasound, as shown in Figure 1-3. Based on the duration of bubbles, the cavitation is classified into two types: stable cavitation and transient cavitation [27]. For the stable cavitation, the bubbles oscillate non-

linearly around the equilibrium size. They are relatively stable and last for many cycles of the acoustic pressure. While for the transient cavitation, the bubbles usually oscillate for much shorter time. They explosively grow into a cavity with a size of many times of their original sizes and then collapse violently. When the bubble collapses, it produces transient micro "hot spot" that can have temperatures of about 5000K, pressures above 1000 atms, and heating and cooling rates above 10^{10} K/s, high speed liquid jets of up to 300m/s [26]. Moreover, acoustic streaming can induce violent stirring in liquids [28]. Due to these intense effects, the cavitation can effectively mix and also break particle agglomerates into well-dispersed particles in the liquid.

With the assistance of ultrasonic cavitation, the fabrication of micro/nanoparticle reinforced metal matrix composites has been successfully demonstrated [11, 20, 24, 29]. The dispersion of nanoparticles in aluminum A356 alloy melts was attained using the ultrasonic cavitation based technique on small, laboratory samples (1~2lbs). With only 1.0 wt.% of nano-sized SiC reinforcement, the ultimate tensile strength and yield strength of the aluminum alloy A356 were enhanced approximately 60%~80% while the ductility was retained [24]. The study on micro/nano structures of the nanocomposites validates that a roughly uniform distribution and effective dispersion of nanoparticles in the matrix were achieved, as shown in Figure 1-4. Thus, ultrasonic cavitation is promising as a reliable and cost effective tool for nanoparticle dispersion in metal melts.
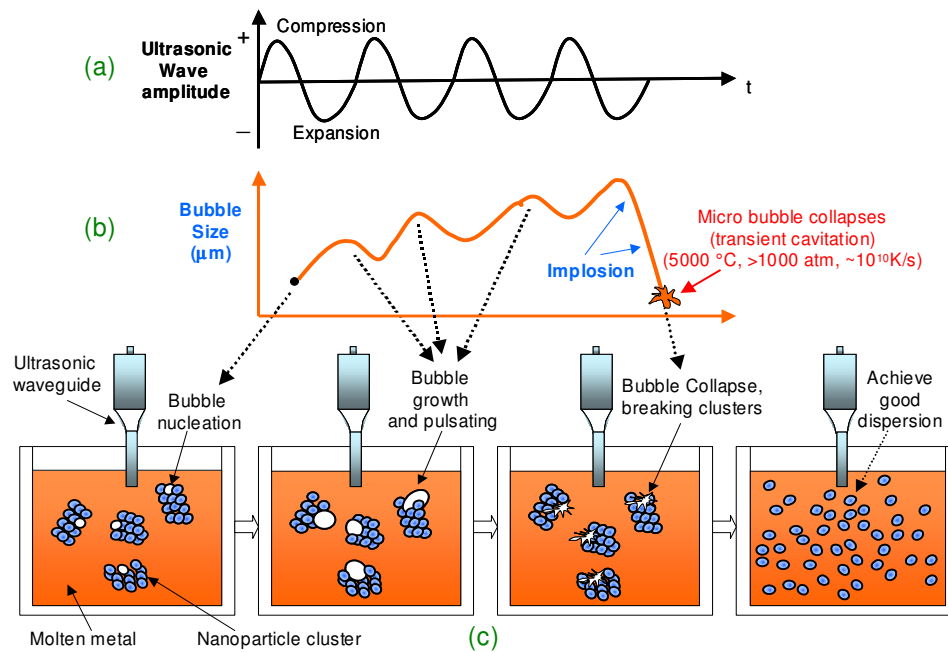
Figure 1-3: Ultrasonic dispersion of nanoparticles in melts
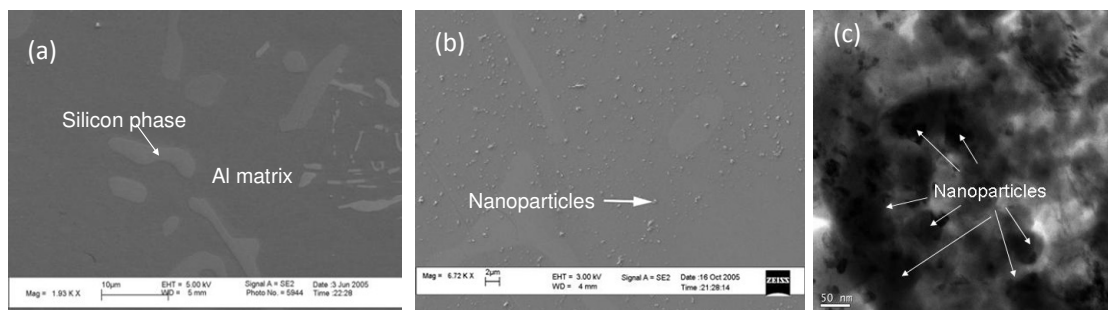
Figure 1-4: (a) Scanning electronic microscope (SEM) image of pure A356 alloy; (b) SEM image of nanoparticle dispersion in A356; (c) transmission electron microscopy (TEM) image of SiC nanoparticles embedded in Al allogy marix

1.2 Motivation and Research Objectives

Although ultrasonic cavitation based fabrication techniques are very promising, there are significant and fundamental challenges in scaling up the system to mass production of high quality MMNCs. The tremendous complexity and the lack of fundamental understanding in the

relationship among the processing parameters (e.g., ultrasonic power, cavitation duration), microstructure and material properties make it very difficult to optimize and control the process effectively for a scale-up production. Besides, to reach an economical scale-up production, an effective yet easy-to-implement quality inspection technique to evaluate the quality of nanoparticle dispersion in the final product and the quality of microstructures is required. At present the standard inspection method is based on the microscopic images, e.g., SEM images, optical microscope images and TEM images, which are costly and time-consuming to obtain. The skill requirement for foundry workers is also high to operate these microscopes. Therefore, a lack of easy and effective quality inspection techniques will also prevent scaling up the production from small laboratory samples of simple geometry to mass industrial production.
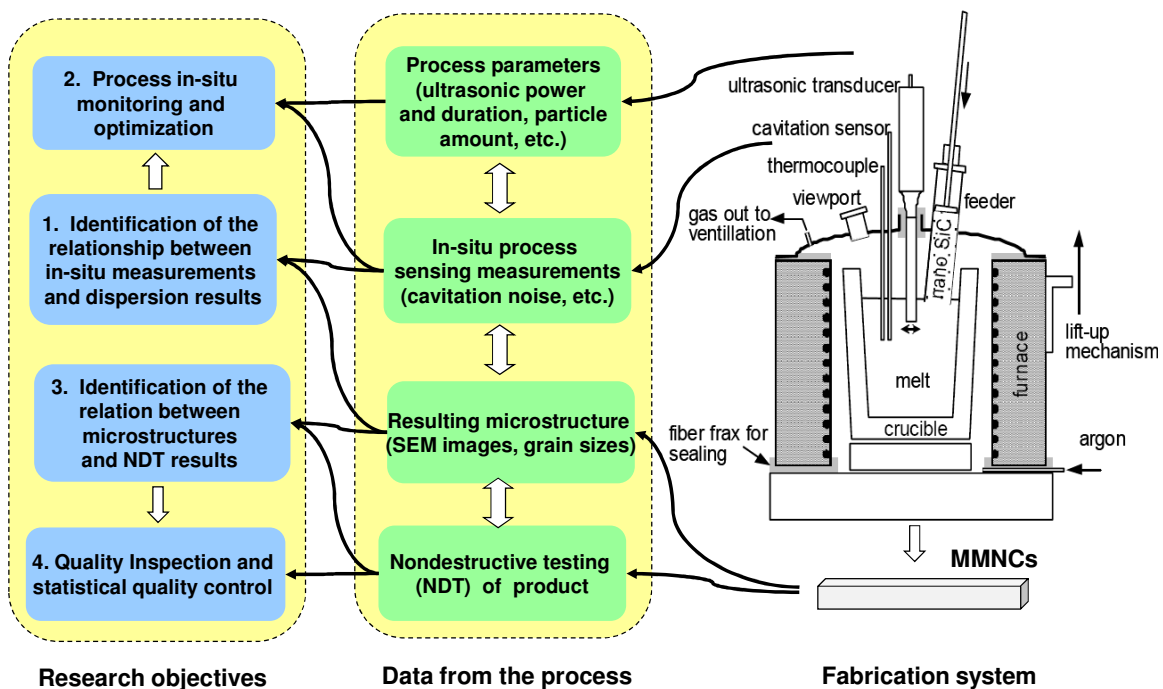
Figure 1-5: Research objectives of this dissertation

The fundamental objective of this dissertation is to address these two abovementioned critical issues, i.e., to control the quality of the fabrication of MMNCs from both ***on-line*** and ***off-line*** aspects. The overall framework of this dissertation is illustrated in Figure 1-5. In the *on-line* aspect, the research objective is to discover the fundamental relationship between the quality of particle dispersion and the in-situ process sensing measurements through the integration of statistical and physical analysis and then utilize this relationship for process optimization and control. In the *off-line* aspect, the research objective is to develop a fast-yet-effective ultrasonic nondestructive testing (NDT) based quality inspection method. Similarly, we have two tasks in this objective: to identify the relationship between the microstructures and the NDT measurements, and then based on this relationship to develop quality inspection and control methods.

The experimental set-up used to fabricate MMNCs is depicted in the right panel of Figure 1-5. The system consists of a resistance heating furnace to melt the alloys, a nanoparticle feeding system, gas protection system and an ultrasonic processing system. Commercially available ultrasonic sonicator with acoustic energy up to 3.5 KW and frequency of 20 KHz is used. The ultrasonic vibrations are transferred into metal melts via a niobium ultrasonic probe, which can withstand temperatures as high as 1200 °C for 300 hours. Al alloys will be superheated (50~150 °C above its melting temperature) and processed with suitable ultrasonic intensity under the protection of argon. The nanoparticles are fed into the melt through the nanoparticle feeding system during the ultrasonic processing.

The data to be collected in this research include the process parameters (ultrasonic power, cavitation duration, particle volume fraction, etc.), in-situ measurements of cavitation noise

through the acoustic cavitation sensor, microscopic images and NDT measuring data of the fabricated MMNCs, etc.

1.3 Specific Research Tasks and Challenges

The specific tasks and challenges are listed as follows:

(1) **To discover the relationship among the characteristics of the in-situ measured cavitation noise signal, the process parameters and nanoparticle dispersion condition.** There are two big challenges in this task. The first one is the design of high speed data collection system. In the fabrication process, the temperature of the molten alloys can reach up to 1000 °C. How to effectively collect the in-situ noise without damaging the data acquisition system is an issue. Besides, the frequency of cavitation noise is extremely high. In order to fully capture the characteristics of the noise, the sampling frequency is required to be as high as 1 MHz, which results in high requirement on both the sampling frequency and data storage memory. The second challenge is that there is lack of fundamental understanding of how process parameters and nanoparticle dispersion status will influence the cavitation noise signals. The cavitation based dispersion process involves many complex physical processes, which makes the relationship difficult to identify.

(2) **To optimize the fabrication process and develop real-time monitoring algorithms for in-situ process control**. In ultrasonic cavitation based material dispersion and processing, the ultrasonic power and processing time are usually chosen somewhat arbitrarily. Unnecessarily high ultrasonic power level or long processing time may result in waste of time and energy, or even damage of cavitation system, while too low a power level or too short a processing time

may lead to insufficient treatment. Based on the work in task 1, we seek to select optimal processing power and also to determine when to stop the cavitation processing. The challenge of this task is that the developed monitoring and control scheme need to be not only accurate but also timely to detect the nanoparticle dispersion finishing time.

(3) **To identify the qualitative relationship between the microstructures and NDT measurements**. The microstructure provides an ultimate measure of the final product. However, it is very costly to obtain the microstructure images. In this task, we seek to use cheaper ultrasonic testing measurement to qualitatively characterize the MMNCs microstructures. Although ultrasonic testing has been widely used in industry, most of the applications are for flaw detection and dimension measurement. Considerable research has been done to characterize material microstructures using ultrasonic testing, but most of these studies are limited to single-phase or two-phase materials, and also there are no wide industrial applications. Alloys based MMNCs have more than three phases in the microstructures, which makes it challenging to characterize the microstructure quality, especially the distribution of nanoparticles using ultrasonic testing methods.

(4) **To quantitatively evaluate and monitor the quality of the fabricated MMNCs using ultrasonic NDT data**. In the quality inspection, it is critical to infer the dispersion of nanoparticles in microstructures and the grain size of Al primary phase based on the ultrasonic testing measurement. However, due to the complexity of ultrasound propagation in the MMNCs, and the limited experimental data because of the difficulty of fabricating MMNCs samples with planned microstructural features, it is very difficult to get the analytical relationship between the microstructural features (grain size, nanoparticle distribution, etc.) and ultrasonic testing

measurement. In this task, we seek to combine numerical modeling of microstructures and wave propagation, and statistical modeling of attenuation profiles for quality inference and control of MMNCs.

1.4   Outline of the Dissertation

The remainder of the dissertation is organized as follows. Chapter 2 addresses the first task mentioned in the previous section. In this chapter, the relationship among the cavitation noise signals, the processing parameters, and the dispersion status has been identified, which provides insightful guidance to optimize and monitor the micro/nanoparticle dispersion process. It is found that the steady state of the cavitation signal is an indicator of the completeness of the dispersion process. In Chapter 3, a robust steady state detection algorithm is developed, where a multiple change-point model is used to model any signals, and particle filtering techniques are developed and improved to approximate the posterior distribution of model parameters for steady state detection. Chapter 4 proposes an alternative steady state algorithm which applies exact Bayesian inference to the multiple change-point models. This algorithm is more accurate and computationally efficient. Chapter 5 investigates the qualitative relationship between the ultrasonic attenuation profiles and the microstructures of MMNCs. Significant non-uniformity of ultrasonic attenuation is observed on the bad samples with large primary dendrites, long inter-metallic network, and unevenly distributed nanoparticles. Chapter 6 proposes a hierarchical linear model to model the relationship between the microstructural features and the ultrasonic attenuation profiles for quality inference and control. Chapter 7 summarizes the contributions of this dissertation and discusses the future work.

2 Acoustic Emission Monitoring for Ultrasonic Cavitation Based Dispersion Process[*]

In this chapter, a real-time monitoring technique is developed to monitor the micro/nanoparticle dispersion process based on the cavitation noise signals. The contribution of this work is the discovery of the relation between the particle dispersion condition and the characteristics of cavitation noise, or specifically, the formulation of particle dispersion monitoring into the problem of steady state detection, and the guidance of how to select optimal process parameters (i.e., ultrasonic power, processing time) in the ultrasonic cavitation assisted fabrication of MMNCs.

2.1 Overview of Ultrasonic Cavitation

Ultrasonic cavitation is an effective method to disperse micro/nanoparticles [20, 24, 25, 30, 31]. The basic idea is to shoot a beam of ultrasonic sound through the particle-liquid system. Then due to local violent pressure variations caused by ultrasonic vibrations [32], we will get a "cavitation" phenomenon, which refers to the formation, growth, oscillation, and implosive collapse of gas or vapor bubbles in liquids. Based on the duration of bubbles, the cavitation is classified into two types: stable cavitation and transient cavitation [27]. For the stable cavitation,

---

the bubbles oscillate non-linearly around the equilibrium size. They are relatively stable and last for many cycles of the acoustic pressure. While for the transient cavitation, the bubbles usually oscillate for much shorter time. They explosively grow into a cavity with a size of many times of their original sizes and then collapse violently. When the bubble collapses, it produces transient micro "hot spot" that can have temperatures of about 5000 K, pressures above 1000 atms, and heating and cooling rates above 10^{10} K/s, high speed liquid jets of up to 300 m/s [32]. Due to these intense effects, the cavitation can effectively mix and also break particle agglomerates into well-dispersed particles in the liquid.

There are several methods to detect and monitor cavitation process, including high-speed photography [33, 34], laser diffraction technique [35], phase-Doppler technique[35, 36], acoustic attenuation method [37, 38] and cavitation noise spectrum analysis technique [25, 39-44] etc. The cavitation noise spectrum analysis is the most popular method due to its low cost, easiness to implement and its ability to capture various information of cavitation using acoustic transducers. The fundamental mechanism of acoustic cavitation has been experimental and theoretically studied in the last several decades to interpret the cavitation noise spectrum. It is known that the cavitation noise spectrum consists of continuous components and various discrete frequency components [45-48] close to $\frac{nf}{m}$ where f is the fundamental or driving frequency, and m, n are integers. These discrete components are: harmonics ($\frac{n}{m}$ is integer), subharmonics ($n = 1, m = 2,3, ...$) and ultraharmonics ($m > n$, $\frac{n}{m}$ is non-integer). The continuous components are the broadband components (also called "white noise" [27]) that lie between the discrete components. The harmonics of the fundamental frequency are easily explained by the non-linear characteristic of forced pulsations of bubbles [49]. However, for the other components, the origin is still under

debate. Many theories have been proposed [44, 50]. For the origin of "white noise", there also exist different explanations. One explanation is that it originates from the shock waves produced by the collapsing bubbles [40, 51]. Using numerical simulation, Yasui [52] explained that the temporal fluctuation in the number of bubbles results in the broad-band noise. In other words, the transient cavitation results in the broad-band noise. Stable cavitation does not cause the broad-band noise even if it emits shock waves. All these explanations lead to that the broad-band noise can be used as an indicator of the intensity of acoustic cavitation.

Although the mechanism of cavitation has been intensively studied, the works on real-time monitoring of the ultrasonic cavitation based material processing is very limited. The ultrasonic power and processing time are usually chosen somewhat arbitrarily in practice. An unnecessarily high ultrasonic power level or long processing time may result in waste of time and energy, while too low a power level or too short a processing time may lead to insufficient treatment. Some research works have been conducted to study the relationships between the ultrasonic cavitation parameters and processing efficiencies [25, 31, 42]. Although these studies provided insights on how to select optimal processing parameters, these studies are essentially off-line studies on specific system configuration. Thus, the results may not be applicable to general situations since the processing efficiency depends on many factors, such as volume, particle concentration, viscosity and temperature. Therefore an effective on-line technique to monitor the ultrasonic cavitation based dispersion process is critically important in engineering practices.

In this Chapter, we developed a real-time monitoring technique to monitor micro/nanoparticle dispersion in aqueous liquid. This technique is tested in tap water with an addition of Al_2O_3 particles. The remainder of this chapter is organized as follows. In Section 2.2,

the experimental procedure is introduced. Section 2.3 presents descriptive analysis of the acoustic signals collected. Several off-line and on-line steady state detection methods are presented and compared in Section 2.4. The conclusions are presented in Section 2.5.

2.2 Experimental Procedure

The experimental setup mainly consisted of six components: Misonic Sonicator 4000, an ultrasonic horn/probe, a glass beaker, a titanium rod, an acoustic sensor and a Tektronix DPO7354 Oscilloscope, as shown in Figure 2-1.
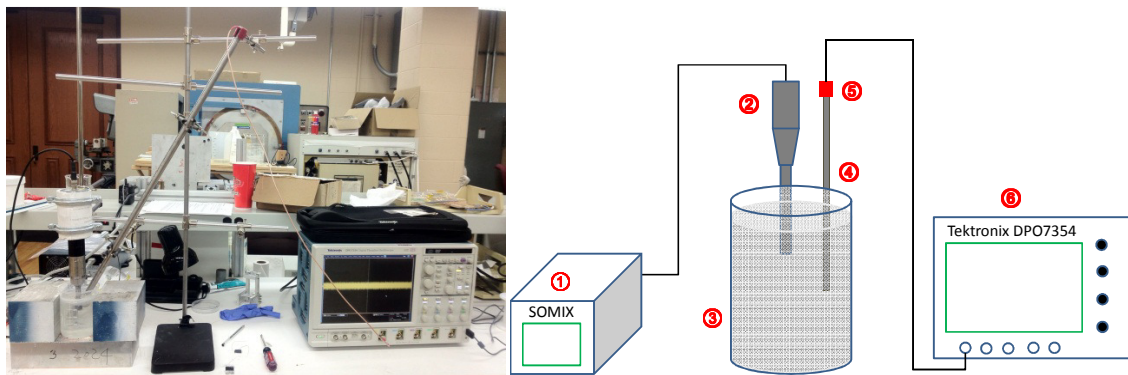
Figure 2-1: Experimental setup (left) and its schematic representation (right): 1. Misonix Sonicator 4000; 2. ultrasonic horn/probe; 3. standard 500 mL glass beaker; 4. titanium rod; 5. acoustic sensor; 6. Tektronix DPO7345 Oscilloscope

The Misonic Sonicator 4000 has an operating frequency of 20 KHz and the output amplitude can be controlled by setting a range from 1 to 100% of the maximum vibration amplitude 55 µm. The tip of the ultrasonic probe, made of niobium alloy C103, is 12.7 mm in diameter. It is positioned in the center of the beaker and the distance between the probe tip and the surface of the water is about 2.0 cm. The vibration and shock waves produced by the ultrasonic cavitation are collected by the titanium rod with a length of 61.72 cm and a diameter of 1.59 cm. The

titanium rod is immersed in the water with length of 3.0 cm and with a distance of 3.0 cm to the probe tip. A MISTRAS R15S acoustic sensor was coupled to the top of the titanium rod by an ultrasonic couplant. The piezoelectric signal of the acoustic sensor was acquired by the Tektronix DPO7345 Oscilloscope.

The experiments were carried out in tap water of 500 mL contained in a standard 500 mL glass beaker. The Al_2O_3 particles with a diameter of 1 µm were added to the tap water along the wall of the glass beaker before the power switch of the ultrasonic sonicator was turned on. The trigger mode was used in the oscilloscope and the cavitation noise signal was immediately acquired after the ultrasonic sonicator was turned on. The memory of the oscilloscope is capable of storing 5×10^8 samples. With a sampling rate of 1×10^6 samples/second, each cycle of signal acquisition lasted about 500 seconds. The signal can be stored to hard drive within about 10 seconds and the next cycle of signal acquisition can resume immediately if necessary. The ultrasonic intensity was controlled by setting the vibration amplitude of the probe tip in the range of 1-100% of the maximum amplitude.

2.3 Descriptive Analysis of the Cavitation Noise Signal

2.3.1 Cavitation Noise Signal

Figure 2-2 shows two representative cavitation noise waveforms with duration of 500 seconds under ultrasonic power 40W from pure tap water and Al_2O_3-particle-filled tap water, respectively. There are 12 seconds of pre-trigger samples in each signal. Both waveforms show three stages: (I) immediately after the ultrasonic power is turned on, there appears a high peak in the waveform; (II) after the peak, the cavitation noise signal reaches the weakest and then

gradually increases; (III) finally the signal enters into steady state. The obvious difference between these two waveforms is that in stage II, for tap water with Al_2O_3 particles, the initial cavitation noise is lower than that without particles, and it increases more significantly than that without particles. This phenomenon is somewhat similar to Wojs's results [25] that for pure water, there was no significant change on the spectrum characteristics at time 0, 15, 30, 60 minutes while for PAA 0.1% solution, the spectrum was moved slightly upwards after 60 minutes.
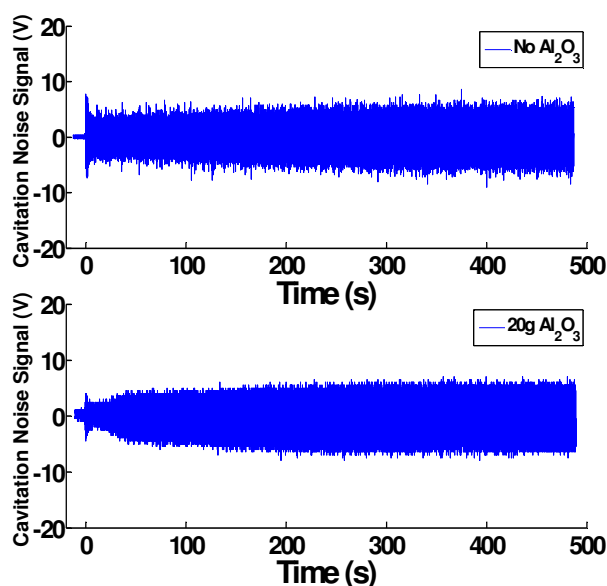
Figure 2-2: Two representative cavitation noise waveforms with ultrasonic power 40 W for pure tap water and tap water with 20 g Al_2O_3 particles.

Stage I reflects the step response of the beaker, water, sonicator system excited by the change of the power status, i.e., from off to on. When the step response diminishes, the cavitation noise falls. In stage II, an increasing number of air bubbles are formed by the rectified diffusion process [53] and thus the intensity of the cavitation noise increases gradually. In this process, the dispersion of initial impurities and the formation of a huge amount of small air bubbles cause

more cavitation nuclei (note that in the pure tap water there are also many impurities). As for stage III, which is characterized as the steady state, the liquid becomes uniform and the cavitation becomes the most intensive.

The influence of Al_2O_3 particles or the possible reasons that result in the difference between tap water with and without Al_2O_3 in stage II are: first, the unwettable Al_2O_3 particles and extra air bubbles brought by these particles in suspension absorb part of the ultrasonic energy in the process of formation, growth of cavitation bubbles, and the vibration and breakage of Al_2O_3 agglomerates. Second, the addition of Al_2O_3 particles increases the ultrasonic attenuation coefficient due to the scattering and absorption effects. Allegra and Hawley [54] studied the attenuation of sound for solid-in-liquid suspensions and the scattering coefficient was obtained by

$$\alpha_s = \frac{1}{2}\epsilon k_c^4 R^3 [\frac{1}{3}\left(\frac{\beta_c - \beta'}{\beta_c}\right)^2 + \left(\frac{\rho' - \rho}{2\rho' + \rho}\right)^2] \tag{2.1}$$

where ϵ is the volume fraction of the suspended particles, k_c is the compressional wave number for the suspending medium, R is the radius of the suspended particles, β_c is the compressibility of the suspending medium, β' is the thermal dilation of the suspended particles, ρ and ρ' are the densities of suspending medium and suspended particles, respectively. Equation (2.1) shows that the scattering coefficient is proportional to the cubic of the particle radius. In the cavitation and dispersion process in stage II, the sizes of Al_2O_3 clusters gradually reduce, which gradually decreases the scattering coefficient. The reduction of attenuation coefficient, the increase of cavitation nuclei caused by the breakage of Al_2O_3 particles, and the fast development of cavitation intensify the cavitation noise in stage II until it enters into stage III where the the

particles are well dispersed and uniformly suspended. Therefore the cavitation noise signal can be effectively used to monitor the status of the cavitation and dispersion.

To confirm the above analysis and statements, we conducted an experiment. The basic idea of this experiment is to disperse the particles with different dispersion time and then we let the mixture sit for a fixed amount of time. Then, we can compare the severity of the segregation occurred after the sitting period. A better dispersed mixture should have less segregation. Specifically, in the experiment, six beakers were used with each beaker containing 20 g Al_2O_3 particles and 500 mL tap water. The first beaker was used as the control group where there was no ultrasonic treatment. For the other 5 beakers, the ultrasonic processing times were 34.2s, 80s, 180s, 300s and 450s respectively. The ultrasonic driving power was 40 W in the experiment. Please note that from Figure 2-2, we can see that after roughly 300s of the dispersion time, the acoustic noise is in the steady state. Figure 2-3 shows the Al_2O_3 suspension immediately after the ultrasonic treatment where Al_2O_3 particles are evenly distributed in the water.

Figure 2-3: Al_2O_3 suspension immediately after the ultrasonic treatment

Figure 2-4 shows the segregation between the clusters of Al_2O_3 particles (the white layer at the bottom) and the water (the clear layer on the top) 26 hours after the ultrasonic treatment with different amount of processing times. It is clear that volume of Al_2O_3 layer increases significantly at first (0-34.2s), and then expands slowly (34.2-300s) and finally become stable (300-450s) as the processing time increased. The reason for this phenomenon is that when the particles are dispersed, the spaces between the neighboring particles are enlarged, and thus the volumes of the Al_2O_3 layer increased. When the particles are completely dispersed, the subsequent increase of ultrasonic processing time will result in no change in the volume, as shown in Figure 2-4 where sample 5 and sample 6 have almost the same volume for the Al_2O_3 layer.
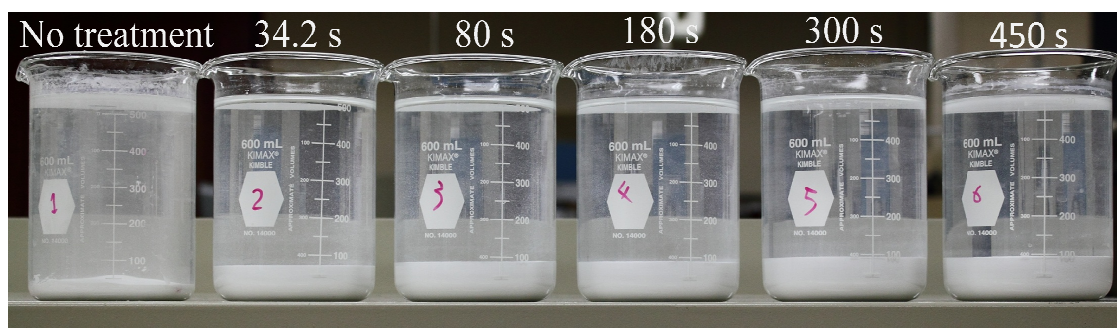
Figure 2-4: Deposited Al_2O_3 particles (Al_2O_3 20 g, ultrasonic driving power 40 W, 26 hours after treatment)

To make this point clear, the volume of the Al_2O_3 layer as a function of processing time is shown in Figure 2-5. Clearly, the trend shown in Figure 2-5 is identical to that of cavitation noise signals. We believe this experiment directly supports our statement that when the cavitation noise signals are steady, the particles are well dispersed. Thus, by detecting when the cavitation noise signals go into steady state, we can determine when the dispersion is sufficient. To achieve

this goal, we shall introduce two quantitative indices that measure the power level of the cavitation noises.
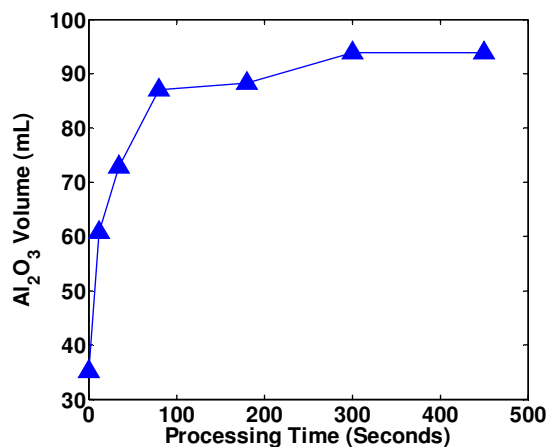
Figure 2-5: The volume of the deposited Al_2O_3 particles as a function of the processing time
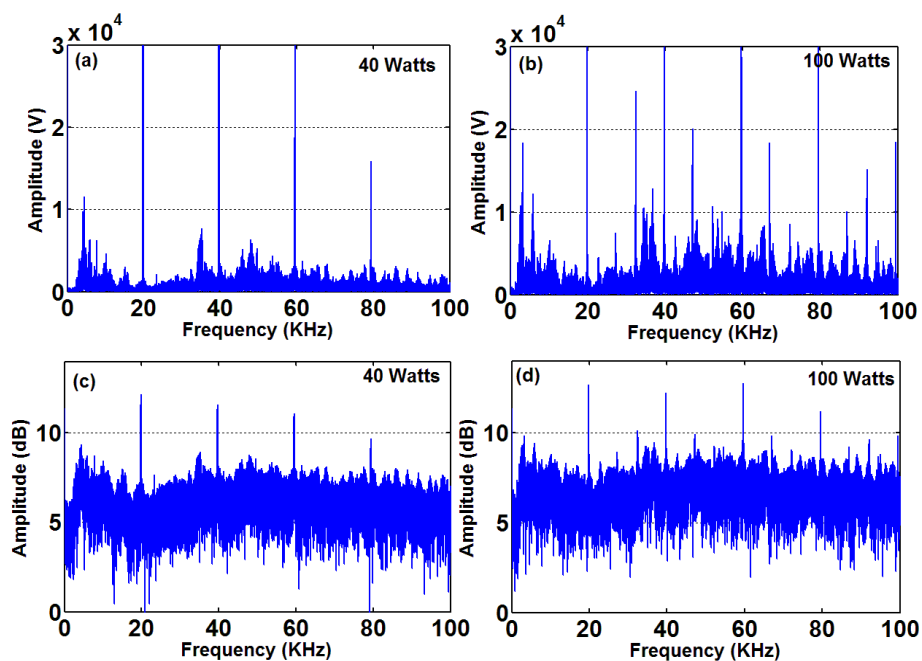
Figure 2-6: Cavitation noise spectrum for tap water with 10 g Al_2O_3 particles at the time of 40 seconds after the ultrasonic power is turned on: (a) 40 W, (b) 100 W, (c) 40 W, natural logarithmic scale, (d) 100 W, natural logarithmic scale.

2.3.2 Indices of Cavitation Noise Power

Figure 2-6 shows the frequency spectrum of the cavitation noise 40 seconds after the ultrasonic power is turned on for (a) 40 W and (b) 100 W ultrasonic powers in tap water with addition of 10 g Al_2O_3. For (c) and (d) in Figure 2-6 the cavitation noise spectrum is expressed in a logarithmic scale. From this figure we can clearly see the harmonics, ultraharmonics, subharmonics, and "white noise". For ultrasonic power 100 W, all of these components, especially the "white noise" and subharmonics, are stronger than that for power 40 W, indicating a more violent cavitation.

Two indices are used to quantitatively describe the cavitation noise power (CNP) in this research. The first one, termed as CNP-1, is defined as the integration of cavitation noise spectrum over frequency from 0-200 KHz in a logarithmic scale to enhance the "white noise" contribution:

$$CNP1 = \int A(f)df \approx \sum A(f)\Delta f \qquad (2.2)$$

where $A(f)$ is the DFT spectrum amplitude in a logarithmic scale and f denotes the frequency. This method was developed by Frohly [44] and later used by Gibson [25], who showed that CNP-1, multiplied with time t, is directly proportional to the ultrasound energy density obtained by the calorimetry technique. The second method, termed as CNP-2, is defined as the averaged square of the cavitation noise signal in each second,

$$CNP2 = \frac{\sum_{i=1}^{n} U_i^2}{n} \qquad (2.3)$$

where U_i is the cavitation noise signal and n is the number of samples in each second. Using Parseval's theorem, it can be proven that CNP-2 is proportional to the summation of the spectral energy density (the square of the spectrum amplitude) across all frequency components.
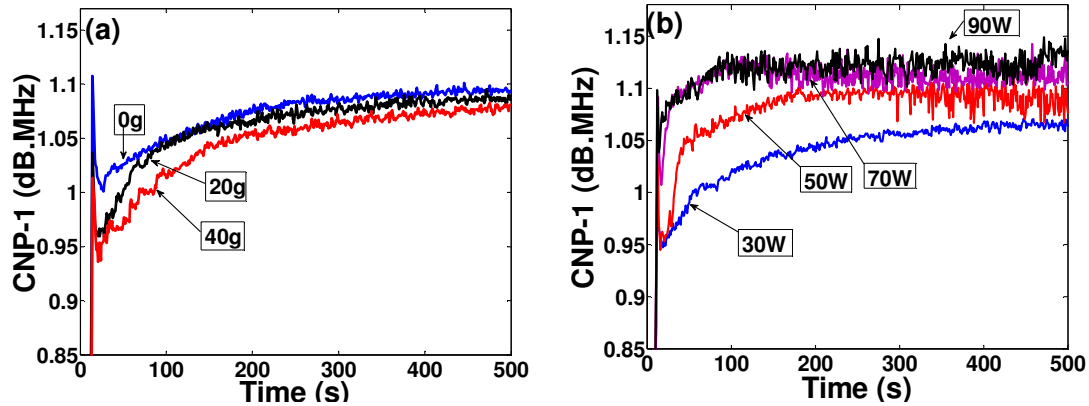
Figure 2-7: The influence of particle concentration and ultrasonic power on CNP-1: (a) CNP-1 as a function of time for different amounts of Al_2O_3 particles with ultrasonic power 40 W, (b) CNP-1 evolves with time for different ultrasonic power in tap water with 30 g Al_2O_3 particles.

In Figure 2-7(a) the CNP-1 is plotted as a function of time for different amounts of Al_2O_3 particles with ultrasonic power 40 W. Three stages are clearly seen in the figure, the initial burst in stage I, the increasing region in stage II, and the steady state in region III. The influence of particles concentration on the cavitation noise power is significant. The suspension with more particles has lower cavitation noise power, especially in stage II. This is consistent with what we expect since Al_2O_3 particles absorb and scatter acoustic energy. The more the particles, the higher the ultrasonic attenuation coefficient and thus the lower the cavitation noise power. After the particles are completely dispersed, the scattering effect is almost eliminated, which can be seen from the CNP-1 curves in the steady state that there is little difference among these curves.

Figure 2-7(b) shows the influence of ultrasonic power on CNP-1 for tap water with 30 g Al_2O_3 particles. We can clearly see that increasing the ultrasonic power could increase the cavitation noise power. Besides, it is faster for CNP-1 to reach steady state with higher ultrasonic driving power. The reason is obvious that increasing the ultrasonic driving power could intensify the cavitation, especially the transient cavitation, and thus increase the cavitation noise power and dispersion efficiency. We can also find that when the ultrasonic driving power is above 70 W, there is almost no significant change on CNP-1 curves. The possible reason is that for the ultrasonic driving power above 70 W, the cavitation is fully developed. The corresponding curves for CNP-2 are shown in Figure 2-8, from which we can find that the variance of CNP-2 bigger than that in CNP-1. Note that we present them separately to avoid overlapping due to large noise. In the following section, we will focus on the dispersion status detection by monitoring the CNP indices.
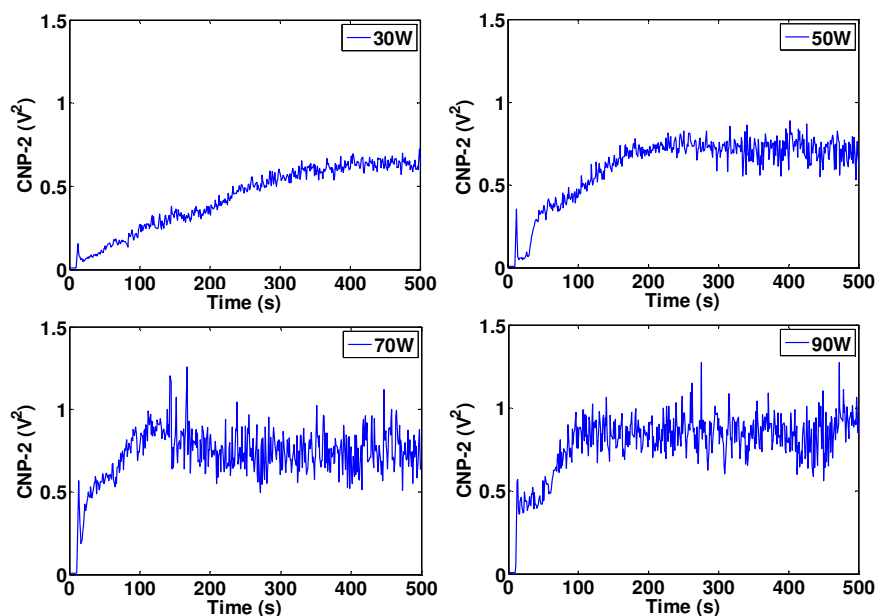
Figure 2-8: CNP-2 as a function of time for different ultrasonic power in tap water with 30 g Al_2O_3 particles

2.4   Steady State Detection

From above discussion, we can see that to monitor the ultrasonic cavitation based dispersion process using the acoustic emission signal, it is critical to detect the steady state of the acoustic signal. In the literatures, there exist some steady state detect techniques. Many of these exiting techniques are developed and used in the discrete-event simulations to remove or truncate the initialization bias [55-58]. These techniques are off-line methods and not applicable for on-line monitoring purpose because they require a large number of observations in the steady state to accurately estimate the truncation point. In real time monitoring, we want to detect the steady state as soon as possible with a very limited number of observations in the steady state. There are very limited on-line steady state detection techniques. Among these methods, a modified variance ratio test (call it R-test here) [54, 59], which was first used in chemical process control, is a very effective and well known method with low computationally cost and relative independence of system noise.

In this section, we will introduce one off-line and two on-line steady state detection methods. The off-line method is called as EWMA-MSER method, where EWMA stands for Exponentially Weighted Moving Average and MSER stands for Marginal Standard Error Rules. This method is refined upon the exiting MSER method to make it more robust to noise. Although EWMA-MSER is an off-line method, it can provide insights to the cavitation based dispersion process and serve as a benchmark to evaluate the performance of on-line detection algorithms. Among the two online methods introduced in this section, one is the newly proposed non-overlapping slope detection method (NSDM) and one is the existing R-test method. The performance of these two online methods will be systematically evaluated and compared as well.

2.4.1 Off-line Detection

2.4.1.1 EWMA-MSER method

The MSER [60] determines the truncation point (steady state point in this research) that minimizes the width of the marginal confidence interval about the truncated sample mean (steady state mean). It outperforms other heuristic algorithms on models that contain exponential shift bias [61] and these models are very similar to CNP signals. A later refinement, MSER-5 [53], was developed where the raw observations are grouped into non-overlapping batches with each batch having 5 observations and MSER is performed on these batch means. It was shown that MSER-5 was better than MSER in most cases [61]. However, MSER-5 didn't work well on CNP signals because using MSER-5 made the sample size very small, which significantly reduced its detection accuracy.

Mathematically, the MSER method can be briefly described as follows. Given the observations $\{Y_i : i = 1, 2, \ldots, n\}$, assume the steady state samples are $\{Y_i : i = d + 1, d + 2, \ldots, n\}$. Then the half-width of the $100(1 - \alpha)\%$ confidence interval for the estimate of the steady state mean is given by

$$CI(d + 1, n) = \frac{z_{\alpha/2} \, S_{n,d}}{\sqrt{n - d}} \tag{2.4}$$

where $z_{\alpha/2}$ is the inverse of the cumulative density function for standard normal distribution at probability $1 - \alpha/2$, and $S_{n,d}$ is the standard sample deviation given by

$$S_{n,d} = \sqrt{\frac{1}{n-d-1} \sum_{i=d+1}^{n} (Y_i - \overline{Y}_{n,d})^2} \tag{2.5}$$

where $\overline{Y}_{n,d} = \frac{1}{n-d} \sum_{i=d+1}^{n} Y_i$. Thus, the optimal truncation point d^* minimizes the confidence interval and is given by

$$d^* = \underset{n \gg d \geq 0}{\arg\min} \big(CI(d+1,n)\big)$$

$$= \underset{n \gg d \geq 0}{\arg\min} \big(CI^2(d+1,n)\big)$$

$$= \underset{n \gg d \geq 0}{\arg\min} \left(\frac{\sum_{i=d+1}^{n} (Y_i - \overline{Y}_{n,d})^2}{(n-d)(n-d-1)} \right) \tag{2.6}$$

Since n ≫ d, the denominator can be simplified from $(n-d)(n-d-1)$ to $(n-d)^2$. Thus, the monitoring statistic of this method, denoted as "MSER", is given as

$$MSER = \frac{1}{(n-d)^2} \sum_{i=d+1}^{n} (Y_i - \overline{Y}_{n,d})^2 \tag{2.7}$$
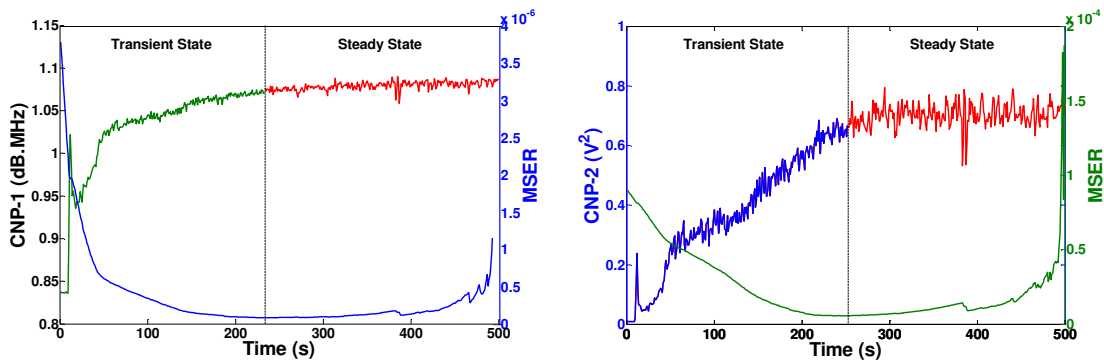
Figure 2-9: Illustration of MSER for CNP signals (power 40 W, Al_2O_3 30 g)

Figure 2-9 is an example of MSER on CNP indices with duration of 500s, which shows that the transition time estimated by MSER is a little shorter than the true transition time. It is

consistent with White's results [61] that MSER failed to truncate all of the bias, particularly when the process noise level is high.

In order to make the method more robust, we propose to use exponentially weighted moving average (EWMA) to smooth out short-term fluctuations without impacting on the long-term trends and then perform MSER on the filtered samples. We call this method as EWMA-MSER. Specifically, for the observations $\{Y_i: i = 1,2,\dots,n\}$, the smoothed samples are given by:

$$Y_{f,i} = \lambda Y_i + (1 - \lambda)Y_{f,i-1} \tag{2.8}$$

where λ is a parameter such that $0 < \lambda \leq 1$. A small λ puts a light weight on the recent observations and more noises are smoothed out. However, too low λ will delay the detection when the process enters into steady state. Here we choose $\lambda = 0.5$ and 0.1 for CNP-1 and CNP-2 respectively and the detected transition times for all power levels are quite consistent with visually examined values. Figure 2-10 shows an example of MSER-EWMA.
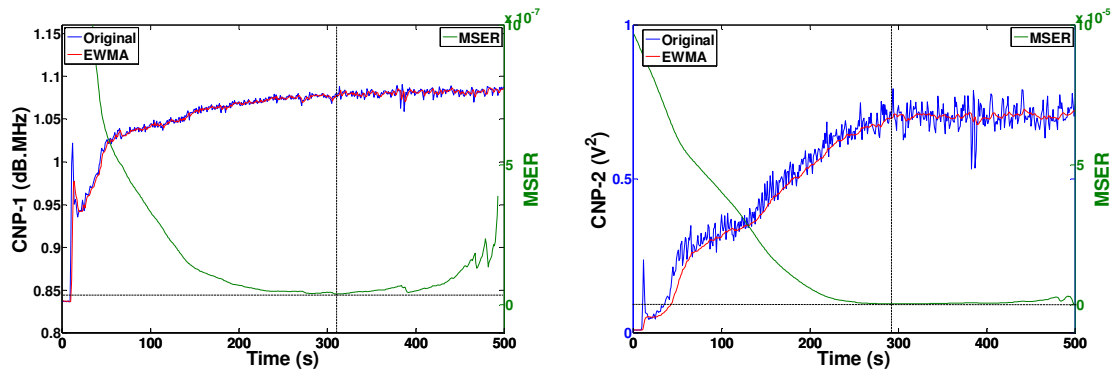
Figure 2-10: An example of MSER-EWMA on CNP signals (40 W, 30 g Al$_2$O$_3$)

2.4.1.2   Results and Discussion on Off-line Steady state Detection for Acoustic Signals

Figure 2-11 shows the MSER and EWMA-MSER determined transition times as a function

of ultrasonic powers for both CNP-1 and CNP-2. There is no significant difference between the

transition times of CNP-1 and CNP-2 using the same detection method, indicating that both

signals can be used to monitor the dispersion status. We can also find that the detection results of

EWMA-MSER are larger than those by MSER, for the reason that MSER-EWMA has

successfully reduced the influence of noise and more accurately detected the transition times

than MSER did. We choose the time instance determined by EWMA-MSER method as the

benchmark in the following work.
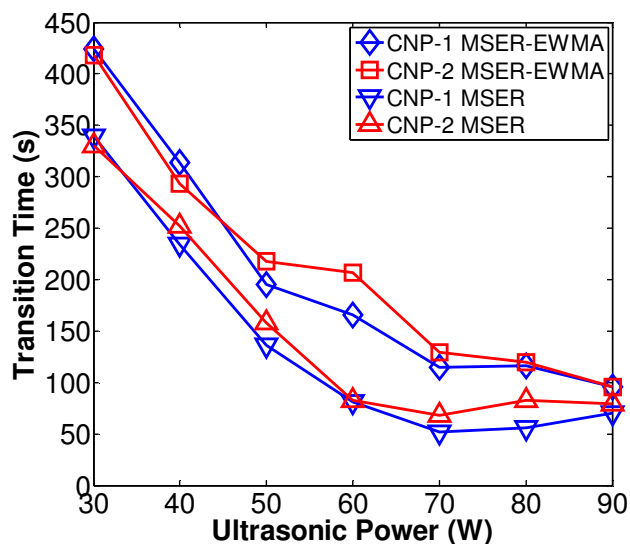
Figure 2-11: MSER and MSER-EWMA detected transition times as functions of ultrasonic
power for CNP-1 and CNP-2 (30 g Al_2O_3)

Figure 2-12 shows the dispersion time (transition time) as a function of Al_2O_3 concentration.

We can see that when the particle concentration is small ($\leq$ 20 g/500mL), there is no significant

change on the dispersion efficiency. This result is consistent with Gibson's finding [25] that

changing particle concentration had relatively little effect (<5%) on the ability of ultrasound to break particles. The reason is that the suspended Al_2O_3 particles could act as cavitation nuclei and enhance the cavitation process. Increasing particle concentration could increase the acoustic energy loss due to attenuation effects. On the other hand, it can also increase the cavitation nuclei, which improves the dispersion process. When the particle concentration is high (> 20 g/500mL), the acoustic attenuation effects overwhelm the influence of cavitation nuclei and therefore the dispersion time needed to break Al_2O_3 particles is significantly increased by adding more Al_2O_3 particles.
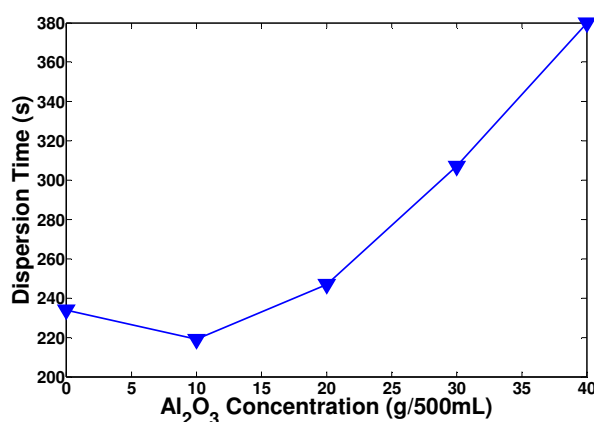
Figure 2-12: The influence of Al_2O_3 concentration on dispersion time estimated by MSER-EWMA on CNP-1 (40W)

Figure 2-13 shows the mean CNP-1 calculated by averaging the CNP-1 indice (Figure 2-7(b)) in the transient state (as marked in Figure 2-9) under different ultrasonic power levels. There are obvious three regions. For the ultrasonic power less than 50 W, the mean CNP-1 grows slowly by increasing the ultrasonic power. The cavitation type under this ultrasonic power level may be mainly stable cavitation. For ultrasonic power from 50 W to 70 W, there appears a fast mean CNP-1 increasing region, which is caused by the onset of transient cavitation. For ultrasonic

power above 70 W, the mean CNP-1 reaches the maximum level and the subsequent increase of the ultrasonic power will not result in any significant changes. We can treat the cavitation in this region as the fully developed transient cavitation. Also in this region, the dispersion efficiency is almost unchanged, as shown in Figure 2-11. Therefore ultrasonic power 70 W can be considered as the optimal cavitation parameter in this experiment.
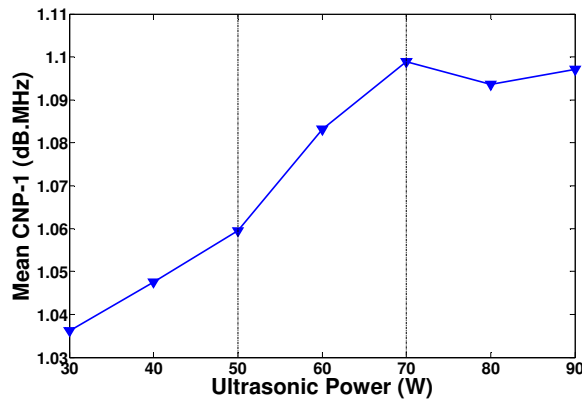
Figure 2-13: Mean CNP-1 in the transient state as a function of ultrasonic power (30 g Al_2O_3)

2.4.2 On-line Steady State Detection

2.4.2.1 *Description of NSDM and R-test Methods*

The algorithm of NSDM is fairly simple and easy to implement. In this method, an ordinary least square (OLS) linear regression over a non-overlapping moving data window with m samples of the CNP signal is performed until the fitted line is "flat" and continuously "flat" for D consecutive windows. Suppose the detected starting point of the stead steady is $\widehat{T_s}$, the estimated slope is $\hat{S}_i$ for i^{th} window and the slope threshold is S_c, then

$$\hat{T}_s = m(N + D - 1) \tag{2.9}$$

where

$$N = \arg \min\{i \mid |\hat{S}_{i+k}| < S_c, k = 0,1,\dots,D-1\}$$

An existing on-line method, the variance ratio test [62], is also an effective method to detect steady state. In this method, the variance of a moving data window is calculated in two different ways: (1) mean squared deviation from the average (V_1) and (2) mean squared difference of successive data (V_2). In the non-steady or transient state, the first variance will be larger than the second variance and the ratio V_1/V_2 is larger than 1. In the steady state, this ratio is expected to approach 1. In the test, the null hypothesis (steady state) will be rejected until the ratio is below a threshold. In order to reduce the computational cost and data storage, Cao and Rhinehart [54, 59] used an recursive method to estimate the variances $S_{1,i}^2$ and $S_{2,i}^2$:

$$Y_{f,i} = \lambda_1 Y_i + (1 - \lambda_1)Y_{f,i-1}$$

$$V_{f,i}^2 = \lambda_2 \left(Y_i - Y_{f,i-1}\right)^2 + (1 - \lambda_2)V_{f,i-1}^2$$

$$\delta_{f,i}^2 = \lambda_3 (Y_i - Y_{i-1})^2 + (1 - \lambda_3)\delta_{f,i-1}^2$$

$$S_{1,i}^2 = (2 - \lambda_1)V_{f,i}^2/2$$

$$S_{2,i}^2 = \delta_{f,i}^2/2$$

Here λ_1, λ_2 and λ_3 are the parameters with $0 < \lambda_j \leq 1$ ($j = 1,2,3$). The ratio is given by

$$R_i = \frac{S_{1,i}^2}{S_{2,i}^2} = \frac{(2 - \lambda_1)V_{f,i}^2}{\delta_{f,i}^2} \tag{2.10}$$

Similarly, suppose the ratio threshold is R_c, then $\hat{T}_s$ is expressed by

$$\hat{T}_s = \arg \min (i \mid R_i < R_c) \tag{2.11}$$

There is a trade-off between rapid tracking of the process and separating the probability density function of R between the steady state and the non-steady state in the selection of the parameters λ_1, λ_2 and λ_3. In general, small parameters can reduce the influences of noise on estimating the variances and lead to bigger separation in the probability distribution of R of the steady state and the non-steady state. However, small parameters may delay the detection. Cao [59] provided some settings of parameters and their detection performance in different situations. Interested readers may refer to their paper for more details.

2.4.2.2 *Performance Evaluation and Comparison*

To evaluate and compare the performance of steady state detection algorithms, it is natural to use the bias in the detection as the evaluation metrics. Thus, in this research, we define a criterion named the expected detection bias (EDB) as

$$\text{EDB} = E|\widehat{T}_s - T_0| \tag{2.12}$$

where $\widehat{T}_s$ and T_0 are the starting point of the steady state detected by the algorithms and the underlying true value, respectively. For the cavitation based dispersion, an early detection, i.e., $\widehat{T}_s < T_0$, will lead to insufficient dispersion and bad quality product. Thus, it is critical to also evaluate the probability of early detection. Toward this goal, we define another criterion named false alarm rate (FAR),

$$\text{FAR} = \text{Pr}\ (\widehat{T}_s < T_0) \tag{2.13}$$

to quantitatively evaluate it.

For NSDM, these criteria (EDB and FAR) can be derived as follows. Given the observations $Y_i = (y_{m(i-1)+1}, y_{m(i-1)+2}, \dots, y_{mi})$ for the ith data window and the time index $T_i = (t_{m(i-1)+1}, t_{m(i-1)+2}, \dots, t_{mi})$, where m is the window size, the OLS estimator of the slope is $\hat{S}_i = \frac{\sum_{k=1}^{m}(t_{m(i-1)+k}-\overline{T_i})y_{m(i-1)+k}}{\sum_{k=1}^{m}(t_{m(i-1)+k}-\overline{T_i})^2}$ where $\overline{T}_i$ is the mean value of the time index. Suppose the observation noises follow independent and identically distributed normal distribution, $\epsilon_{m(i-1)+k} \sim N(0, \sigma^2)$ and $y_{m(i-1)+k} = f(t_{m(i-1)+k}) + \epsilon_{m(i-1)+k}$ where $f(t_{m(i-1)+k})$ is the expected value, then $\hat{S}_i \sim N(\mu_i, \sigma_i^2)$ with

$$\mu_i = \frac{\sum_{k=1}^{m}(t_{m(i-1)+k} - \overline{T}_i) f(t_{m(i-1)+k})}{\sum_{k=1}^{m}(t_{m(i-1)+k} - \overline{T}_i)^2} \tag{2.14}$$

$$\sigma_i^2 = \frac{\sigma^2}{\sum_{k=1}^{m}(t_{m(i-1)+k} - \overline{T}_i)^2} \tag{2.15}$$

Define α_i as the probability that the absolute value of the slope of the ith data window is below the slope threshold S_c, then

$$\alpha_i = \Pr(|\hat{S}_i| < S_c) = \phi((S_c - \mu_i)/\sigma_i) - \phi((-S_c - \mu_i)/\sigma_i) \tag{2.16}$$

Define the probability mass function (PMF) P_n as the probability of receiving the steady state alarm after monitoring the $n^{th}, (n+1)^{th}, \dots, (n+D-1)^{th}$ non-overlapping moving windows (total D windows, suppose we stop the monitoring process immediately after we receive the steady state alarm). Let $\alpha_0 = 0$, then

$$P_n = \Pr(N = n) = \Pr(N = n | N > n - 1 - D) \Pr(N > n - 1 - D)$$

$$= \begin{cases} [(1-\alpha_{n-1})\alpha_n \dots \alpha_{n+D-1}]\left(1-\sum_{i=1}^{n-1-D} P_i\right), \text{for } n > 1+D \\ (1-\alpha_{n-1})\alpha_n \dots \alpha_{n+D-1}, \text{for } n \leq 1+D \end{cases} \quad (2.17)$$

Although there are infinite terms in the expression above, it converges very fast due to the rapid

convergence of P_n and we only need to sum up a small number of terms to calculate it. FAR can

be calculated by

$$\text{FAR} = \sum_{i=1}^{n_0} P_i \quad (2.18)$$

Here $n_0 = \lfloor T_0/m - D + 1 \rfloor$, the largest index of the data window where the following $D-1$

data windows are before the steady state transition time T_0. EDB is expressed as

$$\text{EDB} = E|\hat{T}_s - T_0| = \sum_{n=1}^{\infty} P_n|m(n+D-1) - T_0| \quad (2.19)$$

Clearly, $\hat{T}_s$ is required to be as close as possible to T_0 and thus the smaller the EDB, the higher

the detection accuracy.

For the R-test method, it is very difficult to get the analytical expression for these evaluation

criteria due to the complexity of the algorithm. Thus, Monte Carlo simulations have to be used to

compute them. In the simulation, we will need to simulate the signal with noise many times and

then apply the detection algorithm to the simulated signals. Finally the detection results will be

averaged to obtain the values of EDB and FAR.

To compute EDB and FAR, we need to know the underlying true value of the starting point

of the steady state. Thus, we need to assume an underlying function to describe the changes of

the signal. Here, we select the exponential bias function as the underlying function. This function

was used by Cash [55] and White [61] as a generic function to assess off-line heuristic algorithms. Furthermore, the behavior of this function is quite similar to our CNP signals. The mathematical form of the function is given as

$$f(i) = \begin{cases} C(1 - e^{a(i-1)}), & i \leq T_0(a) \\ C(1 - e^{a(T_0-1)}), & i > T_0(a) \end{cases} \tag{2.20}$$

where $T_0(a)$ is the smallest integer i where the derivative of $C(1 - e^{a(i-1)})$ is less than $C \times 10^{-4}$. $C = 0.7$ is chosen to match the CNP signals. The time series are generated by $Y_i = f(i) + \epsilon_i$ where $\epsilon_i \sim N(0, \sigma^2)$ and $\sigma = 0.04$. Eight values of a and the corresponding T_0, as shown in Table 2-2, were chosen to study the influence of signal changing rate on the detection accuracy. One representative signal generated with $T_0 = 461$ is shown in Figure 2-14.

Table 2-1: Bias function parameters

Model #	1	2	3	4	5	6	7	8
a	0.01	0.012	0.015	0.019	0.026	0.039	0.07	0.1
T_0	461	339	334	276	214	153	94	69
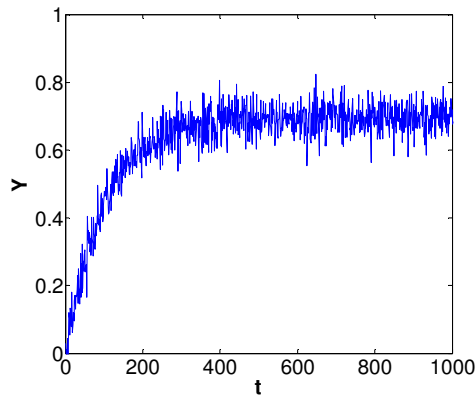
Figure 2-14: An example of generated signal ($a = 0.01, T_0 = 461$)
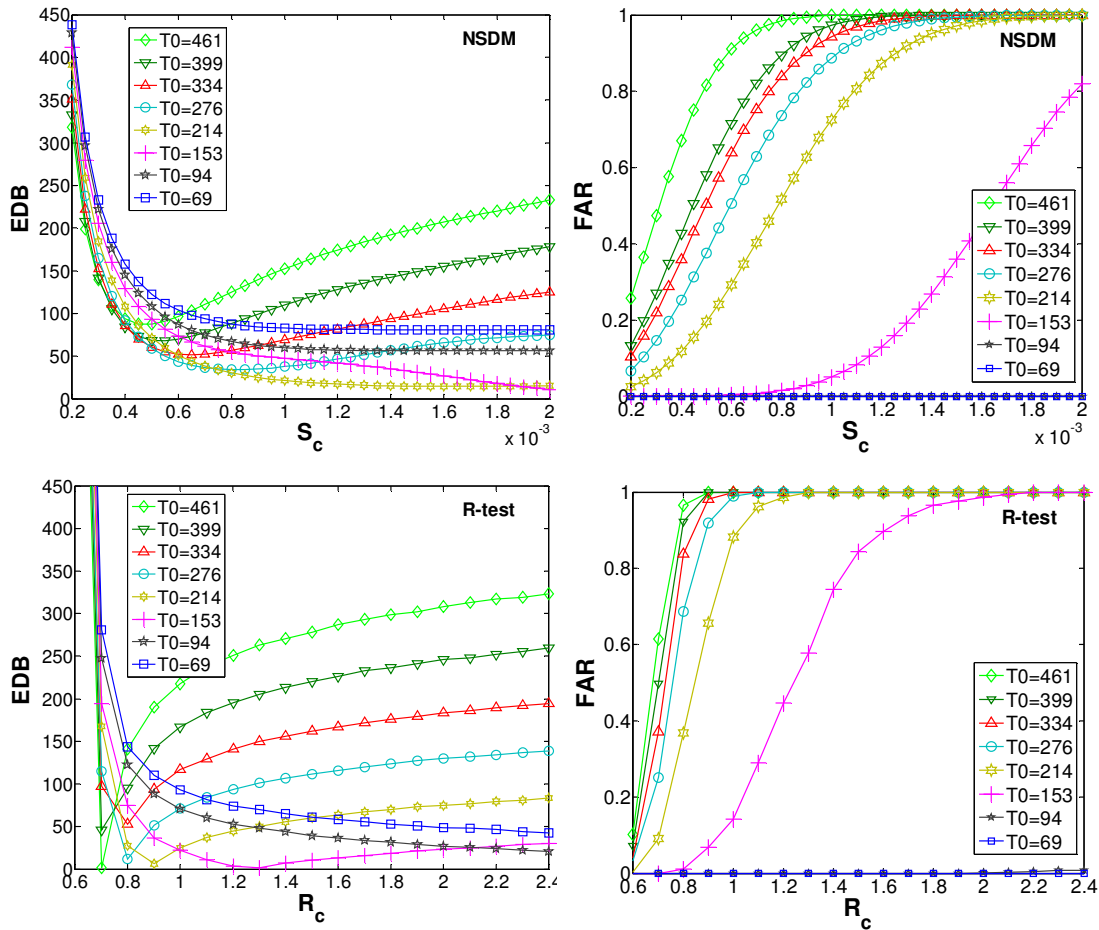
Figure 2-15: The expected detection bias and false alarm rate as functions of detection threshold for NSDM and R-test (NSDM: $m = 50, D = 2$; R-test: $\lambda_1 = 0.05, \lambda_2 = 0.05, \lambda_3 = 0.08$)

Figure 2-15 shows the EDB and FAR as functions of detection threshold for NSDM and *R*-test. EDB and FAR of NSDM were directly calculated by Eq. (2.19) and (2.20) respectively. For R-test, computer simulations were performed where computer experiments were repeated for 30,000 times for each set of detection parameters and signal parameters. For NSDM, $m = 50, D = 2$ and for R-test, $\lambda_1 = 0.05, \lambda_2 = 0.05, \lambda_3 = 0.08$. From Figure 2-15, we can find that:

(1) For both NSDM and R-test, as we increase the detection threshold, EDB decreases rapidly at first, and then gradually increases. FAR is always non-decreasing when the threshold is

increased. The optimal threshold should be the value that has low FAR and also low detection bias.

(2) Both methods perform better on signals with fast changing rate (large a) than on slow changing signals in most cases. For these rapidly changing signals, NSDM and R-test have low detection bias and false alarm rate. Besides, the detection bias is more stable under different detection thresholds. In this situation, the R-test is better than NSDM due to lower computational cost and data storage;

(3) For the signals with low changing rate, the bias and false alarm rate of R-test are more sensitive to the change of detection threshold than NSDM. An optimal detection threshold for one signal may work badly on the other signals;

(4) For R-test, the optimal detection threshold R_c for different signals varies significantly. Two or even more sets of detection parameters are required to make R-test work well on all signals with different T_o. NSDM outperforms R-test on signals with large range of changing rate in terms of easiness in selection of detection parameters and the stability of detection accuracy.

2.4.2.3   *Results of On-line Steady state Detection on CNP Indices*

The detection parameters (shown in Table 2-2) for NSDM and R-test were selected by minimizing the difference between the detected starting points of the steady state with EWMA-MSER detected results.

Table 2-2: Detection parameters for NSDM and R-test

CNP	NSDM				R-test			
	m	D	S_c		λ_1	λ_2	λ_3	R_c
			Power $\leq$ 50W	Power $>$ 50W				
CNP-1	20	2	1×10^{-4}	3×10^{-4}	0.1	0.05	0.05	2
CNP-2	30	2	2×10^{-3}	4×10^{-3}	0.05	0.05	0.08	2
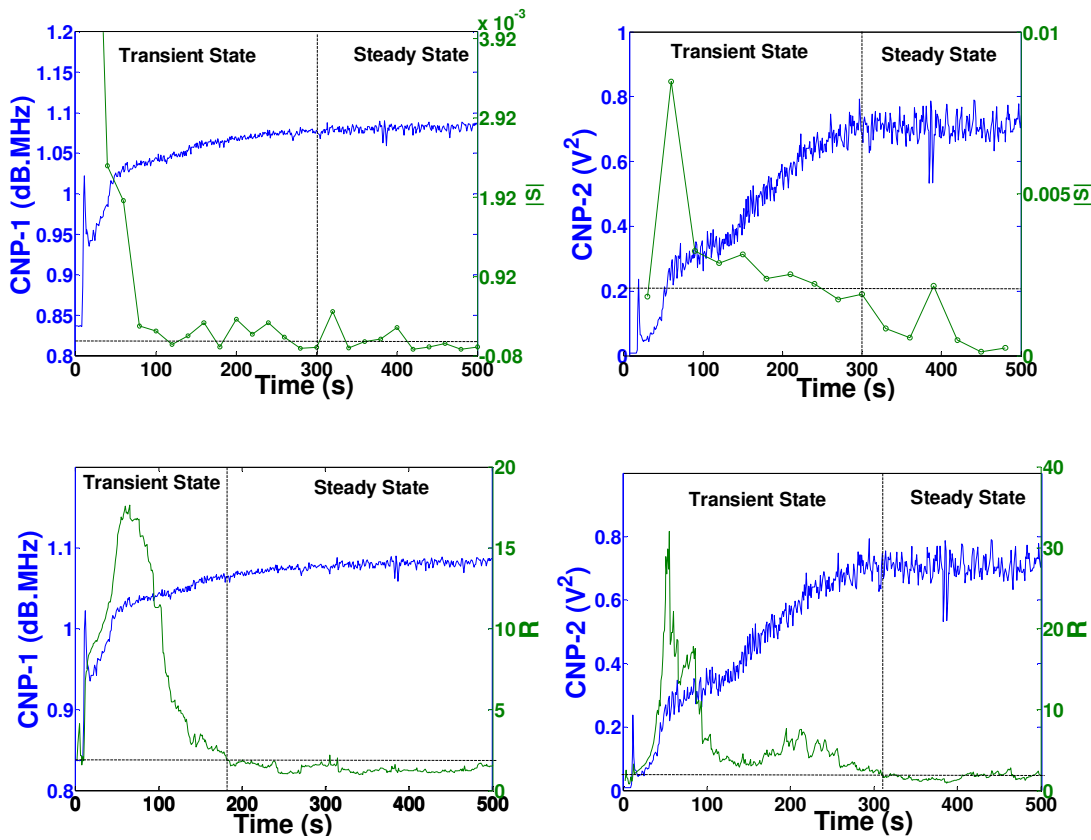
Figure 2-16: Illustration of NSDM (above) and R-test (below) for CNP signals (40W, Al_2O_3 30 g)

An illustration of R-test on CNP signals is shown in Figure 2-16. Figure 2-17 shows the transition time as a function of ultrasonic power detected by EWMA-MSER, NSDM and R-test. It should be noted that the changing rate for CNP-1 before the steady state is lower than CNP-2.

CNP-1 increases rapidly to a level close to the steady state level at first, and then drifts slowly into the steady state, while CNP-2 increases with a relatively constant and high changing rate.

The difference between CNP-1 and CNP-2 leads to different performance of the detection methods. R-test works better on CNP-2 signals than on CNP-1 signals, which is consistent with the simulation results that for high changing rate, R-test performs well with only one threshold while for signals with low changing rate, it is hard to find a threshold that works for all signals. NSDM works well on both CNP-1 and CNP-2 signals.
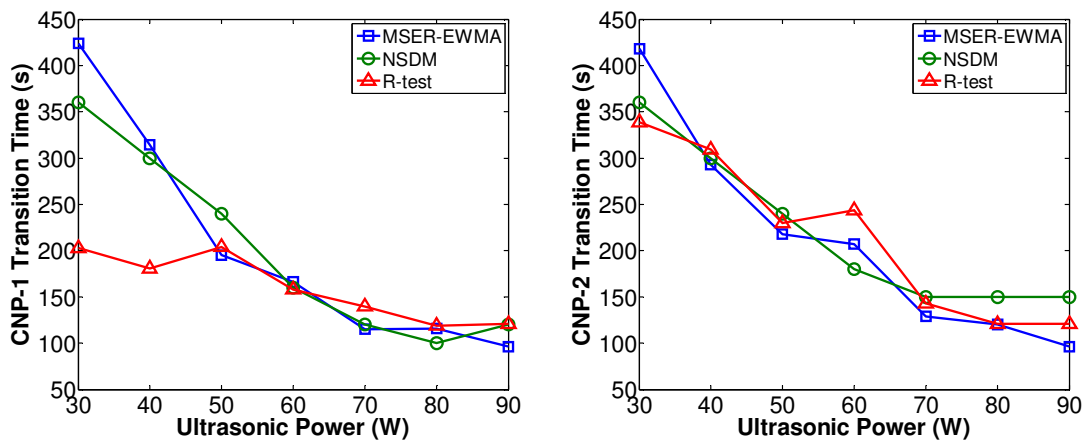
Figure 2-17: Transition time detected by MSER-EWMA, NSDM and R-test (Al_2O_3 30 g).

The above results show that R-test and CNP-2 are the optimal choice in our current experiments. R-test is less influenced by the noise. In addition, R-test requires less calculation and data storage than NSDM. In the real-world application, however, the signals may show wide range of changing rate, where NSDM may be preferred. CNP-2 is better than CNP-1 for detection purpose since it has larger changing rate than CNP-1. Besides, CNP-2 is computationally less expensive to calculate than CNP-1 since the latter requires Fourier transform.

2.5 Cavitaion Signal in Molten Al Alloy

We also collected the cavitation signals from molten Al alloys with Al_2O_3 particles using a new data acquisition system installed in a desktop. The experimental setup and its schematic illustration are shown in Figure 2-18. The raw signal and its CNP-2 signal are shown in Figure 2-19 and Figure 2-20, respectively. Note in Figure 2-19 the signal is not centered (i.e., mean voltage is not zero). The CNP-2 signal in Figure 2-20 is obtained from the centered raw signal. As we can see, these signals are quite similar to those obtained from tap water. It is what we have expected since the fundamental physical processes are the same, except that in tap water the bubbles are made of air while in molten metal the bubbles are mainly hydrogen.
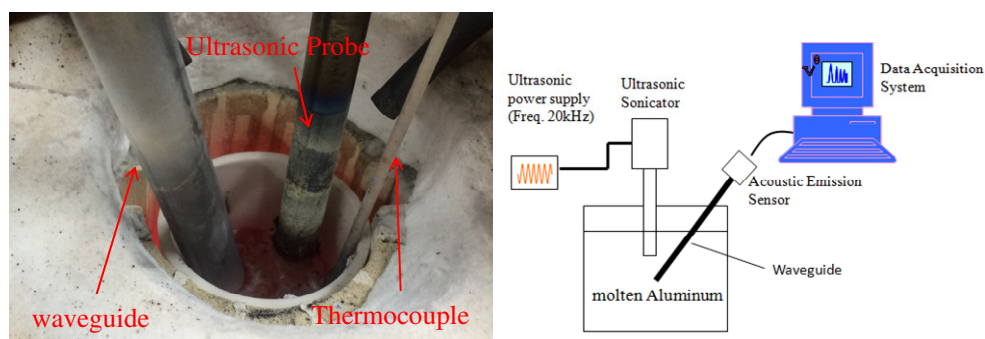
Figure 2-18: Experimental setup and schematic illustration
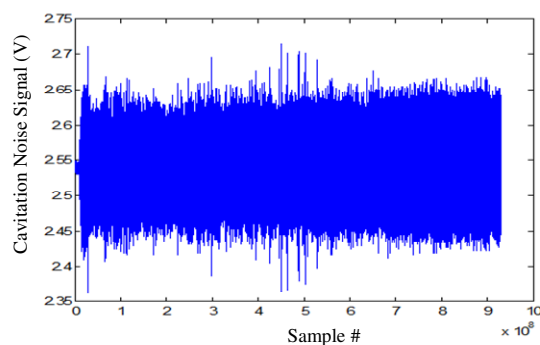
Figure 2-19: Raw cavitation signal
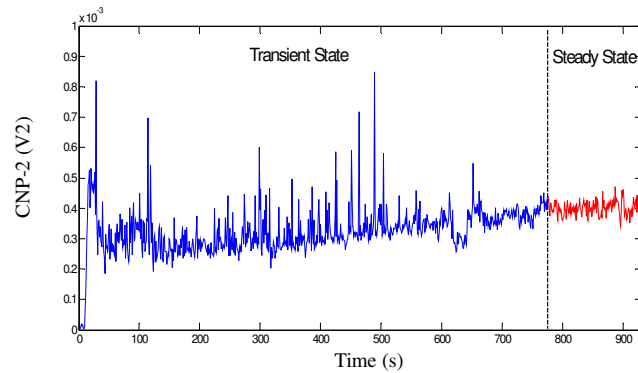
Figure 2-20: CNP-2 signal obtained from the centered cavitation noise signal

2.6 Conclusion

In the present work we have proposed a method based on the cavitation noise to monitor the particle dispersion process. The cavitation noise signals and their spectrum are analyzed and discussed in details. The cavitation noise signals are divided into three stages. The first stage corresponds to the step response of the cavitation system. The second stage is the most important stage which characterizes the evolving of the cavitation and the dispersion process. The third stage is the steady state in which the particles are dispersed well. The Al_2O_3 particles can reduce the strength of the cavitation noise by increasing the acoustic attenuation characterized as absorption and scattering of the acoustic wave. The attenuation effect is reduced as the particles are well dispersed. These characteristics of the cavitation noise can be used to monitor the dispersion status.

Two quantitative indices (CNP-1 and CNP-2) are chosen to capture the evolution of the cavitation noise and CNP-2 is better in terms of computational cost and detection accuracy. The off-line method MSER and its modification EWMA-MSER are used to identify the dispersion

steady state. The proposed EWMA-MSER works quite well and its detection results are used as the benchmark to develop and evaluate the on-line detection methods. Two online methods, NSDM and R-test are applied and systematically compared. In the comparison, we proposed to use the expected detection bias and the false alarm probability to quantitatively evaluate the performance of these two detection methods. We further derived the analytical expressions for these quantities for the proposed non-overlapping slope detection method. With these expressions, we can easily calculate the average run length, expected detection bias and false alarm rate for a given signal. We also obtained these quantities for R-test using numerical methods. Both methods work well on signals with high changing rate and R-test outperforms NSDM in terms of computational costs and data storage. For signals with large range changing rate, NSDM outperforms R-test in terms of easiness in selection parameters in the algorithm and the stability of detection accuracy.

We also tested this monitoring technique in ultrasonic cavitation-assisted fabrication of Al MMNCs. Similar signal trend and characteristics are also observed. The results of this research provide useful guidelines for establishing a real-time process monitoring and control scheme for ultrasonic cavitation based dispersion processes, which is a critical process in the manufacturing of many composite materials.

3 On-line Steady State Detection Using Multiple Change-point Models and Particle Filters[*]

In Chapter 2 we showed that the nanoparticles are considered completely dispersed when the CNP signals are stationary. Therefore is it critical to accurately and timely detect the steady state of the cavitation noise signals. In this chapter we develop a more robust and accurate steady state detection algorithm using multiple change-point models and particles filtering techniques. It is a general algorithm which can be applied to not only nanoparticle dispersion monitoring, but also many other process control areas. This chapter is organized as follows. Section 3.1 presents the literature review of steady state detection problems. In Section 3.2, the multiple change-point model for the steady state detection is formulated as a non-standard state space model. In Section 3.3, a particle filter algorithm is developed to estimate this state space model and detect the steady state. Section 3.4 presents the numerical analysis of the proposed steady state algorithm and the comparison with several existing methods. The discussion and conclusion are given in Section 3.5.

---

[*] This chapter is based on the paper: **Jianguo Wu**, Yong Chen, Shiyu Zhou, Xiaochun Li, "On-line Steady State Detection for Process Control Using Multiple Change-point Models and Particles Filters", *IEEE Transactions on Automation Science and Engineering (2015, in press)*

3.1 Literature Review

Steady state detection of noisy process signals is critical in process performance assessment, data reconciliation [63, 64], fault detection and diagnosis [65, 66], process optimization [67] and process control [54, 68, 69]. In these applications, the steady state refers to the state where the mean of the time series is unchanging. Unlike the traditional statistical process control (SPC) which usually employs control charts to monitor the change from the normal condition (steady state) to the abnormal state (another steady state or transient state), the steady state detection uses statistical methods to monitor or detect the change from the transient state to the steady state to facilitate process control, performance evaluation and optimization, etc. In discrete-event simulation, for example, the simulated data consist of warm-up period (or start-up period) and the steady state period. Only the data in the steady state period represents the true steady state performance of the system and therefore the start of the steady state period in the simulation outputs has to be identified (also called the initialization bias elimination problems) [53, 57, 60, 61, 70, 71]. In the online process control, the steady state needs to be detected to trigger the next stage of the process or operation. For example, in the batch processes manufacturing [72], where the batch operations in start-up period are unsteady and cannot guarantee the satisfied product qualities due to the unstablized material or machine conditions (i.e., temperature). An efficient online steady state detection of the operation state can avoid expensive laboratory analysis of product quality. In the chemical industry, the steady state of the operation conditions such as the temperature, flow rate, pressure and pH value etc, needs to be detected for process modeling, control and optimization [54, 73]. Most of the fault detection and diagnosis methodologies on the cooling systems are based on the steady state assumption [65, 74]. Steady state detection can also

used as the stopping criteria for iterative numerical methods, such as nonlinear regression, optimization, neural network training [75]. The procedure can be stopped when the objective function (e.g., sum of squared error) reaches steady state.

During the past several decades, various *off-line* steady state detection methods, mostly from the discrete-event simulation literature, have been developed to remove the warm-up period in the initialization bias elimination problems [76]. According to Robinson [76-78], these methods can be classified into five categories: 1. Graphical methods where visual inspection and human judgment are used to truncate the time-series data. The representative methods in this category include the simple time-series inspection [79], CUSUM plots [80], exponentially weighted moving average control charts [81] and statistical process control method (SPC) [78], etc.; 2. Heuristic rules among which the marginal standard error rules (MSER and MSER-5) [60, 61] are among the most popular methods. These methods are simple and straightforward and free of subjectivity of the graphical methods; 3. Statistical methods which apply the principles of statistics to estimate the warm-up period. The representative methods include the goodness-of-fit test [82] and wavelet-based spectral method [83], etc; 4. Initialization bias tests which determine whether initialization bias is present in a series of data to estimate the warm-up period. These methods include batch-means based tests [70], students t-tests and compound test method [84] etc. and 5. Hybrid methods which employ initialization bias tests in conjunction with graphical or heuristic approaches. Two methods of this type are the sequential method [82] and the scale invariant truncation point method [85].

Although the *off-line* steady state detection has been extensively studied, the *on-line* steady state detection, which is only based on the observations up to the current time, is more difficult

and not well-developed. The existing *on-line* methods, which are mostly from the process control literature, can be summarized as: (a) slope detection method (SDM) where linear regression is performed over a moving data window and the fitted slope is monitored [69, 86, 87]; (b) performing a *t*-test on two recently computed means of two adjacent windows with pooled standard-deviation [88]; (c) monitoring the standard deviation of a moving window [65]; and (d) performing an F-test on the ratio of variances of a moving window calculated using two different methods, the mean-squared-deviation and the mean of squared differences of successive data [62]. Based on the last method, Cao [54] developed a computationally efficient method in which the variances are calculated recursively using exponentially weighted moving average. These existing methods have certain limitations. One common disadvantage is that a data window has to be used. Too long a moving window may delay the detection while too short a moving window may increase the false detection rate. Another disadvantage is that the optimal detection parameters (i.e. window size, threshold) often depend on the characteristics of signals, e.g. variance of signal noises (for SDM, *t*-test and standard deviation method) or signal changing rate (for variance ratio test [69]). The characteristics may be different across different signals or even in a single signal. These existing methods with fixed detection parameters are not sufficiently flexible to be effective in various situations. Therefore a more robust method with more flexibility is desirable.

In this chapter a novel steady state detection method is developed where signals are sequentially fitted to a piecewise linear model using Bayesian inference techniques and the observations in the latest linear segment are mainly used for steady state detection. The multiple change-point models have been actively studied and widely used in many practical fields, e.g.,

economics, muscle activation, climatic time-series, DNA sequences and neuronal activity in the brain [89-95]. In our steady state detection method, the given time series are modeled as linear segments connected at change-points. Then the steady state detection problem becomes an inference problem for multiple change-point models. The Bayesian inference is one of the most common and effective approaches, where a joint prior distribution is placed over the change-points and model parameters and the posterior distribution is obtained based on the prior information and observations. In the proposed method, the particle filtering algorithm as an online Bayesian inference technique is used to update the posterior distribution of the latest change-point and other model parameters (e.g., slope, intercept, noise variance) sequentially. The slope parameter since the latest change-point is then used to determine if the signal is steady. The key challenges of the particle filter are the efficiency of importance sampling, the particle degeneracy and impoverishment issues, and its computational cost. In this work we develop a stratified sampling technique for the importance sampling and a partial Gibbs resample-move technique to solve the particle degeneracy and impoverishment problem and reduce the computational cost for the specific steady state detection problem. We also propose a timeliness improvement strategy to reduce the detection delay which is inherent for on-line change-point detection.

3.2 Multiple Change-point Model for Steady State Detection

In this method, a piecewise linear model is used as the multiple change-point model for the signal, as illustrated in Figure 3-1. The steady state is inferred by estimating the parameters (e.g. slope) of the current linear segment. The proposed method has one key advantage over these moving window based methods which utilize only the data in the current moving window for

detection. The window may contain both transient state observations and steady state observations, or may contain oscillating signals with unchanging mean, which may influence the testing effectiveness. The proposed method seeks to use the observations in the current linear segment for steady state detection and therefore it is expected to be more robust.
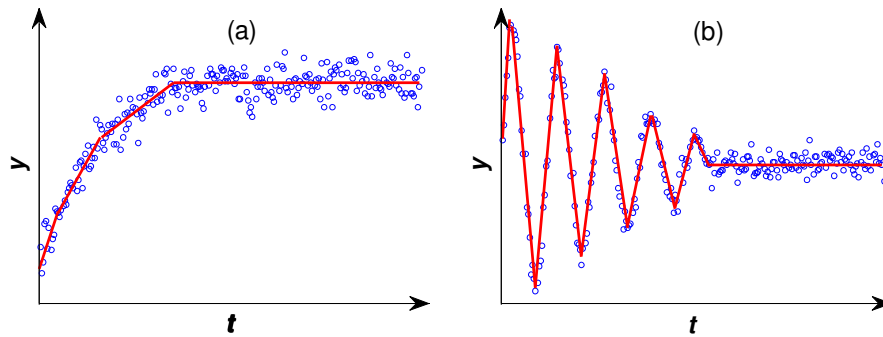
Figure 3-1: Illustration of approximating nonlinear functions using piece linear model: (a) signal generated using exponential function and noise; (b) oscillating function

Note that we can alternatively use polynomials with higher order instead of the linear model in each segment to approximate the signals, which will reduce the number of change-points needed. However, higher-order polynomials can significantly increase the computational cost and complexity. Another alternative is to use the step function as the model or constant function in each segment. The status of the process is monitored by sequentially estimating the duration of the current segment. However, this method cannot handle signals with small changing rates, e.g., linear signals with a very small slope. Due to these reasons discussed above, we adopt the segmented linear model in our work.

The Bayesian inference of the latest change-point (LCP) and other model parameters is illustrated in Figure 3-2, where their posterior distributions are sequentially updated, i.e., re-estimated when a new data point is obtained. For example, at time t_2, with the emergence of the

new linear segment starting at t_1, the center of the posterior of LCP (the second row in Figure 3-2) jumps from $t = 1$ to the location around t_1 and the posterior is almost zero at the locations far before t_1. Therefore mainly the observations between t_1 and t_2 are used to estimate the other models parameters (e.g., slope, noise variance) of the current linear segment.
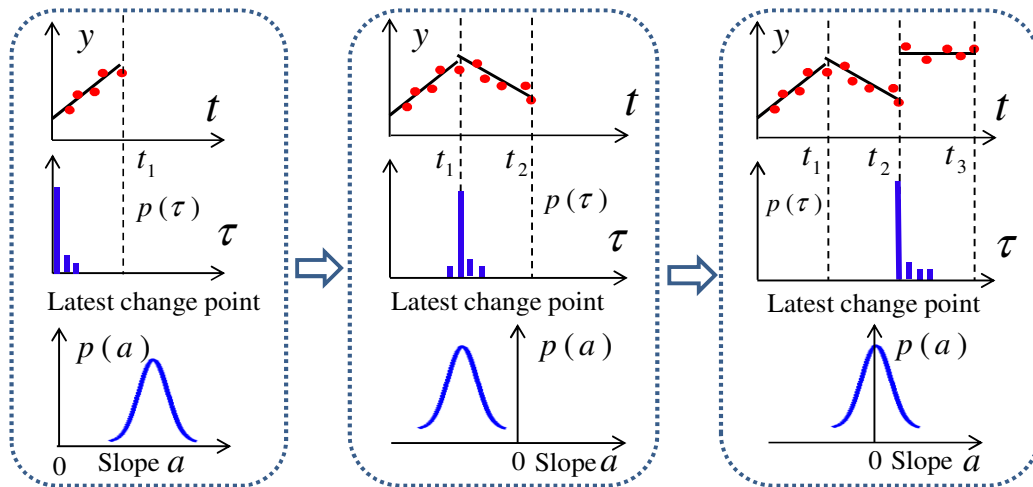
Figure 3-2: Illustration of the segmented linear model and Bayesian inference.

Suppose the model parameter at time t is $\boldsymbol{\xi}_t = (a_t, b_t, \sigma_t^2)$ where a_t is the slope, b_t is the intercept of the linear segment, and σ_t^2 is the variance of the noise corresponding to time t. Denote the LCP at time t as τ_t and the prior transition probability of change occurring at time t given that the LCP at $t-1$ is i as $p(\tau_t = t | \tau_{t-1} = i)$. The most popular and simplest prior for the change-point is a geometric prior [90, 96] applied on the segmental duration, which corresponds to a Markov transition process with a constant prior transition probability. Other common priors include Poisson distribution and gamma distribution, which are often used in speech segmentation [97]. For the purpose of simplicity, we select a constant prior transition probability p in this work.

To facilitate the online sequential Bayesian estimation of the model parameters, we propose a non-standard state-space model. Let $x_t = (\xi_t, \tau_t)$ and denote y_t as the observation at time t. At each time step, the state transition process can be formulated as

$$x_t = \begin{cases} x_{t-1} & \text{with probability } 1-p \\ (\xi', t) & \text{with probability } p \end{cases} \tag{3.1}$$

where ξ' is sampled from $f(\cdot)$, the prior distribution of ξ_t. The observation y_t is modeled as $y_t = a_t t + b_t + \varepsilon_t$ where ε_t is the noise and $\varepsilon_t \sim N(0, \sigma_t^2)$.

If there are no change-points ($\tau_t = 1$ for all t), the above model degenerates to a simple linear state-space model with constant model parameters as the state vectors, which can be easily inferred using the conventional Kalman filtering techniques. However, due to the unknown change-points, this state-space model is nonlinear, which makes the inference more difficult. Particle filtering techniques which are based on the sequential importance sampling are particularly effective for non-linear state space models [95]. In the following section a particle filtering algorithm is developed to solve this problem.

3.3 Particle Filtering for Multiple Change-point Model Estimation

3.3.1 Review of Particle Filtering Techniques

For the sake of completeness, we provide a brief review of the particle filtering technique. The basic idea in the particle filtering technique is the sequential importance sampling (SIS). Suppose the state space model is expressed as [95]

$$x_1 \sim f(x)$$

$$x_t | x_{t-1} \sim f(x_t | x_{t-1})$$

$$y_t | x_t \sim g(y_t | x_t) \tag{3.2}$$

Denote the posterior distribution as $\pi_n(x_{1:n})$,

$$\pi_n(x_{1:n}) = p(x_{1:n} | y_{1:n}) = \frac{p(x_{1:n}, y_{1:n})}{p(y_{1:n})} = \frac{f(x_1) \prod_{t=2}^n f(x_t | x_{t-1}) \prod_{t=1}^n g(y_t | x_t)}{p(y_{1:n})} \tag{3.3}$$

where for any sequence $\{z_n\}_{n \geq 1}$, and any $i \leq j$, $z_{i:j}$ is defined as the vector $(z_i, z_{i+1}, \ldots, z_j)$. If we select an importance distribution with the following structure

$$q_n(x_{1:n}) = q_1(x_1) \prod_{t=2}^n q_t(x_t | x_{1:t-1}) \tag{3.4}$$

then the unnormalized weight for particle $x_{1:n}$ can be expressed as

$$\omega_n(x_{1:n}) = \frac{p(x_{1:n}, y_{1:n})}{q_n(x_{1:n})} =$$

$$\left[\frac{f(x_1) g(y_1 | x_1)}{q_1(x_1)} \right] \left[\frac{g(y_2 | x_2) f(x_2 | x_1)}{q_2(x_2 | x_1)} \right] \cdots \left[\frac{g(y_n | x_n) f(x_n | x_{n-1})}{q_n(x_n | x_{1:n-1})} \right]$$

$$= \omega_1(x_1) \prod_{t=2}^n \alpha_t \tag{3.5}$$

where

$$\omega_1(x_1) = \frac{f(x_1) g(y_1 | x_1)}{q_1(x_1)} \tag{3.6}$$

$$\alpha_t = \frac{g(y_t | x_t) f(x_t | x_{t-1})}{q_t(x_t | x_{1:t-1})} \tag{3.7}$$

Equation (3.5) indicates that the weight can be calculated recursively or sequentially, i.e., knowing $\omega_{t-1}(\boldsymbol{x}_{1:t-1})$, we can calculate $\omega_t(\boldsymbol{x}_{1:t})$ by multiplying $\omega_{t-1}(\boldsymbol{x}_{1:t-1})$ with α_t at time step t.

The expectation of any function $\varphi_n(\boldsymbol{x}_{1:n})$ with respect to the posterior probability $\pi_n(\boldsymbol{x}_{1:n})$ can be estimated by

$$E(\varphi_n(\boldsymbol{x}_{1:n})|y_{1:n}) \approx \sum_{i=1}^{N_s} W_n^{(i)} \varphi_n(\boldsymbol{x}_{1:n}^{(i)}) \tag{3.8}$$

where $W_n^{(i)}$ is the normalized weight of particle $\boldsymbol{x}_{1:n}^{(i)}$ and N_s is the number of particles . Denote $\delta_n^{SIS}(\varphi) = \sum_{i=1}^{N_s} W_n^{(i)} \varphi_n(\boldsymbol{x}_{1:n}^{(i)})$ and $I_n(\varphi) = E(\varphi_n(\boldsymbol{x}_{1:n})|y_{1:n})$, then

$$\sqrt{N_s}\left(\delta_n^{SIS}(\varphi) - I_n(\varphi)\right) \xrightarrow{D} N(0, \phi_{q_n}^2)$$

with the asymptotic variance given by

$$\phi_{q_n}^2 = \int \frac{\pi_n^2(\boldsymbol{x}_{1:n})}{q_n(\boldsymbol{x}_{1:n})} (\varphi_n(\boldsymbol{x}_{1:n}) - I_n(\varphi))^2 d\boldsymbol{x}_{1:n} \tag{3.9}$$

The estimate is biased for finite N_s and the asymptotic bias is given as

$$\lim_{N_s \to \infty} N_s(\delta_n^{SIS}(\varphi) - I_n(\varphi))$$

$$= -\int \frac{\pi_n^2(\boldsymbol{x}_{1:n})}{q_n(\boldsymbol{x}_{1:n})} (\varphi_n(\boldsymbol{x}_{1:n}) - I_n(\varphi)) d\boldsymbol{x}_{1:n} \tag{3.10}$$

The generic particle filtering algorithm is shown in Algorithm 3.1. Note in the algorithm there is a resampling step (Step 3) which is a "Darwinian" procedure that obtains samples distributed approximately as $\pi_n(\boldsymbol{x}_{1:n})$. It has the advantage of removing particles with low

weights and keeping particles with high weights at a high probability. The multinomial resampling is one of the most common resampling methods and is used in this work. In the following subsections, the specific challenges of the particles filtering algorithm for our steady state detection problem will be discussed with Subsection 3.3.2 addressing the importance sampling step (Step 1 and 2), Subsection 3.3.3 solving the particle degeneracy and impoverishment problems by adding an extra step after the resampling step (Step 3), and Subsection 3.3.4 proposing a timeliness improvement strategy to reduce the detection delay.

Algorithm 3.1. Sequential Monte Carlo Filtering Algorithm

At time $t = 1$,

1. Sample $x_1^{(i)} \sim q_1(x_1)$, $i = 1,2, \cdots N_s$
2. Compute the weights $\omega_1(x_1^{(i)})$ and normalized weights $W_1^{(i)} = \frac{\omega_1(x_1^{(i)})}{\sum_{i=1}^{N_s} \omega_1(x_1^{(i)})}$
3. Resample $\{W_1^{(i)}, x_1^{(i)}\}$ according to the particle weight $W_1^{(i)}$ to obtain N_s equally weighted particles $\{\frac{1}{N_s}, \bar{x}_1^{(i)}\}$ and set $\{W_1^{(i)}, x_1^{(i)}\} \leftarrow \{\frac{1}{N_s}, \bar{x}_1^{(i)}\}$.

At time $t \geq 2$,

1. Sample $x_t^{(i)} \sim q_t(x_t | x_{1:t-1}^{(i)})$, set $x_{1:t}^{(i)} \leftarrow (x_{1:t-1}^{(i)}, x_t^{(i)})$
2. Compute $\alpha_t(x_{1:t}^{(i)})$ and $W_t^{(i)} \propto \alpha_t(x_{1:t}^{(i)})$
3. Resample $\{W_t^{(i)}, x_{1:t}^{(i)}\}$ to obtain particles $\{\frac{1}{N_s}, \bar{x}_{1:t}^{(i)}\}$ and set $\{W_t^{(i)}, x_{1:t}^{(i)}\} \leftarrow \{\frac{1}{N_s}, \bar{x}_{1:t}^{(i)}\}$

3.3.2 Importance Density and Sampling Methods

One common issue with particle filtering is the particle degeneracy problem, which means that, after a few iterations, the weight may concentrate only on a few particles and most particles will have negligible weights, especially when the particle weights are highly skewed [95, 98]. A

natural way to reduce the effect of degeneracy problem is to select the importance density that minimizes the variances of the importance weights. Doucet [99] showed that the optimal importance density is $q_t\left(x_t\big|x_{1:t-1}^{(i)}\right) = p(x_t|x_{t-1}^{(i)}, y_t)$. In practice, however, the optimal importance density is often not obtainable and instead the most common and convenient choice is to select the prior as the importance density function

$$q_t\left(x_t\big|x_{1:t-1}^{(i)}\right) = f(x_t|x_{t-1}^{(i)}) \tag{3.11}$$

This greatly simplifies the computation since after the resampling step the importance weights at time t is simply $\omega_t = g\left(y_t\big|x_t^{(i)}\right)$. In our model we select the prior $f(x_t|x_{t-1})$ as the importance density function which is a mixture distribution as shown in Eq. (3.1). An efficient sampling method is the stratified sampling method [100] where we sample from $f(x)$ with a deterministic sample size n_0 and resample from the particles obtained at time $t-1$ with $n_1 = N_s - n_0$ samples. Note the particles at time $t-1$ are approximately distributed as $\pi_{t-1}(x_{t-1})$. The target distribution is $\pi_t(x_t) = p(x_t|y_{1:t}) = \frac{p(x_t|y_{1:t-1})g(y_t|x_t)}{p(y_t|y_{1:t-1})}$ and the importance density is

$$p(x_t = x|y_{1:t-1})$$

$$= pf(x) + (1-p)\pi_{t-1}(x_{t-1} = x) \tag{3.12}$$

Suppose $x_{t,0}^{(1)}, x_{t,0}^{(2)}, \dots, x_{t,0}^{(n_0)}$ are independent random samples from $f(x)$ and $x_{t,1}^{(1)}, x_{t,1}^{(2)}, \dots, x_{t,1}^{(n_1)}$ are from $\pi_{t-1}(x_{t-1})$. Define $U_{t,j} = \frac{1}{n_j}\sum_{i=1}^{n_j} \varphi\left(x_{t,j}^{(i)}\right)\omega_t(x_{t,j}^{(i)})$ and $V_{t,j} = \frac{1}{n_j}\sum_{i=1}^{n_j} \omega_t(x_{t,j}^{(i)}), j = 0,1$ where $\omega_t(x_{t,j}^{(i)}) = g(y_t|x_{t,j}^{(i)})$. Let

$$\delta_t = \frac{pU_{t,0} + (1-p)U_{t,1}}{pV_{t,0} + (1-p)V_{t,1}} \tag{3.13}$$

then we can derive the following results of the asymptotic distribution. The proof of Theorem 1

(1) can be found in Raghavan's work [101] and the proof of Theorem 3.1 (2) and (3) is given in

the Appendix.

Theorem 3.1 *Denote* $h_0 = f$, $h_1 = \pi_{t-1}(\boldsymbol{x}_{t-1})$ *and* $h = p(\boldsymbol{x}_t|y_{1:t-1}) = pf + (1-p)h_1$. *Assume for* $j = 0,1$, $E_{h_j}(\varphi(x_t)^2 \omega_t(x_t)^2) < \infty$ *and* $E_{h_j}(\varphi(x_t)^2) < \infty$. $n_0 \to \infty$, $n_1 = N_s - n_0 \to \infty$ *and* $\frac{n_0}{N_s} \to q$. *Also assume that the samples* $\boldsymbol{x}_{t-1}$ *at time* $t-1$ *are directly sampled from* $\pi_{t-1}(\boldsymbol{x}_{t-1})$ *(neglect the variance accumulated before time* $t-1$). *then*

(1) $\sqrt{N_s}\left(\delta_t - E_{\pi_t}(\varphi(\boldsymbol{x}_t))\right) \xrightarrow{D} N(0, V_t(q))$ *with the asymptotic variance* $V_t(q)$ *given as*

$$V_t(q) = \frac{p^2}{q}V_{h_0} + \frac{(1-p)^2}{1-q}V_{h_1} \tag{3.14}$$

where for $j = 0,1$

$$V_{h_j} = \frac{1}{[p(y_t|y_{1:t-1})]^2}Var_{h_j}\left[\left(\varphi(\boldsymbol{x}_t) - E_{\pi_t}(\varphi(\boldsymbol{x}_t))\right)\omega_t\right]$$

(2)   The estimate is biased for finite N_s *with the asymptotic bias given by*

$$\lim_{N_s \to \infty} N_s\left(\delta_t - E_{\pi_t}[\varphi(\boldsymbol{x}_t)]\right) = \frac{p^2}{q}B_0 + \frac{(1-p)^2}{1-q}B_1 \tag{3.15}$$

where for $j = 0,1$

$$B_j = -\frac{1}{[p(y_t|y_{1:t-1})]^2}Cov_{h_j}\left([\varphi(\boldsymbol{x}_t) - E_{\pi_t}(\varphi(\boldsymbol{x}_t))]\omega_t, \omega_t\right)$$

(3)   The asymptotic variance reaches its minimum when $q_{opt} = \frac{pV_{h_0}}{pV_{h_0}+(1-p)V_{h_1}}$. *Denote* V_t^* *as the asymptotic variance of direct sampling from h using the composition method, then* $V_t(q_{opt}) \leq V_t(p) \leq V_t^*$.

Note V_{h_j} and B_j in Theorem 1 are slightly different from the asymptotic variance and bias of the importance sampling calculated using only h_j as the importance density. Chopin [102] summarized the structure of a particle filter as three steps at each iteration: mutation, correction and selection. The asymptotic variance of the particle filter can be calculated iteratively based on these three steps. In Theorem 1 we only consider the asymptotic variance of the mutation and correction processes over one time step, which may provide some insights on the total asymptotic variance of the particle filter.

Theorem 3.1 (3) tells us that there exists an optimal q_{opt} which can minimize the asymptotic variance. However, in practice this value is always changing along iterations and it is also very difficult or even impossible to calculate. In the real application we can use the proportional allocation, i.e., $q = p$ or $n_0 = N_s p$ to reduce the variance. In this work we select $n_0 = N_s p$. Note that usually there is a tradeoff between minimizing the bias and minimizing the variance. It is very hard to directly compare their asymptotic biases using (3.10) and (3.15). However, in this case the variance is more important than the bias since in the application we may adjust the detection threshold to reduce the bias effect.

From (3.13) we know that using the deterministic sample size n_0 and n_1, the normalized importance weight for particle $\boldsymbol{x}_{t,j}^{(i)}$ can be expressed as

$$W_{t,j}^{(i)} = \begin{cases} \dfrac{n_1 p \omega_t\left(x_{t,0}^{(i)}\right)}{n_1 p \sum_{i=1}^{n_0} \omega_t\left(x_{t,0}^{(i)}\right) + n_0(1-p) \sum_{i=1}^{n_1} \omega_t\left(x_{t,1}^{(i)}\right)}, if\ j = 0 \\ \dfrac{n_0(1-p)\omega_t\left(x_{t,1}^{(i)}\right)}{n_1 p \sum_{i=1}^{n_0} \omega_t\left(x_{t,0}^{(i)}\right) + n_0(1-p) \sum_{i=1}^{n_1} \omega_t\left(x_{t,1}^{(i)}\right)}, if\ j = 1 \end{cases} \tag{3.16}$$

When $q = p$, the weight for each particle is simply $\omega_t(x_t)$, the same as using the composition resampling method. The sampling algorithm with deterministic sample size is shown in Algorithm 3.2.

Algorithm .3.2. Stratified Sampling with Deterministic Sample Size

At time step $t = 1$,

1. Sample $x_1^{(i)} \sim f(x), i = 1,2, \dots, N_s$
2. Compute $\omega_1\left(x_1^{(i)}\right) = g(y_1|x_1^{(i)})$ and $W_1^{(i)}$

At time step $t > 1$,

1. Sample $x_{t,0}^{(i)} \sim f(x), i = 1,2, \dots, n_0$ to obtain n_0 new particles. Resample $\{W_{t-1}^{(i)}, x_{t-1}^{(i)}\}$ to obtain $n_1 = N_s - n_0$ particles $\bar{x}_{t-1}^{(i)}, i = 1,2, \dots, n_1$ and set $x_{t,1}^{(i)} \leftarrow \bar{x}_{t-1}^{(i)}$
2. Set $x_t \leftarrow \{x_{t,0}, x_{t,1}\}$ and compute $W_t^{(i)}$ using Eq. (3.16)

3.3.3 Partial Gibbs Move

Although the resampling step could reduce the particle degeneracy effect, it may reduce the particle diversity to cause another problem, the particle impoverishment, where there may be less and less unique particles along iterations. For our state space model, this problem could become

serious because the state variable is unchanged with some probability. Besides, the resampling step cannot solve the particle degeneracy issue completely when the sample size is small. The resample-move algorithm proposed by Gilks [103] is a common way to reduce both particle degeneracy and impoverishment problem. In this algorithm, a "move" step is added following the resampling step (Step 3 in Algorithm 3.1) to generate new particles through MCMC kernels with the posterior as the invariant distributions. Resample-move algorithm not only diversifies particles, but also produces more particles with significant weights. Because of this, it can significantly reduce the required number of particles in the calculations. This is critical for *on-line* detection algorithm which requires low computational cost. The MCMC move step is often implemented using a Metropolis-Hastings move. In our model, we use the one-step Gibbs sampler to move only the model parameters $\xi = [\beta^T, \sigma^2]^T$ where $\beta = [a, b]^T$.

It is common to assume a normal distribution as the prior of β and an inverse Gamma distribution as the prior of σ^2 where $\beta \sim N(\mu_0, \Sigma_0)$ and $\sigma^2 \sim IG(\alpha_1, \alpha_2)$. The conditional posterior distribution of β and σ^2 can be computed using Lemma 1 (the proof is included in the Appendix of this chapter)

Lemma 3.1 *Assume σ^2 and β are independent and $\beta \sim N(\mu_0, \Sigma_0)$, $\sigma^2 \sim IG(\alpha_1, \alpha_2)$ where $\mu_0, \Sigma_0, \alpha_1, \alpha_2$ are known parameters. Denote*

$$X_t = \begin{bmatrix} \tau_t & 1 \\ \tau_t + 1 & 1 \\ \vdots & \vdots \\ t & 1 \end{bmatrix} \text{ and } Y_t = y_{\tau_t:t}, \text{ then}$$

$$(\sigma_t^2 | y_{1:t}, \beta_t, \tau_t) \sim IG\left(\alpha_1 + \frac{t - \tau_t + 1}{2}, \alpha_2 + \frac{\|Y_t - X_t \beta_t\|^2}{2}\right)$$

$$(\boldsymbol{\beta}_t|y_{1:t}, \sigma_t^2, \tau_t) \sim N(\boldsymbol{\mu}_t, \boldsymbol{\Sigma}_t) \tag{3.17}$$

where

$$\boldsymbol{\mu}_t = \left[\frac{\boldsymbol{X}_t^T \boldsymbol{X}_t}{\sigma_t^2} + \boldsymbol{\Sigma}_0^{-1}\right]^{-1} \left[\frac{\boldsymbol{X}_t^T \boldsymbol{Y}_t}{\sigma_t^2} + \boldsymbol{\Sigma}_0^{-1} \boldsymbol{\mu}_0\right]$$

$$\boldsymbol{\Sigma}_t = \left[\frac{\boldsymbol{X}_t^T \boldsymbol{X}_t}{\sigma_t^2} + \boldsymbol{\Sigma}_0^{-1}\right]^{-1} \tag{3.18}$$

Sampling based on (3.17) and (3.18) can diversify particles and produce more particles close to the true state. Note that particles that have low weights may have significant weights in the following time steps. That is why we also need more unique particles. Besides, the Gibbs move strategy can also increase the survival rate of newly generated particles from prior in the resampling step and thus increase the change-point detection timeliness.

Usually it is desirable to have a constant computational cost in each time step for particle filtering algorithms, which is particularly critical for the real-time monitoring purpose. However, the introduction of Gibbs-move step breaks the balance. Denote the duration since the latest change-point as d_t which is expressed as $d_t = t - \tau_t + 1$. It is observed that the longer the duration, the higher the computational cost of the Gibbs move. Note that the increase of the computational cost here is due to the Gibbs move, not the re-sampling process, new particle generation or the calculation of P_t. To control the computational cost of each time step, we apply the "partial move" strategy proposed by Chopin [90] where we move only a subset of resampled particles. The subset is obtained by randomly drawing particles without replacement among the resampled particles until the sum of $d_t^{(i)}$ is larger than some constant C. Another advantage of "partial move" strategy is that it will improve the detection timeliness because it can increase the

disappearing rate of old particles with large d_t and boost the survival of new particles at the transition region that can fit the most recent signals better. In summary, the improved particle filtering algorithm is given in Algorithm 3.3.

Algorithm 3.3. Particle Filtering Algorithm

At time step $t = 1$,

1. Sample $x_1^{(i)} \sim f(x), i = 1,2, \dots, N_s$
2. Compute $\omega_1\left(x_1^{(i)}\right) = g(y_1|x_1^{(i)})$ and $W_1^{(i)}$
3. Resample $\{W_1^{(i)}, x_1^{(i)}\}$ to obtain $\{\frac{1}{N_s}, \bar{x}_1^{(i)}\}$ and set $\left\{W_1^{(i)}, x_1^{(i)}\right\} \leftarrow \{\frac{1}{N_s}, \bar{x}_1^{(i)}\}$

For time step $t > 1$,

1. Sample $x_t^{(i)}$ according to Algorithm 3.2.
2. Compute $W_t^{(i)}$ according to Algorithm 3.2.
3. Resample $\{W_t^{(i)}, x_t^{(i)}\}$ to obtain $\{\frac{1}{N_s}, \bar{x}_t^{(i)}\}$ and set $\left\{W_t^{(i)}, x_t^{(i)}\right\} \leftarrow \{\frac{1}{N_s}, \bar{x}_t^{(i)}\}$
4. Gibbs move: select a subset S of resampled particles such that $\sum_{j \in S} d_t^{(j)} \leq C$
   - Sample $\bar{\beta}_t^{(j)} \sim N\left(\mu_t^{(j)}, \Sigma_t^{(j)}\right)$ and set $\beta_t^{(j)} \leftarrow \bar{\beta}_t^{(j)}$
   - Sample $\overline{\sigma_t^2}^{(j)} \sim IG(\alpha_1 + \frac{t - \tau_t^{(j)} + 1}{2}, \alpha_2 + \frac{\left\| Y_t - X_t^{(j)} \beta_t^{(j)} \right\|^2}{2})$ and set $(\sigma_t^2)^{(j)} \leftarrow \overline{\sigma_t^2}^{(j)}$

3.3.4 Timeliness Improvement Strategy

The timeliness is a very important factor for *on-line* steady state detection. In the simulation, we observe that the posterior distribution of the model parameters conditioning on the LCP concentrates on a small region around the true model parameters, as the number of observations following this model accumulates. Since the prior is typically far different from the posterior

distribution, only a small number of new particles generated from the prior are close to the true model parameters, i.e., having significant weights. Therefore it becomes harder for these new particles to survive in the resampling step when the duration of the current model becomes very large. This may lead to a large detection delay because of the lack of survived new particles generated around the period where the model changes. In this work we propose a heuristic timeliness improvement strategy to overcome this issue: at each time t we randomly select n' particles among n_1 particles resampled from $\pi_{t-1}(x_{t-1})$ in the sampling step (Step 1) and "move" the discrete component τ_t of the selected particles to integers which are randomly sampled from $[1,2,\dots,t]$. It can diversify the discrete component of particles and increase the number of particles with τ_t close to the true value. We observe that selecting only several particles can lead to a significant timeliness improvement for signals with long linear segments.

3.3.5 Steady state Detection Based on the Particle Filtering Estimation

Define detection index P_t as the probability that the absolute value of the slope $|a_t|$ is below a threshold s_0 at time step t. It is estimated as

$$P_t = Pr(|a_t| < s_0|y_{1:t}) \approx \sum_{i=1}^{N_s} W_t^{(i)} I_{\{|a_t^{(i)}|<s_0\}}\left(x_t^{(i)}\right) \tag{3.19}$$

where $I(\cdot)$ is an indicator function with

$$I_{\{|a_t^{(i)}|<s_0\}}\left(x_t^{(i)}\right) = \begin{cases} 1 & if \ \left|a_t^{(i)}\right| < s_0 \\ 0 & otherwise \end{cases}$$

The estimated observation $\hat{y}_t$ is calculated as

$$\hat{y}_t = \hat{a}_t t + \hat{b}_t = \sum_{i=1}^{N_s} W_t^{(i)}(a_t^{(i)}t + b_t^{(i)}) \tag{3.20}$$

When $P_t > p_0$, the signal is considered steady. Typically there is a rapid increase of P_t around the steady state entering. Therefore p_0 is not considered as a tuning parameter and is set to be 0.9 in the algorithm. Note the above calculations and detection are performed after Step 3 in Algorithm 3.3. For the purpose of clarity, we refer to the entering time from transient state (or steady state) to the steady state (or transient state) as the transition point in the rest of the article.

In implementation, we need to specify the prior parameters for $\boldsymbol{\beta} \sim N(\boldsymbol{\mu}_0, \boldsymbol{\Sigma}_0)$ and $\sigma^2 \sim IG(\alpha_1, \alpha_2)$. For σ^2, we can roughly estimate the variance of the historical data in the application and choose appropriate α_1 and α_2. In practice the change of α_1 and α_2 will not result in significant difference on the detection results since we use Gibbs sampler to move particles in the algorithm. For $\boldsymbol{\beta}$, we can use a noninformative prior with $\boldsymbol{\mu}_0 = \mathbf{0}$ and $\boldsymbol{\Sigma}_0 = \sigma_0^2 \boldsymbol{I}$ where $\boldsymbol{I}$ is the identity matrix and σ_0^2 is a large variance. As for the transition probability p, any value in the interval [0.1,0.5] works quite well in numerical studies.

3.4 Case Studies for Performance Evaluation and Comparison

3.4.1 Illustration

In the numerical study the signals are generated using bias functions and noises. The bias functions consist of transient state and steady state. In total five bias functions are used in this work: linear, quadratic, exponential, oscillating and trapezoidal functions, as shown in Table 3-1. The first four bias functions are most commonly used to test off-line heuristic algorithms in initial bias elimination problems [53, 61, 70, 76]. Without loss of generality we only consider the

negative bias scenarios, i.e. non-decreasing before steady state, for the first three types of bias functions. The oscillating and trapezoidal bias functions are used to illustrate the detection process.

Table 3-1: Five bias functions

Type	Function $y(t)$
Linear	$y(t) = \begin{cases} \dfrac{t}{T_0}h & ,t = 1, \dots, T_0 \\ h & ,t = T_0 + 1, \dots, n \end{cases}$
Quadratic	$y(t) = \begin{cases} h\left[1 - \dfrac{(t - T_0)^2}{(T_0 - 1)^2}\right] & ,t = 1, \dots, T_0 \\ h & ,t = T_0 + 1, \dots, n \end{cases}$
Trapezoidal	$y(t) = \begin{cases} \dfrac{t}{T_0}h & ,t = 1, \dots, T_0 \\ h & ,t = T_0 + 1, \dots, n - T_0 \\ \dfrac{h(n - t)}{n - T_1} & ,t = n - T_0 + 1, \dots, n \end{cases}$
Oscillating	$y(t) = \begin{cases} h\dfrac{T_0 - t}{T_0 - 1}\sin\left(\dfrac{\pi t}{f}\right) & ,t = 1, \dots, T_0 \\ 0 & ,t = T_0 + 1, \dots, n \end{cases}$
Exponential	$y(t) = \begin{cases} h\left[1 - 10^{\frac{1-t}{T_0-1}}\right] & ,t = 1, \dots, T_0 \\ y(T_0) & ,t = T_0 + 1, \dots, n \end{cases}$

We set $h = 1, n = 500$ and $\sigma_t = 0.1$ in the simulation. $T_0 = 100$ for the trapezoidal signal and $T_0 = 300, f = 30$ (total $\frac{T_0}{f} = 10$ peaks and troughs, fixed in this work) for the oscillating signal. The prior parameters are set to: $\boldsymbol{\mu}_0 = [0,0]^T$, $\boldsymbol{\Sigma}_0 = 100I$ and $\sigma_t^2 \sim IG[10,0.1]$. The state transition probability is set as $p = 0.2$. The slope threshold $s_0 = 0.004$. Total $N_s = 2000$

particles are used in the simulation and the Gibbs move constant C is set as $10N_s$. The parameter

for the timeliness improvement strategy is set $n' = 20$.
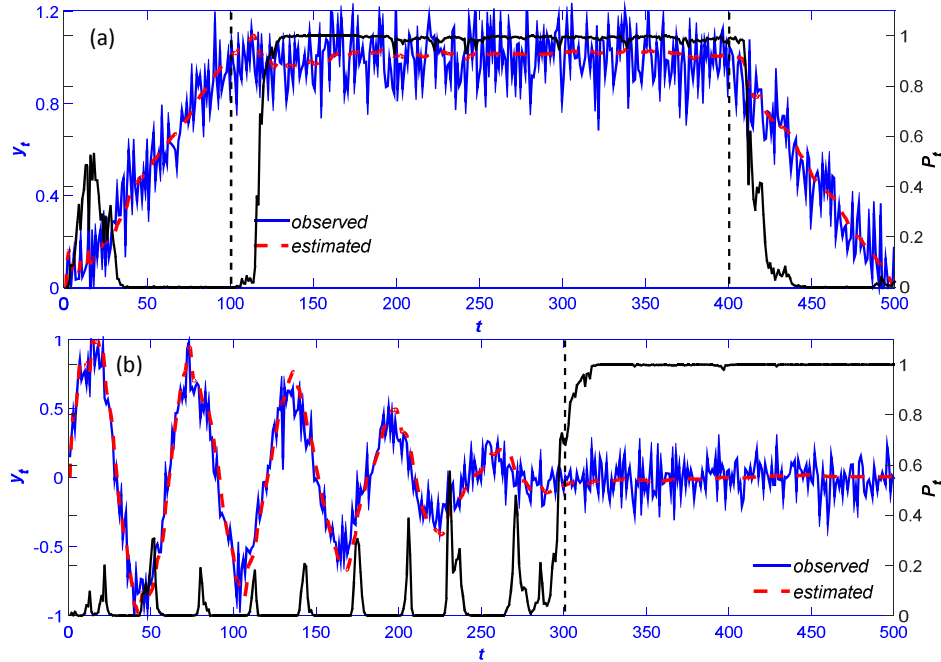
Figure 3-3: Illustration of the steady state detection for (a) trapezoidal signal and (b) oscillating signal. The vertical dashed lines denote the transition points between transient state and steady state (100 and 400 for step signal and 300 for oscillating signal).

Figure 3-3 illustrates the steady state detection process where the solid black line is the

detection probability indicator and the dashed vertical lines denote the steady state transition

point. We can see that the detection index changes steeply near the transition points between the

transient state and steady state. The estimated values of the observations are also close to the true

value. Select $p_0 = 0.9$ as the probability threshold, then the detected state transition times for the

step signal are 123 (true value: 100) and 411 (true value: 400), and for the oscillating signal the

detected value is 308 (true value: 300).
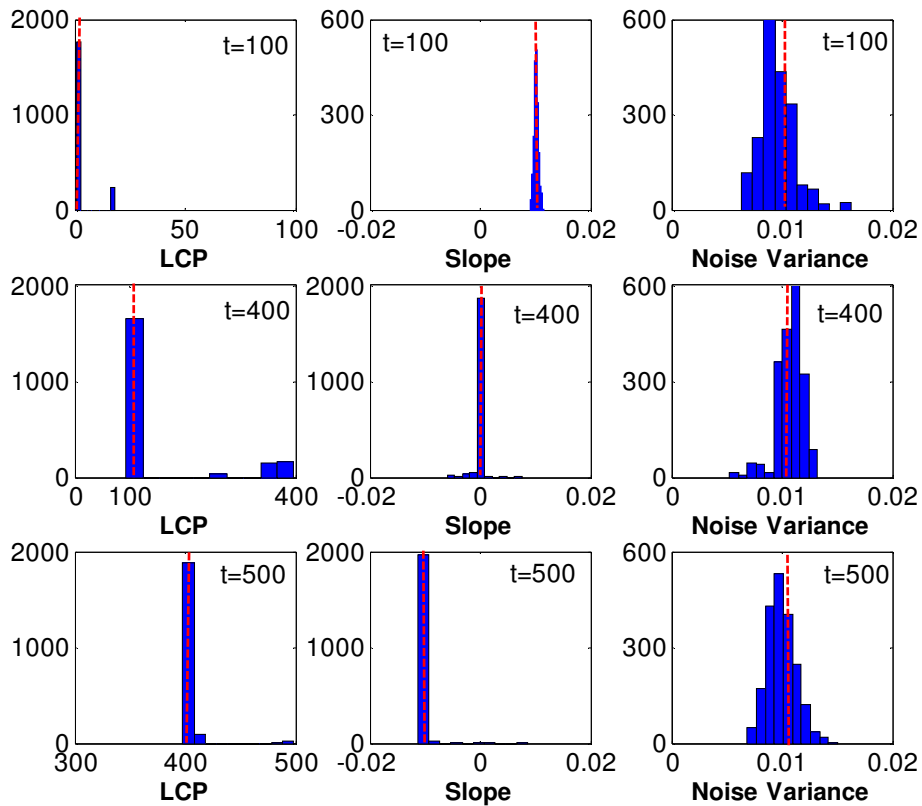
Figure 3-4: Histograms of the estimated values of the latest change-point (LCP), slope and signal noise variance for the trapezoidal signal at different time steps; the true values of the parameters are indicated by the vertical dashed lines.

To see how the model parameters evolve, we have plotted the histograms of the simulated values of the LCP τ_t, the slope a_t and the variance σ_t^2 at different time for the trapezoidal function, as shown in Figure 3-4. At time $t = 100, 400$ and 500 the LCP of all particles are concentrated near the true change-points 1, 100 and 400, respectively. The corresponding slopes and noise variance are also concentrated to the true value. Therefore our algorithm is able to accurately detect the change-points and estimate the model parameters.

3.4.2 Comparison with/without Gibbs Move

To compare the particle filtering algorithms with and without Gibbs move, a signal is generated using the linear bias function with $h = 1, n = 500$ and $T_0 = 200$. The standard deviation of the signal noise is set as 0.1. The detection parameters are the same with those used in the previous subsection. Three conditions are considered: (1) $N_s = 2,000$, no Gibbs move, (2) $N_s = 20,000$, no Gibbs move, and (3) $N_s = 2,000$, Gibbs move.
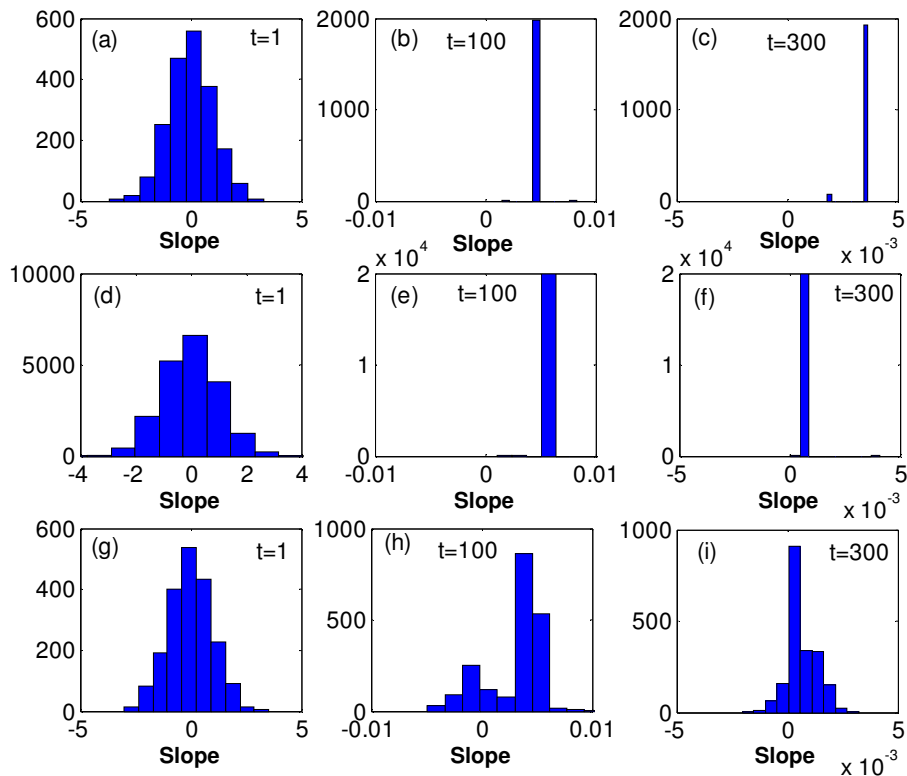
Figure 3-5: Histograms of the slope a_t at time step $t = 1, 100$ and 300 for (a-c) $N_s = 2000$, no Gibbs move; (d-f) $N_s = 20,000$, no Gibbs move; (g-i) $N_s = 2000$, Gibbs move.

The histograms of the slope at $t = 1, 100$ and 300 are shown in Figure 3-5. For the particle filter without Gibbs move, the particle impoverishment is so severe that almost all particles

collapse to a single point at time step $t = 100$ and 300, even if we increase the number of particles from 2000 to 20000. Besides, the particle degeneracy problem also exists for particle filters without Gibbs move, especially when $N_s = 2000$. At time $t = 300$, almost all particles are far away from the true state and thus have negligible weights for $N_s = 2000$ and no Gibbs move, as shown in Figure 3-5 (c). In this case, the particle filter algorithm totally fails to detect the steady state, as shown in Figure 3-6 (a).
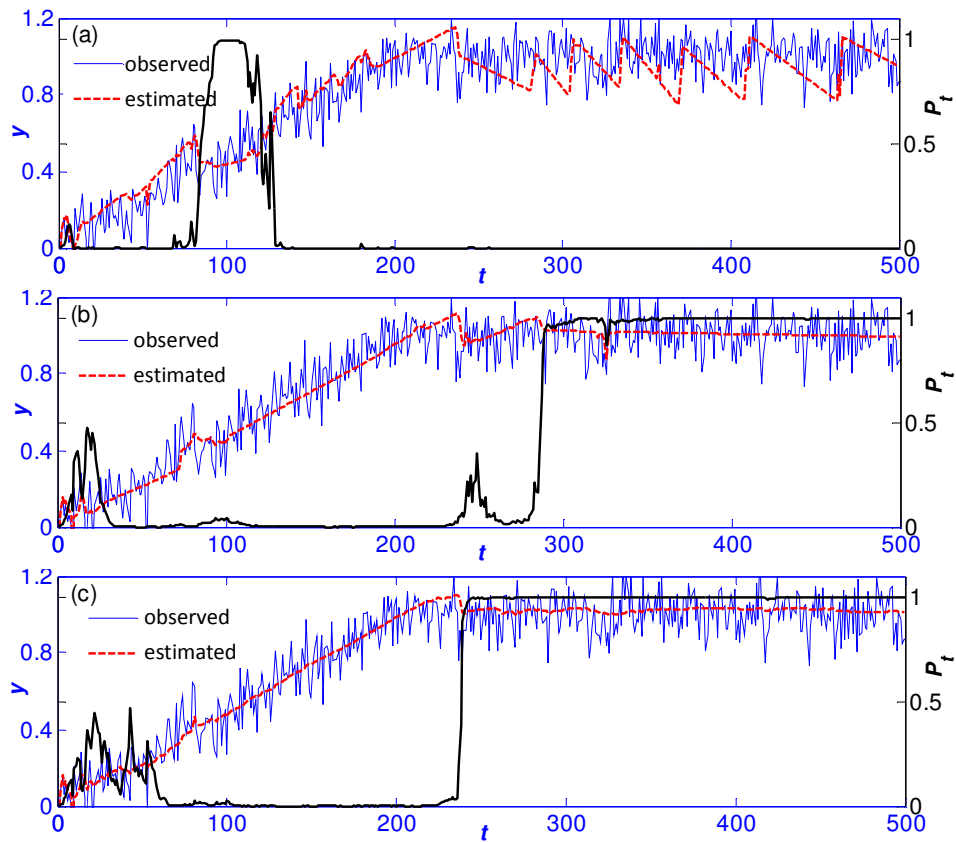
Figure 3-6: Steady state detection using particle filters with (a) $N_s = 2000$, no Gibbs move, (b) $N_s = 20,000$, no Gibbs move and (c) $N_s = 2000$, Gibbs move.

Increasing the sample size from 2000 to 20000 reduces the degeneracy effect, as shown in Figure 3-5 (f), where all particles are close to 0 and thus have more significant weights. However,

the filtered signal is still not smooth and the detection has a large delay, as shown in Figure 3-6 (b) (detected time: 298). Besides, using a very large sample size is impractical in on-line applications since it would significantly increase the computational cost. The Gibbs move strategy has solved both the particle degeneracy and particle impoverishment problems, as can be seen in Figure 3-5 (h-i). Figure 3-5 (h) shows more unique particles and Figure 3-5 (i) shows more particles close to 0. The detected steady state time is 240 (Figure 3-6 (c), detection delay: 40), which is much more timely than that of Figure 3-6 (b). The estimated signal is smoother, indicating a more accurate estimation of model parameters.

3.4.3 Comparison with Other Methods

the statistical monitoring schemes for change-point problems, the performance is typically evaluated by two types of criteria, the false alarm rate (FAR) before the change and the detection delay after a change occurs. In this research the FAR refers to the probability of signaling a steady state alarm when the process is still in the transient state. Usually a required FAR is specified and the corresponding detection delay is used to compare different detection schemes. However, in the steady state detection FAR does not capture the closeness of the detected steady state transition time to the true value. In this research, we develop an evaluation metric, the weighted standard detection error (WSDE) which is defined as

$$\text{WSDE} = \sqrt{\frac{1}{N}\sum_{i=1}^{N} \text{w}(\hat{T}_i)(\hat{T}_i - T_0)^2} \tag{3.21}$$

Here $\hat{T}_i$ is the detected steady state time, N is the number of replications and $\text{w}(\hat{T}_i)$ is the penalty weight. If $w = 1$, we put equal penalty on detection delay and false detection and only consider

the closeness of the detection. Usually the cost of false detection is higher than the detection delay for the same amount of detection bias; therefore we may put more penalties on the false detection and select $w(\hat{T}_i)$ as

$$w(\hat{T}_i) = \begin{cases} w \in (0,1] & if\ \hat{T}_i \geq T_0 \\ 1 & if\ \hat{T}_i < T_0 \end{cases}$$

We compare our method (PF) with three existing *on-line* methods. The first one is the slope detection method (SDM) [86, 87], in which an ordinary least square estimator of the slope of a moving data window is calculated until its absolute value is below a threshold. The second one is the variance ratio test (VRT) [62]. In this method the variance of a moving data window is calculated using two different methods, the mean squared deviation from the average (V_1) and the mean squared differences of the successive data (V_2). The testing statistic is the ratio of these two variances V_1/V_2. In the transient state the ratio is expected to be larger than 1 while in the steady state this ratio is close to 1. The third method is to perform a t-test on two recently computed means of two adjacent windows with pooled standard deviation [88]. Note in this work we do not compare the performance of detecting the change from steady state to transient state, since this kind of detection is relatively easier and has been intensively studied in the statistical process control (SPC) field.

The linear, quadratic, exponential and oscillating bias functions are used to generate simulated signals, as shown in Table 3-1. For each type of signals, three sets of signal parameters are used: (1) $h = 1, T_0 = 200$, (2) $h = 1, T_0 = 300$ and (3) $h = 5, T_0 = 300$. Note here we use different bias functions with different parameters to simulate different shapes and severity of the initial bias before the steady state. In practice the signal noise may not be i.i.d, so we use three

kinds of autoregressive model for the signal noise: no auto-correlation (AR(0)), first-order autoregressive correlation (AR(1)), and second-order autoregressive correlation (AR(2)), as shown in Table 3-2. For AR(0), three noise levels are used, $\sigma_t = 0.06, 0.1$ and 0.14. For AR(1) and AR(2), $\sigma_t = 0.06$ and 0.1 are used.

Table 3-2: Noise Auto-correlation Types and Their Parameters

Type	Equation	Parameter
AR(0)	$\Psi_t^{(0)} = \epsilon_t$	$\epsilon_t \sim N(0, \sigma_t^2)$
AR(1)	$\Psi_t^{(1)} = \phi_1 \Psi_{t-1}^{(1)} + \epsilon_t$	$\phi_1 = 0.6$
AR(2)	$\Psi_t^{(2)} = \phi_2 \Psi_{t-1}^{(2)} + \phi_3 \Psi_{t-2}^{(2)} + \epsilon_t$	$\phi_2 = -0.25, \phi_3 = 0.5$

In the simulation, $N = 500$ replications are generated for each signal. The detection parameters (window size, threshold) for SDM, VRT and t-test are selected in such a way that the overall WSDE among all signals under each autoregressive noise type and penalty weight w is minimized. The number of particles used in PF method is set as $N_s = 1,000$ and threshold parameter s_0 is selected using the same way as used in the other three methods. All other detection parameters are the same as in Section 3.4.1.

Figure 3-7 shows the WSDE and FAR of these four detection methods as functions of w under different noise autoregressive models. Note that here the WSDE and FAR are calculated over all signals for each w. The PF method outperforms all other methods in terms of overall WSDE under all penalty weights and noise autoregressive models. Besides, the FAR of the PF method is also lower than almost all other methods in all cases. Note that if we reduce the FAR of other three methods for each w to that of the PF method by changing the detection parameters,

the advantage of the PF method in term of WSDE over the other methods will be further increased.
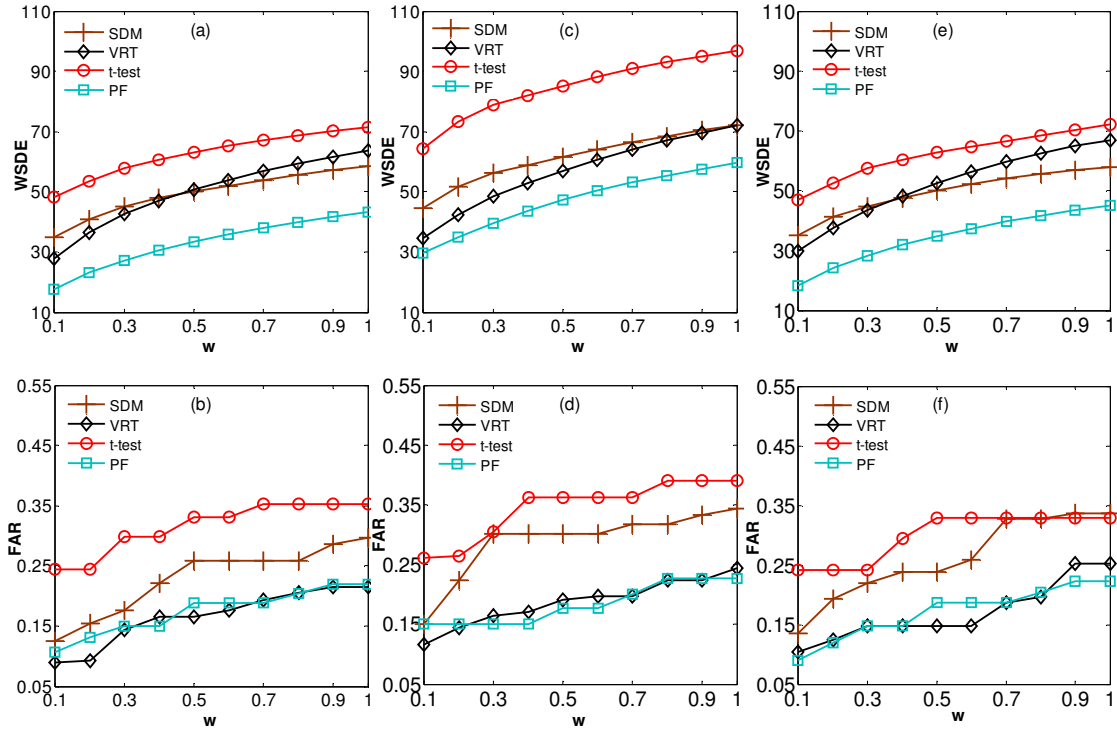
Figure 3-7: The weighted standard detection error and false alarm rate of PF, SDM, VRT and t-test as a function of penalty weight for (a-b) AR(0), (c-d) AR(1) and (e-f) AR(2).

Table 3-3 shows the detailed detection results for $w = 1$ and AR(0) (the results for AR(1) and AR(2) are quite similar and therefore are not put in this dissertation). FAR is used to see the contribution of early detection on WSDE. From this table we can see that the PF method is more robust and accurate in terms of the overall WSDE in handling signals with various shapes and changing rates in the transient period. In other words, the PF method is able to detect the steady state more accurately using only one set of detection parameters. For other three methods, one set of fixed detection parameters are not sufficiently flexible to be effective in different situations.

Table 3-3: Comparison of PF, SDM, VRT and $t\text{-}test$ for $w = 1$ and AR(0). The Detection Parameters Are (1) PF, $s_0 = 0.0024$; (2) SDM, Window Size $m = 51$, Threshold=0.00012; (3) VRT, $m = 93$, Threshold=0.6; (4) $t\text{-}test$, $m = 26$, Threshold=0.004.

Signal		σ_y	WSDE				FAR			
			PF	SDM	VRT	t-test	PF	SDM	VRT	t-test
Linear	h=1,T_0=200	0.06	40.8	53.2	74.8	71.9	0	0	0	0
		0.10	51.6	51.7	65.4	69.5	0	0	0	0
		0.14	66.5	52.2	52.4	60.6	0	0.01	0	0.04
	h=1,T_0=300	0.06	40.1	47.8	65.2	70.6	0	0	0	0
		0.10	56.4	47.8	57.6	73.1	0.01	0.02	0.05	0.09
		0.14	65.8	90.0	138.4	130.8	0.01	0.37	0.86	0.63
	h=5,T_0=300	0.06	42.6	56.0	84.6	78.6	0	0	0	0
		0.10	51.9	58.0	80.6	73.1	0	0	0	0
		0.14	64.2	62.6	77.1	70.8	0	0	0	0
Quad.	h=1,T_0=200	0.06	10.4	25.4	34.1	43.0	0.25	0.01	0	0.06
		0.10	18.3	23.1	18.6	34.2	0.11	0.19	0.16	0.17
		0.14	27.7	32.2	16.4	28.6	0.06	0.33	0.62	0.44
	h=1,T_0=300	0.06	40.0	19.7	18.2	27.9	0.99	0.43	0.5	0.46
		0.10	31.9	34.9	44.6	45.1	0.97	0.77	0.95	0.87
		0.14	26.6	67.2	83.7	83.2	0.82	0.88	1	0.95
	h=5,T_0=300	0.06	22.4	33.6	51.0	52.5	0.05	0	0	0
		0.10	33.1	32.0	42.0	52.0	0.05	0	0	0
		0.14	39.9	38.9	33.1	42.4	0.01	0.04	0	0.03
Exp.	h=1,T_0=200	0.06	12.7	35.5	42.2	48.3	0.33	0.03	0	0.04
		0.10	20.4	35.0	26.1	38.8	0.15	0.24	0.34	0.34
		0.14	30.0	32.6	32.7	40.7	0.08	0.5	0.78	0.66
	h=1,T_0=300	0.06	72.0	34.0	27.9	41.9	1	0.35	0.52	0.40
		0.10	62.2	64.7	72.0	73.5	1	0.88	0.97	0.87
		0.14	49.2	101.2	118.8	109.3	0.99	1	0.99	0.97
	h=5,T_0=300	0.06	38.5	49.2	70.7	63.5	0	0	0	0
		0.10	49.8	51.1	59.5	63.1	0	0	0	0
		0.14	59.4	55.4	47.5	50.4	0.005	0	0	0.01
Osc.	h=1,T_0=200	0.06	24.4	79.3	69.5	71.6	0.01	0.79	0	0.78
		0.10	25.2	88.2	57.3	98.4	0.025	0.81	0	0.82
		0.14	24.6	77.8	48.6	101.4	0.08	0.83	0	0.9
	h=1,T_0=300	0.06	21.0	63.4	58.2	104.0	0.05	0.61	0	0.55
		0.10	24.6	90.3	47.1	78.6	0.32	0.65	0	0.72
		0.14	32.9	113.7	38.6	120.1	0.61	0.67	0	0.78
	h=5,T_0=300	0.06	40.4	46.8	83.3	142.0	0.005	0.2	0	0.52
		0.10	56.5	47.7	79.9	57.0	0	0.13	0	0.41
		0.14	66.2	53.0	77.2	55.6	0	0.19	0	0.53
Overall			43.4	58.5	63.8	71.6	0.21	0.30	0.22	0.35

Note that in order to minimize the overall WSDE, the selection of the slope threshold of the PF method may not guarantee that the detection results of all signals are better than other methods. However, the maximum WSDE among all signals for PF method is far lower than other three methods. From the table we can also see that decreasing the signal changing rate (e.g., changing T_0 from 200 to 300 for linear signals) or increasing the signal noise before the steady state would result in higher FAR. It is intuitive since more bias (deviation from steady state) will be immersed by the noise and thus more difficult to detect when decreasing the changing or increasing the signal noise. That is also why FAR is mostly contributed by quadratic and exponential signals.

The computational time of PF method on a signal of 500 observations is about 12 seconds using MATLAB running on a Q9550 2.83 GHz Intel processor, which is relatively longer than other three methods (less than 1 second). However, the increased execution time could bring considerable robustness in handling different signals. Besides, the selection of N_s and the Gibbs move constant C in the simulation is very conservative. Smaller values may be selected to reduce the computational time without hurting the detection accuracy.

3.4.4 Illustration of Application to CNP signals

We use the same detection parameters as used in Table 3-3 for all methods. Figure 3-8 shows the detection results of the proposed method for the CNP signal with ultrasonic power 70 W and 30 g Al_2O_3 particles. The popular *off-line* method MSER-5 [61, 104] is used as a benchmark to evaluate the proposed method. The MSER-5 detected steady state time is 175. The detection result for the proposed method is 231. In contrast, the detected results for SDM, VRT and *t*-test

are 238, 251 and 240, respectively. As we can see, the proposed method is more accurate than the other three methods.
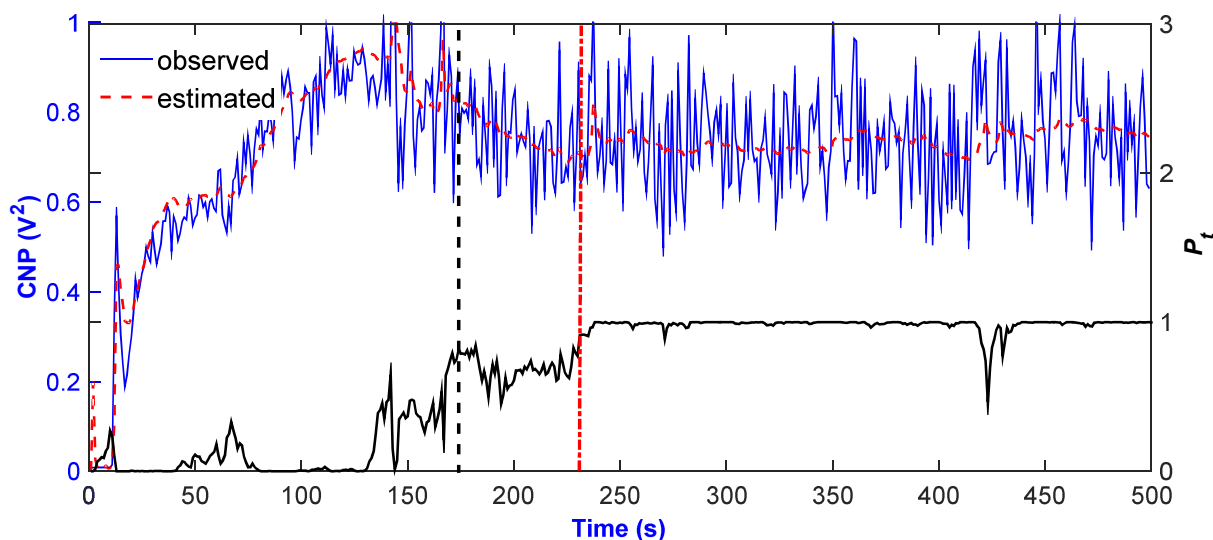
Figure 3-8: Steady state detection of CNP signals in the dispersion of 30 g Al_2O_3 for ultrasonic power 70 W. The vertical dash-dotted line (right) denotes the detected time using the proposed method and the vertical dashed line (left) denotes the *off-line* method MSER-5 detected time.

3.5 Discussion and Conclusion

In this chapter we have proposed a new *on-line* steady state detection algorithm using a multiple change-point model and particle filtering techniques. The multiple change-point model is represented by a non-standard state-space model and the particle filtering algorithm is developed to approximate the posterior of the LCP and other model parameters sequentially.

The mixture importance density is used and sampled using the stratified sampling method, which is proven to have a lower asymptotic variance, and thus more stable than the conventional composition method. The partial Gibbs move algorithm is developed to overcome the particle degeneracy and impoverishment problem and reduce the number of particles needed. To further

balance the computational cost, a "partial move" strategy is used where only part of particles is moved. A timeliness improvement strategy is proposed to reduce the detection delay for signals with long linear segments before the steady state.

Compared with the existing methods, the PF method has the following advantages. First, there is no moving data window in the PF method. For most of existing methods, a moving window is required and it is usually chosen somewhat arbitrarily in practice. Too small a moving window may result in unstable detection and high false alarm rate, while too large a moving window may delay the detection. The PF method functions like a slope detection method with an adaptive window size. Second, the PF method is based on the Bayesian framework and is able to "learn" signals in the monitoring process. It incorporates the information of signal noises to the detection algorithm. Therefore it is able to handle signals with different noise levels more robustly. Although the noninformative priors are used in the current work, in practice the prior knowledge may be available to further improve the detection accuracy. Third, we can sequentially obtain the filtered signal, which may be a useful by-product for many applications.

Admittedly, the higher accuracy of the proposed method is obtained at the price of higher computational burden. However, in the algorithm all the hyperparameters are easy to select and only the detection threshold needs to be tuned in the application. Although computationally intensive, the code of the proposed method is not very complex. With well documented release of this method, people can apply it to their own time series without much difficulty.

3.6 Appendix

3.6.1 Proof of Theorem 3.1 (2) and (3)

Theorem 3.1(2):

Let $\mu_{t,j} = E_{h_j}[\varphi(\boldsymbol{x}_t)\omega_t]$, $v_{t,j} = E_{h_j}(\omega_t)$ and Define $\boldsymbol{Z}_t = \left(U_{t,0}, V_{t,0}, U_{t,1}, V_{t,1}\right)^T$, $\boldsymbol{\mu}_{\boldsymbol{Z}_t} = \left(\mu_{t,0}, v_{t,0}, \mu_{t,1}, v_{t,1}\right)^T$. Let $\delta_t = g(\boldsymbol{Z}_t) = \frac{pU_{t,0}+(1-p)U_{t,1}}{pV_{t,0}+(1-p)V_{t,1}}$, then

$$g\left(\boldsymbol{\mu}_{\boldsymbol{Z}_t}\right) = \frac{pE_{h_0}[\varphi(\boldsymbol{x}_t)\omega_t] + (1-p)E_{h_1}[\varphi(\boldsymbol{x}_t)\omega_t]}{pE_{h_0}(\omega_t) + (1-p)E_{h_1}(\omega_t)} = \frac{E_h(\varphi(\boldsymbol{x}_t)\omega_t)}{E_h(\omega_t)} = E_{\pi_t}[\varphi(\boldsymbol{x}_t)]$$

The asymptotic bias can be computed using the δ-method with a second order Taylor series expansion.

$$g(\boldsymbol{Z}_t) \approx g\left(\boldsymbol{\mu}_{\boldsymbol{Z}_t}\right) + \left[\nabla g\left(\boldsymbol{\mu}_{\boldsymbol{Z}_t}\right)\right]^T\left(\boldsymbol{Z}_t - \boldsymbol{\mu}_{\boldsymbol{Z}_t}\right) + \frac{1}{2}\left(\boldsymbol{Z}_t - \boldsymbol{\mu}_{\boldsymbol{Z}_t}\right)^T \nabla^2 g\left(\boldsymbol{\mu}_{\boldsymbol{Z}_t}\right)\left(\boldsymbol{Z}_t - \boldsymbol{\mu}_{\boldsymbol{Z}_t}\right)$$

where

$$\nabla g\left(\boldsymbol{\mu}_{\boldsymbol{Z}_t}\right) =$$

$$\left(\frac{p}{E_h(\omega_t)}, \frac{-pE_h(\varphi(\boldsymbol{x}_t)\omega_t)}{E_h^2(\omega_t)}, \frac{1-p}{E_h(\omega_t)}, \frac{-(1-p)E_h(\varphi(\boldsymbol{x}_t)\omega_t)}{E_h^2(\omega_t)}\right)^T$$

Since $U_{t,0}, V_{t,0}$ are independent of $U_{t,1}, V_{t,1}$,

$$E\left(g(\boldsymbol{Z}_t) - g\left(\boldsymbol{\mu}_{\boldsymbol{Z}_t}\right)\right) \approx$$

$$\frac{p^2 E_h(\varphi(\boldsymbol{x}_t)\omega_t)}{n_0 E_h^3(\omega_t)} Var_{h_0}(\omega_t) + \frac{(1-p)^2 E_h(\varphi(\boldsymbol{x}_t)\omega_t)}{n_1 E_h^3(\omega_t)} Var_{h_1}(\omega_t)$$

$$-\frac{p^2}{n_0 E_h^2(\omega_t)} Cov_{h_0}(\varphi(\boldsymbol{x}_t)\omega_t, \omega_t) - \frac{(1-p)^2}{n_1 E_h^2(\omega_t)} Cov_{h_1}(\varphi(\boldsymbol{x}_t)\omega_t, \omega_t)$$

$$= \frac{1}{N_s} \left[\frac{p^2 E_h(\varphi(\boldsymbol{x}_t)\omega_t)}{q E_h^3(\omega_t)} Var_{h_0}(\omega_t) + \frac{(1-p)^2 E_h(\varphi(\boldsymbol{x}_t)\omega_t)}{(1-q)_s E_h^3(\omega_t)} Var_{h_1}(\omega_t) - \frac{p^2}{q E_h^2(\omega_t)} Cov_{h_0}(\varphi(\boldsymbol{x}_t)\omega_t, \omega_t) \right.$$
$$\left. - \frac{(1-p)^2}{(1-q) E_h^2(\omega_t)} Cov_{h_1}(\varphi(\boldsymbol{x}_t)\omega_t, \omega_t) \right]$$

$$= \frac{1}{N_s E_h^2(\omega_t)} \left[\frac{p^2}{q} Cov_{h_0}\left(\left[E_{\pi_t}(\varphi(\boldsymbol{x}_t)) - \varphi(\boldsymbol{x}_t) \right]\omega_t, \omega_t \right) \right.$$
$$\left. + \frac{(1-p)^2}{1-q} Cov_{h_1}\left(\left[E_{\pi_t}(\varphi(\boldsymbol{x}_t)) - \varphi(\boldsymbol{x}_t) \right]\omega_t, \omega_t \right) \right]$$

Therefore

$$\lim_{N_s \to \infty} N_s \left(\delta_t - E_{\pi_t}[\varphi(\boldsymbol{x}_t)] \right) = \frac{p^2}{q} B_0 + \frac{(1-p)^2}{1-q} B_1$$

where for $j = 0,1$

$$B_j = -\frac{1}{[p(y_t|y_{1:t-1})]^2} Cov_{h_j}\left(\left[\varphi(\boldsymbol{x}_t) - E_{\pi_t}(\varphi(\boldsymbol{x}_t)) \right]\omega_t, \omega_t \right)$$

Theorem 3.1(3):

$$\frac{dV_t}{dq} = 0 \implies q_{opt} = \frac{pV_{h_0}}{pV_{h_0} + (1-p)V_{h_1}}$$

When $q = p$, the asymptotic variance becomes

$$V_t(q) = pV_{h_0} + (1-p)V_{h_1}$$

$$= \frac{1}{[p(y_t|y_{1:t-1})]^2} \left\{ pVar_{h_0}\left[\left(\varphi(\boldsymbol{x}_t) - E_{\pi_t}(\varphi(\boldsymbol{x}_t)) \right)\omega_t \right] + (1-p)Var_{h_1}\left[\left(\varphi(\boldsymbol{x}_t) - E_{\pi_t}(\varphi(\boldsymbol{x}_t)) \right)\omega_t \right] \right\}$$

$$= \frac{1}{[p(y_t|y_{1:t-1})]^2} \left\{ pE_{h_0}\left[\left(\varphi(\boldsymbol{x}_t) - E_{\pi_t}(\varphi(\boldsymbol{x}_t))\right)\omega_t\right]^2 + (1-p)E_{h_0}\left[\left(\varphi(\boldsymbol{x}_t) - E_{\pi_t}(\varphi(\boldsymbol{x}_t))\right)\omega_t\right]^2 \right.$$

$$\left. - p\left(E_{h_0}\left[\left(\varphi(\boldsymbol{x}_t) - E_{\pi_t}(\varphi(\boldsymbol{x}_t))\right)\omega_t\right]\right)^2 - (1-p)\left(E_{h_1}\left[\left(\varphi(\boldsymbol{x}_t) - E_{\pi_t}(\varphi(\boldsymbol{x}_t))\right)\omega_t\right]\right)^2 \right\}$$

If we use the composition method and directly sample from $h = pf + (1-p)\pi_{t-1}$, then according to (2.9), the asymptotic is given by

$$V_t^* = \frac{1}{[p(y_t|y_{1:t-1})]^2} Var_h\left[\left(\varphi(\boldsymbol{x}_t) - E_{\pi_t}(\varphi(\boldsymbol{x}_t))\right)\omega_t\right]$$

$$= \frac{1}{[p(y_t|y_{1:t-1})]^2}\left\{ E_h\left[\left(\varphi(\boldsymbol{x}_t) - E_{\pi_t}(\varphi(\boldsymbol{x}_t))\right)\omega_t\right]^2 \right.$$

$$\left. - \left(E_h\left[\left(\varphi(\boldsymbol{x}_t) - E_{\pi_t}(\varphi(\boldsymbol{x}_t))\right)\omega_t\right]\right)^2 \right\}$$

Since $E_h\left[\left(\varphi(\boldsymbol{x}_t) - E_{\pi_t}(\varphi(\boldsymbol{x}_t))\right)\omega_t\right] = E_h[\varphi(\boldsymbol{x}_t)\omega_t] - E_{\pi_t}(\varphi(\boldsymbol{x}_t))E_h(\omega_t) = 0$, then we have

$$V_t^* = \frac{E_h\left[\left(\varphi(\boldsymbol{x}_t) - E_{\pi_t}(\varphi(\boldsymbol{x}_t))\right)\omega_t\right]^2}{[p(y_t|y_{1:t-1})]^2}$$

$$= \frac{1}{[p(y_t|y_{1:t-1})]^2}\left\{ pE_{h_0}\left[\left(\varphi(\boldsymbol{x}_t) - E_{\pi_t}(\varphi(\boldsymbol{x}_t))\right)\omega_t\right]^2 \right.$$

$$\left. + (1-p)E_{h_0}\left[\left(\varphi(\boldsymbol{x}_t) - E_{\pi_t}(\varphi(\boldsymbol{x}_t))\right)\omega_t\right]^2 \right\}$$

Therefore

$$V_t^* - V_t = \frac{1}{[p(y_t|y_{1:t-1})]^2}\left\{ p\left(E_{h_0}\left[\left(\varphi(\boldsymbol{x}_t) - E_{\pi_t}(\varphi(\boldsymbol{x}_t))\right)\omega_t\right]\right)^2 \right.$$

$$\left. + (1-p)\left(E_{h_1}\left[\left(\varphi(\boldsymbol{x}_t) - E_{\pi_t}(\varphi(\boldsymbol{x}_t))\right)\omega_t\right]\right)^2 \right\} \geq 0$$

3.6.2 Proof of Lemma 3.1

Denote $X_t = \begin{bmatrix} \tau_t & 1 \\ \tau_t+1 & 1 \\ \vdots & \vdots \\ t & 1 \end{bmatrix}$ and $Y_t = y_{\tau_t:t}$, then

$$P(\sigma_t^2|y_{1:t},\boldsymbol{\beta}_t,\tau_t) \propto P(\sigma_t^2)P(y_{\tau_t:t}|\sigma_t^2,\boldsymbol{x}_t) \propto (\sigma_t^2)^{-(\alpha_1+1)}e^{-\frac{\alpha_2}{\sigma_t^2}}(\sigma_t^2)^{-\frac{(t-\tau_t+1)}{2}}e^{-\frac{\|Y_t-X_t\boldsymbol{\beta}_t\|^2}{2\sigma_t^2}}$$

$$\propto (\sigma_t^2)^{-\left(\alpha_1+\frac{(t-\tau_t+1)}{2}-1\right)}\exp\left(-\frac{\alpha_2+\frac{\|Y_t-X_t\boldsymbol{\beta}_t\|^2}{2}}{\sigma_t^2}\right)$$

Therefore

$$(\sigma_t^2|y_{1:t},\boldsymbol{\beta}_t,\tau_t)\sim IG(\alpha_1+\frac{(t-\tau_t+1)}{2},\alpha_2+\frac{\|Y_t-X_t\boldsymbol{\beta}_t\|^2}{2})$$

$$P(\boldsymbol{\beta}_t|y_{1:t},\sigma_t^2,\tau_t) \propto P(\boldsymbol{\beta}_t)P(y_{\tau_t:t}|\sigma_t^2,\boldsymbol{\beta}_t,\tau_t)$$

$$\propto \exp\left[-\frac{(\boldsymbol{\beta}_t-\boldsymbol{\mu}_0)^T\boldsymbol{\Sigma}_0^{-1}(\boldsymbol{\beta}_t-\boldsymbol{\mu}_0)}{2}\right]\exp\left(-\frac{\|Y_t-X_t\boldsymbol{\beta}_t\|^2}{2\sigma_t^2}\right)$$

$$\propto \exp\left[-\frac{(\boldsymbol{\beta}_t-\boldsymbol{\mu}_0)^T\boldsymbol{\Sigma}_0^{-1}(\boldsymbol{\beta}_t-\boldsymbol{\mu}_0)}{2}\right]\exp\left(-\frac{(Y_t-X_t\boldsymbol{\beta}_t)^T(Y_t-X_t\boldsymbol{\beta}_t)}{2\sigma_t^2}\right)$$

$$\propto \exp\left\{-\frac{1}{2}\left[\boldsymbol{\beta}_t^T\left(\boldsymbol{\Sigma}_0^{-1}+\frac{X_t^TX_t}{\sigma_t^2}\right)\boldsymbol{\beta}_t-2\left(\boldsymbol{\mu}_0^T\boldsymbol{\Sigma}_0^{-1}+\frac{Y_t^TX_t}{\sigma_t^2}\right)\boldsymbol{\beta}_t\right]\right\}$$

$$\propto \exp[-\frac{1}{2}(\boldsymbol{\beta}_t-\boldsymbol{\mu}_t)^T\boldsymbol{\Sigma}_t^{-1}(\boldsymbol{\beta}_t-\boldsymbol{\mu}_t)]$$

where

$$\boldsymbol{\mu}_t = \left[\frac{X_t^TX_t}{\sigma_t^2}+\boldsymbol{\Sigma}_0^{-1}\right]^{-1}\left[\frac{X_t^TY_t}{\sigma_t^2}+\boldsymbol{\Sigma}_0^{-1}\boldsymbol{\mu}_0\right]$$

and

$$\boldsymbol{\Sigma}_t = \left[\frac{\boldsymbol{X}_t^T \boldsymbol{X}_t}{\sigma_t^2} + \boldsymbol{\Sigma}_0^{-1}\right]^{-1}$$

Therefore

$$(\boldsymbol{\beta}_t | y_{1:t}, \sigma_t^2, \tau_t) \sim N(\boldsymbol{\mu}_t, \boldsymbol{\Sigma}_t)$$

4   On-line Steady State Detection Using Multiple Change-point Models and Exact Bayesian Inference[*]

In Chapter 3 a robust steady state detection algorithm is developed using multiple change-point models and particle filters. Compared with other existing methods, this method is much more robust in handling different kinds of signals with only one set of detection parameters. However, the robustness and accuracy is at a price of relatively high computational burden. In this chapter, we develop a new on-line steady state detection algorithm with less computational cost by using exact Bayesian inference method. In this algorithm, conjugate priors are used and the explicit analytical form of the posterior distribution is obtainable, which is more efficient than using particle filtering techniques to approximate the posterior distribution. In this method, the piecewise linear model is used to approximate the noisy signals sequentially and the exact Bayesian inference used to calculate the posterior distribution of the latest change-point and model parameters sequentially. The exact Bayesian inference is implemented with a recursive message-passing algorithm [105, 106] to calculate the posterior distribution of latest change-point. The steady state can be detected when the probability of the slope amplitude of the latest linear segment is below a certain threshold.

---

[*] This chapter is based on the paper: **Jianguo Wu**, Yong Chen, Shiyu Zhou, "On-line Steady State Detection using Multiple Change-point Models and Exact Bayesian Inference", *submitted to IIE Transactions*

4.1 Exact Calculation of Posterior Distribution of the Latest Change-point

Since the steady state detection is mainly based on the observations in the latest linear segment, it is critical to calculate the posterior distribution of the latest change-point. In this section, the recursive algorithm [105, 106] to obtain the posterior will be introduced. To facilitate the on-line inference, we first formulate the multiple change-point model into a non-standard state-space model

Denote y_t as the observation at time step t. The corresponding model parameter is defined as $\xi_t = (a_t, b_t, \sigma_t^2)$ where a_t is the slope of the line segment, b_t is the intercept, and σ_t^2 is the variance of the signal noise. The multiple change-point models can be expressed as

$$\xi_t = \begin{cases} \boldsymbol{\theta}_1 & if\ 1 \leq t < C_1 \\ \boldsymbol{\theta}_2 & if\ C_1 \leq t < C_2 \\ \vdots & \vdots \\ \boldsymbol{\theta}_m & if\ C_{m-1} \leq t < C_m \\ \boldsymbol{\theta}_{m+1} & if\ C_m \leq t \leq n \end{cases} \tag{4.1}$$

where $\boldsymbol{\theta}_i \in \mathcal{R}^3$, n is the number of observations, m and $C_i, i = 1,2,\dots,m$ are the number and locations of the change-points. The parameters are assumed to be independent across different segments. The observation y_t is modeled as $y_t = a_t t + b_t + \varepsilon_t$ where ε_t is the *i.i.d.* Gaussian noise and $\varepsilon_t \sim N(0, \sigma_t^2)$.

Denote the state vector $\boldsymbol{x}_t = (\xi_t, \tau_t)$, where τ_t is the latest change-point at time t. Suppose the prior probability mass function and cumulative distribution function for the length of the

linear segments is $g(\cdot)$ and $G(\cdot)$, respectively. Then the prior transition probability can be expressed as

$$p(\tau_t = j | \tau_{t-1} = i) = \begin{cases} \dfrac{1 - G(t-i)}{1 - G(t-i-1)}, if \ j = i \\ 1 - \dfrac{1 - G(t-i)}{1 - G(t-i-1)}, if \ j = t \\ \qquad 0, \qquad otherwise \end{cases} \tag{4.2}$$

where $i \leq t - 1$. At each time step, the state transition process can be formulated as

$$x_t = \begin{cases} (\xi_{t-1}, \tau_{t-1}) \text{ with probability } p(\tau_t = \tau_{t-1} | \tau_{t-1}) \\ (\xi', t), \text{ with probability } p(\tau_t = t | \tau_{t-1}) \end{cases} \tag{4.3}$$

where ξ' is different from ξ_{t-1}. Let $y_{s:t} = (y_s, y_{s+1}, \dots, y_t)^T$. For $j = 1, 2, \cdots, t + 1$, the posterior for the latest change-point at time step $t + 1$ can be calculated recursively as

$$P(\tau_{t+1} = j | y_{1:t+1}) \propto P(\tau_{t+1} = j, y_{t+1} | y_{1:t}) = P(y_{t+1} | \tau_{t+1} = j, y_{1:t}) P(\tau_{t+1} = j | y_{1:t}) \tag{4.4}$$

$$P(\tau_{t+1} = j | y_{1:t}) = \sum_{i=1}^{\min(j,t)} P(\tau_{t+1} = j | \tau_t = i) P(\tau_t = i | y_{1:t}) \tag{4.5}$$

$$P(y_{t+1} | \tau_{t+1} = j, y_{1:t}) = \begin{cases} \dfrac{P(y_{j:t+1} | \tau_{t+1} = j)}{P(y_{j:t} | \tau_{t+1} = j)} & if \ j \leq t \\ \qquad\qquad P(y_{t+1}) & if \ j = t + 1 \end{cases} \tag{4.6}$$

Define $P(s, t) = P(y_{s:t} | y_{s:t}$ is in the same linear segment), and substitute Eq. (4.5) and (4.6) into Eq. (4.4) we can get

$$P(\tau_{t+1} = j | y_{1:t+1}) \propto \begin{cases} \dfrac{P(j, t+1)}{P(j, t)} P(\tau_{t+1} = j | \tau_t = j) P(\tau_t = j | y_{1:t}) \ if \ j \leq t \\ P(t+1, t+1) \displaystyle\sum_{i=1}^{t} P(\tau_{t+1} = j | \tau_t = i) P(\tau_t = i | y_{1:t}) \ if \ j = t + 1 \end{cases} \tag{4.7}$$

From Eq. (4.7) we can see that the distribution of the latest change-point at time $t + 1$ can be recursively calculated based on the previously calculated distribution at time t. The terms $\frac{P(j,t+1)}{P(j,t)}$ and $P(t + 1, t + 1)$ are the only terms that incorporates the information of the newest observation y_{t+1} into the updating of the posterior distribution of the latest change-point. Therefore, they play the decisive role on the detection of change-point. For example, if the latest true change-point is at time step $t + 1$ with y_{t+1} significantly different from $y_{1:t}$, then $\frac{P(j,t+1)}{P(j,t)}$ is expected to be much smaller than $P(t + 1, t + 1)$ and thus more weight is put on time step $t + 1$ as the latest change-point.

The calculation of $P(s, t)$ is the key part in the above recursion equation. By using conjugate priors for model parameters, it can be calculated analytically and involves no complex numerical integrations. Let $\boldsymbol{\beta}$ be the parameter of the linear segment, $\boldsymbol{\beta} = (a, b)^T$. The joint prior distribution for $\boldsymbol{\beta}$ and noise variance σ^2 can be assigned using Gaussian and inverse Gamma distribution as

$$\sigma^2 \sim IG\left(\frac{v}{2}, \frac{\gamma}{2}\right)$$

$$\boldsymbol{\beta}|\sigma^2 \sim N(\boldsymbol{\beta}_0, \sigma^2 \boldsymbol{\Sigma}) \tag{4.8}$$

where v, γ, $\boldsymbol{\beta}_0$ and $\boldsymbol{\Sigma}$ are known parameters. Define $\boldsymbol{X}_{st} = \begin{bmatrix} s & 1 \\ s+1 & 1 \\ \vdots & \vdots \\ t & 1 \end{bmatrix}$. The term $P(s, t)$ in Eq.

(4.7) then can be calculated by integrating out β and σ^2:

$$P(s, t) = \pi^{-(t-s+1)/2} \left(\frac{|\boldsymbol{M}_{st}|}{|\boldsymbol{\Sigma}|}\right)^{\frac{1}{2}} \frac{\gamma^{\frac{v}{2}}}{(H_{st})^{(t-s+1+v)/2}} \frac{\Gamma(\frac{t-s+1+v}{2})}{\Gamma(v/2)} \tag{4.9}$$

where

$$M_{st} = (X_{st}^T X_{st} + \Sigma^{-1})^{-1}$$

$$N_{st} = (\Sigma^{-1}\boldsymbol{\beta}_0 + X_{st}^T y_{s:t})$$

$$H_{st} = y_{s:t}^T y_{s:t} + \gamma + \boldsymbol{\beta}_0^T \Sigma^{-1} \boldsymbol{\beta}_0 - N_{st}^T M_{st} N_{st} \tag{4.10}$$

The deviation of Eq. (4.9) is shown in the Appendix of this chapter.

4.2 Steady State Detection

In the steady state detection, we conduct the Bayesian inference on the slope of the latest linear segment. When the amplitude of the slope $|a_t|$ is sufficiently small, the signal can be claimed to be steady. Naturally we can use the estimated slope amplitude of the latest linear segment $|\hat{a}_t|$ as the detection index. In this research we use a more flexible and stable detection index P_t, which is defined as the probability of $|a_t|$ being less than a threshold s_0 given observations $y_{1:t}$:

$$P_t = \Pr(|a_t| < s_0|y_{1:t}) = \sum_{i=1}^{t} P(|a_t| < s_0|\tau_t = i, y_{i:t}) P(\tau_t = i|y_{1:t}) \tag{4.11}$$

In the above equation, the probability of the latest change-point $P(\tau_t = i|y_{1:t})$ can be calculated by Eq. (4.7) and $P(|a_t| < s_0|\tau_t = i, y_{i:t})$ can be calculated based on Lemma 4.1 as follows (see Appendix for proof).

Lemma 4.1. *Suppose* $\sigma^2 \sim IG(\frac{v}{2}, \frac{\gamma}{2})$ *and* $\boldsymbol{\beta}|\sigma^2 \sim N(\boldsymbol{\beta}_0, \sigma^2\Sigma)$. *Define* $X_{st} = \begin{bmatrix} s & 1 \\ s+1 & 1 \\ \vdots & \vdots \\ t & 1 \end{bmatrix}$, *then*

*(1) $(\boldsymbol{\beta}_t|\tau_t = s, y_{s:t})$ follows bivariate t distribution with degrees of freedom $d_{st} = t - s +$
$1 + v$,   mean $\boldsymbol{\mu}_{st} = \boldsymbol{M}_{st}\boldsymbol{N}_{st}$ and covariance matrix $\frac{d_{st}}{d_{st}-2}\boldsymbol{\Sigma}_{st}$ ($d_{st} > 2$) where $\boldsymbol{\Sigma}_{st} = \frac{\boldsymbol{H}_{st}\boldsymbol{M}_{st}}{d_{st}}$,
$\boldsymbol{M}_{st}, \boldsymbol{N}_{st}$ and H_{st} are defined in Eq. (4.10). Denote it as $(\boldsymbol{\beta}_t|\tau_t = s, y_{s:t}) \sim t_2(d_{st}, \boldsymbol{\mu}_{st}, \boldsymbol{\Sigma}_{st})$.*

*(2)   Suppose $\boldsymbol{\Sigma}_{st} = \boldsymbol{K}_{st}\boldsymbol{R}_{st}\boldsymbol{K}_{st}^T$ where $\boldsymbol{R}_{st}$ is the correlation matrix and $\boldsymbol{K}_{st}$ is a diagonal
matrix with positive diagonal entries $k_{st}^{(i,i)}$, then*

$$(\boldsymbol{K}_{st}^{-1}\boldsymbol{\beta}_t|\tau_t = s, y_{s:t}) \sim t_2(d_{st}, \boldsymbol{K}_{st}^{-1}\boldsymbol{\mu}_{st}, \boldsymbol{R}_{st})$$

and

$$(\frac{a_t}{k_{st}^{(1,1)}}|\tau_t = s, y_{s:t}) \sim t_1\left(d_{st}, (\boldsymbol{K}_{st}^{-1}\boldsymbol{\mu}_{st})^{(1)}, 1\right)$$

or $(\frac{a_t - \mu_{st}^{(1)}}{k_{st}^{(1,1)}}|\tau_t = s, y_{s:t})$ follows standard t distribution with degrees of freedom d_{st}. Here
$(\boldsymbol{K}_{st}^{-1}\boldsymbol{\mu}_{st})^{(1)}$ and $\boldsymbol{\mu}_{st}^{(1)}$ denote the first element of the vector $\boldsymbol{K}_{st}^{-1}\boldsymbol{\mu}_{st}$ and $\boldsymbol{\mu}_{st}$ respectively.

Based on Lemma 1, the detection index P_t can be calculated as

$$P_t = \sum_{i=1}^{t}\left[\Psi_{d_{it}}\left(\frac{s_0 - \mu_{it}^{(1)}}{k_{it}^{(1,1)}}\right) - \Psi_{d_{it}}\left(\frac{-s_0 - \mu_{it}^{(1)}}{k_{it}^{(1,1)}}\right)\right]P(\tau_t = i|y_{1:t}) \tag{4.12}$$

where $\Psi_{d_{it}}(\cdot)$ is the cumulative distribution function (CDF) of standard t distribution with
degrees of freedom d_{it}. The filtered observation $\hat{y}_t$ at time t can be calculated as

$$\hat{y} = \sum_{i=1}^{t}\left(\mu_{it}^{(1)}t + \mu_{it}^{(2)}\right)P(\tau_t = i|y_{1:t}) \tag{4.13}$$

In the development of decision rule, we need to specify or tune the thresholds for both the
slope amplitude and the probability detection index. However, in the application, the probability
index often increases rapidly to 0.9 at certain time after the signals enter into steady state.

Therefore, to simplify the algorithm, we just set the threshold for the probability index to be 0.9 in the application and treat the slope amplitude threshold as a tuning parameter. This will also be illustrated in the numerical illustration section.

In Bayesian inference, informative priors are often preferable if prior knowledge or historical data are available. However, when we know very little about the data and we just want the data to "speak" for themselves, the non-informative priors then would be a better choice. In the steady state detection, we often face nonlinear signals which may need multiple linear segments with both increasing and decreasing trends for approximation. Besides, the amplitude of slopes and line durations may also vary significantly among different segments. In such cases a non-informative prior for $\boldsymbol{\beta}$ is recommended. We can assign flat priors for $\boldsymbol{\beta}$ with zero mean ($\boldsymbol{\beta}_0 = \mathbf{0}$) and large variance, i.e., large value for the diagonal entries of $\boldsymbol{\Sigma}$ and to describe the uncertainty of the slope and intercept. For the signal noise, typically we can select an informative prior. The noise amplitude for each signal in most cases is fixed and we can roughly estimate it based on the historical data or prior knowledge. For simplicity, we still set the prior transition probability $p(\tau_t|\tau_{t-1})$ as a constant value p in this method.

The steady state detection process can be summarized in Algorithm 4.1. After the posterior of the latest change-points $P(\tau_t|y_{1:t})$ are calculated for all time steps $t = 1, 2, \dots, n$, we can easily reconstruct the trajectories of all change-points backwards for the purpose of illustration using Algorithm 4.2.

Algorithm 4.1 Steady state Detection Algorithm Using Exact Calculation

1. Specify $v, \gamma, \beta_0, \Sigma, p$ and s_0

2. Set $P_1 = 0$ and $P(\tau_1 = 1|y_1) = 1$

3. For $t = 2, 3, \cdots, n$

   - For $i = 1, 2, \cdots, t$

     Calculate the un-normalized $P(\tau_t = i|y_{1:t})$ based on Eq. (4.7)

     End

   - Calculate the normalized $P(\tau_t|y_{1:t})$: $P(\tau_t = i|y_{1:t}) = \frac{P(\tau_t=i|y_{1:t})}{\sum_{j=1}^{t} P(\tau_t=j|y_{1:t})}$

   - Calculate the probability index P_t based on Eq. (4.12)

   - If $P_t > 0.9$, the signal is steady and stop

   End

Algorithm 4.2 Simulation of Change-point Trajectories in N Realizations

1. Count[i]=0 for $i = 1, 2, \ldots, n$

2. For $rep = 1:N$

   - Simulate t_1 from $P(\tau_n|y_{1:n})$. Set Count[t_1]=Count[t_1]+1 and $k = 1$

   - While $t_k > 1$

     Simulate t_{k+1} from the support $\{1, 2 \ldots, t_k - 1\}$ with the discrete probability proportional to $P(\tau_{t_k-1}|y_{1:t_k-1})p(\tau_{t_k} = t_k|\tau_{t_k-1})$.

     Set $k = k + 1$ and Count[t_k]=Count[t_k]+1

     End

   End

3. Calculate the frequency $f_i = $ Count[i]$/N$ for $i = 1, 2, \ldots, n$

4.3 Computational Issues and Approximation

Algorithm 4.1 uses the exact calculation for the posterior distribution and is expected to be very accurate. However, there may be various computational issues that may limit its applications. The first and most important issue is that the computational cost and memory cost in the recursive calculation of $P(\tau_t|y_{1:t})$ increase significantly with time t. For example, at time t, we have to calculate t discrete probabilities. The calculation of each probability $P(\tau_t = t|y_{1:t})$ also increases rapidly with j in the recursion. A natural way to reduce the computational cost is to approximate the calculated $P(\tau_t|y_{1:t})$ using another probability mass function with fixed size of support $m < t$. In practice when t is large, $P(\tau_t|y_{1:t})$ almost equals to zero in many locations. Setting $P(\tau_t|y_{1:t})$ to be zero at these locations can reduce the computational cost in the calculation of $P(\tau_{t+1}|y_{1:t+1})$ and P_t.

In this work, we use this strategy: at each time step t ($t > m$), we only calculate the probability $P(\tau_t|y_{1:t})$ at m certain locations that are very likely to be the latest change-points. The specific steps are: (1) select $m - 1$ locations from $\{1, 2, \cdots t - 1\}$ using weighted sampling without replacement [107]. The weight for location i is $P(\tau_{t-1} = i|y_{1:t-1})$; (2), normalizing the weights of the selected locations; (3) calculate $P(\tau_t|y_{1:t})$ at t and these $m - 1$ selected locations; (4) Set $P(\tau_t|y_{1:t}) = 0$ at other locations. In other words, this method is to select location $\tau_t = t$ and other $m - 1$ locations from the support of $P(\tau_{t-1}|y_{1:t-1})$ of size m to be the support for $P(\tau_t|y_{1:t})$. In this strategy, the computation is almost balanced at large time step t.

Another computational issue is the calculation of $\frac{P(j,t+1)}{P(j,t)}$, which can be expressed as

$$\frac{P(j,t+1)}{P(j,t)} = \frac{1}{\sqrt{\pi}} \left(\frac{|M_{j,t+1}|}{|M_{j,t}|}\right)^{\frac{1}{2}} \left(\frac{H_{jt}}{H_{j,t+1}}\right)^{\frac{t-j+v-1}{2}} \frac{1}{\sqrt{H_{j,t+1}}} \frac{\Gamma\left(\frac{t-j+v+2}{2}\right)}{\Gamma\left(\frac{t-j+v+1}{2}\right)} \tag{4.14}$$

In the above equation, the calculation of $\Gamma\left(\frac{t-j+v+1}{2}\right)$ may be a problem as $t-j$ increases to a very large value. For example, in MATLAB, $\Gamma(172)$ becomes infinite because of the precision issue. One way to solve this issue is to compute the difference of the natural logarithm of the gamma function $\Gamma\left(\frac{t-j+v+2}{2}\right)$ and $\Gamma\left(\frac{t-j+v+1}{2}\right)$ instead and then calculate the exponential function of this difference. Another method that is more preferable in terms of the computational cost is to use Stirling's series to approximate the ratio of the Gamma function [108]:

$$\frac{\Gamma(z+z_1)}{\Gamma(z+z_2)} = z^{z_1-z_2}\left[1 + \frac{(z_1-z_2)(z_1+z_2-1)}{2z} + O(|z|^{-2})\right]$$

The Gamma ratio in Eq. (4.14) can thus be approximated as

$$\frac{\Gamma\left(\frac{t-j+v+2}{2}\right)}{\Gamma\left(\frac{t-j+v+1}{2}\right)} \approx \sqrt{\frac{t-j+v+1}{2}}\left[1 - \frac{1}{4(t-j+v+1)}\right] \tag{4.15}$$

This approximation has high accuracy and can be calculated very fast.

The calculation of P_t in Eq. (4.12) involves many cumulative distribution functions $\Psi_d(\cdot)$ of t distribution, which can also be approximated to reduce the computational cost. The first method is to use normal approximation. It is well-known that the Student's t distribution can be well approximated by a normal distribution with the same mean and variance when $d \geq 30$ [109]. Therefore, for $d \geq 30$, $\Psi_d(x) \approx \Phi(x/\sqrt{d/(d-2)})$ where $\Phi(\cdot)$ is the cumulative distribution function of standard normal distribution. An alternative method is to use the

estimated $\widehat{\sigma_t^2}$ to calculate the posterior distribution $(\boldsymbol{\beta}_t | \tau_t = s, y_{s:t})$ based on Lemma 4.2 as follows.

Lemma 4.2 *All the definitions and notations are the same as in Lemma 1. Then*

$$(1) \ (\sigma_t^2 | \tau_t = s, y_{s:t}) \sim IG\left(\frac{d_{st}}{2}, \frac{H_{st}}{2}\right)$$

$$(2) \ (\boldsymbol{\beta}_t | \tau_t = s, \sigma_t^2, y_{s:t}) \sim N(\boldsymbol{\mu}_{st}, \sigma_t^2 \boldsymbol{M}_{st})$$

The mean value of σ_t^2 given $\tau_t = s$ and $y_{s:t}$ is $\widehat{\sigma_t^2} = \frac{H_{st}}{d_{st}-2}$. We can use $\left(\boldsymbol{\beta}_t | \tau_t = s, \sigma_t^2 = \widehat{\sigma_t^2}, y_{s:t}\right)$ to approximate $(\boldsymbol{\beta}_t | \tau_t = s, y_{s:t})$. Based on Lemma 2, $\left(\boldsymbol{\beta}_t | \tau_t = s, \sigma_t^2 = \widehat{\sigma_t^2}, y_{s:t}\right)$ follows the normal distribution as

$$\left(\boldsymbol{\beta}_t | \tau_t = s, \sigma_t^2 = \widehat{\sigma_t^2}, y_{s:t}\right) \sim N(\boldsymbol{\mu}_{st}, \frac{H_{st} \boldsymbol{M}_{st}}{d_{st} - 2}) \tag{4.16}$$

Interestingly, this approximation is exactly equivalent to the first method, i.e., using $\Phi(x/\sqrt{d/(d-2)})$ to approximate $\Psi_d(x)$ in the calculation of P_t in Eq. (4.12).

4.4 Approximation of the Average Run Length (ARL) for Steady State Time Series

The average run length (ARL) is an important performance criterion used to evaluate a detection scheme, and it is commonly used in the statistical process control charts. Similarly, ARL on the stead-state time series can also provide insight and guidance on understanding and tuning the algorithm in application. In this section, we developed an approximation of ARL for a steady state time series as follows.

Suppose the detection probability index is approximated using the normal CDF described in Section 4.3.3 as

$$P_t \approx \sum_{i=1}^{t} \left[\Phi\left(\frac{s_0 - \mu_{it}^{(1)}}{k_{it}^{(1,1)}\sqrt{d_{it}/(d_{it}-2)}} \right) - \Phi\left(\frac{-s_0 - \mu_{it}^{(1)}}{k_{it}^{(1,1)}\sqrt{d_{it}/(d_{it}-2)}} \right) \right] P(\tau_t = i|y_{1:t})$$

Suppose $y_1, y_2, \ldots y_n$ is a steady state time series and $y_i \sim iid\ N(0, \sigma^2)$. In the detection process, it is observed that the posterior $P(\tau_t|y_{1:t})$ is almost focused on $t = 1$ or $P(\tau_t = 1|y_{1:t}) \approx 1$ for linear signals (see Figure 4-2 for details). Therefore

$$P_t \approx \left[\Phi\left(\frac{s_0 - \mu_{1t}^{(1)}}{k_{1t}^{(1,1)}\sqrt{d_{1t}/(d_{1t}-2)}} \right) - \Phi\left(\frac{-s_0 - \mu_{1t}^{(1)}}{k_{1t}^{(1,1)}\sqrt{d_{1t}/(d_{1t}-2)}} \right) \right]$$

When $\Sigma^{(i,i)} \to \infty$ and $\boldsymbol{\beta}_0 = \mathbf{0}$ (flat prior for $\boldsymbol{\beta}$), $\boldsymbol{\mu}_{1t} \approx (\boldsymbol{X}_{1t}^T \boldsymbol{X}_{1t})^{-1} \boldsymbol{X}_{1t} y_{1:t}$, which is the ordinary least square estimator for $\boldsymbol{\beta}_t$ and therefore $\boldsymbol{\mu}_{1t} \approx \mathbf{0}$. $\Sigma_{1t} \approx [y_{1:t}^T(\boldsymbol{I} - \boldsymbol{P})y_{1:t} + \gamma](\boldsymbol{X}_{1t}^T \boldsymbol{X}_{1t})^{-1}/d_{1t}$ where $\boldsymbol{P}$ is the projection matrix $\boldsymbol{P} = \boldsymbol{X}_{1t}(\boldsymbol{X}_{1t}^T \boldsymbol{X}_{1t})^{-1}\boldsymbol{X}_{1t}^T$. Therefore

$$k_{1t}^{(1,1)} \approx \sqrt{[y_{1:t}^T(\boldsymbol{I} - \boldsymbol{P})y_{1:t} + \gamma]\frac{12}{t(t^2 - 1)d_{1t}}}$$

and

$$P_t \approx 2\Phi\left(s_0 \sqrt{\frac{t(t^2 - 1)(t - 2 + v)}{12[y_{1:t}^T(\boldsymbol{I} - \boldsymbol{P})y_{1:t} + \gamma]}} \right) - 1$$

Suppose the detection will be stopped when $P_t \geq \alpha$, that is

$$\frac{y_{1:t}^T(\mathbf{I} - \mathbf{P})y_{1:t}}{\sigma^2} \leq \frac{s_0^2 t(t - 2 + v)(t^2 - 1)}{12 z_{(1+\alpha)/2}^2 \sigma^2} - \frac{\gamma}{\sigma^2} \tag{4.17}$$

where $z_{(1+\alpha)/2}$ is the quantile for standard normal distribution with $\Phi\left(z_{(1+\alpha)/2}\right) = (1 + \alpha)/2$.

Denote $Y_t = \frac{y_{1:t}^T(\mathbf{I}-\mathbf{P})y_{1:t}}{\sigma^2}$ and $h(t) = \frac{s_0^2 t(t-2+v)(t^2-1)}{12 z_{(1+\alpha)/2}^2 \sigma^2} - \frac{\gamma}{\sigma^2}$. It is well known that $Y_t \sim \chi_{t-2}^2$. Based

on Eq. (4.17) it is almost impossible to get the exact analytical form for ARL since it involves

multiple integrals and conditional distributions. For example, ARL can be expressed as

$$ARL = \sum_{t=1}^{\infty} t \Pr(Y_t \leq h(t)|Y_i > h(i) \text{ for } i < t)$$

where the conditional probability $\Pr(Y_t \leq h(t)|Y_i > h(i) \text{ for } i < t)$ is hard to derive. Here we use

an approximation method as follows.
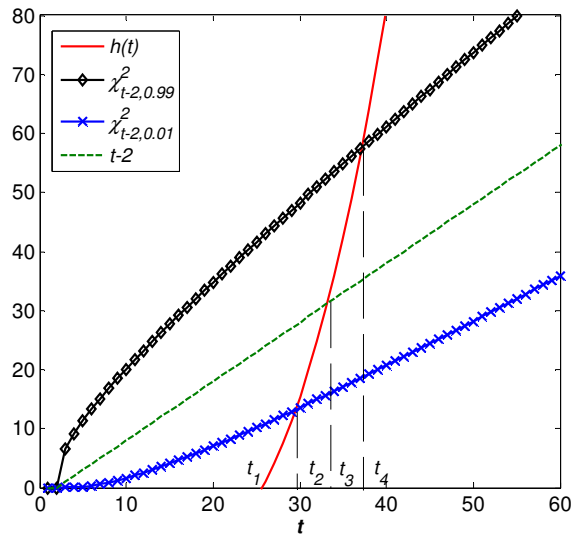
Figure 4-1: Illustration of the change of $h(t)$, $\chi_{t-2,0.99}^2$, $\chi_{t-2,0.01}^2$ and $E(\chi_{t-2}^2)$ with t

Suppose we select $s_0 = 0.003$, $\sigma = 0.1$, $v = 20$, $\gamma = 0.2$ and $\alpha = 0.9$. Figure 4-1 shows the

function $h(t)$, the 0.99 and 0.01 quantiles of χ_{t-2}^2 distribution and the mean of χ_{t-2}^2. From it we

can see that $h(t) \leq 0$ for $t \leq t_1$ and then increases much more rapidly (polynomial of 4th order)

than other three curves. For $t \leq t_1$, Y_t is always larger than $h(t)$ and the detection will not stop.

At $t = t_2$, $P(Y_t \leq h(t)) = 0.01$ and $P(Y_t \leq h(t)) \ll 0.01$ in the interval $[t_1, t_2)$ because of the

rapid decreasing of the probability density function of the χ_{t-2}^2. Similarly, at $t = t_4$, $P(Y_t \leq$

$h(t)) = 0.99$ and in the interval (t_4, ∞), $P(Y_t \leq h(t)) \gg 0.99$. Therefore, it is highly possible

that the stopping time will be in the time interval $[t_2, t_4]$. Since the width of the interval is small,

we use t_4 as the ARL:

$$ARL \approx \arg \min_t \{t | \chi_{t-2,0.99}^2 \leq h(t)\} \qquad (4.18)$$

We found that this approximation is very close to the simulated ARL under different values of s_0,

σ, v, γ and α, which will be shown in Section 4.5.3.
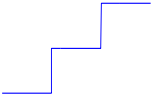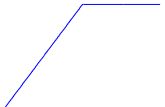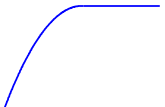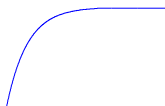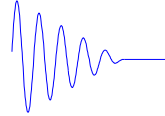
4.5 Case Studies for Illustration and Comparison

4.5.1 Illustration

Simulated signals are used to illustrate the detecting process of this steady state algorithm

and compare it with other existing algorithms. They are generated using bias functions and

noises, where the bias functions consist of initial transient state and steady state. Total five bias

functions are used: step function, linear function, quadratic function, exponential function and

oscillating function, as shown in Table 4-1. Note the step function is not strictly bias function

since it is composed of piecewise steady state period. The last four bias functions are often used

to test off-line heuristic truncation algorithms used in the discrete-event simulations [53, 61, 70, 76]. For simplicity, only the negative bias scenarios (i.e., increasing before steady state) are considered for the linear, quadratic and exponential functions.

Table 4-1: Five bias functions and their shapes

Signal	Function	Shape
Step	$y(t) = \begin{cases} h_1 & ,t = 1, \dots, T_1 \\ h_2 & ,t = T_1 + 1, \dots, T_2 \\ h_3 & ,t = T_2, \dots, n \end{cases}$	
Linear	$y(t) = \begin{cases} \dfrac{t}{T_0} h & ,t = 1, \dots, T_0 \\ h & ,t = T_0 + 1, \dots, n \end{cases}$	
Quadratic	$y(t) = \begin{cases} h\left[1 - \dfrac{(t - T_0)^2}{(T_0 - 1)^2}\right] & ,t = 1, \dots, T_0 \\ h & ,t = T_0 + 1, \dots, n \end{cases}$	
Exponential	$y(t) = \begin{cases} h\left[1 - 10^{\frac{1-t}{T_0-1}}\right] & ,t = 1, \dots, T_0 \\ y(T_0) & ,t = T_0 + 1, \dots, n \end{cases}$	
Oscillating	$y(t) = \begin{cases} h\dfrac{T_0 - t}{T_0 - 1} sin\left(\dfrac{\pi t}{f}\right) & ,t = 1, \dots, T_0 \\ 0 & ,t = T_0 + 1, \dots, n \end{cases}$	

The step function and oscillating functions are used to illustrate the detection process for signals with fixed noise amplitude. For the step function, $h_1 = 0$, $h_2 = 0.5$, $h_3 = 1$ $T_1 = 200$ and $T_2 = 400$. For the oscillating function, $h = 1$, $T_0 = 400$ and $f = 30$ (total 10 peaks and troughs). For both signals, number of observations $n = 600$ and noise $\sigma_y = 0.14$. The priors for

the steady state detection algorithm are set to be: $\boldsymbol{\beta}_0 = \mathbf{0}$, $\boldsymbol{\Sigma} = 1 \times 10^4 \boldsymbol{I}$, $v = 20$, $\gamma = 0.2$ and $p = 0.2$, where I is the 2×2 identity matrix. The detection results are not very sensitive to the value of the prior transition probability p in most cases. The interval $[0.01, 0.5]$ is suggested for p in applications. The moving window is not used here. The size of the support m for the posterior $P(\tau_t | y_{1:t})$ is set to be 50 and the slope threshold s_0 is set to be 0.003.
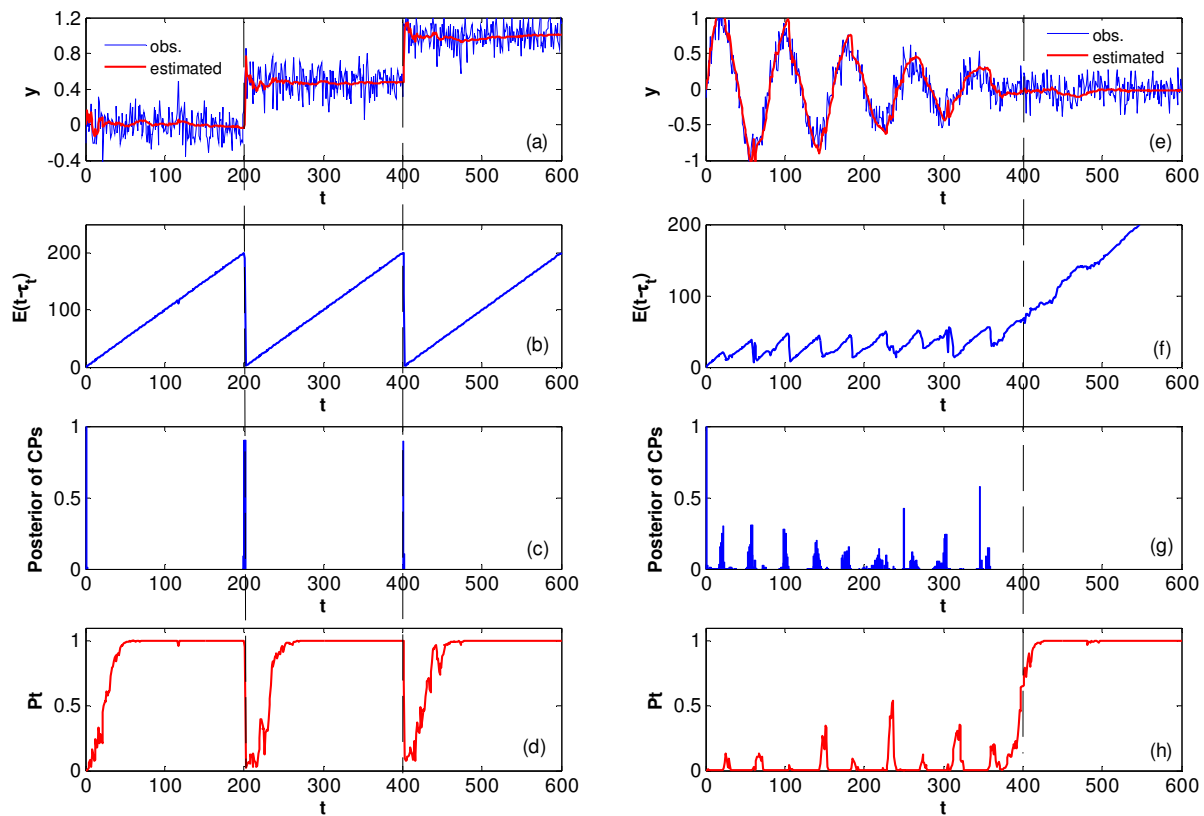
Figure 4-2: Illustration of the steady state detection using step function and oscillating function: (a)-(d): step function; (e)-(f): oscillating function; (a) and (e): simulated observations y and estimated values $\hat{y}$ using Eq. (4.13). The dotted vertical lines indicate the starting point of the steady state; (b) and (f): the estimated duration of the latest linear segment; (c) and (g): simulated posterior (frequencies) of change-points (CPs) using Algorithm 4.2. (d) and (h): the probability index P_t.

Figure 4-2 shows the steady state detection process for the step signal and oscillating signal. Figure 4-2 (a) and (e) show the observations and estimated signals, where the estimated values are very close to the true values. Besides, the estimations become smoother and smoother as the length of the linear segments grows. Figure 4-2 (b) and (f) show the sequentially estimated durations of the latest linear segments and Figure 4-2 (c) and (g) show the simulated frequencies of all change-points using Algorithm 4.2. They are used to capture the jump of the center of the posterior $P(\tau_t|y_{1:t})$. For the step signal, there are immediate jumps at the mean shift locations. The reason is that $P(t, t)$ in Eq. (4.7) is significantly larger than $P(j, t)/P(j, t - 1)$ for a mean shift or jump change at time t and thus the change can be immediately detected without any delay. Besides, the posterior of the latest change-point is focused almost on the starting time of the linear segment, which is the assumption in the approximation of ARL, and therefore the estimated duration of the latest linear segment almost equals to the true value. For the oscillating signal, there are nine jumps, which correspond to the movement of posterior at nine peaks and troughs of the oscillating signal. The last trough is disappeared into the signal noise and is difficult to detect. The probability detection indices are shown in Figure 4-2 (d) and (h), from which we can see that the detection index rise sharply around the steady state starting point. This can be explained by Eq. (4.17), where $h(t)$ is a 4$^{\text{th}}$ order polynomial of t and increases rapidly with t shortly after the steady state transition.

In many applications, the signals have a decaying variance while the mean is unchanging. In such cases, the slope detection method and t-test on the mean of two adjacent moving windows may totally fail. To see effectiveness of our algorithm, we use the signal with zero mean and noise amplitude as:

$$\sigma(t) = \begin{cases} 30^{(T_0-t)/(T_0-1)}\sigma_0 & if\ t \le T_0 \\ \sigma_0 & if\ t > T_0 \end{cases}$$

where $T_0 = 300$ and $\sigma_0 = 0.1$. The detection results in Figure 4-3 show that the steady state can also be effectively detected with small detection delay.
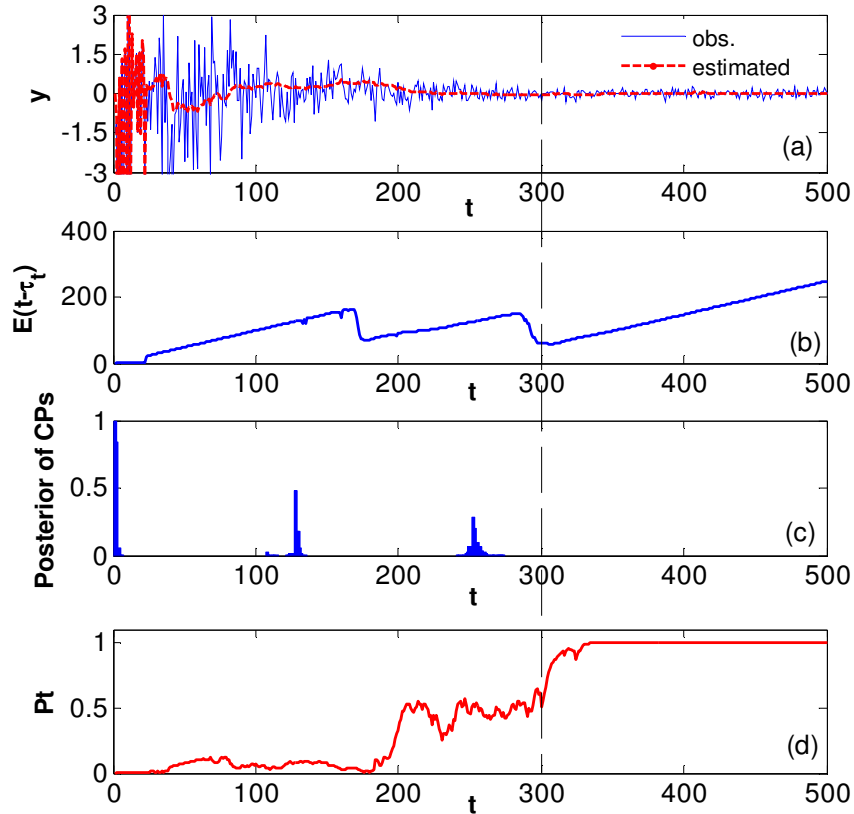
Figure 4-3: Steady state detection for the signal with zero mean and exponentially decreasing variance.

4.5.2 Computational Cost

Figure 4-4 shows the computational cost of each time step using three different number of support: $m = 50, 100$ and 150. As we can see, the computational cost per step is linearly increasing with t when $t < m$. When $t \ge m$, the computational cost per step is fully controlled.

Without setting fixed m, the total computational cost would increase quadratically. Note the selection of $m = 50$ is conservative. In the application, m may be set as low as 10 to further reduce the execution time. The computational time ($m = 10$) for 500 observations is about 1.5 seconds using MATLAB running on a Q9550 2.83 GHz Intel processor, which is much lower than the particle filter based method (12 seconds for 500 observations with 1000 particles).
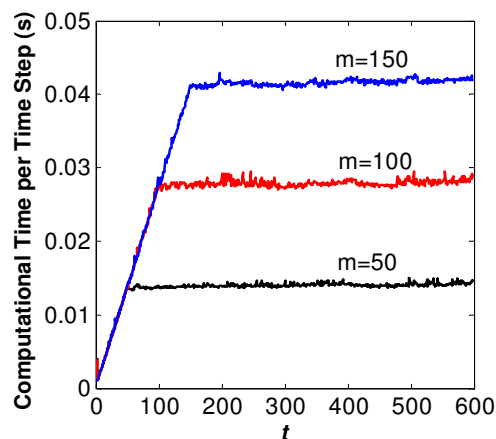
Figure 4-4: Computational cost each time step for number of support $m = 50, 100$ and 150

4.5.3 Average Run Length

To see how accurate the ARL approximation is and how ARL is influenced by algorithm and signal parameters, we calculated the ARL using both Monte Carlo simulation and approximation method. In the simulation, $\Sigma = 1 \times 10^4 I$, $\beta_0 = 0$ and $m = 50$, where I is the identity matrix. The signals are generated using zero mean and Gaussian noise. The other signal parameters and detection parameters are set as $\alpha = 0.9$, $s_0 = 0.003$, $\sigma = 0.1$, $p = 0.2$, $v = 20$, and $\gamma = 0.2$ for both simulation and approximation except for the changing parameters. The simulation is repeated 500 times for each parameter setting.
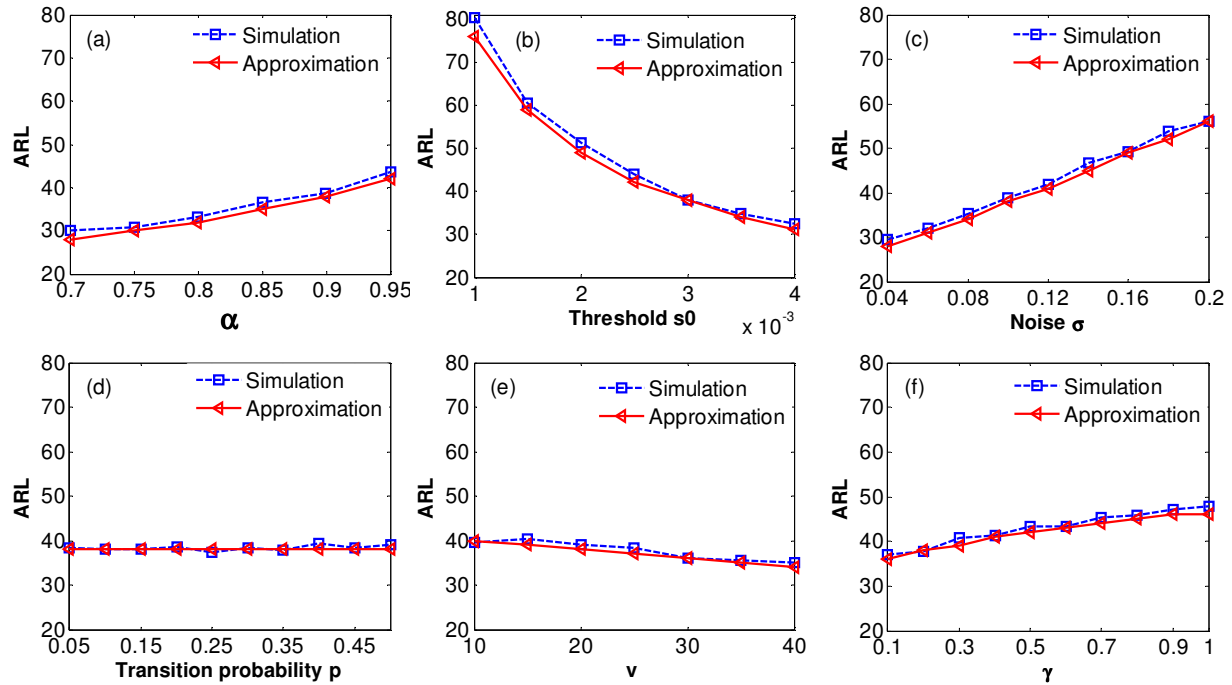
Figure 4-5: Average run length (ARL) calculated using Monte Carlo simulation and approximation Eq. (4.18). The parameters are set as $\alpha = 0.9$, $s_0 = 0.003$, $\sigma = 0.1$, $p = 0.2$, $v = 20$, and $\gamma = 0.2$ for all calculations except the changing parameter.

Figure 4-5 shows the ARL as functions of different parameters calculated using both simulation and approximation method. As we can see, the approximated ARL is almost identical to the simulated one in all cases. We also observe that the simulated ARL is slightly higher than calculated one in most cases. The reason is that the posterior of the latest change-point is not completely focused on $t = 1$, i.e., there is more than 1 support, yet in the approximation we assume $t = 1$ is the only support.

The ARL is not very sensitive to α, as shown in Figure 4-5 (a), therefore α is not treated as a tuning parameter and we suggest using $\alpha = 0.9$ in the application. The transition prior probability p almost has no influence on the ARL in the range [0.05, 0.5], as shown in Figure 4-5 (d). The ARL is also not sensitive to the noise prior parameters v and γ. In the application we

can roughly predict the noise amplitude and select v and γ accordingly. The only tuning parameter is the slope threshold s_0, which influence the ARL most significantly. Figure 4-5 (c) shows that the ARL increases almost linearly with signal noise amplitude. This is an advantage of this algorithm since it could automatically adjust the ARL to reduce the false alarm rate when signal noise is large and reduce the detection delay when the noise is small.

4.5.4 Evaluation and Comparison with Other Methods

In the comparison, we still use the weighted standard detection error (WSDE) defined in Eq. (3.21) as the evaluation metric to evaluate and compare the proposed method (EB: exact Bayesian inference) with other methods. EB is compared with four other methods, the particle filters based method (PF) proposed in Chapter 3, the slope detection method (SDM) [69, 86, 87], the variance ratio test method (VRT) [54, 62], and the t-test method [88]. The linear, quadratic, exponential and oscillating signals are used to generate for comparison. For each type of signal, two sets of signal parameters are used: (1) $h = 1, T_0 = 200$, (2) $h = 1, T_0 = 300$ to simulate different severity of the initial bias. To test the algorithm for both Gaussian/non-Gaussian noise, we use three kinds of autoregressive noise: no auto-correlation (AR(0)), first-order autoregressive correlation (AR(1)), and second-order autoregressive correlation (AR(2)), as shown in Table 4-2. Three noise amplitudes $\sigma_t = 0.06, 0.1, 0.14$ are used for AR(0) and $\sigma_t = 0.06$ and 0.1 are used for AR(1) and AR(2). In the simulation, $N = 500$ signals (replications) are generated for each set of signal parameters. For each set of penalty weight w and noise type, the detection parameters (window size and threshold for SDM, VRT and t-test, slope threshold s_0 for PF and EB) are selected that minimize the overall WSDE of all

generated signals (e.g., $4 \times 2 \times 3 \times 500$ for AR(0)). The support size $m = 10$ for EB and the other algorithm parameters are the same as in Section 4.1.

Table 4-2: Noise types and their parameters

Auto-correlation type	Equation	Parameter
AR(0)	$\psi_t^{(0)} = \epsilon_t$	$\epsilon_t \sim N(0, \sigma_t^2)$
AR(1)	$\psi_t^{(1)} = \phi_1 \psi_{t-1}^{(1)} + \epsilon_t$	$\phi_1 = 0.4$
AR(2)	$\psi_t^{(2)} = \phi_2 \psi_{t-1}^{(2)} + \phi_3 \psi_{t-2}^{(2)} + \epsilon_t$	$\phi_2 = -0.25, \phi_3 = 0.5$
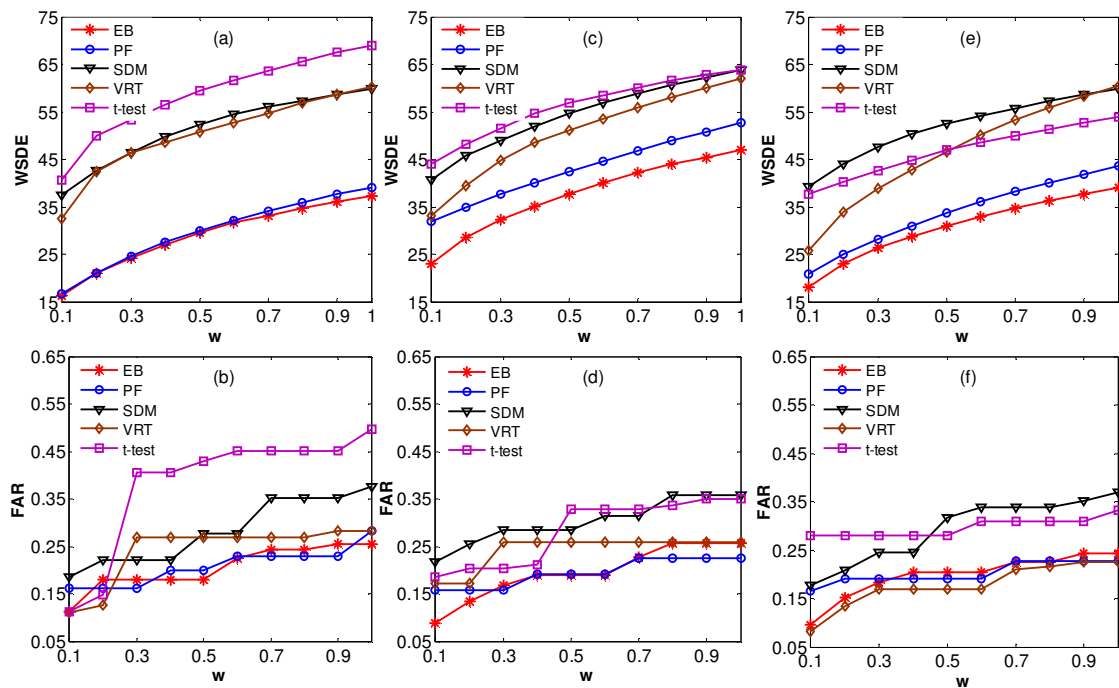
Figure 4-6: The weighted standard detection error (WSDE) and false alarm rate (FAR) of the proposed method (EB), PF, SDM, VRT and t-test as a function of penalty weight w for (a)-(b): AR(0); (c)-(d): AR(1) and (e)-(f): AR(2).

Figure 4-6 shows the WSDE and FAR as functions of w for each noise autoregressive type. Here FAR is only used to provide extra detection information. As we can see, the proposed

method EB and PF are much more accurate than SDM, VRT and t-test in terms of WSDE in all penalty weights. Besides, EB is slightly better comparing with PF method. The FAR of the proposed method is also lower than other methods in most cases.

Table 4-3: Comparison of EB, PF, SDM, VRT and t-test for $w = 1$ and noise type AR(0). The detection parameters are (1) EB, $s_0 = 0.0020$; (2) PF, $s_0 = 0.0022$; (2) SDM, window size $m = 50$, threshold= 8×10^{-5}; (3) VRT, $m = 98$, threshold=0.6; (4) t-test, $m = 28$, threshold=0.9.

Signal		σ_y	WSDE					FAR				
			EB	PF	SDM	VRT	t-test	EB	PF	SDM	VRT	t-test
Lin.	T_0=200	0.06	38.0	42.0	59.8	78.6	79.0	0	0	0	0	0
		0.10	47.8	53.9	60.7	66.1	65.8	0	0	0	0	0
		0.14	55.4	64.5	57.6	60.4	81.4	0	0	0	0	0.02
	T_0=300	0.06	37.5	40.9	58.0	70.9	92.1	0	0	0	0	0
		0.10	38.3	53.1	55.9	56.6	65.0	0	0	0	0.04	0.04
		0.14	47.2	70.4	58.6	121.6	122.0	0.02	0.01	0.03	0.75	0.44
Quad.	T_0=200	0.06	15.3	12.1	33.6	37.6	39.1	0	0.11	0	0	0.04
		0.10	25.7	21.2	31.9	26.7	32.7	0.06	0.04	0.02	0.04	0.16
		0.14	37.2	33.7	28.2	18.5	40.8	0	0.06	0.14	0.36	0.58
	T_0=300	0.06	34.0	33.8	22.4	16.3	46.4	1	1	0.11	0.33	0.2
		0.10	32.8	28.1	23.9	37.5	49.8	0.98	0.93	0.45	0.83	0.72
		0.14	34.6	22.4	34.5	72.8	70.0	0.84	0.62	0.62	0.93	0.84
Exp.	T_0=200	0.06	18.4	16.6	45.9	44.4	58.0	0.06	0.12	0	0	0.02
		0.10	24.7	26.3	40.5	23.2	48.6	0.1	0.08	0.03	0.30	0.22
		0.14	40.7	35.0	34.8	26.1	47.5	0.08	0.06	0.17	0.73	0.7
	T_0=300	0.06	54.0	61.7	35.5	27.2	41.0	1	1	0.04	0.51	0.28
		0.10	54.9	49.4	32.2	67.3	65.1	0.96	0.98	0.38	0.96	0.8
		0.14	52.6	40.1	55.7	107.8	103.6	0.94	0.88	0.82	0.99	0.98
Osc.	T_0=200	0.06	23.3	27.1	94.9	74.4	60.0	0	0.01	1	0	1
		0.10	31.6	27.6	90.2	61.5	70.1	0	0.04	0.99	0	0.98
		0.14	35.1	26.6	94.0	54.1	82.8	0	0.06	1	0	0.94
	T_0=300	0.06	21.7	23.0	156	63.6	73.2	0	0.04	1	0	1
		0.10	24.7	25.7	156	49.8	71.5	0	0.2	0.99	0	0.98
		0.14	24.2	29.4	152	40.6	72.5	0.1	0.55	1	0	0.98
Overall			37.3	39.1	59.9	60.3	69.0	0.25	0.28	0.38	0.28	0.50

Table 4-3 shows the detailed detection results among different bias signals and noise amplitudes in the case of $w = 1$ and Gaussian noise. The proposed method is much more robust

than other methods in handling different bias signals with different severity and noise amplitude. The maximum WSDE among different signals, as well as the overall WSDE are much lower than other methods. For other methods, especially SDM, VRT and t-test, only one set of detection parameters is not sufficiently flexible to be effective in all cases.

4.6 Application in the Micro/nanoparticle Dispersion Process
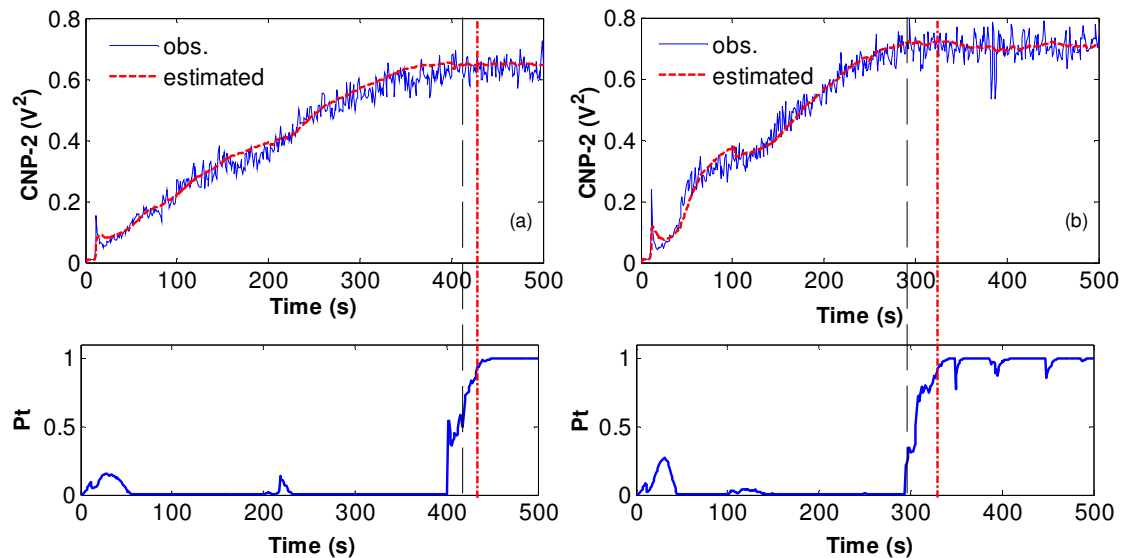
Figure 4-7: Steady state detection of CNP signals in the dispersion of 30 g Al_2O_3 for (a) ultrasonic power 30 W and (b) ultrasonic power 40 W. The dash-dotted line denotes the detected time using the proposed method and the dashed line denotes the EWMA-MSER (off-line) [69] detected time.

In this section, we use cavitation noise power (CNP) signals taken from the micro/nanoparticle dispersion to illustrate the application of the proposed steady state detection. Figure 4-7 shows the detection of CNP signals in the dispersion of 30 g Al_2O_3 particles under ultrasonic power 30 W (a) and 40 W (b). We use the same detection parameters except the threshold as used in the simulation. The new threshold is set as 0.001. The offline method

EWMA-MSER [69] developed in Chapter 2 is used as a benchmark to evaluate the proposed method. The offline method detected steady state times are 418 and 293 for CNP signals of power 30 and 40 W, respectively. In contrast, the detection results for the proposed method are 434 and 329, or the detection delays are 16 and 35 respectively, both of which are below 40.

4.7 Discussion and Conclusion

In this chapter, we have developed a new on-line steady state detection method using the multiple change-point models and exact Bayesian inference method. The signals are formulated as piecewise linear models and state space models and the posterior of the latest change-point is recursively calculated using a recursive message-passing algorithm. The slope and intercept of the current linear segment conditioning on the latest change-point and observations is proved to follow nonstandard bivariate student t distribution. Based on this finding, a probability index is developed to detect the steady state.

A fixed support size strategy for the posterior of the latest change-point is proposed using weighted sampling without replacement to control and balance the computational cost of each time step. Other approximation strategies for the Gamma ratio and probability index are also proposed for further reduction of computational cost. The computational cost of the proposed method is significantly lower than the particle filters based method. An accurate approximation formula for the average run length on the steady state observations are derived to provide insight and guidance on understanding and tuning the proposed method.

The performance of the proposed method is evaluated based on the weighted standard detection error. The simulation results demonstrate that the proposed method is much more robust in detecting different bias signals under different noise levels/types and bias severity. It functions like an adaptive slope detection method, using mainly the observations since the latest change-point and adaptive window sizes based on the bias shape and noise amplitude. In this numerical illustration only the non-informative priors are used for change-point model parameters. In practice, however, we may have prior knowledge about the signals (e.g., bias shapes, steady state transition point interval, etc), and thus informative priors could be applied for further improvement of the detection accuracy.

4.8 Appendix

4.8.1 Calculation of $P(s, t)$

$$P(s,t) = \int P(y_{s:t}|\sigma^2, \boldsymbol{\beta})p(\sigma^2)p(\boldsymbol{\beta}|\sigma^2)d\sigma^2 d\beta$$

$$= \int \left[\frac{\left(\frac{\gamma}{2}\right)^{\frac{v}{2}}}{\Gamma\left(\frac{v}{2}\right)}(\sigma^2)^{-\frac{v}{2}-1}e^{-\frac{\gamma}{2\sigma^2}}\right]\left[(2\pi)^{-1}|\sigma^2\boldsymbol{\Sigma}|^{-\frac{1}{2}}e^{-\frac{(\boldsymbol{\beta}-\boldsymbol{\beta}_0)^T\boldsymbol{\Sigma}^{-1}(\boldsymbol{\beta}-\boldsymbol{\beta}_0)}{2\sigma^2}}\right]\left[(2\pi)^{-\frac{t-s+1}{2}}(\sigma^2)^{-\frac{t-s+1}{2}}e^{-\frac{\|y_{s:t}-X_{st}\boldsymbol{\beta}\|^2}{2\sigma^2}}\right]d\sigma^2 d\boldsymbol{\beta}$$

$$= \int \frac{\left(\frac{\gamma}{2}\right)^{\frac{v}{2}}}{\Gamma\left(\frac{v}{2}\right)}(2\pi)^{-\frac{t-s+3}{2}}(\sigma^2)^{-\frac{t-s+v+5}{2}}|\boldsymbol{\Sigma}|^{-\frac{1}{2}}\exp[-\frac{H_{st}}{2\sigma^2}]\exp[-\frac{(\boldsymbol{\beta}-\boldsymbol{\mu}_{st})^T(X_{st}^TX_{st}+\boldsymbol{\Sigma}^{-1})(\boldsymbol{\beta}-\boldsymbol{\mu}_{st})}{2\sigma^2}]d\sigma^2 d\boldsymbol{\beta}$$

$$= \int \frac{\left(\frac{\gamma}{2}\right)^{\frac{v}{2}}}{\Gamma\left(\frac{v}{2}\right)}(2\pi)^{-\frac{t-s+1}{2}}(\sigma^2)^{-\frac{t-s+v+3}{2}}|\boldsymbol{\Sigma}|^{-\frac{1}{2}}\exp\left[-\frac{H_{st}}{2\sigma^2}\right]|X_{st}^TX_{st}+\boldsymbol{\Sigma}^{-1}|^{-\frac{1}{2}}d\sigma^2$$

$$= \pi^{-(t-s+1)/2}\left(\frac{|M_{st}|}{|\boldsymbol{\Sigma}|}\right)^{\frac{1}{2}}\frac{\gamma^{\frac{v}{2}}}{(H_{st})^{(t-s+1+v)/2}}\frac{\Gamma(\frac{t-s+1+v}{2})}{\Gamma(v/2)}$$

where

$$M_{st} = (X_{st}^T X_{st} + \Sigma^{-1})^{-1}$$

$$N_{st} = (\Sigma^{-1}\beta_0 + X_{st}^T y_{s:t})$$

$$\mu_{st} = M_{st} N_{st}$$

$$H_{st} = y_{s:t}^T y_{s:t} + \gamma + \beta_0^T \Sigma^{-1} \beta_0 - N_{st}^T M_{st} N_{st}$$

4.8.2 Proof of Lemma 4.1

(1) For simplicity, we use β and σ^2 instead of β_t and σ_t^2 in the following derivation.

$$P(\beta|\tau_t = s, y_{s:t}) = \int P(\beta, \sigma^2|\tau_t = s, y_{s:t})\, d\sigma^2 = \int \frac{P(\beta, \sigma_t^2)P(y_{s:t}|\beta, \sigma^2, \tau_t = s)}{P(s,t)}\, d\sigma^2$$

$$= \frac{1}{P(s,t)}\int \left[\frac{\left(\frac{\gamma}{2}\right)^{\frac{v}{2}}}{\Gamma\left(\frac{v}{2}\right)}(\sigma^2)^{-\frac{v}{2}-1}e^{-\frac{\gamma}{2\sigma^2}}\right]\left[(2\pi)^{-1}|\sigma^2\Sigma|^{-\frac{1}{2}}e^{-\frac{(\beta-\beta_0)^T\Sigma^{-1}(\beta-\beta_0)}{2\sigma^2}}\right]\left[(2\pi)^{-\frac{t-s+1}{2}}(\sigma^2)^{-\frac{t-s+1}{2}}e^{-\frac{\|y_{s:t}-X_{st}\beta\|^2}{2\sigma^2}}\right]d\sigma^2$$

$$= \frac{\left(\frac{\gamma}{2}\right)^{\frac{v}{2}}}{P(s,t)\Gamma\left(\frac{v}{2}\right)}|\Sigma|^{-\frac{1}{2}}(2\pi)^{-\frac{t-s+3}{2}}\Gamma\left(\frac{t-s+3+v}{2}\right)\left[\frac{(\|y_{s:t}-X_{st}\beta\|^2 + (\beta-\beta_0)^T\Sigma^{-1}(\beta-\beta_0)+\gamma)}{2}\right]^{-\frac{t-s+3+v}{2}}$$

$$\propto \left[\frac{(\|y_{s:t}-X_{st}\beta\|^2 + (\beta-\beta_0)^T\Sigma^{-1}(\beta-\beta_0)+\gamma)}{2}\right]^{-\frac{t-s+3+v}{2}}$$

$$\propto \left[(\beta-\mu_{st})^T(X_{st}^T X_{st}+\Sigma^{-1})(\beta-\mu_{st}) + y_{s:t}^T y_{s:t} + \beta_0^T\Sigma^{-1}\beta_0 + \gamma\right.$$
$$\left. - (y_{s:t}^T X_{st} + \beta_0^T\Sigma^{-1})(X_{st}^T X_{st}+\Sigma^{-1})^{-1}(X_{st}^T y_{s:t}+\Sigma^{-1}\beta_0)\right]^{-\frac{t-s+3+v}{2}}$$

$$\propto \left[1 + \frac{1}{t-s+v+1}(\beta-\mu_{st})^T\Sigma_{st}^{-1}(\beta-\mu_{st})\right]^{-\frac{t-s+3+v}{2}}$$

where

$$\mu_{st} = M_{st} N_{st}$$

$$\Sigma_{st} = \frac{H_{st}M_{st}}{(t-s+v+1)}$$

Therefore

$$(\boldsymbol{\beta}_t | \tau_t = s, y_{s:t}) \sim t_2(t - s + v + 1, \boldsymbol{\mu}_{st}, \boldsymbol{\Sigma}_{st})$$

(2) Suppose $\boldsymbol{\Sigma}_{st} = \boldsymbol{K}_{st} \boldsymbol{R}_{st} \boldsymbol{K}_{st}^T$ where $\boldsymbol{K}_{st} = \begin{bmatrix} k_{st}^{(1,1)} & 0 \\ 0 & k_{st}^{(2,2)} \end{bmatrix}$ and $\boldsymbol{R}_{st}$ is the correlation matrix. Let

$\boldsymbol{\beta}^* = \boldsymbol{K}_{st}^{-1} \boldsymbol{\beta}_t$, then

$$P(\boldsymbol{\beta}^* | \tau_t = s, y_{s:t}) \propto \left[1 + \frac{1}{t - s + v + 1} (\boldsymbol{\beta}^* - \boldsymbol{K}_{st}^{-1} \boldsymbol{\mu}_{st})^T \boldsymbol{R}_{st}^{-1} (\boldsymbol{\beta}^* - \boldsymbol{K}_{st}^{-1} \boldsymbol{\mu}_{st}) \right]^{-\frac{t-s+3+v}{2}}$$

Therefore

$$(\boldsymbol{\beta}^* | \tau_t = s, y_{s:t}) \sim t_2(t - s + v + 1, \boldsymbol{K}_{st}^{-1} \boldsymbol{\mu}_{st}, \boldsymbol{R}_{st})$$

According to [110], the marginal distribution

$$\left(\frac{a_t}{k_{st}^{(1,1)}} \middle| \tau_t = s, y_{s:t} \right) \sim \left(t - s + v + 1, (\boldsymbol{K}_{st}^{-1} \boldsymbol{\mu}_{st})^{(1)}, 1 \right)$$

or $\left(\frac{a_t - \mu_{st}^{(1)}}{k_{st}^{(1,1)}} \middle| \tau_t = s, y_{s:t} \right)$ follows standard univariate t distribution with degrees of freedom

$t - s + v + 1$.

4.8.3 Proof of Lemma 4.2

(1) $P(\sigma_t^2 | \tau_t = s, y_{s:t}) = \int P(\boldsymbol{\beta}_t, \sigma_t^2 | \tau_t = s, y_{s:t}) d\boldsymbol{\beta}_t \propto \int P(\boldsymbol{\beta}_t, \sigma_t^2) P(y_{s:t} | \boldsymbol{\beta}_t, \sigma_t^2, \tau_t = s) d\boldsymbol{\beta}_t$

$$\propto \int \left[\frac{\left(\frac{\gamma}{2}\right)^{\frac{v}{2}}}{\Gamma\left(\frac{v}{2}\right)} (\sigma_t^2)^{-\frac{v}{2}-1} e^{-\frac{\gamma}{2\sigma_t^2}} \right] \left[(2\pi)^{-1} |\sigma_t^2 \boldsymbol{\Sigma}|^{-\frac{1}{2}} e^{-\frac{(\boldsymbol{\beta}_t - \boldsymbol{\beta}_0)^T \boldsymbol{\Sigma}^{-1} (\boldsymbol{\beta}_t - \boldsymbol{\beta}_0)}{2\sigma_t^2}} \right] \left[(2\pi)^{-\frac{t-s+1}{2}} (\sigma_t^2)^{-\frac{t-s+1}{2}} e^{-\frac{\|y_{s:t} - X_{st}\boldsymbol{\beta}_t\|^2}{2\sigma^2}} \right] d\boldsymbol{\beta}_t$$

$$\propto \int \left[(\sigma_t^2)^{-\frac{v}{2}-1-\frac{1}{2}-\frac{t-s+1}{2}} \right] \left[e^{-\frac{(\boldsymbol{\beta}_t - \boldsymbol{\beta}_0)^T \boldsymbol{\Sigma}^{-1} (\boldsymbol{\beta}_t - \boldsymbol{\beta}_0)}{2\sigma_t^2} - \frac{\|y_{s:t} - X_{st}\boldsymbol{\beta}_t\|^2}{2\sigma^2} - \frac{\gamma}{2\sigma_t^2}} \right] d\boldsymbol{\beta}_t$$

$$\propto (\sigma_t^2)^{-\frac{t-s+v+3}{2}} \exp\left[-\frac{H_{st}}{2\sigma_t^2} \right]$$

Therefore

$$(\sigma_t^2 | \tau_t = s, y_{s:t}) \sim IG(\frac{t - s + v + 1}{2}, \frac{H_{st}}{2})$$

(2)

$$P(\boldsymbol{\beta}_t | \sigma_t^2, \tau_t = s, y_{s:t}) \propto P(\boldsymbol{\beta}_t | \sigma_t^2) P(y_{s:t} | \sigma_t^2, \boldsymbol{\beta}_t, \tau_t = s)$$

$$\propto \exp\left[-\frac{(\boldsymbol{\beta}_t - \boldsymbol{\beta}_0)^T \boldsymbol{\Sigma}^{-1}(\boldsymbol{\beta}_t - \boldsymbol{\mu}_0)}{2\sigma_t^2}\right] \exp\left(-\frac{\|y_{s:t} - \boldsymbol{X}_{st}\boldsymbol{\beta}_t\|^2}{2\sigma_t^2}\right)$$

$$\propto N(\boldsymbol{\mu}_{st}, \sigma_t^2 \boldsymbol{M}_{st})$$

Therefore

$$(\boldsymbol{\beta}_t | y_{1:s}, \sigma_t^2, \tau_t = s) \sim N(\boldsymbol{\mu}_{st}, \sigma_t^2 \boldsymbol{M}_{st})$$

5 Ultrasonic Attenuation based Inspection Method for Scale-up Production of A206 Metal Matrix Nanocomposites[*]

In Chapter 2, 3 and 4 we have developed the nanoparticle dispersion monitoring and control methods for the fabrication of MMNCs. In this chapter, a new quality inspection method is developed using ultrasonic nondestructive testing method. The main contribution of this work is the discovery of the relation between ultrasonic attenuation curves and microstructures of Al MMNCs.

5.1 Introduction

Recently, there has been a growing market for high performance lightweight materials, especially in the automotive, aerospace, and defense industries. Aluminum-Copper alloy A206 is such a kind of promising material. It has a chemical composition of Al (93.5-95.3%), Cu (4.2-5.0%), Fe ($\leq$0.1%), Mg (0.15-0.35%), Mn (0.2-0.5%) and Ti (0.15-0.3%). It offers superior mechanical properties with excellent high strength at both room and elevated temperature and long fatigue life [111]. However, due to its long solidification range and the formation of a long continuous intermetallic phase, A206 alloy is extremely susceptible to hot tearing in the casting process, which limits its widespread applications [111, 112].

---

[*] This chapter is based on the paper: **Jianguo Wu**, Shiyu Zhou, Xiaochun Li, "Ultrasonic Attenuation Based Inspection Method for Scale-up Production of A206-Al$_2$O$_3$ Metal Matrix Nanocomposites", *ASME Transactions, Journal of Manufacturing Science and Engineering,137(1), 011013)*

A206-Al$_2$O$_3$ metal matrix nanocomposites (MMNCs) provide a promising solution to improve hot tearing resistance [111]. The A206-Al$_2$O$_3$ MMNCs are fabricated by dispersing nano-sized Al$_2$O$_3$ particles into the A206 metal matrix using the ultrasonic cavitation method during the liquid phase and then casting into required solid shape [20, 113-116]. The well-dispersed Al$_2$O$_3$ nanoparticles in A206 work as heterogeneous nucleation agents which could significantly reduce the grain size of α-Al and refine the θ-Al$_2$Cu network, thus reducing the hot tearing susceptibility and enhance the mechanical properties, e.g., strength and ductility [117].

The amount and distribution of Al$_2$O$_3$ in A206 play a significant role in grain refinement and eutectic morphology modification [69, 111]. Due to their high surface energy, large surface-to-volume ratio, and poor wettability in liquid, Al$_2$O$_3$ nanoparticles tend to agglomerate and cluster together in the fabrication process [11, 23, 69, 118], which may limit their effectiveness. The microscopic images, e.g., the scanning electron microscope (SEM) images, are typically used to analyze the distribution of Al$_2$O$_3$ particles and the grain refinement of A206. However, the microscopic images are very expensive and time-consuming to obtain. As a result, the inspection of microstructure based on microscopic images cannot satisfy the quality control needs for the scale-up production of A206-Al$_2$O$_3$ MMNCs. It is highly desirable to develop a simpler and more economical method for the quality control of the fabrication process of A206-Al$_2$O$_3$ MMNCs.

In this work, we investigate the feasibility of relating the ultrasonic attenuation with the microstructure of A206-Al$_2$O$_3$ MMNCs for the purpose of quality control. Ultrasonic techniques have been widely used for material characterization [119-124]. In these techniques, ultrasonic velocity and attenuation are two typical indicators used to evaluate microstructures and material properties, such as density, porosity, elastic constant, and grain size. The variation of ultrasonic

velocity with frequency is typically very small in solid (<1%) [125]. Therefore, ultrasonic attenuation is used more frequently than the velocity measurement in characterizing solids since it provides a better characterization of the microstructure [126].

Acoustic attenuation is the decaying rate of the acoustic wave as it propagates through materials. It arises from two loss mechanisms: material absorption and scattering. Material absorption is the conversion of the mechanical energy of the acoustic wave into thermal energy and it usually dominates the acoustic attenuation at low frequencies. Material absorption involves various kinds of mechanisms [125], including hysteresis absorption, thermoelastic losses and thermal conduction. Hysteresis absorption is caused by physical relaxation mechanism and it typically occurs in single crystals, amorphous solids, and especially polymers [127]. It is observed to be proportional to the frequency [127, 128]. Thermoelastic absorption is defined as coupling of the thermal and elastic fields created by the propagating acoustic wave and is present in almost all materials [125]. The acoustic scattering arises at the boundaries between materials, grains or inclusions with different acoustic properties. The total attenuation coefficient is the sum of the acoustic absorption coefficient and scattering coefficient. In the low frequency range, the absorption losses dominate the attenuation while at high frequencies, the absorption losses are negligible and the attenuation is mainly caused by the scattering losses.

Although considerable work has been done on the relationship between ultrasonic attenuation and material microstructures, most of the studies are focused on the single-phase materials where the scattering is mainly caused by the grains with different orientations. The attenuation of two-phase systems has also been studied where each phase is often modeled as a continuum and the scattering only occurs at the boundary of different phases [126, 129-133]. These models match

well with experimental results for solid or liquid particles in the liquid continuum. While in the two-phase system with both phases are solid, the scattering effects in the grain boundaries of the same phase may dominate in the total attenuation, which makes these models inaccurate. For A206-Al_2O_3 MMNCs, the attenuation is much more complex since there are three phases, the α-Al base phase, θ-Al_2Cu intermetallic phase and Al_2O_3 clusters.

In this research, the relationship between the ultrasonic attenuation and the microstructure of A206-Al_2O_3 MMNCs is investigated through experiments and statistical analysis, which provides a useful guideline for the quality control in the manufacturing of A206-Al_2O_3 MMNCs. The chapter is organized as follows. In Section 5.2, the fabrication of the samples and the ultrasonic attenuation measurement are introduced. Section 5.3 first presents the microstructures of A206 and its nanocomposites and the morphology modification mechanisms of Al_2O_3. Then the relationship between the ultrasonic attenuation and microstructures are discussed in details. The conclusions are presented in Section 5.4.

5.2 Experimental Procedure

5.2.1 Sample Preparation

Figure 5-1 shows the experimental setup for ultrasonic processing before casting of A206-Al_2O_3 MMNCs. It consists of a resistance heating furnace, an ultrasonic cavitation based processing system (Misonic Sonicator 3000) with a niobium probe of 12.7 mm in diameter and 92 mm in length, a temperature control system and a gas protection system. A graphite crucible with an inner diameter of 88.9 mm and a height of 101.6mm was used for melting. The ultrasonic probe vibrates with the operating frequency of 20 KHz and power of 4.0 KW. Due to

their low density and poor wettability with A206, Al_2O_3 particles tend to float on the surface of A206 melt. Therefore, the double-capsulate feeding method [117] is used where the Al_2O_3 particles are wrapped by ultrathin aluminum foils and discharged into the melt.
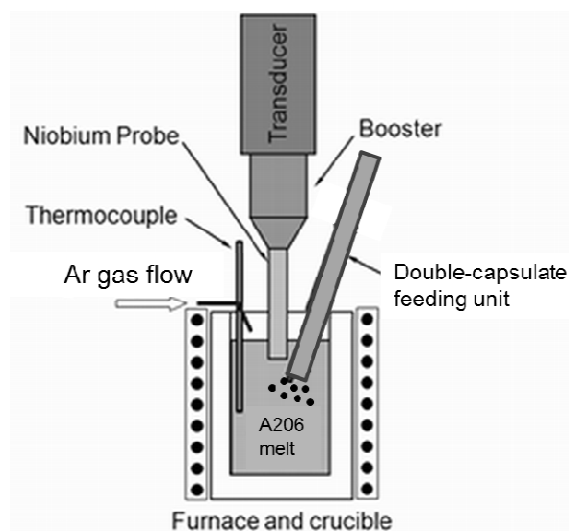
Figure 5-1: The experimental set-up for ultrasonic processing

Table 5-1: Details of fabricated samples

Sample ID	Sample	Al_2O_3 (wt%)	Ultrasound (minutes)
1	A206 pure	0	0
2	A206 pure	0	15
3	A206-Al_2O_3	1%	15
4	A206-Al_2O_3	5%	0
5	A206-Al_2O_3	5%	15

About 500 g A206 alloy was first melted in the graphite crucible under the protection of argon gas and the temperature was controlled to be at 700 ℃. Then the ultrasonic cavitation

system was turned on and the γ-Al$_2$O$_3$ nanoparticles with a diameter of 50 nm were added into the molten melt. After all Al$_2$O$_3$ nanoparticles were added, the ultrasonic cavitation continued for 15 minutes and then the ultrasonic probe was lifted out of the melt. After that, the molten melt was heated up to 740 ℃ and then poured into a steel permanent mold with a preheated temperature of 400 ℃. Total 5 samples were fabricated, as shown in Table 5-1. The casted samples were cut and polished to 8.5cm×8.5cm×1.6cm blocks, as shown in Figure 5-2. Note for sample 4, only mechanical stirring was applied to disperse Al$_2$O$_3$ nanoparticles.
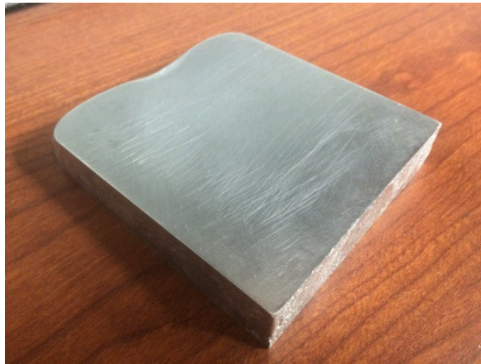
Figure 5-2: A representative casted sample

5.2.2 Attenuation Measurement

Figure 5-3 illustrates the ultrasonic attenuation measurement process using the spectral ratio analysis technique [134-136]. The attenuations were measured using the Olympus Epoch 1000 series NDT device with two dual element transducers working in pulse-echo mode: transducer D785-RP with diameter of 6 mm and nominal central frequency of 2.25MHz, and transducer MTD705 with diameter of 3.8 mm and nominal central frequency of 5MHz. The transducer was coupled to the largest surface of samples (thickness 1.6cm) using couplant glycerin with acoustic impedance of 2.42×10^5 g/(cm$^2 \cdot$ sec). The first and the second back wall echoes $S_1(t)$ and

$S_2(t)$ were extracted from the measured signals using a rectangular window. Note that in Figure 5-3 there is a time shift for $S_1(t)$ and $S_2(t)$.
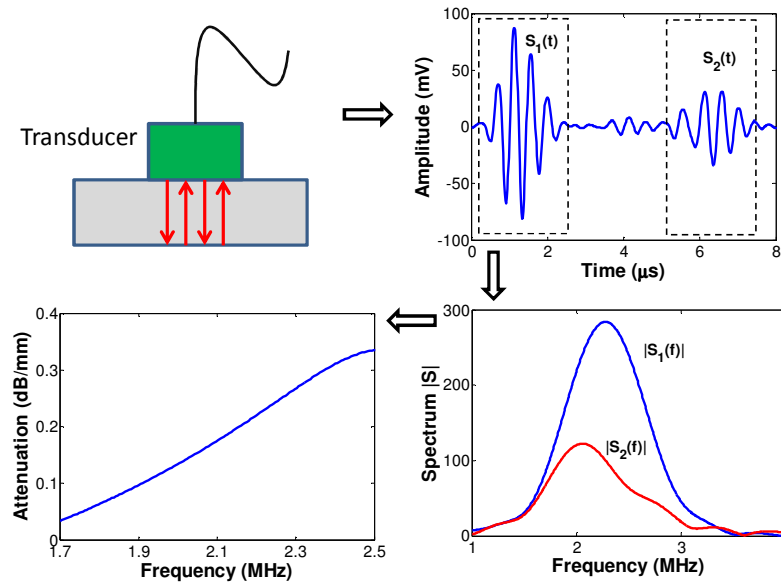
Figure 5-3: Illustration of the attenuation measurement using spectral ratio technique

The frequency spectra were obtained by performing the Fast Fourier Transform (FFT) on the extracted echoes. The spectra $S(f)$ can be expressed as [134, 137, 138]

$$S_1(f) = R_{bottom}D(f, 2d)S_0(f)\exp(-2\alpha(f)d)\exp(i(2\pi ft - 2dk(f)))$$

$$(5.1)$$

$$S_2(f) = R_{top}R_{bottom}^2 D(f, 4d)S_0(f)\exp(-4\alpha(f)d)\exp(i(2\pi ft - 4dk(f)))$$

where $\alpha(f)$ is the attenuation coefficient, $S_0(f)$ is the source spectrum, R_{top} and R_{bottom} are the acoustic reflection coefficients for the top surface and bottom surface, respectively, k is the wave number, t is the traveling time, d is the thickness of the sample, and $D(f, z)$ is the diffraction coefficient [139]. $D(f, z)$ is given as

$$D(f,z) = 1 - \exp\left(-\frac{i2\pi}{s}\right)\left[J_0\left(\frac{2\pi}{s}\right) + iJ_1\left(\frac{2\pi}{s}\right)\right] \tag{5.2}$$

where J_0 and J_1 are the cylindrical Bessel functions and $s = \frac{2\pi z}{kr^2}$ with r being the radius of the transducer. The compressive wave velocity (6320 m/s) for Al material is used to calculate the wave number. The attenuation can be calculated using Eq. (5.1) as

$$\alpha(f) = \frac{1}{2d}\left[\ln\left|\frac{S_1}{S_2}\right| - \ln\left|\frac{D(f,2d)}{D(f,4d)}\right| + \ln\left|R_{top}R_{bottom}\right|\right] \tag{5.3}$$

Note that the unit of the calculated attenuation is Nepers/mm using Eq. (5.3), which equals 8.686 dB/mm. The reflection coefficient $R_{bottom} \approx 1$ and R_{top} can be approximated using the formula [119]

$$R_{top} = \frac{Z_2 - Z_1}{Z_2 + Z_1} \tag{5.4}$$

where $Z_1 = 2.42 \times 10^5$ g/(cm$^2 \cdot$ sec) and $Z_2 = 17.1 \times 10^5$ g/(cm$^2 \cdot$ sec) are the acoustic impedances of glycerin and aluminum, respectively. Since the spectrum with large deviation from the central frequency has low accuracy, about -6dB bandwidth is selected such that only the center 50% of the frequency range is used to calculate the attenuation.

5.3 Experimental Results and Analysis

5.3.1 Microstructures and Morphology Modification Mechanism

Figure 5-4 shows the micrographs of the pure A206 alloy and A206-1wt%Al$_2$O$_3$ nanocomposite in as-cast form taken at random positions of the samples. For the pure A206 alloy,

there are large dendritic primary α-Al phases surrounded by continuous θ-Al$_2$Cu intermetallic phases. These θ-Al$_2$Cu phases accumulate along the grain boundaries of the primary α-Al phases with the morphology of long continuous network. For the A206-1wt% Al$_2$O$_3$ nanocomposites, the morphology of the primary α-Al phases is changed from the large dendritic structures to small equiaxed crystals. Besides, the θ-Al$_2$Cu phases become thinner and much less continuous. It should be noted that the ultrasonic processing for the pure A206 has almost no influence on the microstructure. Choi *et al* [111] found that the average grain size for pure A206 with ultrasonic processing is slightly reduced compared with pure A206 without ultrasonic processing.
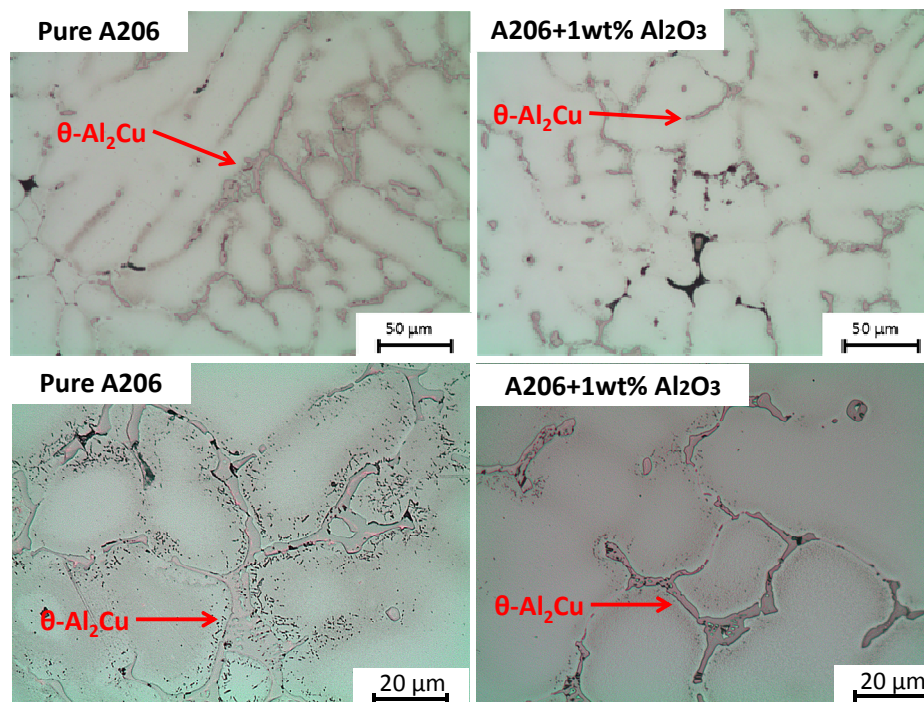
Figure 5-4: Optical micrographs of as-cast pure A206 and A206-1wt%Al$_2$O$_3$ MMNCs with 15 min ultrasonic processing

The polarized-light micrographs of the pure A206 alloy and A206-1wt%Al$_2$O$_3$ MMNCs are shown in Figure 5-5. The average grain size for the primary α-Al phases of the pure A206 is

about 160 µm measured using the linear intercept method. Compared with pure A206, the average grain size for A206-1wt%Al$_2$O$_3$ is significantly reduced by almost 50%. It indicates that the Al$_2$O$_3$ nanoparticles work as heterogeneous nucleation agents and thus could noticeably reduce the grain size of α-Al and refine the θ-Al$_2$Cu network.
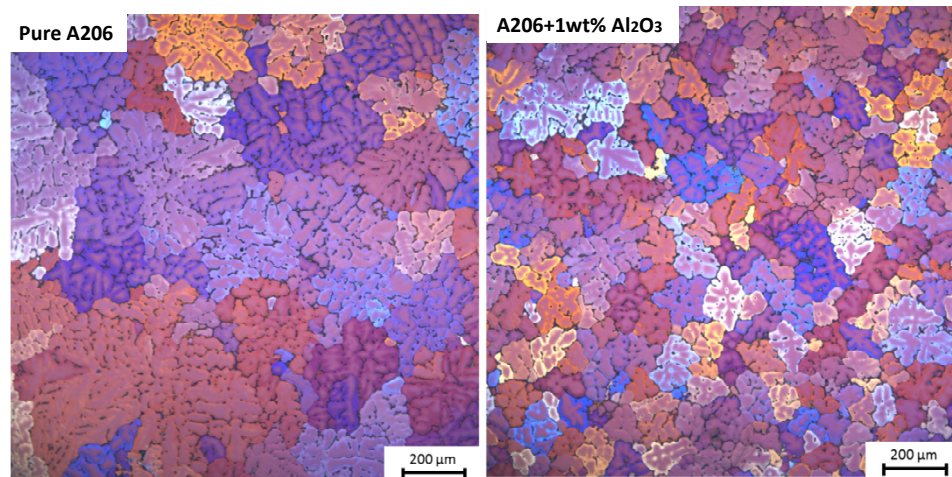
Figure 5-5: Polarized light micrographs of as-cast pure A206 and A206-1wt%Al$_2$O$_3$ MMNCs with 15 min ultrasonic processing

The mechanisms for the formation of continuous network of the eutectic θ-Al$_2$Cu phase in the pure A206 and the morphology modification by Al$_2$O$_3$ in A206-Al$_2$O$_3$ nanocomposites are well studied [20, 111, 117, 140]. For the pure A206 alloys, the primary α-Al phases will first nucleate and grow to large dendritic structure in the solidification process. Due to the high supercooling of the θ-Al$_2$Cu phase nucleation, the Cu solute will be pushed out of α-Al phases into the remaining liquid phase and accumulates between dendrite arms and adjacent dendrites. When the Cu content increases to the eutectic composition (33%Cu), the θ-Al$_2$Cu phase starts to nucleate and grow into a long continuous eutectic microstructure in-between the α-Al dendrites.

For the A206-Al$_2$O$_3$ nanocomposites, the formation mechanism of the eutectic phase is modified with the existence of Al$_2$O$_3$ nanoparticles. Similarly, the Cu solute and the Al$_2$O$_3$ particles are pushed to the remaining liquid in the formation of the primary α-Al phases. The concentrated Al$_2$O$_3$ particles have good nucleant potency and could serve as effective nucleation sites for θ-Al$_2$Cu to nucleate and grow before the remaining liquid reaches the eutectic composition. The depletion of Cu due to the formation of θ-Al$_2$Cu will on the other hand enrich the content of Al around the θ-Al$_2$Cu phases and thus form α-Al phases to block the growth of long θ-Al$_2$Cu phases. Therefore, the Al$_2$O$_3$ nanoparticles can effectively refine both α-Al phases and θ-Al$_2$Cu phases, and thus reduce the hot tearing susceptibility and enhance the material strength and ductility.

5.3.2 Relationship between the Acoustic Attenuation and Microstructures

5.3.2.1 *Non-uniformity of Acoustic Attenuation*

Figure 5-6 shows the ultrasonic attenuations as functions of frequency measured at 25 randomly selected locations using the transducer D785-RP of 2.25MHz as nominal frequency for each casted sample. Note that zero-padding is used as a frequency interpolation method in the Discrete Fourier Transform to increase the number of observations within the selected bandwidth. From this figure we can clearly see that there are large variations for the measured attenuation at each frequency for the first four samples while for sample 5 A206-5%Al$_2$O3 the variation is much lower. Figure 5-7 shows the ultrasonic attenuation measured at 25 randomly selected locations using the transducer MTD705. Similarly, the variations of the attenuation among different locations are very large for the first four samples, especially the sample A206-5%Al$_2$O$_3$

without ultrasonic processing. While for the sample A206-5%Al₂O3 with ultrasonic treatment, the attenuation is quite uniform.
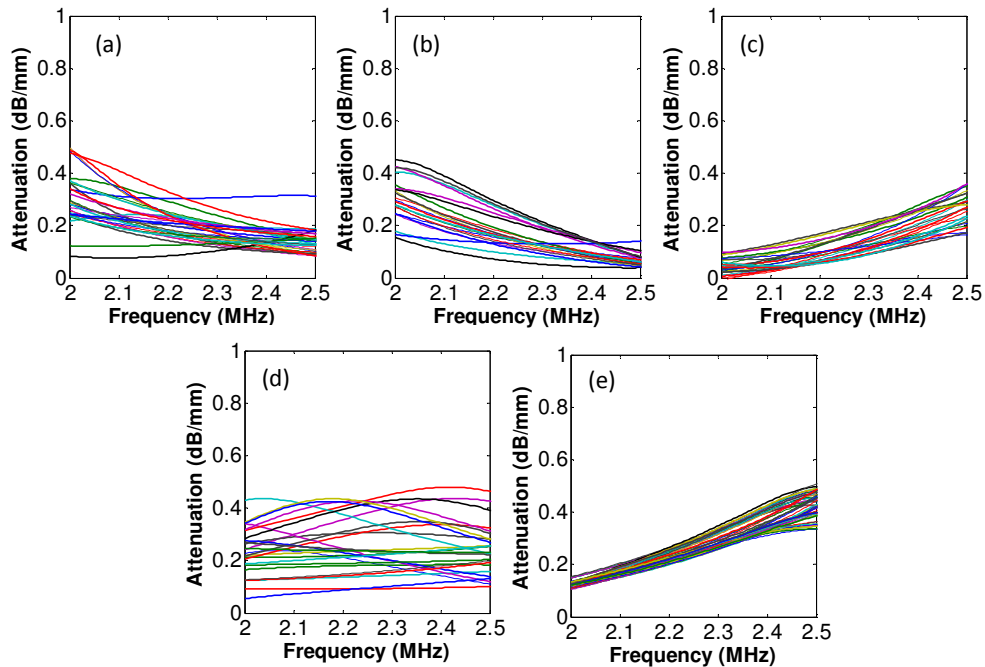
Figure 5-6: Ultrasonic attenuation as function of frequency measured at multiple random locations using transducer with nominal central frequency 2.25 MHz: (a) sample 1, pure A206 without ultrasonic processing; (b) sample 2, pure A206 with ultrasonic processing; (c) sample 3, A206+1%Al$_2$O$_3$+ultrasonic processing; (d) sample 4, A206+5%Al$_2$O$_3$, no ultrasonic processing; (e) sample 5, A206+5%Al$_2$O$_3$+ultrasonic processing.

There are three types of inherited uncertainties in the ultrasonic measurement system itself that may lead to large variation, namely the couplant thickness between the sample and transducer, the reflection or transmission coefficient due to different coupling conditions, and the electronic noises. To determine if these factors are significant in our experiments, we measured the attenuation of sample 2 at 10 randomly selected locations with each location measured 10 times. The results are shown in Figure 5-8. From the results we can clearly see that the variation of the attenuation at the same location is negligible compared with the variation across different

measurement locations. It indicates that the large non-uniformity of the attenuation is mainly due to the variation in microstructures of the samples.
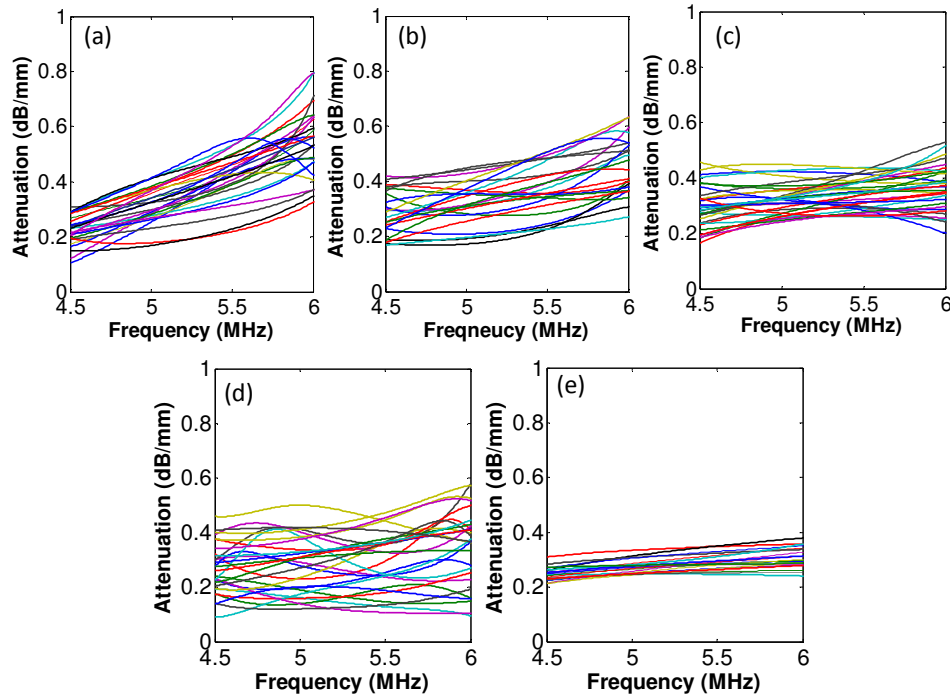
Figure 5-7: Ultrasonic attenuation as function of frequency measured at multiple random locations using transducer with nominal central frequency 5 MHz: (a) sample 1, pure A206 without ultrasonic processing; (b) sample 2, pure A206 with ultrasonic processing; (c) sample 3, A206+1%Al$_2$O$_3$+ultrasonic processing; (d) sample 4, A206+5%Al$_2$O$_3$, no ultrasonic processing; (e) sample 5, A206+5%Al$_2$O$_3$+ultrasonic processing.

This non-uniformity of ultrasonic attenuation is quite similar to the phenomenon of large anisotropies of the acoustic backscattering found in titanium alloys [141-144]. In these alloys (e.g., Ti6242, Ti-6Al-4V [145-147]), there exist microtextures or colonies of crystallites sharing a common crystallographic orientation over a long range. The formation of long microtextures due to the preference of certain orientations directly results in the plastic anisotropy and thus large inhomogeneities of the backscattering or ultrasonic attenuation along different acoustic paths. For example, Mukhopadhyay *et al*. [143] measured the nonlinear ultrasonic (NLU)

parameters at different locations of β heat treated near α titanium alloys under different cooling rates. The slow cooling rate tends to produce microtexture structures while fast cooling rate results in fine acicular α structure with random orientation in the primary β phase. Their results showed that the variance of NLU parameter was significant for the specimen with slowest cooling rate and the variance decreased with increasing cooling rate.
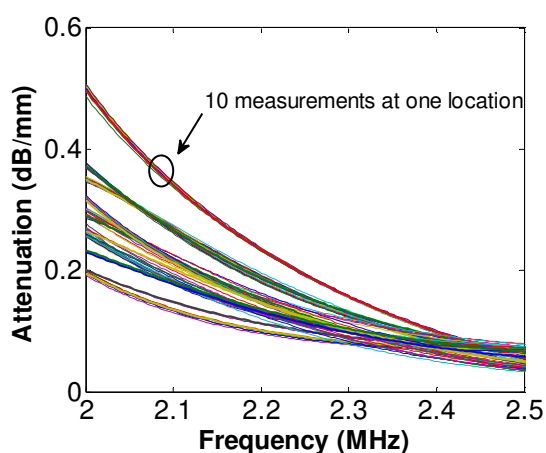
Figure 5-8: Ultrasonic attenuation of the pure A206 with ultrasonic processing (sample 2) measured at 10 random locations with each location measuring 10 times using the transducer D785-RP.

The non-uniformity of the acoustic attenuation in A206/A206-Al$_2$O$_3$ can be explained in a similar way. Three main sources may cause the non-uniformity of attenuation: the primary α-Al phase, the θ-Al$_2$Cu phase and the cluster of Al$_2$O$_3$ nanoparticles in the A206-Al$_2$O$_3$ MMNCs. In the pure A206 with/without ultrasonic processing, the primary α-Al phase exhibits large dendritic structures with grain size up to several hundred micrometers, as shown in Figure 5-4 and Figure 5-5. Typically the orientations of these dendrites are not randomly distributed due to the preference of certain crystalline orientations, e.g. the heat flow direction, in different locations. Besides, the θ-Al$_2$Cu phase along the grain boundaries exists in the morphology of

long continuous network. The interfaces between the α-Al phase and the θ-Al$_2$Cu phase are quite anisotropic along different acoustic paths. Since the difference of acoustic properties between α-Al and θ-Al$_2$Cu are much more significant than that between α-Al grains with different orientations, the acoustic non-uniformity is mainly caused by the θ-Al$_2$Cu network.
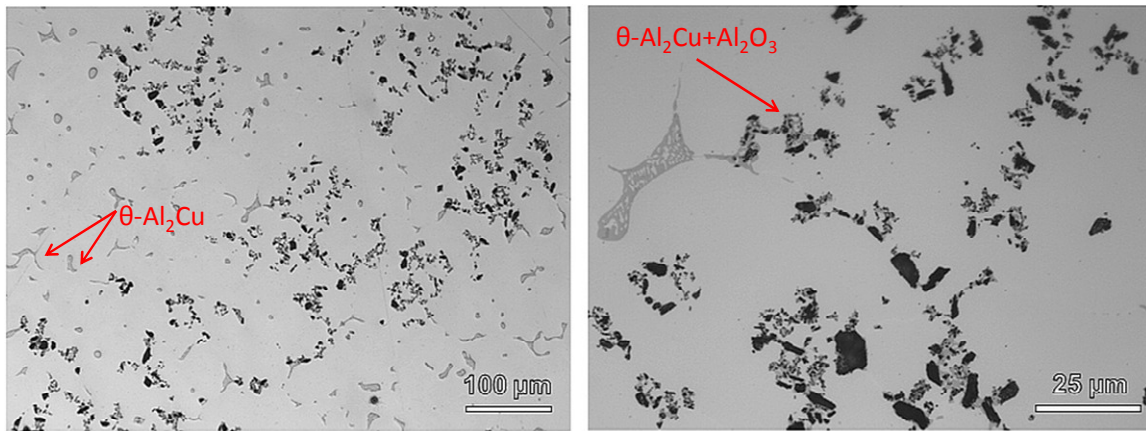
Figure 5-9: Optical micrographs of A206-5wt% Al$_2$O$_3$ nanocomposites with ultrasonic processing treatment

For the A206-5% Al$_2$O$_3$ nanocomposites with ultrasonic processing, due to the enhanced nucleation by evenly distributed Al$_2$O$_3$ nanoparticles, both the grain size of the primary phase and the long continuous θ-Al$_2$Cu phase are significantly reduced, which makes the material much more isotropic. Figure 5-9 shows the optical micrographs of the A206-5wt%Al$_2$O$_3$ nanocomposites with ultrasonic processing, from which we can clearly see that the θ-Al$_2$Cu network is totally broken and the boundaries of the primary phase are much more difficult to recognize.
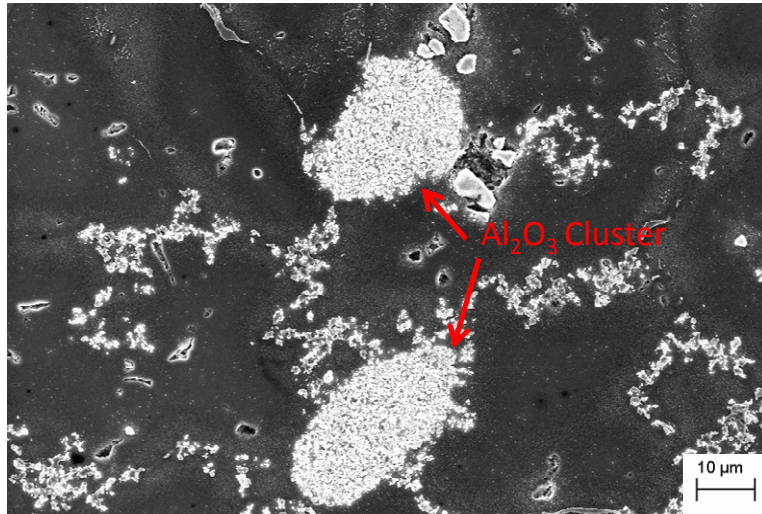
Figure 5-10: SEM image of A206-Al$_2$O$_3$ nanocomposites showing big Al$_2$O$_3$ clusters

For the A206-5wt% Al$_2$O$_3$ nanocomposites without ultrasonic processing, the Al$_2$O$_3$ particles agglomerate together and form big clusters (Figure 5-10), which could significantly reduce their effectiveness in refining grain sizes. Besides, without ultrasonic processing, the Al$_2$O$_3$ nanoparticles or clusters may not be evenly distributed in the nanocomposites, which may make the material even more anisotropic. For the A206-1% Al$_2$O$_3$ nanocomposites, there still exists long θ-Al$_2$Cu phase, though less continuous and thinner. Therefore the non-uniformity is still notable compared with A206-5wt% Al$_2$O$_3$ nanocomposites.

5.3.2.2 *Quantification of the Non-uniformity in Ultrasonic Attenuation*

To quantitatively describe the non-uniformity, we use the variance in the ultrasonic attenuation and built a model to estimate it as follows. Denote α_{ij} as the attenuation of the *j*-th location under the frequency f_i and it is given as

$$\alpha_{ij} = \mu_i + \epsilon_{ij} \tag{5.5}$$

where μ_i is the mean attenuation at frequency f_i and ϵ_{ij} is the attenuation bias for the j-th location at frequency f_i. Assume that ϵ_{ij} follows independent and identically distributed (i.i.d.) normal distribution. $\epsilon_{ij} \sim iid\ N(0, \sigma^2)$. It is reasonable to assume i.i.d. normal distribution since at different measuring locations the attenuation at a specific frequency is random and at a specific location, the attenuation at different frequencies is somehow independent in many cases when the frequency increment is large. The unbiased estimator for the mean μ_i and variance σ^2 can be calculated as

$$\hat{\mu}_i = \frac{1}{m} \sum_{j=1}^{m} \alpha_{ij} \tag{5.6}$$

$$\widehat{\sigma^2} = S^2 = \frac{\sum_{i=1}^{n} \sum_{j=1}^{m} \left(\alpha_{ij} - \hat{\mu}_i \right)^2}{n(m-1)} \tag{5.7}$$

where n and m are the number of frequencies (no zero-padding) and number of measuring locations at each frequency, respectively.
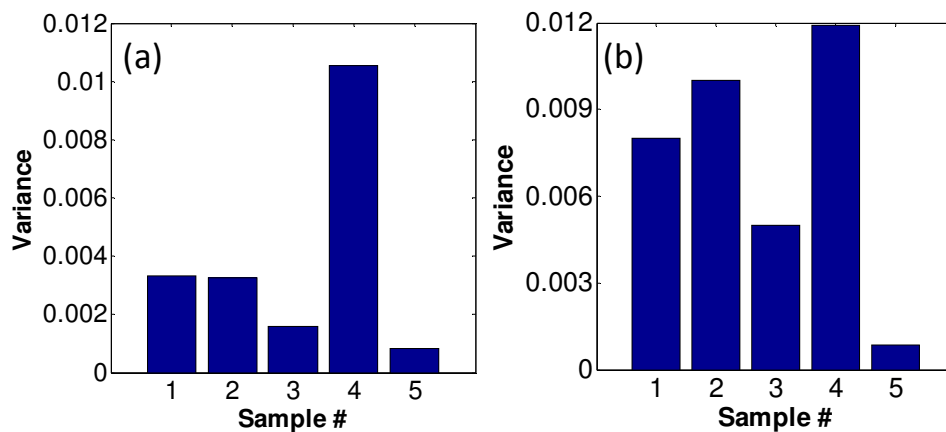
Figure 5-11: The estimated variance of the acoustic attenuation measured using (a) transducer with nominal central frequency 2.25MHz; (b) transducer with nominal central frequency 5MHz

Figure 5-11 shows the estimated variance of the ultrasonic attenuation measured using these two transducers. It clearly shows that sample 4 (A206+5%Al$_2$O$_3$, no ultrasonic processing) has the highest variances while sample 5 (A206+5%Al$_2$O$_3$, ultrasonic processing) has the lowest variances for both transducers. Sample 3 has the second lowest variance of the attenuation. It is consistent with the discussion above that sample 5 has the most uniform structure and it is followed by sample 3. For sample 4, due to the unevenly distributed Al$_2$O$_3$ particles and formation of large Al$_2$O$_3$ clusters, the microstructure becomes the most inhomogeneous. In addition, the variances for the first three sample in Figure 5-11 (a) are much lower than in Figure 5-11 (b), indicating that at low frequencies, the ultrasonic attenuation is more isotropic. This result is similar to Han's theoretical result [142] that at high frequencies, the backscattering is much more anisotropic. For sample 1 and sample 2, there is almost no difference in the variance in Figure 5-11 (a) and the former is a little lower than the latter in Figure 5-11 (b).

From the discussion above we know that the non-uniformity of the acoustic attenuation can provide insight on the microstructures of A206/A206-Al$_2$O$_3$ nanocomposites. When there exist long continuous intermetallic phase and large dendrites, the variance is significant. Therefore, in the scale-up production, the estimated variance can be used as an indicator to inspect the quality of A206-Al$_2$O$_3$ nanocomposites.

Specifically, suppose we have a good sample with evenly-distributed Al$_2$O$_3$ and well refined microstructures, and a target sample to be inspected. We can construct a hypothesis test based on the estimated variances as follows. The null hypothesis (H_0) and the alternative hypothesis (H_1) are defined as

$$H_0: \sigma_2^2 \leq \sigma_1^2$$

$$H_1: \sigma_2^2 > \sigma_1^2$$

where σ_1^2 and σ_2^2 are the attenuation variances for the good sample and the target sample, respectively. If the null hypothesis is accepted, then the target sample can be determined as a good sample. On the other hand, if the null hypothesis is rejected and the alternative is accepted, then the target sample is deemed as a poor sample. The estimated variances for the good sample and the target sample are S_1^2 and S_2^2, respectively. Then we have

$$\frac{S_2^2/\sigma_2^2}{S_1^2/\sigma_1^2} \sim F(n_2(m_2 - 1), n_1(m_1 - 1)) \tag{5.8}$$

where n_i and m_i are the number of frequencies and number of measuring locations for good sample ($i = 1$) and the target sample ($i = 2$). The test statistic is defined as

$$R = \frac{S_2^2}{S_1^2} \tag{5.9}$$

The critical value for the test with significance level α'(upper bound of type I error, typically select 0.05) is given as $F_{1-\alpha'}(n_2(m_2 - 1), n_1(m_1 - 1))$, namely, the $(1 - \alpha')$-th quantile for the F distribution with freedom $n_2(m_2 - 1)$ and $n_1(m_1 - 1)$. The null hypothesis H_0 can be rejected if

$$R > F_{1-\alpha'}(n_2(m_2 - 1), n_1(m_1 - 1)) \tag{5.10}$$

In practice, 1wt% Al_2O_3 nanoparticles are sufficient to improve the A206-Al_2O_3 nanocomposites to reach the desired material properties [111, 117]. Suppose we select Sample 3

as the reference sample with acceptable properties. $n_1 = n_2 = 3$ and $m_1 = m_2 = 25$ in the frequency range 2.0~2.5MHz. The critical value with $\alpha' = 0.05$ is 1.4656. Then if $S_2^2 > 1.4656S_1^2 = 0.0023$, the null hypothesis can be rejected. From Figure 5-11 (a) we can see that Sample 1, 2, and 4 have variance larger than 0.0023. In the quality inspection we can treat them as poor samples. The testing results are the same if we use the attenuation data in the frequency range 4.5~6MHz. Note that the critical value in Eq. (5.10) is specifically related to the selected frequency range and the number of measuring locations.

5.3.2.3 *Frequency Dependency of Acoustic Attenuation*

Besides the attenuation variance, the mean attenuation also highly depends on the microstructures and it is also used to characterize the microstructures. In this section, the frequency dependency of the attenuation for both absorption and scattering mechanisms was first introduced and then used to interpret the experimental results.

As mentioned in the introduction section, the attenuation can be split into two parts, the absorption loss and the scattering loss. The main absorption mechanisms include the thermoelastic losses and thermal conduction. For the thermoelastic losses can be classified into two types: interparticle and intraparticle thermoelastic absorption. The intraparticle thermoelastic absorption α_{te1} can be expressed as [125]

$$\alpha_{te1} \approx \frac{2\pi(E_S - E_T)}{E_S} \frac{ff_{01}}{f^2 + f_{01}^2} \tag{5.11}$$

where E_s and E_T are the elastic moduli under adiabatic and isothermal conditions respectively, f is the acoustic frequency and f_{01} is the frequency of the maximum attenuation given as

$$f_{01} \approx \frac{\pi}{2} \frac{\chi}{a^2 C_V} \tag{5.12}$$

where χ is the thermal conductivity of the particle and a is the particle size or grain size and C_V is the specific heat at constant volume. The interparticle thermoelastic absorption α_{te2} is given as [125]

$$\alpha_{te2} \approx \frac{\mathcal{R}_a (C_P - C_V)}{C_V} \frac{f f_{02}}{f^2 + f_{02}^2} \tag{5.13}$$

where $\mathcal{R}_a$ is the anisotropy factor, C_P and C_V are specific heat at constant pressure and volume. Here f_{02} is given as

$$f_{02} \approx \frac{3\pi}{2} \frac{\chi}{a^2 C_V} \tag{5.14}$$

The thermal conduction absorption α_{tc} has similar dependence on f and can be given as [125]

$$\alpha_{tc} = \pi \left(\frac{V^2}{V_0^2} \right) \left(\frac{M_S - M_Y}{M_T} \right) \frac{f f_{03}}{f^2 + f_{03}^2} \tag{5.15}$$

where V is the acoustic velocity at the current frequency, V_0 is the velocity at zero frequency, M_S and M_T are the combinations of the elastic constants under adiabatic and isothermal conditions, and f_{03} is the frequency where α_{tc} reaches maximum and it is given as

$$f_{03} = \frac{1}{2\pi} \left(\frac{C_V V^2}{\chi} \right) \frac{M_S}{M_T} \tag{5.16}$$

The scattering coefficient α_s depends on the ratio of the grain or inclusion size a to the wavelength λ and the functional dependence of scattering losses on frequency can be expressed as [121, 148]

$$\alpha_s \propto \begin{cases} a^3 \cdot f^4, & Rayleigh\ region\ \dfrac{2\pi a}{\lambda} \ll 1 \\[2mm] a \cdot f^2, & Stochastic\ region\ \dfrac{2\pi a}{\lambda} \approx 1 \\[2mm] \dfrac{1}{a}, & Diffusive\ region\ \dfrac{2\pi a}{\lambda} \gg 1 \end{cases} \tag{5.17}$$

Typically the scattering is of the Rayleigh type when $\lambda > 8 \sim 10a$ [125]. Based on the absorption and scattering equations above, the idealized attenuation coefficient may have the shape shown in Figure 5-12, where there are three regions: the increasing region caused by the absorption loss before f_0 (denoted as Region I), the decreasing region after f_0 (Region II), and the increasing region dominated by the scattering loss (Region III). It will be used to explain the attenuation results of the A206/A206-Al$_2$O$_3$ nanocomposites as follows.
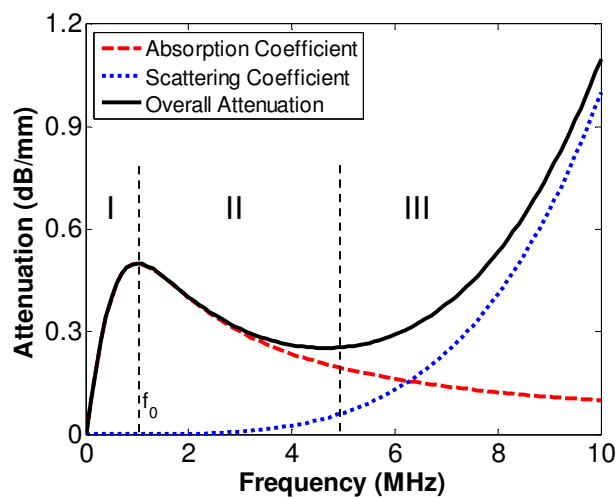
Figure 5-12: Idealized attenuation coefficient identifying absorption and scattering dominant regions based on theoretical models

Figure 5-13 shows the average ultrasonic attenuations of these five samples measured using these two selected transducers. In the frequency range of 2~2.5 MHz, the attenuation of the pure A206 with/without ultrasonic treatment (UT) decreases with increasing frequency, which corresponds to Region II in Figure 5-12 and indicates that the absorption losses dominate the attenuation in this low frequency range. Similar decreasing trend of attenuation has also been reported on the cement-based materials in the low frequency range [129]. As for the scattering loss, since the wavelength is about 2.5mm~3.16mm (wave speed 6320m/s), there may exist both Rayleigh scattering and stochastic scattering.
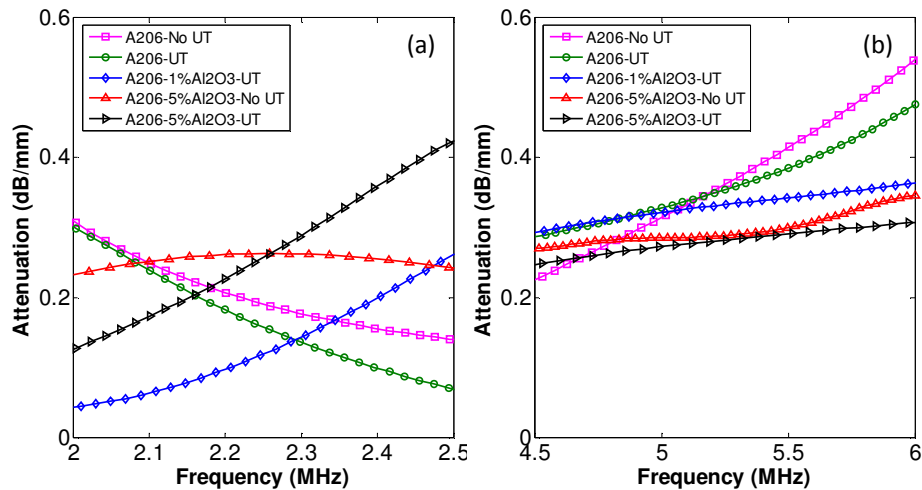
Figure 5-13: The average ultrasonic attenuation as a function of frequency measured using transducer with nominal central frequency 2.25MHz; (b) transducer with nominal central frequency 5MHz.

For both A206-1% Al_2O_3 and A206-5% Al_2O_3 nanocomposites with ultrasonic treatment, the attenuation increases with frequency. One possible reason is that as the grain size decreases, f_0 increases since $f_0 \propto \frac{1}{a^2}$ as described in Eq. (5.12) and (5.14). The frequency range lies in the Region I of Figure 5-12 and the absorption increases with the increasing of frequency. The

attenuation of A206-1% Al_2O_3 is higher than A206-5% Al_2O_3 with ultrasonic treatment. The possible reason is that a large amount of Al_2O_3 particles increases the absorption losses. For these two samples, the Rayleigh scattering dominates due to the significant reduction of grain sizes. For A206-5% Al_2O_3 without ultrasonic treatment, the attenuation is much more complex due to the clusters of nanoparticles and the attenuation is essentially flat.

In the frequency range of 4.5~6 MHz, the attenuation for all samples increases with increasing frequencies, as shown in Figure 5-13 (b). In this frequency range, the attenuation is dominated by the scattering losses (Region III in Figure 5-12) and the absorption losses may be negligible. The A206-5% Al_2O_3 with ultrasonic treatment has the lowest attenuations while the pure A206 w/o UT have the largest attenuations in the high frequency range. The attenuations of A206-1% Al_2O_3 with UT and A206-5% Al_2O_3 without UT lie between the two extreme cases. The results are consistent with what we expected since the attenuations are dominated by the scattering along the grain boundaries at high frequency range and increasing the grain size could increase the scattering effects.

5.4 Conclusion and Discussion

In this chapter, we propose a new method to evaluate the microstructures of MMNCs using ultrasonic nondestructive detection methods. We have two main findings in this work: (1) Due to the large primary dendrites, long continuous intermetallic phase and unevenly distributed Al_2O_3 nanoparticles, the acoustic attenuations will be non-uniform at different locations of the same sample of A206-Al_2O_3 MMNC. As a result, the variance of the acoustic attenuation could be used as an indicator of the microstructure of MMNCs. A statistical hypothesis test based on the

estimated variance is constructed and through this test, we can tell the quality of microstructure refinement of the A206-Al_2O_3 MMNCs. (2) The functional form of the average attenuation at different frequencies is also highly related with the microstructures of MMNCs. For the pure A206, the attenuation function decreases with increasing frequencies at low frequency range where the absorption mechanism dominates the attenuation losses. For the A206-Al_2O_3 nanocomposites, the average attenuation increases with frequencies in the low frequency range. In the high frequency range, the attenuation curves for all samples have increasing trend and the samples with smaller grain sizes have lower attenuations due to the reduced scattering losses. These results provide useful insight and promising tools on using ultrasonic non-destructive testing techniques to examine the quality of A206-Al_2O_3 nanocomposites.

6 Bayesian Hierarchical Linear Modeling of Ultrasonic Attenuation Profiles with Heterogeneous Level-2 Variances in the Production of A206-Al$_2$O$_3$ Nanocomposites[*]

6.1 Introduction

In Chapter 5, we found that well-dispersed samples with more homogeneous microstructures (i.e., smaller grain size, thinner and less continuous Al$_2$Cu intermetallic phase, and well dispersed Al$_2$O$_3$ nanoparticles) have lower between-curve variation of attenuations measured at randomly selected locations, as shown in Figure 5-6 (c) and (e). This phenomenon has also been observed by Liu *et al* [149] through microstructural modelling and wave propagation simulation approach. The attenuation profiles from both experiment and physical simulation have the following characteristics: (1) the attenuation linearly increases with frequency for each profile in a selected frequency range; (2) for each nanocomposite sample, the attenuation profiles can be well modelled using linear mixed-effects model (LME) where each profile can be modeled by polynomials and the coefficients of the polynomials follow normal distribution; (3) the mean and variance of the polynomial coefficients vary across samples with different microstructural quality.

---

[*] This chapter is based on the paper: **Jianguo Wu**, Yuhang Liu, Shiyu Zhou, "Bayesian Hierarchical Linear Modeling of Ultrasonic Attenuation Profiles with Heterogeneous Level-2 Variances in the Scale-up Production of A206-Al$_2$O$_3$ Nanocomposites", *(to be submitted)*

To capture the above mentioned characteristics, we propose a hierarchical linear model (HLM), or specifically a two-level model, with heterogeneous level-2 variances in modelling of the attenuation profiles. There are three parts in the proposed model: (1) the attenuation is modeled as a linear function of ultrasonic frequency in level-1; (2) the coefficients in level-1 are modeled as linear functions of the microstructural parameters in level-2 with diagonal residual covariance matrix; (3) the residual variances in level-2 are modeled as log-linear functions of the microstructural parameters. Note that the model with only the first two parts is a hierarchical linear model, which is a variant term for multilevel model or for what are broadly called LME model. In this chapter, we use the term HLM instead of LME to differentiate the new model from the common LME model used in [150]. The third part of the proposed model is an embedded variance regression to characterize the heterogeneity of the coefficient variance under different microstructures. Therefore our model can capture not only the within and between-profile variations for a specific microstructure, but also the variations across different microstructures. The purpose of this study is twofold, (1) to establish a general methodology to incorporate underlying relevant parameters, e.g., microstructural parameters, into the profile modelling, (2) to ultimately infer the microstructural parameters based on the established model for simultaneous profile monitoring and diagnosis in quality control. Note that compared with the traditional LME model based profile modeling and monitoring [150, 151], our model has the advantage of directly relating the qualitative parameters with profiles and diagnosing the qualitative parameters.

HLM has been widely used to model hierarchically structured data in the biomedical and social research [152, 153]. Extensions of the HLM with heterogeneous within-profile noise

variances (e.g., residual variance in level-1 model) have also been intensively studied [154-156]. However, there is very limited work on modeling heterogeneous variances for random effects. For the standard HLM, model parameters can be estimated using two general methods, the maximum likelihood (ML) and the restricted maximum likelihood (REML) [157]. However, these methods cannot be directly applied to the proposed model, as the addition of the log-linear model makes the optimization much more complicated. In this chapter, we propose to estimate the model using the Markov chain Monte Carlo (MCMC) simulation under the Bayesian framework. This approach can not only efficiently estimate the model parameters, but also provide another two benefits, one being the model selection (e.g., determining the degree of polynomial, which coefficient is random) which is critically important in model building, and the other one being the Bayesian inference of microstructural parameters based on newly observed attenuation profiles, which is our ultimate goal in profile monitoring and diagnosis for quality control.

The remainder of this chapter is organized as follows. In Section 6.2 the new HLM with heterogeneous variances is formulated. The MCMC estimation of model parameters and model selection are given in Section 6.3 and Section 6.4 respectively. Section 6.5 evaluates the performance of model selection and estimation through numerical simulations. Section 6.6 presents the case study where the proposed model is applied to the ultrasonic attenuation profiles of MMNCs. The conclusions and discussions are given in Section 6.7.

6.2 Two-level Hierarchical Linear Model with Heterogeneous Level-2 Variances

Sample 1 $(\boldsymbol{\theta}_1)$ $\cdots\cdots$ Sample m $(\boldsymbol{\theta}_m)$

Profile 1 $(\boldsymbol{y}_{11})$ $\cdots$ Profile l $(\boldsymbol{y}_{1l})$ $\cdots\cdots$ Profile 1 $(\boldsymbol{y}_{m1})$ $\cdots$ Profile l $(\boldsymbol{y}_{ml})$

Obs. 1 (y_{111}) $\cdots$ Obs. n (y_{11n}) $\cdots\cdots$ Obs. 1 (y_{ml1}) $\cdots$ Obs. n (y_{mln})
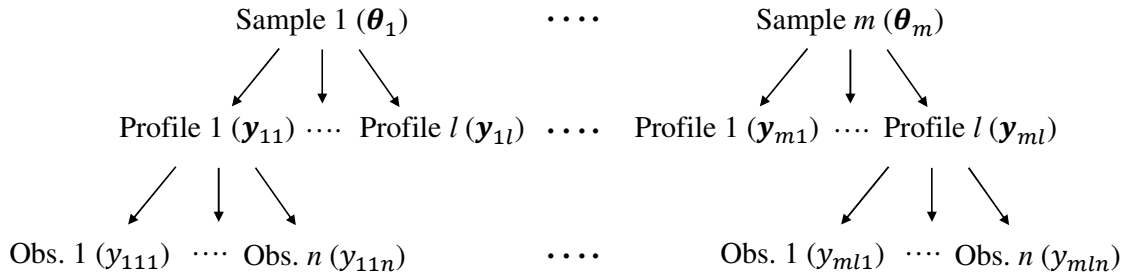
Figure 6-1: Illustration of the hierarchical data structure.

Figure 6-1 shows the hierarchical data structure. Suppose the data are obtained from m samples of different microstructures, where each sample was measured multiple times using ultrasonic testing at randomly selected locations on the polished surface. For each measurement we obtain one attenuation profile, which is the attenuation coefficient as function of ultrasonic frequency. Without loss of generosity, we assume that each sample has l attenuation profiles and each profile has n observations at the same frequencies. Let $\boldsymbol{\theta}_i$ denote the microstructural parameters of the i-th sample, $\boldsymbol{y}_{ij}$ be the j-th profile of sample i, and x_k be the k-th frequency. The hierarchical linear model with heterogeneous level-2 variances is defined as follows:

Level-1:

$$y_{ijk} = \boldsymbol{h}_1'(x_k)\boldsymbol{\alpha}_{ij} + \epsilon_{ijk} \tag{6.1}$$

where $i = 1, \dots, m$ is the index of samples, $j = 1, \dots, l$ is the index of profiles, and $k = 1, \dots, n$ is the index of frequencies, $\boldsymbol{h}_1(x)$ is a vector of p explanatory variables at x, e.g., $\boldsymbol{h}_1(x) =$

$(x^2, x, 1)'$ for quadratic polynomial, $\boldsymbol{\alpha}_{ij}$ is a $p \times 1$ vector of regression coefficients, and ϵ_{ijk} is the within-profile error which follows i.i.d. Gaussian distribution, $\epsilon_{ijk} \sim N(0, \sigma_\epsilon^2)$. We assume a homogeneous within-profile variance, as all profiles are smooth with very small random errors.

Level-2:

$$\boldsymbol{\alpha}_{ij} = \boldsymbol{H}_2(\boldsymbol{\theta}_i)\boldsymbol{\beta} + \boldsymbol{\xi}_{ij} \tag{6.2}$$

where $\boldsymbol{H}_2(\boldsymbol{\theta}_i) = \boldsymbol{I}_p \otimes \boldsymbol{h}_2^T(\boldsymbol{\theta}_i)$ is a $p \times pq$ matrix ($\otimes$: Kronecker product operator), $\boldsymbol{h}_2(\boldsymbol{\theta}_i)$ is a $q \times 1$ vector of q explanatory variables, $\boldsymbol{\beta} = (\boldsymbol{\beta}_1', \dots, \boldsymbol{\beta}_p')'$ with $\boldsymbol{\beta}_d$ being a $q \times 1$ vector of regression coefficients for d-th component of $\boldsymbol{\alpha}$, and $\boldsymbol{\xi}_{ij}$ is the error term, which is a random vector following i.i.d. p-dimensional Gaussian distribution for each i:

$$\boldsymbol{\xi}_{ij} \sim N(\boldsymbol{0}, \boldsymbol{\Sigma}_i) \tag{6.3}$$

Submodel (6.2) is used to model the dependence of coefficients in Submodel (6.1) on the sample parameter $\boldsymbol{\theta}$ by the mean term, and to account for correlation among observations within the same profile by the error term. Combining (6.1) and (6.2) we obtain the general LME model as

$$\boldsymbol{y}_{ij} = \boldsymbol{H}_1(\boldsymbol{x})\boldsymbol{H}_2(\boldsymbol{\theta}_i)\boldsymbol{\beta} + \boldsymbol{H}_1(\boldsymbol{x})\boldsymbol{\xi}_{ij} + \boldsymbol{\epsilon}_{ij} \tag{6.4}$$

where $\boldsymbol{y}_{ij} = (y_{ij1}, \dots, y_{ijn})'$, $\boldsymbol{x} = (x_1, \dots, x_n)'$, $\boldsymbol{H}_1(\boldsymbol{x}) = (\boldsymbol{h}_1(x_1), \dots, \boldsymbol{h}_1(x_n))'$, and $\boldsymbol{\epsilon}_{ij} \sim N(\boldsymbol{0}, \sigma_\epsilon^2 \boldsymbol{I}_n)$.

Heterogeneous Level-2 Variances:

To model the variance heterogeneity, we assume the covariance matrix $\boldsymbol{\Sigma}_i$ in Eq. (6.3) is dependent on the sample parameter $\boldsymbol{\theta}$, which is modeled as

$$\boldsymbol{\Sigma}_i = \text{diag}\big(\sigma_1^2(\boldsymbol{\theta}_i), \dots, \sigma_p^2(\boldsymbol{\theta}_i)\big)$$

$$\log \sigma_d^2 = \boldsymbol{h}_3(\boldsymbol{\theta})^{'} \boldsymbol{\gamma}_d + \delta_d, d = 1,2,\dots,p \qquad (6.5)$$

where $\boldsymbol{h}_3(\boldsymbol{\theta})$ is a $r \times 1$ vector of explanatory variables, $\boldsymbol{\gamma}_d$ is a $r \times 1$ vector of coefficients, and $\delta_d \sim N(0, \sigma_{\delta_d}^2)$. This part is used to model the heterogeneity of residual variance in Eq. (6.2). The log-linear model is commonly used in variance function regression or heteroscedastic regression [158, 159]. In these studies, however, the error term δ_d is often neglected. In this research, we add the error term to make the model more flexible.

In the proposed model, level-1 is to model each individual profile or within-profile variations, level-2 is to model both the model heterogeneity across different samples and the between-profile variations within each sample, and the log-linear model is to capture the heterogeneity of residual variance of the level-2 model. After the new model is proposed, the remaining issues are how to efficiently estimate the model parameters and how to accurately select the right models among a set of candidate ones. In the model estimation, the parameters of interest include the fixed effects $\boldsymbol{\beta}$, within-profile error term variance σ_ϵ^2, variance component regression coefficients $\{\boldsymbol{\gamma}_d, d = 1, \dots, p\}$ and the error term variances $\{\sigma_{\delta_d}^2, d = 1, \dots, p\}$. Denote $\boldsymbol{\psi} = \big\{\boldsymbol{\beta}, \sigma_\epsilon^2, \{\boldsymbol{\gamma}_d\}, \{\sigma_{\delta_d}^2\}\big\}$. The likelihood function for the model can be expressed by integrating out nuisance parameters, which include all unobservable random effects $\boldsymbol{\xi} = \{\boldsymbol{\xi}_{ij}, i = 1, \dots, m, j = 1, \dots, l\}$ and variance components $\boldsymbol{\sigma}_\xi^2 = \{\sigma_d^2(\boldsymbol{\theta}_i), i = 1, \dots, m, d = 1, \dots, p\}$, as

$$L(\boldsymbol{\psi}|\boldsymbol{Y}) = \int f(\boldsymbol{Y}|\boldsymbol{\psi},\boldsymbol{\xi},\sigma_\xi^2)\, f(\boldsymbol{\xi}|\sigma_\xi^2,\boldsymbol{\psi}) f(\sigma_\xi^2|\boldsymbol{\psi}) d\sigma_\xi^2 d\boldsymbol{\xi} \tag{6.6}$$

where $\boldsymbol{Y}$ is the vector of all observations, $\boldsymbol{Y} = (\boldsymbol{y}'_{11}, \boldsymbol{y}'_{12}, \dots, \boldsymbol{y}'_{1l}, \dots, \boldsymbol{y}'_{ml})'$. Eq. (6.6) involves high dimensional integration and is not analytically tractable, which makes the maximum likelihood estimation very challenging. In this research, we propose to estimate the model parameters under the Bayesian framework. The posterior distribution of the models parameters are approximated using blocked Gibbs sampling method, which will be given in detail in the next section. Another issue in model building is the model selection, where the predictor variables, or the degrees of polynomials if polynomial regression is used, for all three submodels have to be determined. The detailed model selection process will be given in Section 6.4.

6.3 Bayesian Model Estimation using Blocked Gibbs Sampler

6.3.1 Blocked Gibbs Sampling for Posterior Estimation

Under the Bayesian framework, the model estimation is to calculate the posterior distribution of model parameters conditioning on observations. Once the posterior is obtained, we can either use the mean or median of the posterior as the point estimates of model parameters, or directly use the posterior distribution for future model estimation and inference. In this research, the posterior distribution of interest is $P(\boldsymbol{\psi}|\boldsymbol{Y}) = P(\boldsymbol{\beta}, \sigma_\epsilon^2, \{\boldsymbol{\gamma}_d\}, \{\sigma_{\delta_d}^2\}|\boldsymbol{Y})$. As the nuisance parameters, i.e. random effects $\boldsymbol{\xi} = \{\boldsymbol{\xi}_{ij}, i = 1, \dots, m, j = 1, \dots, l\}$ and variance components $\boldsymbol{\sigma}_\xi^2 = \{\sigma_d^2(\boldsymbol{\theta}_i), i = 1, \dots, m, d = 1, \dots, p\}$ are not observable, the join posterior distribution including all nuisance parameters need to be found and the posterior of interest can be obtained by marginalizing out all nuisance parameters. The joint posterior distribution is written as

$$P\left(\boldsymbol{\beta}, \sigma_\epsilon^2, \{\boldsymbol{\gamma}_d\}, \{\sigma_{\delta_d}^2\}, \xi, \boldsymbol{\sigma}_\xi^2 \middle| Y\right) \tag{6.7}$$

Since the joint posterior is not analytically tractable, it cannot be directly sampled. Gibbs sampling [160, 161] is one of the most popular Markov Chain Monte Carlo (MCMC) methods to estimate hierarchical models by generating sequence of random samples that approximately follow the target posterior distribution. The basic idea is to repeatedly replace the value of each component with a sample from its distribution conditioning on the current values of all other components. The blocked Gibbs sampler [162] is a more efficient version of Gibbs sampler, where the variables are grouped into blocks, and each entire block is sampled from its conditional distribution given the other components. In this study, we propose to use a blocked Gibbs sampler to draw samples from the joint conditional posterior distribution. For the standard Bayesian LME model all conditional distributions can be directly sampled [150]. However, due to the log-linear heterogeneity variance regression, the nuisance parameters $\boldsymbol{\sigma}_\xi^2$ in our model cannot be directly sampled through their conditional distributions. To overcome this problem we propose a Metropolis-Hastings [163] algorithm to sample $\boldsymbol{\sigma}_\xi^2$ in the blocked Gibbs sampling process.

In the sampling procedure, the parameters including those of interest and nuisance parameters can be divided into 4 groups as follows:

G1: The fixed effects $\boldsymbol{\beta}$ and within-profile variance of random error σ_ϵ^2

G2: The random effects $\boldsymbol{\xi} = \{\boldsymbol{\xi}_{ij}, i = 1, \dots, m, j = 1, \dots, l\}$

G3: The variance components $\boldsymbol{\sigma}_\xi^2 = \{\sigma_d^2(\boldsymbol{\theta}_i), i = 1, \dots, m, d = 1, \dots, p\}$

G4: The variance heterogeneity regression coefficients $\{\boldsymbol{\gamma}_d, d = 1, \dots, p\}$ and variance of random error $\{\sigma_{\delta_d}^2, d = 1, \dots, p\}$

The Gibbs sampling procedure can be summarized using the following steps:

Step 1: Sampling G1 parameters from their conditional posterior distribution

$$P\big(\boldsymbol{\beta}, \sigma_\epsilon^2 \big| \{\boldsymbol{\gamma}_d\}, \{\sigma_{\delta_d}^2\}, \boldsymbol{\xi}, \boldsymbol{\sigma}_\xi^2, \boldsymbol{Y}\big) = P\big(\boldsymbol{\beta}, \sigma_\epsilon^2 | \boldsymbol{\xi}, \boldsymbol{Y}\big)$$

Step 2: Sampling G2 parameters from their conditional posterior distribution

$$P\big(\boldsymbol{\xi} \big| \boldsymbol{\beta}, \sigma_\epsilon^2, \{\boldsymbol{\gamma}_d\}, \{\sigma_{\delta_d}^2\}, \boldsymbol{\sigma}_\xi^2, \boldsymbol{Y}\big) = P\big(\boldsymbol{\xi} | \boldsymbol{\beta}, \sigma_\epsilon^2, \boldsymbol{\sigma}_\xi^2, \boldsymbol{Y}\big)$$

Step 3: Sampling G3 parameters from their conditional posterior distribution

$$P\big(\boldsymbol{\sigma}_\xi^2 \big| \boldsymbol{\beta}, \sigma_\epsilon^2, \{\boldsymbol{\gamma}_d\}, \{\sigma_{\delta_d}^2\}, \boldsymbol{\xi}, \boldsymbol{Y}\big) = P\big(\boldsymbol{\sigma}_\xi^2 \big| \{\boldsymbol{\gamma}_d\}, \{\sigma_{\delta_d}^2\}, \boldsymbol{\xi}\big)$$

Step 4: Sampling G4 parameters from their conditional posterior distribution

$$P\big(\{\boldsymbol{\gamma}_d\}, \{\sigma_{\delta_d}^2\} \big| \boldsymbol{\beta}, \sigma_\epsilon^2, \boldsymbol{\sigma}_\xi^2, \boldsymbol{\xi}, \boldsymbol{Y}\big) = P\big(\{\boldsymbol{\gamma}_d\}, \{\sigma_{\delta_d}^2\} \big| \boldsymbol{\sigma}_\xi^2\big)$$

By iteratively drawing samples from the conditional posterior distributions in the above four steps, a sequence of samples will be obtained, which constitutes a Markov chain with the stationary distribution following the join posterior distribution of interest. Note that in Step 1 and Step 4 the regression coefficient and the random error variance are sampled together from the join conditional posterior distribution, which is more efficient than sampling from each one individually, e.g., sampling from $P(\boldsymbol{\beta} | \sigma_\epsilon^2, \boldsymbol{\xi}, \boldsymbol{Y})$ and $P(\sigma_\epsilon^2 | \boldsymbol{\beta}, \boldsymbol{\xi}, \boldsymbol{Y})$. The following subsections will discuss the prior specification which is critical in the Bayesian model fitting, and present the detailed conditional posterior distribution for blocked Gibbs sampling.

6.3.2 Specification of Priors

In the Bayesian analysis of the proposed model, the priors for the mean parameters $\boldsymbol{\beta}$, and $\{\boldsymbol{\gamma}_d, d = 1, \dots, p\}$, and variance parameters σ_ϵ^2 and $\{\sigma_{\delta_d}^2, d = 1, \dots, p\}$ need to be specified. For the mean parameters, normal priors and noninformative priors are most commonly used in the Bayesian linear regression [160]. The normal priors often provide the benefit of conjugacy in simple linear regression or conditional conjugacy, i.e., conjugate prior conditioning on other model parameters, in hierarchical linear regression. However, in most cases the prior information beyond the data is not available, and thus noninformative prior is more preferred, which provides both objectiveness and convenience in Bayesian analysis. In this research, we specify the noninformative priors for $\boldsymbol{\beta}$ and $\{\boldsymbol{\gamma}_d, d = 1, \dots, p\}$ as

$$\pi(\boldsymbol{\beta}) \propto 1$$

$$\pi(\boldsymbol{\gamma}_d) \propto 1, d = 1, \dots, p$$

(6.8)

For the variance components, there is a lot of literature discussing how to select appropriate priors [150, 161, 164]. Two types of priors have been widely used, the noninformative prior of the form

$$\pi(\sigma^2) \propto (\sigma^2)^{-(a+1)}$$

(6.9)

and the weakly-informative inverse gamma prior

$$\pi(\sigma^2) \propto IG(\omega, \omega)$$

(6.10)

In the noninformative prior, $a = 0$ corresponds to a uniform prior on $\log \sigma$, i.e., $\pi(\log \sigma) \propto 1$, or equivalently $\pi(\sigma) \propto 1/\sigma$. $a = -1/2$ corresponds to a uniform prior on σ, i.e., $\pi(\sigma) \propto 1$. $a = -1$ corresponds to a uniform prior on σ^2. For the weakly-informative prior, the inverse-gamma distribution is within the conditionally conjugate family, with ω set to a low value, e.g., 1, 0.1 or 0.001. Zeng *et al* [150] used the weekly-informative prior for the variance components of the random effects in LME model to facilitate the computation in model selection. However, Gelman [164] showed that the inferences become very sensitive to ω for datasets in which low values of random effects variance are possible, and the prior distribution hardly looks noninformative. In this research, we select the noninformative priors for both σ_ϵ^2 and $\{\sigma_{\delta_d}^2, d = 1, \ldots, p\}$ for convenience and objectiveness:

$$\pi(\sigma_\epsilon^2) \propto 1$$

$$\pi(\sigma_{\delta_d}^2) \propto 1, d = 1, \ldots, p$$

(6.11)

6.3.3 Conditional Posterior Distributions for Gibbs Sampling

This subsection will show the conditional posterior distributions corresponding to the four steps in Subsection 6.3.1 for Gibbs sampling. The Metropolis-Hastings algorithm used in Step 3 will also be proposed.

(1) $P\left(\beta, \sigma_\epsilon^2 \middle| \{\gamma_a\}, \{\sigma_{\delta_d}^2\}, \xi, \sigma_\xi^2, Y\right) = P(\beta, \sigma_\epsilon^2 | \xi, Y)$

Let H be the stack of $\{H_1(x)H_2(\theta_i)\}$, Ξ be the stack of $\{H_1(x)\xi_{ij}\}$, and E be the stack of $\{\epsilon_{ij}\}$,

$$H = \begin{bmatrix} H_1(x)H_2(\theta_1) \\ H_1(x)H_2(\theta_1) \\ \vdots \\ H_1(x)H_2(\theta_1) \\ H_1(x)H_2(\theta_2) \\ \vdots \\ H_1(x)H_2(\theta_2) \\ \vdots \\ H_1(x)H_2(\theta_m) \end{bmatrix}, \Xi = \begin{bmatrix} H_1(x)\xi_{11} \\ H_1(x)\xi_{12} \\ \vdots \\ H_1(x)\xi_{1l} \\ H_1(x)\xi_{21} \\ \vdots \\ H_1(x)\xi_{2l} \\ \vdots \\ H_1(x)\xi_{ml} \end{bmatrix}, E = \begin{bmatrix} \epsilon_{11} \\ \epsilon_{12} \\ \vdots \\ \epsilon_{1l} \\ \epsilon_{21} \\ \vdots \\ \epsilon_{2l} \\ \vdots \\ \epsilon_{ml} \end{bmatrix}$$

Then

$$Y - \Xi = H\beta + E \tag{6.12}$$

where $\pi(\beta) \propto 1$, $E \sim N(0, \sigma_\epsilon^2 I_{mln})$ and $\pi(\sigma_\epsilon^2) \propto 1$. Given $\{\xi_{ij}, i = 1, \dots, m, j = 1, \dots, l\}$ or Ξ, Eq.

(6.12) is a simple linear model. The joint conditional posterior distribution can be written as

$$P(\beta, \sigma_\epsilon^2 | \xi, Y) = P(\sigma_\epsilon^2 | \xi, y) P(\beta | \xi, \sigma_\epsilon^2, Y)$$

It can be easily proven that [160]

$$\sigma_\epsilon^2 | (\xi, Y) \sim IG\left(\frac{mnl - 2}{2}, \frac{(Y - H\hat{\beta} - \Xi)^{'}(Y - H\hat{\beta} - \Xi)}{2}\right) \tag{6.13}$$

$$\beta | \{\sigma_\epsilon^2, \xi, Y\} \sim N\left(\hat{\beta}, \sigma_\epsilon^2 \left(H^{'} H\right)^{-1}\right)$$

where

$$\hat{\beta} = (H'H)^{-1}H'(Y - \Xi)$$

(2) $P(\xi | \beta, \sigma_\epsilon^2, \{\gamma_d\}, \{\sigma_{\delta_d}^2\}, \sigma_\xi^2, Y) = P(\xi | \beta, \sigma_\epsilon^2, \sigma_\xi^2, Y)$

Given all other parameters, the random effects $\{\boldsymbol{\xi}_{ij}, i = 1, \ldots, m, j = 1, \ldots, l\}$ are independent.

Therefore they can be sampled individually. The distribution for each component $\boldsymbol{\xi}_{ij}$ is

$$P\left(\boldsymbol{\xi}_{ij}|\boldsymbol{\beta}, \sigma_\epsilon^2, \boldsymbol{\sigma}_\xi^2 \boldsymbol{Y}\right) = P\left(\boldsymbol{\xi}_{ij}|\boldsymbol{\beta}, \sigma_\epsilon^2, \boldsymbol{\Sigma}_i, \boldsymbol{y}_{ij}\right)$$

$$\propto \pi\left(\boldsymbol{\xi}_{ij}|\boldsymbol{\Sigma}_i\right)P\left(\boldsymbol{y}_{ij}|\boldsymbol{\beta}, \sigma_\epsilon^2, \boldsymbol{\xi}_{ij}\right) = N\left(\boldsymbol{\xi}_{ij}|\boldsymbol{0}, \boldsymbol{\Sigma}_i\right) \cdot N\left(\boldsymbol{y}_{ij}|\boldsymbol{H}_1(\boldsymbol{x})\boldsymbol{H}_2(\boldsymbol{\theta}_i)\boldsymbol{\beta} + \boldsymbol{H}_1(\boldsymbol{x})\boldsymbol{\xi}_{ij}, \sigma_\epsilon^2\boldsymbol{I}_n\right)$$

It can be shown that the conditional posterior distribution of $\boldsymbol{\xi}_{ij}$ follows multivariate normal distribution [118]:

$$\boldsymbol{\xi}_{ij}|\boldsymbol{\beta}, \sigma_\epsilon^2, \boldsymbol{\Sigma}_i, \boldsymbol{y}_{ij} \sim N\left(\hat{\boldsymbol{\xi}}_{ij}, \hat{\boldsymbol{\Sigma}}_i\right), i = 1, \ldots, m, j = 1, \ldots, l \qquad (6.14)$$

where

$$\hat{\boldsymbol{\xi}}_{ij} = \left[\boldsymbol{H}_1'\boldsymbol{H}_1 + \sigma_\epsilon^2\boldsymbol{\Sigma}_i^{-1}\right]^{-1}\left(\boldsymbol{H}_1'\left(\boldsymbol{y}_{ij} - \boldsymbol{H}_1(\boldsymbol{x})\boldsymbol{H}_2(\boldsymbol{\theta}_i)\boldsymbol{\beta}\right)\right)$$

$$\hat{\boldsymbol{\Sigma}}_i = \sigma_\epsilon^2\left[\boldsymbol{H}_1'\boldsymbol{H}_1 + \sigma_\epsilon^2\boldsymbol{\Sigma}_i^{-1}\right]^{-1}$$

(3) $P\left(\boldsymbol{\sigma}_\xi^2|\boldsymbol{\beta}, \sigma_\epsilon^2, \{\boldsymbol{\gamma}_d\}, \{\sigma_{\delta_d}^2\}, \boldsymbol{\xi}, \boldsymbol{Y}\right) = P\left(\boldsymbol{\sigma}_\xi^2|\{\boldsymbol{\gamma}_d\}, \{\sigma_{\delta_d}^2\}, \boldsymbol{\xi}\right)$

Given all other parameters, the variance components $\boldsymbol{\sigma}_\xi^2 = \{\sigma_d^2(\boldsymbol{\theta}_i), i = 1, \ldots, m, d = 1, \ldots, p\}$ are independent, which can be sampled individually. In this research, we sample p components $\{\sigma_d^2(\boldsymbol{\theta}_i), d = 1, \ldots, p\}$ simultaneously each time for the purpose of convenience. Let $\eta_{id} = \log\left(\sigma_d^2(\boldsymbol{\theta}_i)\right)$, $\boldsymbol{\eta}_i = (\eta_{i1}, \ldots, \eta_{ip})'$, $\boldsymbol{H}_3(\boldsymbol{\theta}_i) = \boldsymbol{I}_p \otimes \boldsymbol{h}_3^T(\boldsymbol{\theta}_i)$, $\boldsymbol{\gamma} = \left(\boldsymbol{\gamma}_1', \ldots, \boldsymbol{\gamma}_p'\right)'$, then

$$\boldsymbol{\eta}_i = \boldsymbol{H}_3(\boldsymbol{\theta}_i)\boldsymbol{\gamma} + \boldsymbol{\delta}$$

where $\boldsymbol{\delta} = \left(\delta_1, \dots, \delta_p \right)' \sim N(0, \text{diag}(\{\sigma_{\delta_d}^2, d = 1, \dots, p\}))$. The conditional posterior of $\boldsymbol{\eta}_i$ is

$$P\left(\boldsymbol{\eta}_i \middle| \{\boldsymbol{\xi}_{ij}, j = 1,2, \dots, l\}, \{\sigma_{\delta_d}^2\}, \boldsymbol{\gamma}\right) \propto P\left(\boldsymbol{\eta}_i \middle| \{\sigma_{\delta_d}^2\}, \boldsymbol{\gamma}\right) P\left(\{\boldsymbol{\xi}_{ij}, j = 1,2, \dots, l\} \middle| \boldsymbol{\eta}_i\right) \tag{6.15}$$

where

$$\left(\boldsymbol{\eta}_i \middle| \{\sigma_{\delta_d}^2, d = 1, \dots, p\}, \boldsymbol{\gamma}\right) \sim N\left(\boldsymbol{H}_3(\boldsymbol{\theta}_i)\boldsymbol{\gamma}, \text{diag}(\{\sigma_{\delta_d}^2, d = 1, \dots, p\})\right)$$

and

$$P\left(\{\boldsymbol{\xi}_{ij}, j = 1,2, \dots, l\} \middle| \boldsymbol{\eta}_i\right) \propto \left(\prod\nolimits_{d=1}^{p} \exp(\eta_{id})\right)^{-\frac{l}{2}} \exp\left(-\frac{1}{2}\sum_{j=1}^{l} \boldsymbol{\xi}_{ij}' \boldsymbol{\Sigma}_i^{-1} \boldsymbol{\xi}_{ij}\right)$$

Since the conditional posterior in Eq. (6.15) cannot be sampled directly, we propose the Metropolis-Hastings algorithm as follows. At each iteration step t in the Gibbs sampling, we propose a new value for $\boldsymbol{\eta}_i$ using a symmetric normal proposal distribution centered at the current value as

$$\boldsymbol{\eta}_i^* = \boldsymbol{\eta}_i^{(t-1)} + N(\boldsymbol{0}, \Delta^2 \boldsymbol{I}_p) \tag{6.16}$$

where $\boldsymbol{\eta}_i^{(t-1)}$ is as sample of $\boldsymbol{\eta}_i$ at step $t - 1$, Δ is the step-width of the random walk or the standard deviation of the proposal distribution.

The Metropolis-Hastings acceptance ratio is given by

$$r_a = \min\left\{1, \frac{P\left(\boldsymbol{\eta}_i^* \middle| \{\sigma_{\delta_d}^2\}^{(t-1)}, \boldsymbol{\gamma}^{(t-1)}\right) P\left(\{\boldsymbol{\xi}_{ij}^{(t)}, j = 1,2,\dots,l\} \middle| \boldsymbol{\eta}_i^*\right)}{P\left(\boldsymbol{\eta}_i^{(t-1)} \middle| \{\sigma_{\delta_d}^2\}^{(t-1)}, \boldsymbol{\gamma}^{(t-1)}\right) P\left(\{\boldsymbol{\xi}_{ij}^{(t)}, j = 1,2,\dots,l\} \middle| \boldsymbol{\eta}_i^{(t-1)}\right)}\right\} \tag{6.17}$$

Set $\boldsymbol{\eta}_i^{(t)} = \boldsymbol{\eta}_i^*$ with probability r_a, otherwise set $\boldsymbol{\eta}_i^{(t)} = \boldsymbol{\eta}_i^{(t-1)}$.

(4) $P\left(\{\boldsymbol{\gamma}_d\}, \{\sigma_{\delta_d}^2\} \middle| \boldsymbol{\beta}, \sigma_\epsilon^2, \sigma_\xi^2, \boldsymbol{\xi}, \boldsymbol{Y}\right) = P\left(\{\boldsymbol{\gamma}_d\}, \{\sigma_{\delta_d}^2\} \middle| \sigma_\xi^2\right)$

Since $\left(\boldsymbol{\gamma}_d, \sigma_{\delta_d}^2\right)$ is independent of $\left(\boldsymbol{\gamma}_{d'}, \sigma_{\delta_{d'}}^2\right)$ for $d \neq d'$, the joint conditional posterior distribution of $(\boldsymbol{\gamma}_d, \sigma_{\delta_d}^2)$, which is similar to Eq. (6.13), can be sampled individually. Let $\boldsymbol{V}_d = (\log \sigma_d^2(\boldsymbol{\theta}_1), \dots, \log \sigma_d^2(\boldsymbol{\theta}_m))'$, $\boldsymbol{H}_4$ is the stack of $\{\boldsymbol{h}_3(\boldsymbol{\theta}_i)^T, i = 1, \dots, m\}$, then similar to (6.13), the conditional posterior distributions follow the distribution as

$$\sigma_{\delta_d}^2 | \boldsymbol{V}_d \sim IG\left(\frac{m-2}{2}, \frac{(\boldsymbol{V}_d - \boldsymbol{H}_4\widehat{\boldsymbol{\gamma}}_d)'(\boldsymbol{V}_d - \boldsymbol{H}_4\widehat{\boldsymbol{\gamma}}_d)}{2}\right)$$

$$\boldsymbol{\gamma}_d | \boldsymbol{V}_d, \sigma_{\delta_d}^2 \sim N\left(\widehat{\boldsymbol{\gamma}}_d, \sigma_{\delta_d}^2\left(\boldsymbol{H}_4'\boldsymbol{H}_4\right)^{-1}\right) \tag{6.18}$$

where

$$\widehat{\boldsymbol{\gamma}}_d = (\boldsymbol{H}_4'\boldsymbol{H}_4)^{-1}\boldsymbol{H}_4'\boldsymbol{V}_d$$

The overall blocked Gibbs sampling is shown in Algorithm 6.1 below. To speed up the convergence efficiency, the initial value for all the models parameters can be set using multiple-stage analysis, i.e., fitting linear regression for each profile and treat each coefficient as response in the level-2 model fitting, and then use the residual variance of level-2 model as the responses

in the variance regression. After the iteration of the Gibbs sampling is finished, the obtained

samples can be truncated to remove the initial bias for the posterior estimation.

Algorithm 6.1. Blocked Gibbs Sampling for Model Estimation

Select the iteration number N_g and step-width Δ

Specify the initial value $\left(\boldsymbol{\beta}^{(0)}, (\sigma_\epsilon^2)^{(0)}, \xi^{(0)}, (\boldsymbol{\sigma_\xi^2})^{(0)}, \boldsymbol{\gamma}^{(0)}, \{\sigma_{\delta_d}^2, d = 1, \dots, p\}^{(0)}\right)$

For $t = 1: N_g$

    (1) Sample $(\sigma_\epsilon^2)^{(t)} \sim P\left(\sigma_\epsilon^2 \Big| \left(\xi^{(t-1)}, \boldsymbol{Y}\right)\right)$ and $\boldsymbol{\beta}^{(t)} \sim P\left(\boldsymbol{\beta} \Big| \left(\xi^{(t-1)}, (\sigma_\epsilon^2)^{(t)}, \boldsymbol{Y}\right)\right)$ using Eq. (6.13)

    (2) Sample $\xi_{ij}^{(t)} \sim P\left(\boldsymbol{\xi}_{ij} \Big| \boldsymbol{\beta}^{(t)}, (\sigma_\epsilon^2)^{(t)}, \boldsymbol{\Sigma}_i^{(t-1)}, \boldsymbol{y}_{ij}\right)$ for $i = 1, \dots, m, j = 1, \dots, l$ using Eq. (6.14)

    (3) Metropolis-Hastings algorithm for $(\boldsymbol{\sigma_\xi^2})^{(t)}$

        For $i = 1: m$

          • Generate $\boldsymbol{\eta}_i^*$ using Eq. (6.16)

          • Calculate r_a based on Eq. (6.17)

          • Sample $u \sim U(0,1)$; if $u \le r_a$, set $(\sigma_i^2)^{(t)} = \exp(\boldsymbol{\eta}_i^*)$; else set $(\sigma_i^2)^{(t)} = (\sigma_i^2)^{(t-1)}$

        End

    (4) Sample $(\sigma_{\delta_d}^2)^{(t)} \sim P(\sigma_{\delta_d}^2 | \boldsymbol{V}_d^{(t)})$ and $\boldsymbol{\gamma}_d^{(t)} \sim P\left(\boldsymbol{\gamma}_d \Big| \boldsymbol{V}_d^{(t)}, (\sigma_{\delta_d}^2)^{(t)}\right)$ using Eq. (6.18) for $d = 1, \dots, p$

End

6.4 Model Selection using Intrinsic Bayes Factor

6.4.1 Introduction of Bayes Factor

The most popular model selection methods are the information criteria based methods, such

as Akaike Information Criteria (AIC;[165]) and Bayesian Information Criteria (BIC;[166]),

where the criteria is to find a model that minimizes an estimate of a criterion consisting of a loss

function ($-2 \times$ log-likelihood) and a penalty function. These methods are commonly used in

linear regressions, where the penalty function is a function of model complexity, or number of parameters. However, for the model proposed in this research, there are both mean parameters and variance parameters at different levels, which have different relative importance in analysis. Therefore it is very challenging to incorporate the relative importance into penalty function in the information criteria.

The Bayes factor (BF) is a very flexible model selection method that can compare models of any forms [167]. For two competing models M_i and M_j, $i \neq j$, the BF of M_i to M_j is defined as the observed marginal densities

$$B_{ij} = \frac{P(\boldsymbol{Y}|M_i)}{P(\boldsymbol{Y}|M_j)} = \frac{\int P(\boldsymbol{Y}|\boldsymbol{\psi_i}, M_i)\pi(\boldsymbol{\psi_i}|M_i)d\boldsymbol{\psi_i}}{\int P(\boldsymbol{Y}|\boldsymbol{\psi_j}, M_j)\pi(\boldsymbol{\psi_j}|M_j)d\boldsymbol{\psi_j}} \tag{6.19}$$

where $P(\boldsymbol{Y}|M_i)$ is the marginal or predictive densities of $\boldsymbol{Y}$, $\boldsymbol{\psi_i}$ is the vector of model parameters and $\pi(\boldsymbol{\psi_i}|M_i)$ is the prior density function of model parameters under model M_i. It can also be interpreted as the weighted likelihood ratio of M_i to M_j, with the priors being the "weighting functions". Intuitively, higher B_{ij} indicates a stronger evidence of M_i against M_j. A set of cutoff values of B_{ij} has been suggested and widely used in literature [168], as shown in Table 6-1:

Table 6-1: Range of BF values and its evidence in favor of M_i

B_{ij}	$2\log(B_{ij})$	Evidence against M_j
1~3	0~2	Barely worth mentioning
3~20	2~6	Positive
20~150	6~10	Strong
>150	>10	Very strong

Although BF is very flexible, a direct computation is very challenging, since the marginal density involves integration over the parameter space of high dimension. A natural approach to solve this issue is MCMC simulation [169], where two popular methods are used, the product space search and the marginal likelihood estimation method. In the product space search method, the BF can be alternatively calculated as

$$B_{ij} = \frac{P(Y|M_i)}{P(Y|M_j)} = \frac{P(M_i|Y)/\pi(M_i)}{P(M_j|Y)/\pi(M_j)} \tag{6.20}$$

where $\pi(M_i)$ is the prior for M_i. To estimate $P(M_i|Y)$, we can first estimate the join posterior $P(M, \boldsymbol{\psi}|Y)$ over the product space $\mathcal{M} \times \prod_{j \in \mathcal{M}} \boldsymbol{\Psi}_j$ through Gibbs sampler, or reversible jump MCMC. The $P(M_i|Y)$ can be estimated by marginalizing out $\boldsymbol{\psi}_i$. Plugging the estimated $P(M_i|Y)$ and $P(M_j|Y)$ into Eq. (6.20) we can get the estimated B_{ij}. In the marginal likelihood estimation method, the BF is estimated as follows

$$\log B_{ij} = \log(P(Y|M_i)) - \log\left(P(Y|M_j)\right) \tag{6.21}$$

6.4.2 Intrinsic Bayes Factor and Computation

When the two competing models have parameters of different dimensions, however, using improper noninformative priors for all models parameters will lead to indeterminate BFs, as the marginal density $P(Y|M_i) = \int P(Y|\boldsymbol{\psi}_i, M_i)\pi(\boldsymbol{\psi}_i|M_i)d\boldsymbol{\psi}_i$ is not well-defined for $\pi(\boldsymbol{\psi}_i|M_i) \propto 1$. To see how this happens, suppose $\pi(\boldsymbol{\psi}_i|M_i) \propto 1$ and $\pi(\boldsymbol{\psi}_j|M_j) \propto 1$ are used as priors for M_i and M_j respectively. Then $c_i\pi(\boldsymbol{\psi}_i|M_i)$ and $c_j\pi(\boldsymbol{\psi}_j|M_j)$ can also be used as improper priors, which results in another BF $c_i/c_j B_{ij}$. To address this issue, Zeng et al [150] assumed that different

models share the same dimension of fixed effects parameters, while they differ only on the dimension of random effects variance in the Bayesian LME model estimation. Under this assumption, the improper noninformative priors are used for fixed effects and weakly-informative priors are used for random effects variance components. However, this approach is not applicable to our case, as the dimensions of parameters could differ in all three submodels. In this research, we propose to use the intrinsic Bayes factor (IBF) [170] for model selection.

Let $Y(s)$ denote the training profiles and $Y(-s)$ denote the remaining profiles for testing. The basic idea of IBF is to use the training profiles $Y(s)$ to convert the improper noninformative priors to proper posterior distributions and then to compute the BF with the remainder of the profiles $Y(-s)$. The IBF can be expressed as

$$IB_{ij} = \frac{P(Y(-s)|Y(s), M_i)}{P(Y(-s)|Y(s), M_j)} = \frac{\int P(Y(-s)|\boldsymbol{\psi}_i)\pi(\boldsymbol{\psi}_i|Y(s))d\boldsymbol{\psi}_i}{\int P(Y(-s)|\boldsymbol{\psi}_j)\pi(\boldsymbol{\psi}_j|Y(s))d\boldsymbol{\psi}_j} \tag{6.22}$$

As we can see, the computation of the marginal densities in IBF is quite similar to the cross-validation technique commonly used in the model validation. Naturally, we can partition all the profiles into several groups and calculate the IBF using each group of profiles as the testing profiles and the remainder as the training profiles. By averaging all the IBFs, we would get a more stable IBF.

Although the marginal density is well-defined with proper posterior distribution $\pi(\boldsymbol{\psi}_i|Y(s))$, the direct computation is still challenging. With the availability of posterior samples of $\pi(\boldsymbol{\psi}_i|Y(s))$ obtained from the blocked Gibbs sampler, we can compute the IBF using MCMC approach as follows. The marginal density for M_i is written as

$$m_i(Y(-s)|Y(s)) = \int f(Y(-s)|\psi_i, (\sigma_\xi^2(-s))_i)\pi((\sigma_\xi^2(-s))_i|\psi_i)\pi(\psi_i|Y(s))d(\psi_i, (\sigma_\xi^2(-s))_i)$$

Note that the nuisance parameters σ_ξ^2 are specific to profiles of consideration. Here $(\sigma_\xi^2(-s))_i$ denote the variances of random effects of the testing profiles $Y(-s)$ under the model M_i. Suppose the posterior samples of the training data $Y(s)$ obtained in the Gibbs sampling are

$$\left\{\left(\psi_i^{(g)}, \xi(s)_i^{(g)}, \left(\sigma_\xi^2(s)\right)_i^{(g)}\right), g = 1, 2, \dots, G\right\}$$

Then for $g = 1, \dots, G$, we can sample the $\left(\sigma_\xi^2(-s)\right)^{(g)}$ conditioning on $\psi^{(g)}$ through the lognormal distribution, as shown in Eq. (6.5). The marginal density could be estimated by

$$m_i(Y(-s)|Y(s)) \approx \frac{1}{G}\sum_{g=1}^{G} f\left(Y(-s)\middle|\psi_i^{(g)}, \left(\sigma_\xi^2(-s)\right)_i^{(g)}\right) \tag{6.23}$$

where the profile $y(\theta)$ given ψ and σ_ξ^2 follows normal distribution based on Eq. (6.4):

$$y(\theta)\,|\psi, \Sigma_\xi(\theta) \sim N(H_1(x)H_2(\theta)\beta, H_1(x)\Sigma_\xi(\theta)H_1(x)' + \sigma_\epsilon^2 I)$$

6.4.3 Inference on the Parameter θ

After the model is selected and estimated through the Gibbs sampler and IBF, we can use it to infer the microstructural parameters θ for quality control and diagnosis. Suppose the measured profiles for a new MMNC sample is Y_{new}, then the posterior of θ_{new} given Y_{new} and model parameters is of interest. We can use the mean or median of the posterior distributions of ψ as the point estimate of the model parameters, denoted by $\widehat{\psi}$, to calculate the posterior of θ_{new}

$P(\boldsymbol{\theta}_{new}|\boldsymbol{Y}_{new}, \widehat{\boldsymbol{\psi}})$. Alternatively, we could use all the Gibbs samples instead of the point estimate for the model parameters. The posterior is expresses as

$$P(\boldsymbol{\theta}_{new}|\boldsymbol{Y}_{new}, \boldsymbol{Y}) \propto \pi(\boldsymbol{\theta}_{new})P(\boldsymbol{Y}_{new}|\boldsymbol{\theta}_{new}, \boldsymbol{Y}) \tag{6.24}$$

where $\pi(\boldsymbol{\theta}_{new})$ is the prior distribution for $\boldsymbol{\theta}$. To estimate this posterior, the importance sampling [171] can be applied with the prior $\pi(\boldsymbol{\theta}_{new})$ as the importance function and $P(\boldsymbol{Y}_{new}|\boldsymbol{\theta}_{new}, \boldsymbol{Y})$ as the weight function, which can be estimated using Eq. (6.23). The expectation of $h(\boldsymbol{\theta}_{new})$ with respect to $P(\boldsymbol{\theta}_{new}|\boldsymbol{Y}_{new}, \boldsymbol{Y})$ where $h(\boldsymbol{\theta}_{new})$ is any function of $\boldsymbol{\theta}_{new}$, can be estimated using the following importance sampling algorithm.

Algorithm 6.2. Importance Sampling for Inference of θ

Specify the number of samples N_s

(1) Draw samples $\boldsymbol{\theta}^{(1)}, \dots, \boldsymbol{\theta}^{(N_s)}$ from $\pi(\boldsymbol{\theta}_{new})$
(2) Calculate the importance weight of each sample using Eq. (6.23)

$$w^{(j)} = P\big(\boldsymbol{Y}_{new}|\boldsymbol{\theta}^{(j)}, \boldsymbol{Y}\big), j = 1, \dots, N_s$$

(3) Approximate the expectation

$$E_{P(\boldsymbol{\theta}|\boldsymbol{Y}_{new}, \boldsymbol{Y})}\big(h(\boldsymbol{\theta})\big) = \frac{\sum_{j=1}^{N_s} w^{(j)}h\big(\boldsymbol{\theta}^{(j)}\big)}{\sum_{j=1}^{N_s} w^{(j)}}$$

6.5 Simulation Study for Performance Evaluation

In this section, simulated profiles are used to evaluate the efficiency of the proposed method for model estimation, model selection, and parameter inference. In total two models are used in

the simulation, with one model for the illustration of posterior sampling and both models for model selection and parameter inference.

6.5.1 Simulation Setup

The models used in the simulation with specified parameters are shown in Table 6-2. For simplicity we assume that θ is a scale parameter and $h_i(\cdot), i = 1,2,3$ are polynomials of degrees $p - 1, q - 1$ and $r - 1$ respectively. For each model, $l = 60$ profiles are generated with $m = 33$ equally spaced design points for θ in [0.1, 0.9], i.e., $\theta = 0.1, 0.125, ..., 0.9$, and $n = 11$ equally spaced design points for x in [2, 3], i.e., $x = 2, 2.1, ..., 3$. The first model will be used to show the efficiency of blocked Gibbs sampling and both models will be used to illustrate the IBF model selection and parameter inferences. Figure 6-2 shows part of the simulated profiles from Model 1, where we can see obvious increase of between-curve dispersion when increasing θ.

Table 6-2: Model setting for simulation

Model 1	Model 2
$p = 2, q = 3, r = 2$	$p = 2, q = 2, r = 2$
$h_1(x) = (x, 1)^{'}$	$h_1(x) = (x, 1)^{'}$
$h_2(\theta) = \left(\theta^2, \theta, 1\right)^{'}$	$h_2(\theta) = (\theta, 1)^{'}$
$h_3(\theta) = (\theta, 1)^{'}$	$h_3(\theta) = (\theta, 1)^{'}$
$\boldsymbol{\beta}_1 = (2,2,2)^{'}, \boldsymbol{\beta}_2 = (-1, -1, -1)^{'}$	$\boldsymbol{\beta}_1 = (2,4)^{'}, \boldsymbol{\beta}_2 = (-1,3)^{'}$
$\boldsymbol{\gamma}_1 = (6, -6)^{'}, \boldsymbol{\gamma}_2 = (4, -4)^{'}$	$\boldsymbol{\gamma}_1 = (4, -5)^{'}, \boldsymbol{\gamma}_2 = (6, -7)^{'}$
$\sigma_\epsilon^2 = 0.01, \sigma_{\delta_1}^2 = \sigma_{\delta_2}^2 = 0.1$	$\sigma_\epsilon^2 = 0.01, \sigma_{\delta_1}^2 = \sigma_{\delta_2}^2 = 0.01$
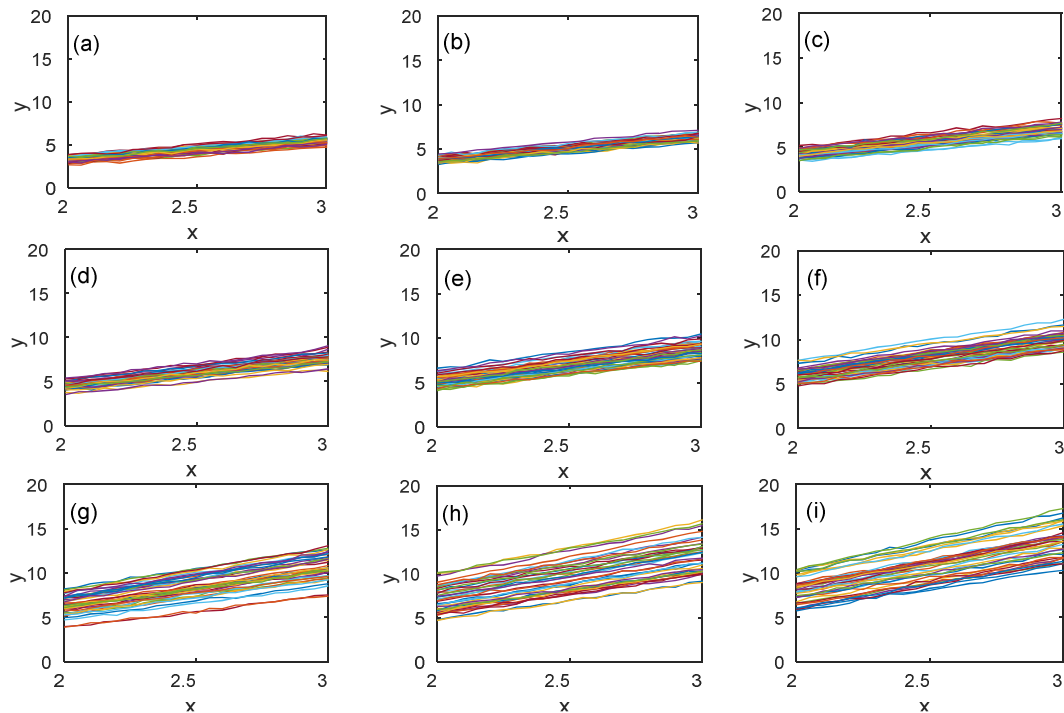
Figure 6-2: Illustration of the simulated profiles from Model 1 with increasing θ from 0.1 to 0.9: (a), (b), ..., (i) corresponds to $\theta = 0.1, 0.2, ..., 0.9$ respectively.

6.5.2 Results of Posterior Sampling

In the posterior sampling, we assume that the true model of the simulated profiles is given but the model parameters are unknown and are to be estimated. The initial values for all parameters are arbitrarily set to 1. The standard deviation of the proposal distribution is set as $\Delta = 0.1$. Figure 6-3 and

Figure 6-4 show the sample paths of mean and variance parameters of Model 1 respectively. As we can see, all the chains gradually move into the true values of the model parameters after about 20K iterations. We also observe that the sequences of samples are highly correlated, i.e., requiring many iterations to forget the starting point and reach the equilibrium distribution. The

step-width Δ could be increased or adjusted to reduce the correlation and speed up the convergence. Since it is not the focus, we will not discuss it here.
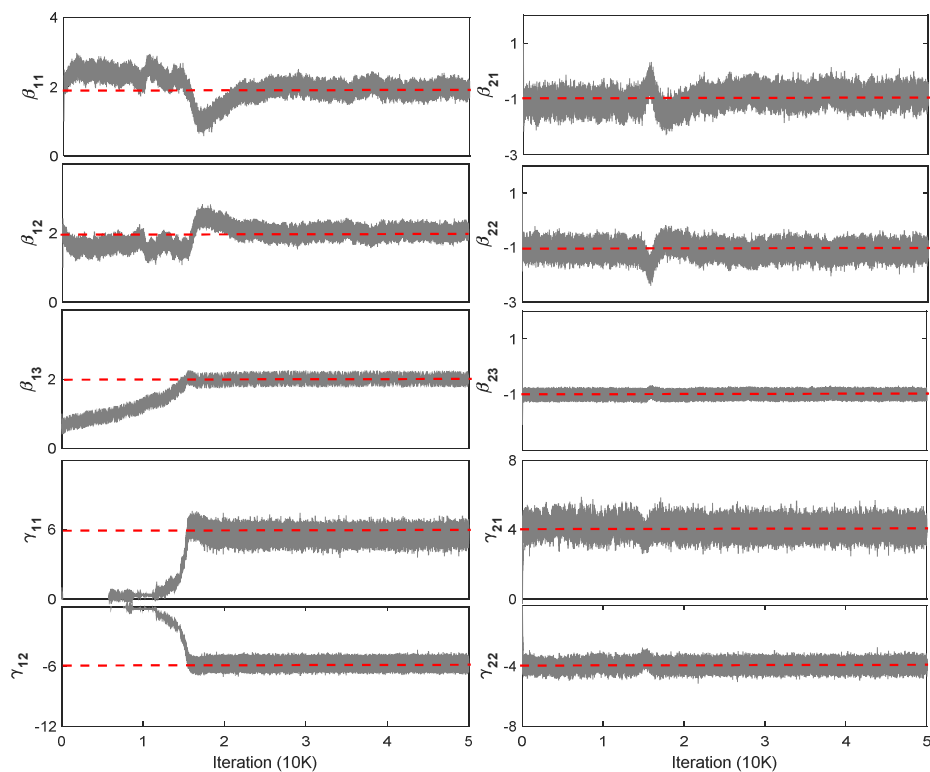
Figure 6-3: Sample paths of the mean parameters $\boldsymbol{\beta}$ and $\boldsymbol{\gamma}$ from blocked Gibbs sampling; the horizontal dashed lines denote the true parameters of the model.
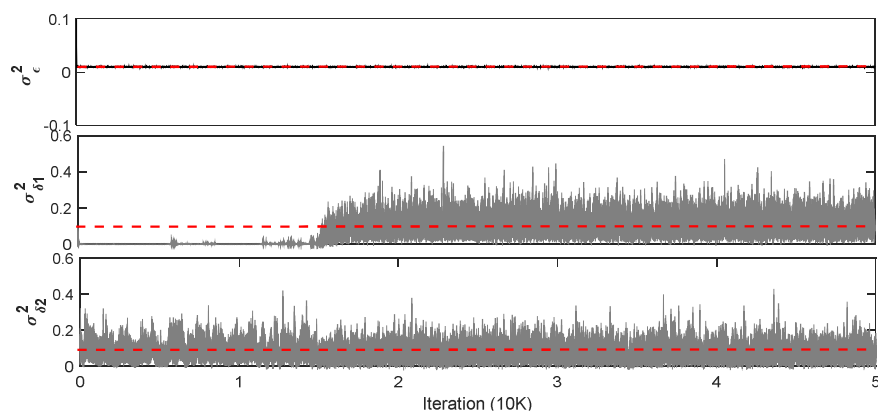
Figure 6-4: Sample paths of the variance parameters $\sigma_\epsilon^2, \sigma_{\delta_1}^2$ and $\sigma_{\delta_2}^2$ from blocked Gibbs sampling; the horizontal dashed lines denote the true parameters of the model.

The histograms of the samples in the equilibrium stage are shown in Figure 6-5, where the last 10K samples of each chain are selected. As we can see, the centers of the posterior are very close to the true values.
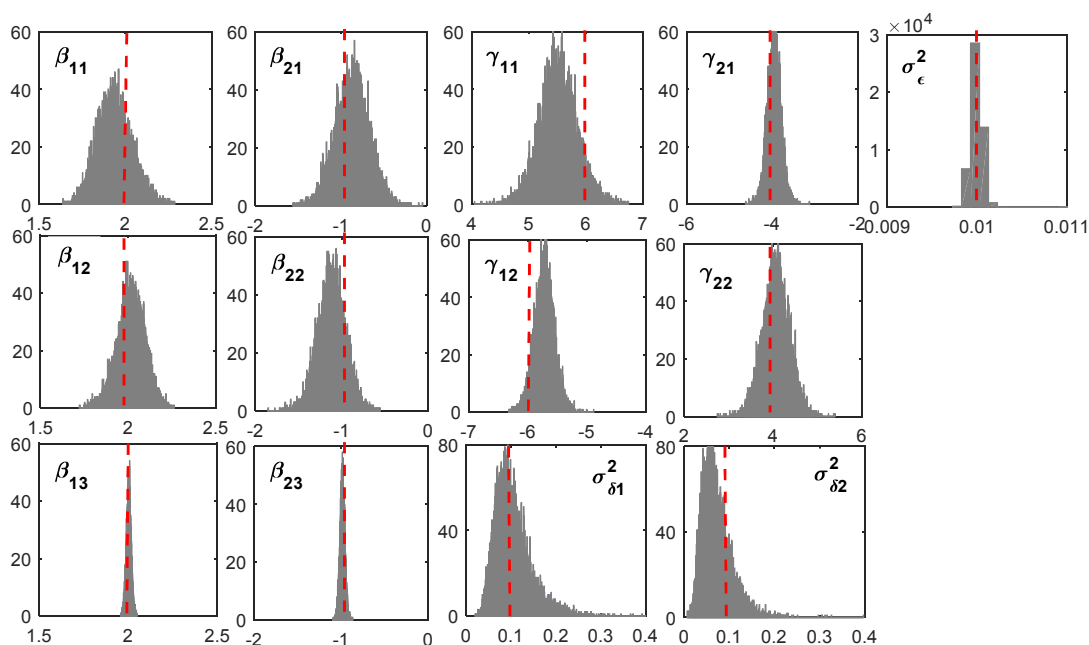
Figure 6-5: Histograms of the parameter samples; the vertical dashed lines denote the true parameters

6.5.3 Model Selection

Changing the degree of the polynomial in each submodel, or setting certain coefficients to zero with fixed degree at each level, will result in many candidate models, which makes it unrealistic to fit all models and compare them all. In application, the multiple-stage analysis (i.e., fitting the model from the first level to the last one, and using fitted parameters in current level as responses in the next level fitting) can be used to select some most likely models and then use IBF to select the best one among them. Alternatively, the forward selection strategy can be used, where one starts from the simplest model, and each time adds one variable that has the most

significant improvement (i.e., increase in marginal density) to the model fitting until there is no significant improvement. For simplicity, we only compare models with different degrees to illustrate the effectiveness of IBF in model selection.

Table 6-3: Candidate models, marginal densities and the IBF of the true models to others

Model	Dimension	Data1		Data2	
		$\log(m_i)$	$2\log(IBF)$	$\log(m_i)$	$2\log(IBF)$
M_1	$p=2, q=1, r=1$	17.3	221.2	92.7	111.2
M_2	$p=2, q=1, r=2$	67.6	120.6	108.6	79.4
M_3	$p=2, q=1, r=3$	58.5	138.8	101.3	94
M_4	$p=2, q=2, r=1$	100.8	54.2	141.4	13.8
M_5	$p=2, q=2, r=2$	123.9	8	148.3	–
M_6	$p=2, q=2, r=3$	123.1	9.6	126.6	43.4
M_7	$p=2, q=3, r=1$	105.9	44	140.0	16.6
M_8	$p=2, q=3, r=2$	127.9	–	148.2	0.2
M_9	$p=2, q=3, r=3$	127.5	0.8	147.1	2.4
M_{10}	$p=3, q=1, r=1$	46.0	163.8	45.7	205.2
M_{11}	$p=3, q=1, r=2$	38.9	178.0	52.3	192
M_{12}	$p=3, q=1, r=3$	26.5	202.8	41.9	212.8
M_{13}	$p=3, q=2, r=1$	53.3	149.2	65.2	166.2
M_{14}	$p=3, q=2, r=2$	64.5	126.8	64.6	167.4
M_{15}	$p=3, q=2, r=3$	45.4	165	59.9	176.8
M_{16}	$p=3, q=3, r=1$	48.9	158	67.5	161.6
M_{17}	$p=3, q=3, r=2$	72.8	110.2	67.5	161.6
M_{18}	$p=3, q=3, r=3$	53.3	149.2	62.2	172.2

In the IBF computation, the profiles with $\theta = 0.1, 0.125, \ldots, 0.725$ are used as training data and others with $\theta = 0.75, 0.775, \ldots, 0.9$ are used as testing data. Table 6-3 shows the candidate models, estimated marginal densities and the IBF for the two set of profile data (Data1 and Data2) generated from Model 1 and Model 2 in Table 6-2. As we can see, the true models for both dataset, i.e., M_8 for Data1 and M_5 for Data2, have the highest marginal densities than all other candidate models. Almost all the IBFs of the true models to other candidate models are significant according to the recommended BF range and evidence given in Table 6-1. Note that the IBF of M_8 to M_9 for Data1 and the IBF of M_5 to M_8 for Data2 are not significant based on Table 6-1. However, M_8 is simpler than M_9 and M_5 is simpler than M_8, indicating that the true models M_8 and M_5 are preferable to M_9 and M_8 for Data1 and Data2 respectively. Therefore, the IBF can effectively select the best model among all candidate models.

6.5.4 Inference of the Designing Parameter θ

$\theta = 0.4, 0.6, 0.8$ are used to generate the new data using Model 1 and Model 2 for parameter inference. 20 profiles are generated for each θ. The prior distribution of θ is assumed to be uniform in the interval [0,1]. The posterior distribution of θ is estimated using the importance sampling algorithm shown in Section 6.4.3. Figure 6-6 shows the estimated posterior distributions. We can see that the center of the posterior is very close to the true value of θ, and the variance of the posterior using 20 profiles is also very small.
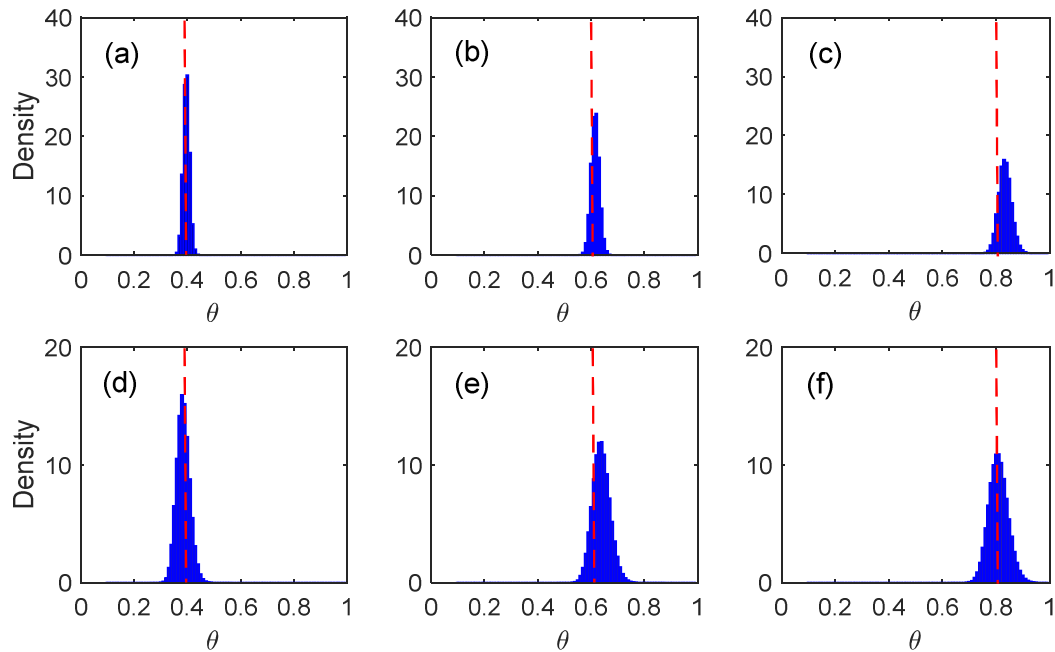
Figure 6-6: Estimated posterior distribution of θ: (a)-(c) for Model 1 and (d)-(f) for Model 2. The vertical dashed lines denote the true θ.

6.6 Case Study

In this section the proposed HLM is applied to build the relationship between the ultrasonic attenuation profiles and microstructural parameters of A206-Al$_2$O$_3$ nanocomposites. Due to high experimental cost and difficulty in fabricating nanocomposites of desired microstructural features, Liu et al [149] recently proposed a microstructural modelling and wave propagation simulation approach to enrich the database of microstructures and the corresponding ultrasonic attenuation profiles, as illustrated in Figure 6-7.
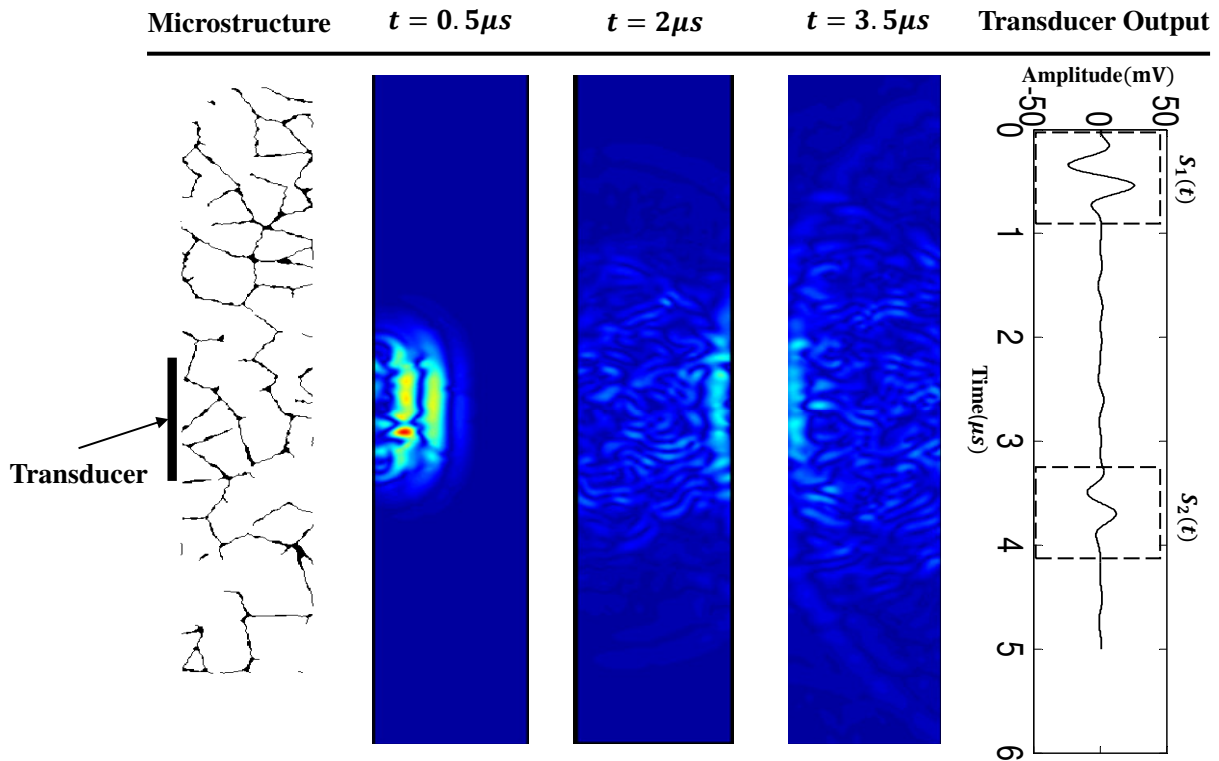
Figure 6-7: Illustration of generated microstructures, wave propagation simulation and transducer output by VEFIT

A Voronoi diagram is modified to simulate the microstructures based on the micrographs and morphology modification mechanism of Al_2O_3 nanoparticles, and an elastodynamic finite integration technique VEFIT [172] is used to simulate the wave propagation. The simulation approach can effectively capture the features of microstructures and reproduce the comparable attenuation profiles. In the microstructure generation, two key parameters are used to control the morphology, the number of cells N, and the percentage of Voronoi edge length left after dissolving, denoted as θ. Figure 6-8 shows the attenuation profiles (20 profiles each sub-figure) of microstructures with $\theta = (0.1, 0.2, ..., 0.9)$ and the corresponding N that keeps the total amount of intermetallic phase unchanged. As we can see, the attenuation profiles linearly increase with frequency in the selected frequency range, and the between-profile variation

increases with θ. Note that for nonlinear profiles or higher order polynomials, the spectrum length can be reduced to get approximately linear profiles.
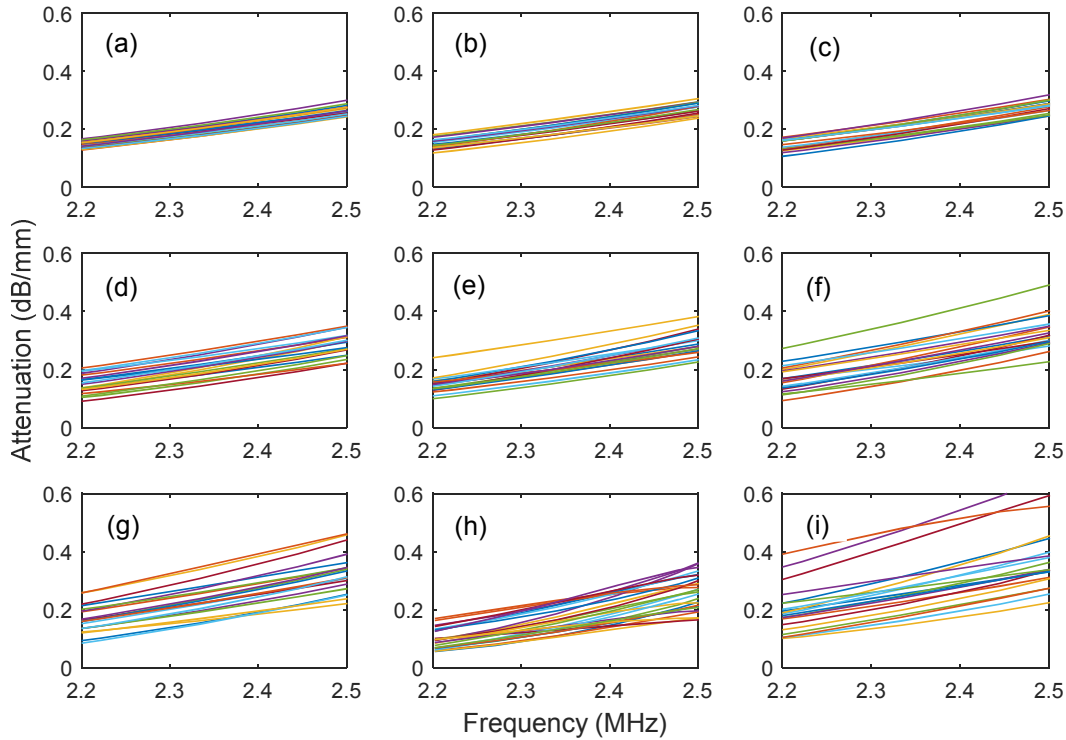
Figure 6-8: Attenuation profiles for microstructures with $\theta = (0.1, 0.2, \dots, 0.9)$ from (a) to (i).

Figure 6-9 shows the exploratory analysis of the attenuation profiles using the multiple-stage analysis, where the slope, intercept, and their log-variances are shown for each θ. We can see that the slope, intercept and their log-variances are quite linear with θ. The model selection is applied to the data and the best model with $p = 2$, $q = 2$ and $r = 2$ is selected. The mean of the posterior samples obtained in the Gibbs sampling are $\beta_{11} = 0.231$, $\beta_{12} = 0.253$, $\beta_{21} = -0.489$, $\beta_{22} = -0.396$, $\sigma_\epsilon^2 = 4.95 \times 10^{-4}$, $\gamma_{11} = 9.92$, $\gamma_{12} = -12.72$, $\gamma_{21} = 11.31$, $\gamma_{22} = -12.68$, $\sigma_{\delta_1}^2 = 0.0077$ and $\sigma_{\delta_2}^2 = 0.01$.
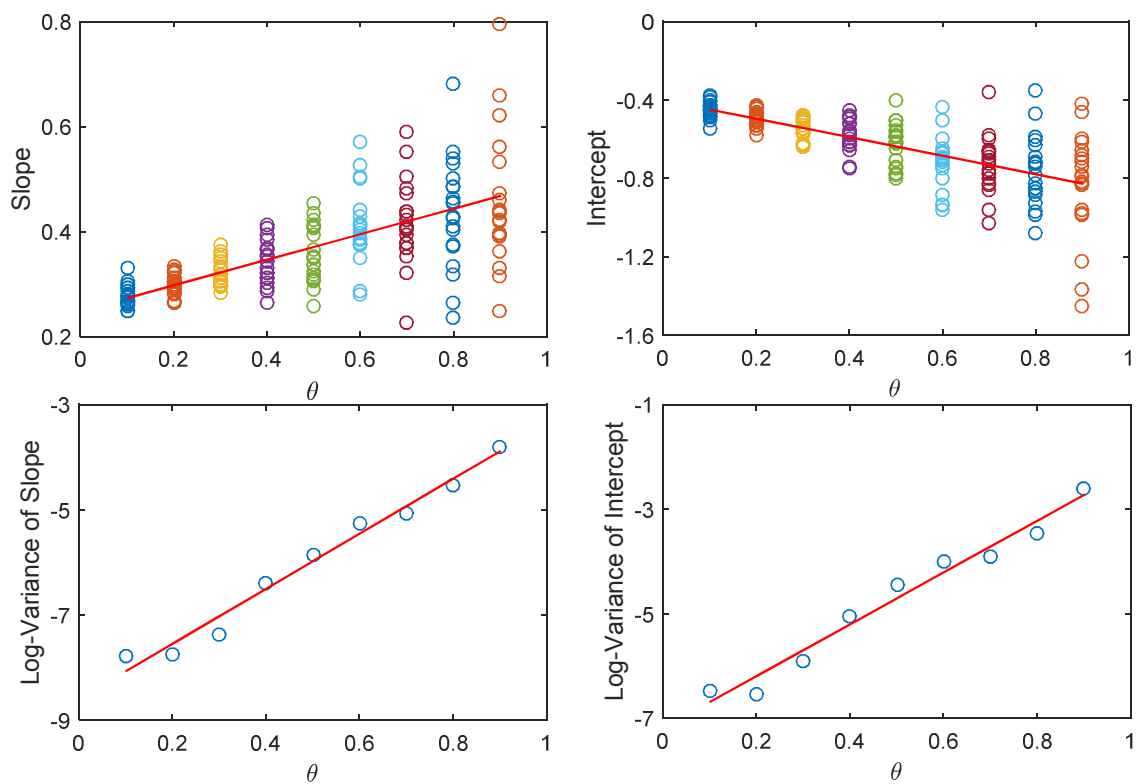
Figure 6-9: Exploratory analysis for the attenuation profiles using multiple-stage analysis. The solid lines denote the simple linear regression lines.
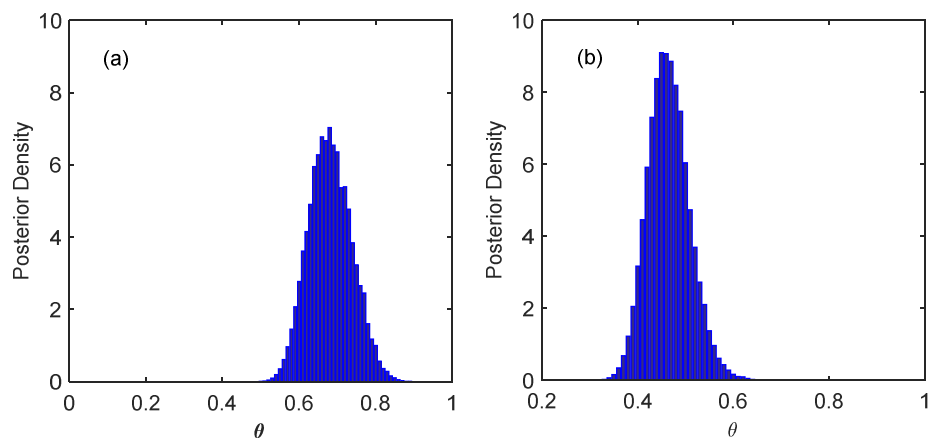
Figure 6-10: Posterior distribution of θ for (a): A206+1wt%Al$_2$O$_3$, and (b): A206+5wt%Al$_2$O$_3$

The estimated model is used to diagnose the microstructural features of two fabricated samples with attenuation profiles shown in Figure 5-6 (c) and (e). Figure 6-10 shows the posterior distribution of θ with uniform prior distribution $U(0,1)$. The mean estimates of the posteriors are 0.68 and 0.46 for Figure 6-10 (a) and (b), respectively. We can see that the θ of first sample is higher than the second one, which is consistent with the experimental result that the second sample has smaller grain size and more homogeneous microstructure. By setting a threshold θ_0 for θ, the posterior can be used to estimate the probability of $\theta < \theta_0$ and use it to for quality control. Therefore the estimated posterior distribution can be used for both quality control and microstructure diagnosis in the ultrasonic attenuation based quality inspection of nanocomposites.

6.7 Conclusion and Discussion

In this chapter, we propose a hierarchical linear model with level-2 variance heterogeneity to model the ultrasonic attenuation profiles in the quality inspection of Al based nanocomposites. The integrated Bayesian framework for model estimation and selection is proposed through the blocked Gibbs sampling and intrinsic Bayes factor. The inference of the microstructural parameters based on the estimated model is proposed using importance sampling. The numerical study shows that the proposed approach can effectively identify the true model, estimate the model parameters, and infer designing parameters for new profiles. The proposed approach is also applied to the ultrasonic attenuation profiles. The results show that this approach can be effectively used for quality control and diagnosis.

We have to admit that there are still two issues that need to be addressed in the ultrasonic attenuation based quality inspection, which will be our future work. The first issue is that the simulated attenuation profiles rather than the experimental data are used to build the model. Although simulated microstructures can effectively capture the key microstructural features, they may not be sufficient to describe the complex microstructures. In the future, more MMNCs samples need to be fabricated and the corresponding microstructural parameters need to be characterized and quantified for model building. The second issue is that for some microstructures with big nanoparticle clusters, the attenuation profiles may not follow the model developed using well dispersed samples. Therefore new hypothesis testing method needs to be developed to test if the new profiles follow the estimated model. Note that the application of the proposed modeling framework is not limited to ultrasonic attenuation profiles. It can be extended to other profiles monitoring where the relationship between the underlying parameters and the profiles is of interest.

7   Conclusions and Future Work

Achieving uniform dispersion of nanoparticle reinforcements in the base material is the key challenge in the fabrication of high performance lightweight MMNCs. The research presented in this dissertation aimed to develop and implement dispersion process monitoring, control and quality inspection techniques and methodologies for the ultrasonic cavitation based scale-up production of MMNCs. It can be classified into two tasks, the online dispersion process monitoring and control, and the offline quality inspection.

In the online process monitoring and control, a high speed data acquisition system was developed to collect the cavitation noise signals from molten metal. Based on the cavitation mechanism, acoustic scattering theory and experimental validation, the dispersion was found to be finished when the cavitation noise signals enter into steady state. Therefore, the monitoring and control of the dispersion process can be achieved by detecting the steady state of cavitation noise signals. Two robust online steady state detection algorithms were developed using multiple change-point models and Bayesian inference. In both methods, piecewise linear models were used to model process signals, and the flatness of the latest line segment was used to evaluate the steadiness of signals. In the first method, the posterior of the parameters for the latest line segment is approximated using particle filters. The second algorithm used exact Bayesian inference to calculate the posterior distribution by selecting conjugate priors. Numerical analysis showed that both methods are much more accurate and robust than other moving window based methods.

In the offline quality inspection, ultrasonic testing based quality inspection of MMNCs was investigated. It was found that large primary dendrites, long continuous intermetallic phase and unevenly distributed Al_2O_3 nanoparticles cause large between-curve variation among attenuation profiles measured at different surface locations of the fabricated MMNCs. Therefore, the variation of the acoustic attenuation profiles can be used as an indicator to evaluate the microstructural quality. A hierarchical linear model with level-2 variance heterogeneity is developed to establish the relationship between ultrasonic attenuation profiles and the microstructural parameters for inference of microstructural features and quality control using ultrasonic profiles. An integrated Bayesian framework with MCMC approach was developed for model estimation, model selection and parameter inference. The proposed framework is able to infer the microstructural features accurately.

The contributions of this dissertation include the following five aspects: (1) development of a novel data acquisition system for dispersion process monitoring, (2) discovery of the relation between the ultrasonic cavitation noise and nanoparticle dispersion conditions, (3) two robust on-line steady state detection algorithms with broad applications, (4) discovery of qualitative relation between ultrasonic attenuation and microstructures of MMNCs, (5) hierarchical linear modeling of ultrasonic attenuation profiles for microstructural quality inference and control of MMNCs.

The enabling process and quality control methodologies for MMNCs manufacturing is critical to facilitate the scale-up production and bring the impact on the economic growth. However, there are still many issues that can be further investigated or extended to improve the process and quality control. The potential future directions are listed as follows:

(1) *Particle dispersion process monitoring*: Currently the steady state of the cavitation noise power index in used to monitor the nanoparticle dispersion. To make the monitoring and control process more reliable and accurate, further signal analysis and experiment validation may be needed. For example, instead of using the cavitation noise power, certain components (i.e., harmonics, ultraharmonics, subharmonics, white noise) of the frequency spectrum of the cavitation noise may be used for particle dispersion process monitoring. To verify the effectiveness of the monitoring scheme, more MMNCs with different ultrasonic dispersion times need to be fabricated and examined.

(2) *Statistical process control (SPC) of MMNCs based on the attenuation profiles*: In this dissertation, it is observed that the attenuation profiles are highly dependent on the microstructural quality. Therefore the SPC control charts on the attenuation profiles will be a good research direction in the future.

(3) 3*D microstructural modeling, wave propagation simulation and uncertain quantification*: In this dissertation, different microstructures and attenuation profiles were generated through 2D microstructure modeling and wave propagation simulation to build the relationship between the microstructural features and attenuation profiles. In the future, the 2D microstructure modelling and wave propagation simulation can be extended to 3-dimention to better represent the real microstructures and wave propagation processes. In addition, the hierarchical linear model developed in this dissertation did not utilize the experimental attenuation profiles. In the future, the model emulation and calibration can be used to incorporate both experimental and simulation data for microstructural quality inference and control.

8   References

[1]   L. W. Cheah, "Cars on a diet: the material and energy impacts of passenger vehicle weight reduction in the US," Massachusetts Institute of Technology, 2010.

[2]   C. Borgonovo and D. Apelian, "Manufacture of Aluminum Nanocomposites: A Critical Review," in *Materials Science Forum*, 2011, pp. 1-22.

[3]   P. M. Ajayan, L. S. Schadler, and P. V. Braun, *Nanocomposite science and technology*: John Wiley & Sons, 2006.

[4]   I. Ibrahim, F. Mohamed, and E. Lavernia, "Particulate reinforced metal matrix composites—a review," *Journal of materials science,* vol. 26, pp. 1137-1156, 1991.

[5]   H. Akbulut and M. Durman, "Temperature dependent strength analysis of short fiber reinforced Al–Si metal matrix composites," *Materials Science and Engineering: A,* vol. 262, pp. 214-226, 1999.

[6]   Y. Iwai, T. Honda, T. Miyajima, Y. Iwasaki, M. Surappa, and J. Xu, "Dry sliding wear behavior of Al_2O_3 fiber reinforced aluminum composites," *Composites science and technology,* vol. 60, pp. 1781-1789, 2000.

[7]   J. Zhang, R. Perez, M. Gupta, and E. Lavernia, "Damping behavior of particulate reinforced 2519 Al metal matrix composites," *Scripta metallurgica et materialia,* vol. 28, pp. 91-96, 1993.

[8]   F. A. Mohamed, K.-T. Park, and E. J. Lavernia, "Creep behavior of discontinuous SiC-Al composites," *Materials Science and Engineering: A,* vol. 150, pp. 21-35, 1992.

[9]   M. Horstemeyer, N. Yang, K. Gall, D. McDowell, J. Fan, and P. Gullett, "High cycle fatigue of a die cast AZ91E-T4 magnesium alloy," *Acta Materialia,* vol. 52, pp. 1327-1336, 2004.

[10]   "Ducker Worldwide survey: 2015 North American Light Vehicle Aluminun Content Study," 2014.

[11]   Y. Yang and X. Li, "Ultrasonic cavitation based nanomanufacturing of bulk aluminum matrix nanocomposites," *Journal of manufacturing science and engineering,* vol. 129, pp. 497-501, 2007.

[12] F. Zhang, W. Kaczmarek, L. Lu, and M. Lai, "Formation of Al-TiN metal matrix composite via mechanochemical route," *Scripta Materialia,* vol. 43, pp. 1097-1102, 2000.

[13] M. Sherif El-Eskandarany, "Mechanical solid state mixing for synthesizing of SiCpAl nanocomposites," *Journal of alloys and Compounds,* vol. 279, pp. 263-271, 1998.

[14] E. Hochreiter, C. Kowanda, and B. Ortner, "Preparing particle reinforced Al-MMCs by mechanical alloying," *Le Journal de Physique IV,* vol. 3, pp. C7-1829-C7-1832, 1993.

[15] F. Audebert, F. Prima, M. Galano, M. Tomut, P. J. Warren, I. C. Stone, and B. Cantor, "Structural characterisation and mechanical properties of nanocomposite Al-based alloys," *Materials transactions,* vol. 43, pp. 2017-2025, 2002.

[16] P. Bhattacharya, V. Bhattacharya, and K. Chattopadhyay, "Morphology and thermal characteristics of nano-sized Pb–Sn inclusions in Al," *Journal of Materials Research,* vol. 17, pp. 2875-2883, 2002.

[17] X. Tong and H. Fang, "Al-TiC composites In Situ-processed by ingot metallurgy and rapid solidification technology: Part I. Microstructural evolution," *Metallurgical and Materials Transactions A,* vol. 29, pp. 875-891, 1998.

[18] X. Tong and H. Fang, "Al-TiC composites in situ-processed by ingot metallurgy and rapid solidification technology: Part II. Mechanical behavior," *Metallurgical and Materials Transactions A,* vol. 29, pp. 893-902, 1998.

[19] Y.-H. Seo and C.-G. Kang, "The effect of applied pressure on particle-dispersion characteristics and mechanical properties in melt-stirring squeeze-cast SiCp/Al composites," *Journal of Materials Processing Technology,* vol. 55, pp. 370-379, 1995.

[20] Y. Yang, J. Lan, and X. Li, "Study on bulk aluminum matrix nano-composite fabricated by ultrasonic dispersion of nano-sized SiC particles in molten aluminum alloy," *Materials Science and Engineering: A,* vol. 380, pp. 378-383, 2004.

[21] G. Cao, H. Konishi, and X. Li, "Mechanical properties and microstructure of Mg/SiC nanocomposites fabricated by ultrasonic cavitation based nanomanufacturing," *Journal of manufacturing science and engineering,* vol. 130, 2008.

[22] A. Gedanken, "Doping nanoparticles into polymers and ceramics using ultrasound radiation," *Ultrasonics sonochemistry,* vol. 14, pp. 418-430, 2007.

[23] H. Liu, S. Zhou, and X. Li, "Inferring the Size Distribution of 3D Particle Clusters in Metal Matrix Nanocomposites," *Journal of Manufacturing Science and Engineering,* vol. 135, pp. 011013-011013, 2013.

[24]   X. Li, Y. Yang, and D. Weiss, "Ultrasonic Cavitation Based Dispersion of Nanoparticles in Aluminum Melts for Solidification Processing of Bulk Aluminum Matrix Nanocomposite: Theoretical Study, Fabrication and Characterization," 2007.

[25]   J. H. Gibson, H. Hon, R. Farnood, I. G. Droppo, and P. Seto, "Effects of ultrasound on suspended particles in municipal wastewater," *Water research,* vol. 43, pp. 2251-2259, 2009.

[26]   K. S. Suslick, Y. Didenko, M. M. Fang, T. Hyeon, K. J. Kolbeck, W. B. McNamara, M. M. Mdleleni, and M. Wong, "Acoustic cavitation and its chemical consequences," *Philosophical Transactions of the Royal Society of London. Series A: Mathematical, Physical and Engineering Sciences,* vol. 357, pp. 335-353, 1999.

[27]   E. A. Neppiras, "Acoustic cavitation," *Physics Reports,* vol. 61, pp. 159-251, 1980.

[28]   W. Nyborg, "Acoustic streaming," *Physical acoustics,* vol. 2, p. 265, 1965.

[29]   L.-Y. Chen, J.-Q. Xu, H. Choi, H. Konishi, S. Jin, and X.-C. Li, "Rapid control of phase growth by nanoparticles," *Nature communications,* vol. 5, 2014.

[30]   Y. Yang and X. Li, "Ultrasonic cavitation-based nanomanufacturing of bulk aluminum matrix nanocomposites," *Journal of manufacturing science and engineering,* vol. 129, p. 252, 2007.

[31]   B. Bittmann, F. Haupert, and A. K. Schlarb, "Ultrasonic dispersion of inorganic nanoparticles in epoxy resin," *Ultrasonics sonochemistry,* vol. 16, pp. 622-628, 2009.

[32]   K. S. Suslick, Y. Didenko, M. M. Fang, T. Hyeon, K. J. Kolbeck, W. B. McNamara, M. M. Mdleleni, and M. Wong, "Acoustic cavitation and its chemical consequences," *Philosophical Transactions of the Royal Society of London. Series A: Mathematical, Physical and Engineering Sciences,* vol. 357, pp. 335-353, February 15, 1999 1999.

[33]   W. Hentschel and W. Lauterborn, "New speed record in long series holographic cinematography," *Applied optics,* vol. 23, pp. 3263-3265, 1984.

[34]   W. Lauterborn and W. Hentschel, "Cavitation bubble dynamics studied by high speed photography and holography: part one," *Ultrasonics,* vol. 23, pp. 260-268, 1985.

[35]   F. Burdin, N. Tsochatzidis, P. Guiraud, A. Wilhelm, and H. Delmas, "Characterisation of the acoustic cavitation cloud by two laser techniques," *Ultrasonics sonochemistry,* vol. 6, pp. 43-51, 1999.

[36]   N. Tsochatzidis, P. Guiraud, A. Wilhelm, and H. Delmas, "Determination of velocity, size and concentration of ultrasonic cavitation bubbles by the phase-Doppler technique," *Chemical engineering science,* vol. 56, pp. 1831-1840, 2001.

[37]   R. Nishi, "The scattering and absorption of sound waves by a gas bubble in a viscous liquid," *Acustica,* vol. 33, p. 2, 1975.

[38]   R. Duraiswami, S. Prabhukumar, and G. L. Chahine, "Bubble counting using an inverse acoustic scattering method," *The Journal of the Acoustical Society of America,* vol. 104, p. 2699, 1998.

[39]   P. Vaughan, "Investigation of acoustic cavitation thresholds by observation of the first subharmonic," *Journal of Sound and Vibration,* vol. 7, pp. 236-246, 1968.

[40]   E. Neppiras, "Subharmonic and Other Low-Frequency Emission from Bubbles in Sound-Irradiated Liquids," *The Journal of the Acoustical Society of America,* vol. 46, p. 587, 1969.

[41]   B. Avvaru and A. B. Pandit, "Oscillating bubble concentration and its size distribution using acoustic emission spectra," *Ultrasonics sonochemistry,* vol. 16, pp. 105-115, 2009.

[42]   H. Puga, J. Barbosa, J. Gabriel, E. Seabra, S. Ribeiro, and M. Prokic, "Evaluation of ultrasonic aluminium degassing by piezoelectric sensor," *Journal of Materials Processing Technology,* 2011.

[43]   S. Labouret, J. Frohly, and F. Rivart, "Evolution of an 1MHz ultrasonic cavitation bubble field in a chopped irradiation mode," *Ultrasonics sonochemistry,* vol. 13, pp. 287-294, 2006.

[44]   J. Frohly, S. Labouret, C. Bruneel, I. Looten-Baquet, and R. Torguet, "Ultrasonic cavitation monitoring by acoustic noise power measurement," *The Journal of the Acoustical Society of America,* vol. 108, p. 2012, 2000.

[45]   M. Hodnett, R. Chow, and B. Zeqiri, "High-frequency acoustic emissions generated by a 20 kHz sonochemical horn processor detected using a novel broadband acoustic sensor: a preliminary study," *Ultrasonics sonochemistry,* vol. 11, pp. 441-454, 2004.

[46]   V. Ilyichev, V. Koretz, and N. Melnikov, "Spectral characteristics of acoustic cavitation," *Ultrasonics,* vol. 27, pp. 357-361, 1989.

[47]   W. Lauterborn, "Numerical investigation of nonlinear oscillations of gas bubbles in liquids," *The Journal of the Acoustical Society of America,* vol. 59, p. 283, 1976.

[48]   A. Prosperetti, L. A. Crum, and K. W. Commander, "Nonlinear bubble dynamics," *The Journal of the Acoustical Society of America,* vol. 83, p. 502, 1988.

[49]   F. R. Young, *Cavitation*: McGraw-Hill New York, 1989.

[50]   G. t. W, "Nichtlineare Schwingungen von Luftblasen in Wasser," *Acustica,* vol. 6, pp. 532-538, 1956.

[51]   A. Coleman, M. Choi, J. Saunders, and T. Leighton, "Acoustic emission and sonoluminescence due to cavitation at the beam focus of an electrohydraulic shock wave lithotripter," *Ultrasound in medicine & biology,* vol. 18, pp. 267-281, 1992.

[52]   K. Yasui, T. Tuziuti, T. Kozuka, and A. Towata, "Origin of the broad-band noise in acoustic cavitation."

[53]   S. Spratt, "Heuristics for the startup problem," *Department of Systems Engineering, University of Virginia,* 1998.

[54]   S. Cao and R. R. Rhinehart, "An efficient method for on-line identification of steady state," *Journal of Process Control,* vol. 5, pp. 363-374, 1995.

[55]   C. R. Cash, B. L. Nelson, D. G. Dippold, J. M. Long, and W. P. Pollard, "Evaluation of tests for initial-condition bias," pp. 577-585, 1992.

[56]   D. Goldsman, L. W. Schruben, and J. J. Swain, "Tests for transient means in simulated time series," *Naval Research Logistics (NRL),* vol. 41, pp. 171-187, 1994.

[57]   S. Robinson, "New simulation output analysis techniques: a statistical process control approach for estimating the warm-up period," 2002, pp. 439-446.

[58]   W. W. Franklin, "The theoretical foundation of the MSER algorithm," University of Virginia, 2010.

[59]   S. Cao, "Statistically based techniques for process control applications," Texas Tech University, 1996.

[60]   J. K Preston White, "An effective truncation heuristic for bias reduction in simulation output," *Simulation,* vol. 69, pp. 323-334, 1997.

[61]   K. P. White Jr, M. J. Cobb, and S. C. Spratt, "A comparison of five steady-state truncation heuristics for simulation," 2000, pp. 755-760.

[62]   E. L. Crow, F. A. Davis, and M. W. Maxfield, *Statistics manual: with examples taken from ordnance development* vol. 3369: Dover Publications, 1960.

[63]   M. Schladt and B. Hu, "Soft sensors based on nonlinear steady-state data reconciliation in the process industry," *Chemical Engineering and Processing: Process Intensification,* vol. 46, pp. 1107-1115, 2007.

[64]   S. A. Bhat and D. N. Saraf, "Steady-state identification, gross error detection, and data reconciliation for industrial process units," *Industrial & engineering chemistry research,* vol. 43, pp. 4323-4336, 2004.

[65]   M. Kim, S. H. Yoon, P. A. Domanski, and W. Vance Payne, "Design of a steady-state detector for fault detection and diagnosis of a residential air conditioner," *International Journal of Refrigeration,* vol. 31, pp. 790-799, 2008.

[66]   J. Chen and J. Howell, "A self-validating control system based approach to plant fault detection and diagnosis," *Computers & Chemical Engineering,* vol. 25, pp. 337-358, 2001.

[67]   A. Mhamdi, W. Geffers, F. Flehmig, and W. Marquardt, *On-line optimization of MSF desalination plants*: LPT, RWTH, 1999.

[68]   S. K. Mahuli, R. Russell Rhinehart, and J. B. Riggs, "Experimental demonstration of non-linear model-based in-line control of pH," *Journal of Process Control,* vol. 2, pp. 145-153, 1992.

[69]   J. Wu, S. Zhou, and X. Li, "Acoustic Emission Monitoring for Ultrasonic Cavitation Based Dispersion Process," *Journal of Manufacturing Science and Engineering,* vol. 135, pp. 031015-031015, 2013.

[70]   C. R. Cash, B. L. Nelson, D. G. Dippold, J. M. Long, and W. P. Pollard, "Evaluation of tests for initial-condition bias," 1992, pp. 577-585.

[71]   W. D. Kelton and A. M. Law, "A new approach for dealing with the startup problem in discrete event simulation," *Naval Research Logistics Quarterly,* vol. 30, pp. 641-658, 1983.

[72]   Y. Yao, C. Zhao, and F. Gao, "Batch-to-Batch Steady State Identification Based on Variable Correlation and Mahalanobis Distance," *Industrial & Engineering Chemistry Research,* vol. 48, pp. 11060-11070, 2009.

[73]   T. Jiang, B. Chen, X. He, and P. Stuart, "Application of steady-state detection method based on wavelet transform," *Computers & chemical engineering,* vol. 27, pp. 569-578, 2003.

[74]   H. Li, "A decoupling-based unified fault detection and diagnosis approach for packaged air conditioners," 2004.

[75]   S. Natarajan and R. R. Rhinehart, "Automated stopping criteria for neural network training," in *American Control Conference, 1997. Proceedings of the 1997*, 1997, pp. 2409-2413.

[76] K. Hoad, S. Robinson, and R. Davies, "Automating warm-up length estimation," *Journal of the Operational Research Society,* vol. 61, pp. 1389-1403, 2009.

[77] S. Robinson, *Simulation: the practice of model development and use*: Wiley, 2004.

[78] S. Robinson, "A statistical process control approach to selecting a warm-up period for a discrete-event simulation," *European Journal of Operational Research,* vol. 176, pp. 332-346, 2007.

[79] G. Gordon, *System Simulation*: Prentice Hall PTR, 1977.

[80] B. L. Nelson, "Statistical analysis of simulation results," *Handbook of Industrial Engineering: Technology and Operations Management, Third Edition,* pp. 2469-2495, 1992.

[81] M. D. Rossetti, Z. Li, and P. Qu, "Exploring exponentially weighted moving average control charts to determine the warm-up period," in *Simulation Conference, 2005 Proceedings of the Winter*, 2005, p. 10 pp.

[82] K. Pawlikowski, "Steady-state simulation of queueing processes: survey of problems and solutions," *ACM Comput. Surv.,* vol. 22, pp. 123-170, 1990.

[83] S. Chick, P. Sánchez, D. Ferrin, and D. Morrice, "A WAVELET-BASED SPECTRAL METHOD FOR STEADY-STATE SIMULATION ANALYSIS."

[84] D. H. Ockerman and D. Goldsman, "Student *t*-tests and compound tests to detect transients in simulated time series," *European Journal of Operational Research,* vol. 116, pp. 681-691, 1999.

[85] P. Jackway and B. M. Desilva, "A methodology for initialisation bias reduction in computer simulation output," 1992.

[86] R. M. Bethea and R. R. Rhinehart, *Applied engineering statistics*: Marcel Dekker, 1991.

[87] W. Holly, R. Cook, and C. Crowe, "Reconciliation of mass flow rate measurements in a chemical extraction plant," *The Canadian Journal of Chemical Engineering,* vol. 67, pp. 595-601, 1989.

[88] S. Narasimhan, C. S. Kao, and R. Mah, "Detecting changes of steady states using the mathematical theory of evidence," *AIChE journal,* vol. 33, pp. 1930-1932, 1987.

[89] P. Fearnhead, "Exact and efficient Bayesian inference for multiple changepoint problems," *Statistics and computing,* vol. 16, pp. 203-213, 2006.

[90] N. Chopin, "Dynamic detection of change points in long time series," *Annals of the Institute of Statistical Mathematics,* vol. 59, pp. 349-366, 2007.

[91] S. Chib, "Estimation and comparison of multiple change-point models," *Journal of econometrics,* vol. 86, pp. 221-241, 1998.

[92] P. J. Green, "Reversible jump Markov chain Monte Carlo computation and Bayesian model determination," *Biometrika,* vol. 82, pp. 711-732, 1995.

[93] E. Punskaya, C. Andrieu, A. Doucet, and W. J. Fitzgerald, "Bayesian curve fitting using MCMC with applications to signal segmentation," *Signal Processing, IEEE Transactions on,* vol. 50, pp. 747-758, 2002.

[94] A. Doucet, N. de Freitas, and N. Gordon, "Sequential Monte Carlo methods in practice," *Statistics,* 2001.

[95] A. Doucet and A. M. Johansen, "A tutorial on particle filtering and smoothing: fifteen years later," *Handbook of Nonlinear Filtering,* vol. 12, pp. 656-704, 2009.

[96] P. Giordani and R. Kohn, "Efficient Bayesian inference for multiple change-point and mixture innovation models," *Journal of Business & Economic Statistics,* vol. 26, 2008.

[97] X. Wang, *Incorporating knowledge on segmental duration in HMM-based continuous speech recognition*: IFOTT, 1997.

[98] M. S. Arulampalam, S. Maskell, N. Gordon, and T. Clapp, "A tutorial on particle filters for online nonlinear/non-Gaussian Bayesian tracking," *Signal Processing, IEEE Transactions on,* vol. 50, pp. 174-188, 2002.

[99] A. Doucet, S. Godsill, and C. Andrieu, "On sequential Monte Carlo sampling methods for Bayesian filtering," *Statistics and computing,* vol. 10, pp. 197-208, 2000.

[100] W. G. Cochran, *Sampling techniques*: John Wiley & Sons, 2007.

[101] N. Raghavan and D. D. Cox, "Adaptive mixture importance sampling," *Journal of Statistical Computation Simulation,* vol. 60, pp. 237-259, 1998.

[102] N. Chopin, "Central limit theorem for sequential Monte Carlo methods and its application to Bayesian inference," *The Annals of Statistics,* vol. 32, pp. 2385-2411, 2004.

[103] W. R. Gilks and C. Berzuini, "Following a moving target—Monte Carlo inference for dynamic Bayesian models," *Journal of the Royal Statistical Society: Series B (Statistical Methodology),* vol. 63, pp. 127-146, 2001.

[104] W. W. Franklin, "The Theoretical Foundation of the MSER Algorithm," University of Virginia, 2009.

[105] R. P. Adams and D. J. MacKay, "Bayesian online changepoint detection," *arXiv preprint arXiv:0710.3742,* 2007.

[106] P. Fearnhead and Z. Liu, "On-line inference for multiple changepoint problems," *Journal of the Royal Statistical Society: Series B (Statistical Methodology),* vol. 69, pp. 589-605, 2007.

[107] C.-K. Wong and M. C. Easton, "An efficient method for weighted sampling without replacement," *SIAM Journal on Computing,* vol. 9, pp. 111-113, 1980.

[108] F. G. Tricomi and A. Erdélyi, "The asymptotic expansion of a ratio of gamma functions," *Pacific J. Math,* vol. 1, pp. 133-142, 1951.

[109] B. Li and B. D. Moor, "A corrected normal approximation for the Student's t distribution," *Computational Statistics & Data Analysis,* vol. 29, pp. 213-216, 1998.

[110] S. Kotz and S. Nadarajah, *Multivariate t-distributions and their applications*: Cambridge University Press, 2004.

[111] H. Choi, W.-h. Cho, H. Konishi, S. Kou, and X. Li, "Nanoparticle-Induced Superior Hot Tearing Resistance of A206 Alloy," *Metallurgical and Materials Transactions A,* pp. 1-11, 2013.

[112] M. Esfahani and B. Niroumand, "Study of hot tearing of A206 aluminum alloy using Instrumented Constrained T-shaped Casting method," *Materials Characterization,* vol. 61, pp. 318-324, 2010.

[113] X. Li, Y. Yang, and D. Weiss, "Theoretical and experimental study on ultrasonic dispersion of nanoparticles for strengthening cast Aluminum Alloy A356," *Met. Sci. Technol,* vol. 26, pp. 12-20, 2008.

[114] Y. Yang and X. Li, "Ultrasonic cavitation-based nanomanufacturing of bulk aluminum matrix nanocomposites," *Journal of Manufacturing Science and Engineering,* vol. 129, pp. 252-255, 2007.

[115] G. Cao, H. Konishi, and X. Li, "Mechanical Properties and Microstructure of Mg⁄ SiC Nanocomposites Fabricated by Ultrasonic Cavitation Based Nanomanufacturing," *Journal of Manufacturing Science and Engineering,* vol. 130, p. 031105, 2008.

[116] Y. Gao, B. Wu, Z. Liu, Y. Zhou, N. Shen, and H. Ding, "Ultrasonic Cavitation Peening of Stainless Steel and Nickel Alloy," *Journal of Manufacturing Science and Engineering,* vol. 136, p. 014502, 2014.

[117] Y. Sun, "Microstructure modification by nanoparticles in aluminum and magnesium matrix nanocomposites," Master Master's thesis, Materials Science, University of Wisconsin--Madison, 2012.

[118] J. Wu, Chen, Yong, Li, Xiaochun, Zhou, Shiyu, "Online Steady-state Detection for Process Control Using Multiple Change-point Models and Particle Filters," *IEEE Transactions on Automation Science and Engineering,* 2014.

[119] L. W. Schmerr, *Fundamentals of ultrasonic nondestructive evaluation: a modeling approach*: Plenum Press New York, 1998.

[120] J. Krautkrämer and H. Krautkrämer, "Ultrasonic testing of materials," 1990.

[121] J. Szilard, "Ultrasonic testing: Non-conventional testing techniques," *JOHN WILEY & SONS, INC., 605 THIRD AVE., NEW YORK, NY 10158, 1982, 640,* 1982.

[122] A. R. Portune, "Nondestructive Ultlrasonic Characterization of Armor Grade Silicon Carbide," Ph.D. PhD thesis, Materials Science and Engineering, The State University of New Jersey, 2011.

[123] S. Bottiglieri, "The Effect of Microstructure in Aluminum Oxide Ceramics on Acoustic Loss Mechanisms," Ph.D. PhD thesis, Materials Science and Engineering, The State University of New Jersey, The State University of New Jersey, 2012.

[124] H. Fukuoka, H. Toda, K. Hirakawa, H. Sakamoto, and Y. Toya, "Nondestructive assessments of residual stresses in railroad wheel rim by acoustoelasticity," *Journal of Manufacturing Science and Engineering,* vol. 107, pp. 281-287, 1985.

[125] A. B. Bhatia, *Ultrasonic absorption: an introduction to the theory of sound absorption and dispersion in gases, liquids, and solids*: DoverPublications. com, 1985.

[126] M. Treiber, J.-Y. Kim, J. Qu, and L. J. Jacobs, "Effects of sand aggregate on ultrasonic attenuation in cement-based materials," *Materials and structures,* vol. 43, pp. 1-11, 2010.

[127] B. Hartmann and J. Jarzynski, "Ultrasonic hysteresis absorption in polymers," *Journal of applied physics,* vol. 43, pp. 4304-4312, 1972.

[128] W. P. Mason and H. McSkimin, "Attenuation and scattering of high frequency sound waves in metals and glasses," *The Journal of the Acoustical Society of America,* vol. 19, p. 464, 1947.

[129] L. J. Jacobs and J. O. Owino, "Effect of aggregate size on attenuation of Rayleigh surface waves in cement-based materials," *Journal of Engineering Mechanics,* vol. 126, pp. 1124-1130, 2000.

[130] S. Biwa, "Independent scattering and wave attenuation in viscoelastic composites," *Mechanics of materials,* vol. 33, pp. 635-647, 2001.

[131] P. S. Epstein and R. R. Carhart, "The absorption of sound in suspensions and emulsions. I. Water fog in air," *The Journal of the Acoustical Society of America,* vol. 25, p. 553, 1953.

[132] R. Challis, J. Tebbutt, and A. Holmes, "Equivalence between three scattering formulations for ultrasonic wave propagation in particulate mixtures," *Journal of Physics D: Applied Physics,* vol. 31, p. 3481, 1998.

[133] D. McClements, "Principles of ultrasonic droplet size determination in emulsions," *Langmuir,* vol. 12, pp. 3454-3461, 1996.

[134] F. M. Sears and B. P. Bonner, "Ultrasonic attenuation measurement by spectral ratios utilizing signal processing techniques," *Geoscience and Remote Sensing, IEEE Transactions on,* pp. 95-99, 1981.

[135] A. Ganguli, R. X. Gao, K. Liang, J. Jundt, and A. Ordonez, "Experimental Investigation of Ultrasound Wave Focusing in Attenuative Solids," *Instrumentation and Measurement, IEEE Transactions on,* vol. 59, pp. 2261-2271, 2010.

[136] W. Xu and J. J. Kaufman, "Diffraction correction methods for insertion ultrasound attenuation estimation," *Biomedical Engineering, IEEE Transactions on,* vol. 40, pp. 563-570, 1993.

[137] R. Zheng, L. H. Le, M. D. Sacchi, D. Ta, and E. Lou, "Spectral ratio method to estimate broadband ultrasound attenuation of cortical bones in vitro using multiple reflections," *Physics in medicine and biology,* vol. 52, p. 5855, 2007.

[138] W. Punurai, J. Jarzynski, J. Qu, K. E. Kurtis, and L. J. Jacobs, "Characterization of entrained air voids in cement paste with scattered ultrasound," *NDT & E International,* vol. 39, pp. 514-524, 2006.

[139] P. H. Rogers and A. Van Buren, "An exact expression for the Lommel-diffraction correction integral," *The Journal of the Acoustical Society of America,* vol. 55, p. 724, 1974.

[140] M. Nave, A. Dahle, and D. St John, "The role of zinc in the eutectic solidification of magnesium-aluminium-zinc alloys," in *Magnesium Technology 2000*, 2000, pp. 243-250.

[141] A. Bhattacharjee, A. Pilchak, O. Lobkis, J. Foltz, S. Rokhlin, and J. Williams, "Correlating ultrasonic attenuation and microtexture in a near-alpha titanium alloy," *Metallurgical and Materials Transactions A,* vol. 42, pp. 2358-2372, 2011.

[142] Y. Han and R. Thompson, "Ultrasonic backscattering in duplex microstructures: theory and application to titanium alloys," *Metallurgical and Materials Transactions A,* vol. 28, pp. 91-104, 1997.

[143] A. Mukhopadhyay, R. Sarkar, S. Punnose, J. Valluri, T. K. Nandy, and K. Balasubramaniam, "Scatter in nonlinear ultrasonic measurements due to crystallographic orientation change induced anisotropy in harmonics generation," *Journal of applied physics,* vol. 111, pp. 054905-054905-11, 2012.

[144] M. Gigliotti, B. Bewlay, J. Deaton, R. Gilmore, and G. Salishchev, "Microstructure-ultrasonic inspectability relationships in Ti6242: Signal-to-noise in fine-grain-processed Ti6242," *Metallurgical and Materials Transactions A,* vol. 31, pp. 2119-2125, 2000.

[145] D. J. Schrock, D. Kang, T. R. Bieler, and P. Kwon, "Phase Dependent Tool Wear in Turning Ti-6Al-4V Using Polycrystalline Diamond and Carbide Inserts," *Journal of Manufacturing Science and Engineering,* vol. 136, p. 041018, 2014.

[146] B. Yilbas, S. Akhtar, A. Matthews, C. Karatas, and A. Leyland, "Microstructure and Thermal Stress Distributions in Laser Carbonitriding Treatment of Ti–6Al–4V Alloy," *Journal of Manufacturing Science and Engineering,* vol. 133, p. 021013, 2011.

[147] M. Dargusch, "Finite Element Modeling of Cutting Force and Chip Formation During Thermally Assisted Machining of Ti6Al4V Alloy," *Simulation,* vol. 17, p. 20, 2013.

[148] E. P. Papadakis, "Ultrasonic attenuation caused by scattering in polycrystalline metals," *The Journal of the Acoustical Society of America,* vol. 37, p. 711, 1965.

[149] Y. Liu, J. Wu, S. Zhou, and X. Li, "Microstructure Modelling and Ultrasonic Wave Propagation Simulation of A206-Al_2O_3 Metal Matrix Nanocomposites for Quality Inspection," *Journal of manufacturing science and engineering,* 2015.

[150] L. Zeng and N. Chen, "Bayesian hierarchical modeling for monitoring optical profiles in low-E glass manufacturing processes," *IIE Transactions,* vol. 47, pp. 109-124, 2015.

[151] W. A. Jensen, J. B. Birch, and W. H. Woodall, "Monitoring correlation within linear profiles using mixed models," *Journal of Quality Technology,* vol. 40, pp. 167-183, 2008.

[152] S. W. Raudenbush and A. S. Bryk, *Hierarchical linear models: Applications and data analysis methods* vol. 1: Sage, 2002.

[153] H. Goldstein, *Multilevel statistical models* vol. 922: John Wiley & Sons, 2011.

[154] X. Lin, J. Raz, and S. D. Harlow, "Linear mixed models with heterogeneous within-cluster variances," *Biometrics,* pp. 910-923, 1997.

[155] J. L. Foulley and R. Quaas, "Heterogeneous variances in Gaussian linear mixed models," *Genetics Selection Evolution,* vol. 27, pp. 211-228, 1995.

[156] H. Zheng, Y. Yang, and K. C. Land, "Variance Function Regression in Hierarchical Age-Period-Cohort Models Applications to the Study of Self-Reported Health," *American sociological review,* vol. 76, pp. 955-983, 2011.

[157] J. C. Pinheiro and D. M. Bates, *Mixed-effects models in S and S-PLUS*: Springer Science & Business Media, 2000.

[158] G. K. Smyth, A. F. Huele, and A. P. Verbyla, "Exact and approximate REML for heteroscedastic regression," *Statistical modelling,* vol. 1, pp. 161-175, 2001.

[159] M. Davidian and R. J. Carroll, "Variance function estimation," *Journal of the American statistical association,* vol. 82, pp. 1079-1091, 1987.

[160] A. Gelman, J. B. Carlin, H. S. Stern, and D. B. Rubin, *Bayesian data analysis* vol. 2: Taylor & Francis, 2014.

[161] J. P. Hobert and G. Casella, "The effect of improper priors on Gibbs sampling in hierarchical linear mixed models," *Journal of the American statistical association,* vol. 91, pp. 1461-1473, 1996.

[162] J. S. Liu, W. H. Wong, and A. Kong, "Covariance structure of the Gibbs sampler with applications to the comparisons of estimators and augmentation schemes," *Biometrika,* vol. 81, pp. 27-40, 1994.

[163] S. Chib and E. Greenberg, "Understanding the metropolis-hastings algorithm," *The american statistician,* vol. 49, pp. 327-335, 1995.

[164] A. Gelman, "Prior distributions for variance parameters in hierarchical models (comment on article by Browne and Draper)," *Bayesian analysis,* vol. 1, pp. 515-534, 2006.

[165] H. Akaike, "Information theory and an extension of the maximum likelihood principle," in *Selected Papers of Hirotugu Akaike*, ed: Springer, 1998, pp. 199-213.

[166] G. Schwarz, "Estimating the dimension of a model," *The Annals of Statistics,* vol. 6, pp. 461-464, 1978.

[167] J. O. Berger, L. R. Pericchi, J. Ghosh, T. Samanta, F. De Santis, J. Berger, and L. Pericchi, "Objective Bayesian methods for model selection: introduction and comparison," *Lecture Notes-Monograph Series,* pp. 135-207, 2001.

[168] R. E. Kass and A. E. Raftery, "Bayes factors," *Journal of the American statistical association,* vol. 90, pp. 773-795, 1995.

[169] C. Han and B. P. Carlin, "Markov chain Monte Carlo methods for computing Bayes factors," *Journal of the American statistical association,* vol. 96, 2001.

[170] J. O. Berger and L. R. Pericchi, "The intrinsic Bayes factor for model selection and prediction," *Journal of the American statistical association,* vol. 91, pp. 109-122, 1996.

[171] J. S. Liu, *Monte Carlo strategies in scientific computing*: springer, 2008.

[172] C. Villagómez, L. Medina, and W. Pereira, "Open source acoustic wave solver of elastodynamic equations for heterogeneous isotropic media," in *Ultrasonics Symposium (IUS), 2012 IEEE International*, 2012, pp. 1521-1524.